PREDICTING INCIPENT INSTABILITIES AND BIFURCATIONS
OF NONLINEAR DYNAMICAL SYSTEMS
MODELLING COMPLIANT OFF-SHORE STRUCTURES

by

LAP MING LEUNG, B.Sc.

A thesis submitted for the degree of Doctor of Philosophy
in the University of London

Department of Civil and Municipal Engineering
University College London
November 1990

ProQuest Number: 10609167

ProQuest 10609167

Abstract

For engineers, the two most important aspects of dynamical analysis are high amplitude resonance vibrations and structural stability, i.e. whether a steady state solution is stable under small perturbations.

For the former case, a novel and simple method based on Poincaré mapping technique has been devised to predict an imminent flip bifurcation. This bifurcation represents the beginning of the second order subharmonic response.

For the latter case, we discovered that while classical quantitative analytical techniques work well in establishing the 'local' structural stability of a steady state solution, the global geometric structure of the catchment region can alter dramatically such that even an initial condition close to the steady state can diverge from it rather than being attracted. This phenomenon known as fractal basin boundary occurs when the invariant manifolds of the saddle separating the steady state solution from any remote attractor cross. The critical point in which the invariant manifolds just touch can be accurately predict by the Melinkov's method. Because of the complicated interwoven nature of the invariant manifolds, it is called a tangle. If the invariant manifolds are originated from the same saddle, the crossing is known as a homoclinic tangle, if originated from different saddle, a heteroclinic tangle. The critical point is then known as homoclinic or heteroclinic tangency.

Tangles are also intimately related to chaotic behaviour. The creation and destruction of chaotic attractors have been observed through a series of homoclinic and heteroclinic tangency. In fact, after the invariant manifolds of an inverting saddle cross, the unstable manifold becomes the chaotic attractor. This leads us to believe that all chaotic attractors are topologically the same.

DEDICATION

This Thesis is dedicated to my parents who have
given up so much for this to be possible.

ACKNOWLEDGEMENTS

First and foremost, I would like to thank my supervisor, Prof. Michael Thompson FRS, for his endless enthusiasm and inspiring discussions during the course of this research. His ceaseless encouragement not only made this research possible but also hugely enjoyable. For this I shall be for ever grateful.

Thanks also go to my colleagues and friends Steve Bishop, Lawrence Virgin, Andreas Kyriacou, Chris Tam, Manou Kashani and Takis Koliopoulos for their constant encouragement and memorable company. A special acknowledgement must go to the University College London Computer Centre system development team for their advice in using system software and hardware and granting me outrageous use of system time. I am also grateful to Dr C. Kass-Petersen of Leeds University for his contribution to the path following technique used in this research.

Finally, the author must extend his gratitude to the Ovearseas Research Student's Award for their financial support.

Contents

Preface

Over the past decade, physicists, biologists, astronomers and economists have found a new way of understanding the growth of complexity in nature. This new science, called chaos offers a new way of seeing order and pattern where formerly only randomness or unpredictability was observed.

Chaos in engineering is a relatively new subject, probably because engineers are more interested in steady state behaviour and large amplitude resonance phenomena. Even when they find some "noisy" behaviour, they would most probably attribute it to some form of numerical error. In 1985, J.M.T. Thompson and R. Ghafarri of University College London, London University were researching into the dynamical behaviour of a mooring tower used in the North Sea. Because of the discontinuity in the restoring force, non-linear dynamical behaviours were found. Typically, a fundamental resonance response curve coexists with a high amplitude subharmonic solution. Coexisting solutions serve as a warning to engineers whose usual practice is to use an existing steady state solution as the initial state when the control parameter is changed, thus probably missing the high amplitude solution.

Most important of all, when the mathematical model of this mooring tower was modified to take into account the condition in which one restoring force was infinitely stronger than the other, a persistent gap was observed between periodic solutions where no steady state solution could be established. They used different numerical methods to solve their mathematical model and observed the same behaviour. Instead of attributing these to numerical errors or even instability, they used the Poincaré mapping technique to look at the phase space of this system and to their amazement, instead of a random behaviour, they discovered a well structured pattern of dots in the phase space. While they could not predict the movement of any one dot after each cycle, they certainly knew that it would stay within the structure. This was the hallmark of chaotic dynamics. After their report of chaos in engineering structures, more engineers have reported the discovery of chaotic behaviour.

This thesis is a continuation of the work since the discoveries of chaotic behaviour exhibit by the mooring tower. Tremendous progress has been made since then. These include research into fractal basin boundaries, tangles and Melinkov's theory.

The thesis will be divided into three parts. The first part will be a discussion of basic theory of bifurcation and chaotic dynamics. The second part will be theory and techniques developed and used in the course of the research. The third part is the applications, where practical problems are developed into mathematical models and extensive investigations have been conducted.

1 Dynamics of Flow

All bodies possessing mass and elasticity are capable of vibration. Thus most engineering structures experience vibrations and their design generally requires consideration of their oscillatory behaviours.

Oscillatory systems can be broadly characterized as linear or nonlinear. For linear systems the principle of superposition holds, and mathematical techniques available for their treatment are well developed[1,2]. In contrast, techniques for the analysis of nonlinear systems are less well known, and difficult to apply. Moreover, techniques like perturbation method and harmonic balance give only approximate solutions[3-6]. As most real-world dynamical problems and engineering structures confronting the analyst are nonlinear, mathematical models very often can only be investigated by numerical simulations. With the wide availability of powerful computers, the qualitative topological approach has now been recognized as an essential tool to the understanding and interpretation of the results produced by numerical techniques. Furthermore, this new approach has given us new insight into the mechanisms in which instabilities occur and from which method of prevention can be devised. Introduction to geometric theory for ordinary differential equations can be found in Jordan and Smith[7], Abraham and Shaw[8-10], Thompson and Stewart[11], and Arnold[12].

The approach we shall adopt in tackling engineering dynamical systems can be broken down into the following steps:

1.)   Construction of a mathematical model.

2.)   Direct numerical integration to obtain general information.

3.)   Topological techniques to classify equilibrium or fixed points and identify instability phenomena.

4.)   Quantify the characteristic of an imminent bifurcation.

Qualitative theory will centre mainly on the identification and study of fixed or equilibrium points. Elementary fixed points include the stable 'centre' and 'sink' and the unstable 'source' and 'saddle point'. We shall see later that a 'centre'

represents a pathological condition between stability and instability which is not 'generic' and hence 'structurally unstable'. Here the essential meaning of stability can be defined as: if any small perturbation close to a fixed point remains close to the fixed point at all time, the fixed point is stable.

We begin in this Chapter a brief examination of dynamical systems theory. Terminology used throughout this thesis will also be defined. Although there is a relatively complete quantitative and analytical theory for linear differential equations, a study of many nonlinear equations involves transformation into a linearized form: hence a brief review of linear oscillators will serve well to illustrate some fundamental concepts and features of the phase plane.

1.1 Autonomous systems

The second order differential equation of general type

$$\ddot{x} = f(x, \dot{x}, t) \tag{1.1}$$

can be interpreted as an equation of motion for a mechanical system. Here x represents displacement of a particle of unit mass, $\dot{x}$ its velocity, $\ddot{x}$ its acceleration and f the applied force, so that equation (1.1) express Newton's law of motion for the particle:

$$\text{acceleration} = \text{force per unit mass.}$$

A mechanical system is in equilibrium if its state does not change with time. This implies that an equilibrium state corresponds to a constant solution of equation (1.1).

We distinguish between two types of equation:

(i)   the autonomous type in which f does not depend explicitly on t.

(ii)   the non-autonomous or forced equation where t appears explicitly in the function f.

A typical autonomous equation of motion is the linear oscillator expressed in the standard form

$$\ddot{x} + b\dot{x} + cx = 0 \tag{1.2}$$

where b characterizes the damping and c the stiffness. Plotting the acceleration $\ddot{x}$ against the displacement x as shown in Figure (1b), we have for light damping the familiar damped oscillatory motions typical of a pendulum vibrating with small amplitude in air. The only equilibrium state is the state of rest, i.e., $(\dot{x}, x) = (0, 0)$ and if the damping b is zero, this is called a centre. Since any damping introduced will destroy the topology of the phase space trajectories, this is structurally unstable, as can be seen by comparing Figure (1a) and Figure (1b).

Stable equilibrium states are not the only attractors that can arise in a two-dimensional phase space. A second type of attractor is the stable limit cycle, namely a steady closed oscillation that attracts all adjacent motions. In order to construct this mechanical oscillator, we must first ensure that for small amplitude oscillations the damping is negative so that amplitude will increase. However, large amplitude oscillations are contained by introducing a positive damping. In effect, a nonlinear damping term is necessary. We consider, then, the oscillator

$$\ddot{x} - c\dot{x} + d\dot{x}^3 + kx = 0$$

and typical trajectories are shown in Figure (2). For given initial conditions $(\dot{x}, x)$ with small amplitude, we can linearize the above equation and drop the $d\dot{x}^3$ term. We then have an unstable focus due to negative damping. Here trajectories spiral outwards away from the centre point repellor. For large amplitudes, the nonlinear term dominates, ensuring that all motions of the system tend towards a stable steady-state oscillation, the limit cycle. In fact, this is the only possible attractor and the whole phase space is its domain of attraction. One can see immediately in this simple example the importance of taking into account nonlinear effects when large amplitude oscillations are possible.

The nature of the solution for the linear oscillator modelled by equation (1.2) can be classified by looking at the characteristic equation. Assuming the solution $x = Ae^{\lambda t}$, and substituting this relation into equation (1.2) gives

$$(\lambda^2 + b\lambda + c)Ae^{\lambda t} = 0$$

For a non-trivial solution we must have

$$\lambda^2 + b\lambda + c = 0$$

The roots of this characteristic equation can be obtained from

$$\lambda_1 = \frac{-b + \sqrt{(b^2 - 4c)}}{2}$$

$$\lambda_2 = \frac{-b - \sqrt{(b^2 - 4c)}}{2}$$

These roots can be real or complex depending on the discriminant D, where

$$D = b^2 - 4c$$

and hence it is this parameter that determines the type of motions.

If D is positive, we have two distinct real roots and the assumed solution is therefore

$$x = A_1 e^{\lambda_1 t} + A_2 e^{\lambda_2 t} \tag{1.3}$$

where A_1 and A_2 are arbitrary integration constants to be found from the initial conditions. If D is negative, we have a pair of complex conjugate roots $\lambda_{1,2} = R \pm Ii$, giving solutions of the form

$$x = e^{Rt} \sin It \tag{1.4}$$

Furthermore from equation (1.3) and (1.4), it can be seen that if the roots are real we have a monotonic convergence or divergence of the trajectories. If the roots are complex then we have trajectories which spiral towards an attractor or away from a repellor. Also, a real and positive eigenvalue or a complex eigenvalue with a positive real part means that the equilibrium solution is unstable. Therefore the eigenvalues characterized stability[13,14] of the equilibrium point and they are sometimes refered to as Liapunov exponents[15]. This is summarized in Figure (3) which shows sketches of the phase portraits next to the corresponding (R, I) Argand diagrams. For thorough stability we must have $b > 0$ and $c > 0$.

1.2 Structural stability and hyperbolicity

We can now define more precisely the meaning of stability. Although an equilibrium is identified by the condition that the vector field vanishes at a point, a full-phase-space picture of different types of equilibria emerges only by considering the structure of trajectories nearby. For a nonlinear dynamical system the basic types of equilibrium can be identified by a local linearized version of the dynamics near the point of equilibrium. That is, the nonlinear equations are replaced by approximate linear equations; this approximation is only correct in a small region of phase space surrounding the equilibrium point and when the equilibrium is not critical.

Consider an n-dimensional system of first-order differential equations, where x is an n-dimensional vector and F is a real n-dimensional vector function:

$$\dot{x} = F(x)$$

and suppose that the point $P^E = (x^E)$ is an equilibrium state characterized by:

$$F(x^E) = 0$$

This equilibrium point is stable if every nearby solution stays nearby for all future time. If the equilibrium configuration is represented by the point P^E in the space of the variables x, it is clear that a perturbation can be represented by a point P in the neighbourhood of P^E. We will say that P^E is Liapunov stable[16] if, for every neighbourhood U of P^E in this phase space, there exists a smaller neighbourhood U_1 of P^E contained in U, such that every solution starting in U_1 will remain in U for all t>0.

If all solutions tend to the equilibrium as t tends to infinity, then P^E is said to be asymptotically stable. Conversely, if it is possible to find any local perturbation that moves the system away from rest, P^E is called an unstable equilibrium point. Hence while a centre is stable it is not asymptotically stable or structurally stable. These three different qualities of equilibria are illustrated in Figure (4).

Consider again our n-dimensional system of first-order differential equations, according to our definition, we must superimpose a disturbance ξ to x^E, obtaining the perturbed equation:

$$\dot{\xi} = F(x^E + \xi)$$

Next, $F(x^E + \xi)$ can be expanded in a Taylor series around x^E, so that:

$$\dot{\xi} = F(x^E) + F_x(x^E)\xi + \frac{1}{2}F_{xx}(x^E)\xi^2 + \ldots$$

where for example $F_x(x^E)\xi$ is the Jacobian of F evaluated at the rest state.

Since stability can be detected by examining a small neighbourhood of the equilibrium point, so ξ can be assumed small, and its successive powers $\xi^2, \xi^3, \ldots$ can normally be neglected. On the other hand $F(x^E)$ is zero for equilibrium, and the following linear variational equation can be written:

$$\dot{\xi} = F_x(x^E)\xi$$

The solution $\xi(t) = \{\xi_1(t), \ldots, \xi_n(t)\}$ must tend to vanish when t goes to infinity, if the equilibrium state is to be asymptotically stable. The condition for this is that the real parts of all the eigenvalues of $H = F_x(x^E)$ must be negative.

Hence the topological condition has been converted into an algebraic condition. To examine the stability of a normal equilibrium point we have now merely to solve the characteristic equation, and to examine the real parts of its roots. An equilibrium point whose local linearization involves only eigenvalues with non-zero real parts is called *hyperbolic*. Here we can define the index of an equilibrium point as the number of eigenvalue with positive real part, as illustrated for example by Abraham and Shaw[10]. If this index is equal to zero, then in the linear approximation the equilibrium is stable. Increasing values of the index correspond to increasing degrees of instability near the equilibrium point; we might therefore refer to this integer as the *instability index*.

Once the instability index of an equilibrium point is determined by counting the signs of the real parts of the eigenvalues, additional information can be found in the imaginary parts of the eigenvalues. If the ordinary differential equations are written, as we have assumed, for real quantities, the local linearizations must have only real coefficients, and so complex eigenvalues occur only in conjugate pairs.

Figure (5) shows a sequence of different dynamics, each having an equilibrium point with complex conjugate eigenvalues. The clockwise angular speed on each trajectory in each system is the same, because the imaginary parts of the eigenvalues are the same; but the trajectories wind down rapidly, slowly, or not at all depending on the real part of the eigenvalues. In either of the first two cases, small changes in the dynamics can change the rate of decay but not the qualitative picture: trajectories of a perturbed system still spiral inwards. In the third case where the fix point is a centre, any perturbation of the dynamics will break the closed loops and cause trajectories all to spiral inwards or all to spirals outwards from the equilibrium. In the qualitative viewpoint, we can regard the non-hyperbolic equilibria, such as the centre in plane phase space, as having atypical structures nearby. Since we consider not just families of trajectories but families of nearby dynamical systems and the nearby systems might include all imaginable small perturbations of the dynamic laws and equations; they might also include all approximations that could be used in constructing a mathematical model. To obtain among all these a non-hyperbolic equilibria is hence atypical. Therefore, only the hyperbolic fixed points are *generic*. The two inward spiralling dynamics can also be qualitatively represented by any sufficiently good approximations. Thus the dynamics near a hyperbolic equilibrium point are structurally stable, while the non-hyperbolic equilibrium point is not structurally stable. For this reason, we believe that local linearization is a valid approximation for hyperbolic fixed points in any number of dimensions.

1.3 Local bifurcation

It is imperative to talk about instabilities with bifurcations. Very often, a loss of stability corresponds to a bifurcation when a control parameter is varied. In the geometric view point, we can define a bifurcation as any point in the control phase space which gives rise to a structurally unstable vector field. In particular, local bifurcation can be characterized near a single point in phase space: hence equilibrium point bifurcations are clearly included. We shall see later that using Poincaré mapping, the bifurcation of periodic orbits can also be characterized at a point and so can be classified as local bifurcations.

Local bifurcations can be studied by their normal form which is a low-order approximation of the original vector field. Typically, if

$$f(\mu, x_0(\mu)) = 0$$

where μ represents a single control parameter, then $x_0(\mu)$ are paths of equilibrium points in control phase space. Linearization of the vector field at each $x_0(\mu)$ give us the eigenvalues. Any value of μ_0 where the linearization has eigenvalues with zero real part is non-hyperbolic and hence a possible bifurcation point. Finally, we can compute the lowest order terms of the nonlinear function f to obtain the local form of bifurcation. Various forms of local bifurcation exist depending on the way in which the eigenvalues traverse the Argand plane.

If a dynamical system is dependent on a control parameter μ then by varying μ, the eigenvalues λ_j will describe some paths in the complex plane. Suppose that at $\mu = \mu_0$ the eigenvalues are all in the negative half plane, so that the system is asymptotically stable, and let μ increases. If the eigenvalues are assumed to cross the imaginary axis transversely, it is easy to see that the simplest ways in which a system can lose its stability are either a real eigenvalue crossing the imaginary axis or a pair of complex conjugate eigenvalues crossing the imaginary axis. The first case involves essentially one eigenvalue, and is therefore the simplest transition that can occur. The second, in which two eigenvalues cross the stability boundary as a pair, involves two eigenvalues, but there are strong simplifications because they are complex conjugate. In the presence of the necessary nonlinear coefficients these two transitions give rise to the only two typical bifurcations of equilibria that can be observed under the influence of a single control parameter. The first manifests itself as the Fold bifurcation[17], associated with an inherent stiffness dropping to zero, while the second gives the Hopf bifurcation[18,19], associated with an inherent damping changing from positive to negative. In either case, the *phase portrait* is structurally unstable at the point of bifurcation.

1.4 Global bifurcation

As we define bifurcations in a geometrical view point, a new class of bifurcation should be incorporated into our definition. These are the global bifurcations which sometime do not manifest themselves as a transfer of stability from one attractor to another like the Hopf or fold bifurcation. Bifurcations of the global type involve a qualitative change in the topology of the invariant manifolds, i.e., the inset and outset

of a saddle. One obvious example is the homoclinic connection in the Lorenz[20-22] system and the boat capsize problem which we shall discuss in a later chapter. Homoclinic tangency occurs when the inset and outset of a saddle touch. This qualitative change can dramatically affect the basin structure of the phase portrait without changing the attractor. Therefore, this special bifurcation can not be observed in the control phase diagram. However, this is especially dangerous as the basin of attraction is quickly eroded after tangency so that instability occurs when a small finite perturbation is given[23].

One example of global bifurcation which leads to a destruction of an attractor is the heteroclinic tangency. Here tangency occurs between the inset and outset of different saddles. This bifurcation again can be observed in the boat capsize problem.

As a further example, consider the Blue Sky Catastrophe[24] in which a homoclinic connection results in a limit cycle disappearing into the blue. This is schematically illustrated in Figure (6). In the leftmost portrait, the inset of the saddle point at the top is a separatrix between two basins. Below this separatrix, all points generate trajectories which eventually settle onto the limit cycle. Above the seperatrix any point will generate trajectories which moves away to a remote attractor. As the control parameter is varied, the inset moves closer to the limit cycle and they eventually coincide at μ^c. The homoclinic orbit now has an infinite period and as the parameter is increased further, the relative position of the inset and outset has interchanged so that all points generate trajectories which diverge to the remote attractor. The inset has ceased to be a separator and the limit cycle has vanished into the blue.

We must note here that this dynamical system has only a two dimensional phase space so that homoclinic connection generates a closed orbit. In a three dimensional case as we shall consider, the inset can cross without forming a closed orbit and an attractor can be destroyed when the inset touches it. Also, Blue Sky catastrophe is a discontinuous bifurcation and in the terminology of Shilnikov[25] this is a dangerous boundary.

A sub-class of the global bifurcations is the local/global bifurcations whereby a local bifurcation, for example a fold catastrophe, triggers a sudden discontinuous transition. This transition is determined by the global structure of invariant manifolds. One such example is the intermittency explosion to a chaotic attractor which occurs

typically in the periodic window during a cascade of period doubling bifurcations. Before the transition to chaos, we can expect the global structure of the phase space will give rise to chaotic transients. (This will become clear in Chapter 3.)

A complete classification by Thompson et al[11,26] of bifurcation arranged according to their topological dimension and incorporating various terminologies is shown in Figure (7). In summary, there are two basic types of bifurcation, one is the local type where bifurcation occurs distinctly in the control phase diagram and usually a normal form analysis can be performed. While the point at which homoclinic tangency occurs can sometimes be obtained analytically using for example the Melinkov's method, global bifurcation involves a study of the phase space itself. Any global bifurcation is determined only by the geometrical or topological configuration of the invariant manifolds. Hence global bifurcations have no algebraic solution.

1.5 Non-autonomous System

A typical non-autonomous system is the periodically forced linear oscillator given by the differential equation

$$m\ddot{x} + f(x, \dot{x}) = F \sin \omega_f t$$

F is the forcing amplitude and ω_f is the forcing frequency. By defining $\tau = \omega_f t$; the ratio of the forcing frequency to the natural frequency of the undamped, undriven oscillator as η; and the ratio of the actual damping to critical damping as ζ; the magnitude of the forcing, along with the stiffness can be incorporated as a scaling factor into the definition of x, and we have for a linear oscillator

$$\eta^2 \ddot{x} + 2\eta\zeta\dot{x} + x = \sin \tau$$

where a dot denotes differentiation with respect to the new scaled time τ. The solution for a driven linear oscillator can be obtained analytically as the sum of its complementary and particular solution. The complementary solution can be written as

$$x_c = \exp(-\zeta\tau/\eta) [A \sin(\omega_d\tau + p)]$$

where

$$\omega_d = \frac{1}{\eta} \sqrt{(1-\zeta^2)}$$

and A and p are just integration constants which can be found from the initial conditions. The particular integral of this equation, which represents the final steady-state, can be written as

$$x_p = \frac{1}{\sqrt{[(1-\eta^2)^2 + (2\eta\zeta)^2]}} \sin(\tau - \psi)$$

where

$$\tan\psi = \frac{2\eta\zeta}{1-\eta^2}$$

The complete general solution is then just the sum of these two contributions, i.e.,

$$x(\tau) = x_c + x_p$$

.

It can be seen that for a positive damped system, the complementary function gives only the transient response and exponentia decay. The system will eventually achieve dynamical equilibrium, i.e., a periodic solution giving by the particular integral. Even for a linear system, there is no Liapunov exponent as such that can be used to define stability so that it is difficult to classify bifurcation. This is where the Poincaré mapping comes in and opens a new horizon to dynamical systems theory.

Poincaré mapping is a standard technique in dealing with the three dimensional phase space $(\dot{x}, x, t)$ of our periodically driven oscillator. In effect, the trajectories in the three-dimensional phase space are projected on to the $(\dot{x}, x)$ plane, thereby reducing the dimension of the phase space by one. Furthermore, trajectories are sampled stroboscopically in step with the forcing frequency, ω_f, i.e., whenever t is a multiple of $T = 2\pi/\omega_f$ as shown in Figure (8). From a three-dimensional flow problem, we have now derived a two dimensional discrete system. While this discrete dynamical system often can not be defined analytically from a flow problem, all

mapping points can be obtained numerically. In particular, a periodic solution now becomes a fixed point and a local normal form analysis can be performed and bifurcations classified. This in fact will be the topic treated in Chapter 2.

2 Discrete Dynamics

In this Chapter, we shall concentrate on the study of mapping as dynamical systems. As we have observed in Chapter 1, a three-dimensional flow problem can be sampled to become a two-dimensional mapping problem. Therefore, stability properties of a map as well as its local bifurcation forms are directly related to the original flow problem. The main advantage of using a mapping is that the original periodic solution is transformed into a fixed point so that a local analysis can be performed with ease. As will be seen in later Chapters, our numerical analysis is based entirely on two dimensional mapping theory. The robustness of our techniques demonstrates the fact that this is an indispensible tool for understanding the behaviour of dynamical systems. As this powerful method is not widely used in engineering, we site here in the reference list a few foundation references[27-30,6].

The first to introduce this point mapping idea is probably Poincaré, and studies are later made by Birkhoff, Arnold and Smale. In recent years the theoretical aspects of discrete time systems as well as their applications to problems in mechanics are investigated by many; for example by Hsu[31], Thompson[32] and Ueda[33].

For our investigations, we take a non-linear differential equation of the form

$$\ddot{x} + f(\dot{x}, x)\dot{x} + g(x) = e(t)$$

where $e(t)$ is periodic of period T. A dot refers to differentiation with respect to t. By setting $\dot{x} = y$, this equation becomes

$$\dot{x} = y$$

$$\dot{y} = -f(x,y)y - g(x) + e(t)$$

or in general

$$\dot{x} = X(x,y,t)$$

$$\dot{y} = Y(x,y,t) \qquad (2.1)$$

where $X(x,y,t)$ and $Y(x,y,t)$ are both periodic in t with period T. Let x(t) and y(t) be the solution of equation (2.1) which starts from a point P_0 in the (x, y) plane. The coordinates of P_0 are then given by x(0), y(0). We focus our attention towards the location of the point P_m at the instant $t = mT$, m being 0, 1, 2,.... Let us call the transformation $P_0 \rightarrow P_1$ the mapping F and express this as $P_1=FP_0$. If a solution $x(t)$, $y(t)$ has period T, then the point P_0 is a fixed point of the mapping F. If x(t), y(t) is a subharmonic of order n, (n=2, 3, 4,....), i.e. a solution of period nT, but not of period T, then the points P_0, P_1,....,P_{n-1} are called periodic points. They are all fixed points of the nth iterate, F^n, of the mapping F. Thus, in order to study the behaviour of the solutions of equation (2.1) as curves in the (x, y, t) space, it is now only necessary to study the successive mapping of a initial point on the (x, y) plane, or in short, the transformation of the xy plane into itself.

2.1 Stability of two dimensional map

Once a fixed point is found, its stability can be investigated by looking at its local linear normal form. Consider now a two-dimensional map given by the equations

$$x_{i+1} = F(x_i, y_i)$$
$$y_{i+1} = G(x_i, y_i) \tag{2.2}$$

This map can be considered as the Poincaré map of a three dimensional flow, in which case the functions can only be obtained numerically. If (x^E, y^E) is a fixed point, so that

$$x^E = F(x^E, y^E)$$
$$y^E = G(x^E, y^E) \tag{2.3}$$

we can examine this fixed point's stability by considering a small perturbation. Let

$$x_i = x^E + \xi_i$$
$$y_i = y^E + \eta_i$$

so that

$$x_{i+1} = x^E + \xi_{i+1} = F(x^E + \xi_i, y^E + \eta_i)$$

$$y_{i+1} = y^E + \eta_{i+1} = G(x^E + \xi_i, y^E + \eta_i)$$

Expanding the functions F and G in Taylor series at the fixed point, and using equation (2.3), we have

$$\xi_{i+1} = F_x\xi_i + F_y\eta_i + \frac{1}{2}(F_{xx}\xi_i^2 + 2F_{xy}\xi_i\eta_i + F_{yy}\eta_i^2) + \dots$$

$$\eta_{i+1} = G_x\xi_i + G_y\eta_i + \frac{1}{2}(G_{xx}\xi_i^2 + 2G_{xy}\xi_i\eta_i + G_{yy}\eta_i^2) + \dots \qquad (2.4)$$

where all the derivatives of F and G are evaluated at the fixed point (x^E, y^E).

Assuming ξ and η are small, we can neglect the nonlinear terms and retain only the first derivatives. Denoting them as a, b, c, and d we can obtain the variational equation as

$$\xi_{i+1} = a\xi_i + b\eta_i$$

$$\eta_{i+1} = c\xi_i + d\eta_i \qquad (2.5)$$

or in matrix notation

$$\zeta_{i+1} = H\zeta_i \qquad (2.6)$$

Let λ_1 and λ_2 be the eigenvalues of the matrix H, which are both real and distinct. Then it is always possible to perform a transformation of coordinates[7], so that equation (2.5) becomes

$$u_{i+1} = \lambda_1 u_i$$

$$v_{i+1} = \lambda_2 v_i \qquad (2.7)$$

Now, the coupled equations become independent, and the stability question is solved immediately. The system is asymptotically stable if $-1 < \lambda_{1,2} < 1$, but unstable if either λ_1 or λ_2 are greater than 1 in absolute value. If one of the eigenvalues has modulus equal to 1 and the other is less than one then the linear approximation is

not sufficient to establish its stability. We should note here that while the eigenvalues of a flow are called Liapunov characteristic exponents; eigenvalues of a map are known also as Poincaré characteristic multipliers.

If λ_1 and λ_2 are complex conjugate eigenvalues, where

$$\lambda_{1,2} = \alpha \pm i\beta$$

it is again possible to perform a transformation of coordinates so that equation (2.5) becomes

$$u_{i+1} = \alpha u_i - \beta v_i$$

$$v_{i+1} = \beta u_i + \alpha v_i \tag{2.8}$$

By introducing polar coordinates and letting

$$u_i = r_i \cos \theta_i$$

$$v_i = r_i \sin \theta_i \tag{2.9}$$

we can rewrite the eigenvalues in the exponential form

$$\lambda_1 = \alpha + i\beta = \rho e^{i\phi}$$

$$\lambda_2 = \alpha - i\beta = \rho e^{-i\phi}$$

so that

$$\alpha = \frac{1}{2}\rho(e^{i\phi} + e^{-i\phi})$$

$$\beta = \frac{1}{2}\rho(e^{i\phi} - e^{-i\phi}) \tag{2.10}$$

Using equation (2.8) we have $(u_0, v_0) = (r_0, \theta_0)$, so that when i=0 we have

$$r_1 \cos \theta_1 = \rho r_0 \cos(\phi + \theta_0)$$

$$r_1 \sin \theta_1 = \rho r_0 \sin(\phi + \theta_0)$$

and when i=1

$$r_2\cos\theta_2 = \rho^2 r_0\cos(2\phi + \theta_0)$$

$$r_2\sin\theta_2 = \rho^2 r_0\sin(2\phi + \theta_0)$$

Hence, in general,

$$r_k = \rho^k r_0 \tag{2.11}$$

$$\theta_k = \theta_0 + k\phi \tag{2.12}$$

Or by substituting equation (2.12) into equation (2.11) gives

$$r_k = r_0\rho^{(\theta_k - \theta_0)/\phi} \tag{2.13}$$

Since r_k is just the radial distance from the fixed point, the fixed point is only asymptotically stable when $\rho < 1$. In this case, trajectories spiral in towards the fixed point while when $\rho > 1$ trajectories sprial outwards and the fixed point is unstable. Again if $\rho = 1$ the linear approximation can no longer establish the fixed point's stability.

Looking at the eigenvalues, one can see immediately that the stability criterion is best discussed in the complex plane. In fact, if both the eigenvalues are within the unit circle of the complex plane, the fixed point is asymptotically stable; if either one of the eigenvalues is outside the unit circle, the fixed point is unstable. Hence, the stability boundary on the complex plane is the unit circle itself. This contrasts markedly with the flow problem where the stable region is the negative half plane. This is worth emphasising because while our mapping problem is derived from a flow using the Poincaré mapping technique, we must treat the problem as a map rather than a flow. A comparision between the stability boundary of a flow to that of a map on the complex plane is shown in Figure (9).

Like the flow problems we discussed in Chapter 1, a discrete dynamical system loses its stability when the stability boundary is crossed. Depending on the way the eigenvalues pass this boundary, different types of bifurcation can occur. This is

summarized in Figure (9) as well. Before we go on to discuss bifurcational behaviour, it is instructive to discuss stability in terms of the invariants of the matrix H. The eigenvalues of this matrix are given by

$$\lambda^2 - (a + d)\lambda + (ad - bc) = 0$$

and writing

$$a + d = \text{trace of } H = T$$

$$ad - bc = \text{determinant of } H = D$$

we can express the eigenvalues in term of these invariants, as

$$\lambda_{1,2} = \frac{1}{2}[T \pm \sqrt{(T^2 - 4D)}]$$

The stability boundaries in the (T, D) plane are sketched in Figure (10). The parabola is defined by the equation

$$T^2 - 4D = 0$$

On the right of the parabola is the region where

$$T^2 - 4D < 0$$

indicating the eigenvalues are complex. On the left of the parabola the opposite is true so that all eigenvalues are real. The three straight lines LN, LM and MN are the boundaries where the eigenvalues are critical. Values outside these boundaries indicate instabilities.

The two dimensional mapping problem derived from a flow as in this case using the Poincaré mapping technique is a special class of general two dimensional map. This is because trajectories in a flow are continuous and can not cross each other so that eigenvalues of different sign are inadmissable. Therefore if one eigenvalue is positive/negative the other one must also be positive/negative. In terms of the stability boundary in the trace-determinant plane, it is only necessary to consider the positive right hand half plane. Furthermore, for a dissipative system, the Jacobian

of the matrix H i.e. ad-bc, is always positive and less than one so that the Neimark bifurcation is not possible. This in turn leads to the conclusion that any local instability will be due either to a flip or a fold bifurcation.

2.2 Bifurcations of two dimensional map

To analyse the fold and flip bifurcations, it is only necessary to consider the map to be essentially one dimensional. This is because at the bifurcation point, only one eigenvalue is critical. Such a reduction is based on the Centre Manifold theorem. A geometrical interpretation of this theorem is that trajectories are attracted towards the centre manifold, (i.e. the critical eigenvector) rapidly and then converge to or diverge from the fixed points. Therefore, this theorem allows us to view this eigenvector as a local approximation of the higher dimensional map.

Let us imagine that we shall neglect all the mapping points until they have converged onto the centre manifold. The centre manifold is thus one dimensional for a two dimensional map. Or one can also imagine that a perturbation is given to the fixed point in a way that the displacement is along the critical eigenvector only. If $x = x^E$ is a fixed point of the map $x_{i+1} = F(x_i)$, so that

$$x^E = F(x^E)$$

we can examine the fixed point's stability using a perturbation technique as before. Therefore, we superimpose a small disturbance to the fixed point x^E,

$$x = x^E + \xi \tag{2.14}$$

so that

$$x_{i+1} = x^E + \xi_{i+1} = F(x_i) = F(x^E + \xi_i)$$

and again, assuming that F has a power series expansion, we may write equation (2.14) as

$$x^E + \xi_{i+1} = F(x^E) + F_x^E \xi_i + \frac{1}{2} F_{xx}^E \xi_i^2 + \ldots$$

where $F_x^E \equiv F_x(x^E)$, etc.

We can now denote the coefficients of the series as C, D, E,... and using the fact that $x^E = F(x^E)$, the mapping becomes

$$\xi_{i+1} = C\xi_i + D\xi_i^2 + E_i^3 + ...$$

Again assuming ξ_{i+1} is small, we retain only the linear term of the expansion so that

$$\xi_{i+1} = C\xi_i \qquad\qquad (2.15)$$

By recurrent, we can put equation (2.15) in terms of the initial point ξ_0 as

$$\xi_i = C^i \xi_0$$

Accordingly, the fixed point is linearly stable only if -1 < C < 1.

If C lies between 0 and 1, any perturbation decays monotonically, while if C is greater than 1, they grow monotonically. This is called divergence. If C lies between -1 and 0, disturbances decay in an oscillatory manner with ξ's sign alternating between postive and negative. While if C is less than -1, any disturbance will grow oscillatorily. This is called flipping. Figure (11) are two examples of a two dimensional map approaching a fold and a flip bifurcation. Of special interest is the way in which the map converges rapidly onto the centre manifold indicated by the thick line.

We are now in a position to discuss the fold and flip bifurcations of the two dimensional map. Bearing in mind that we shall only consider the one dimensional centre manifold.

Consider now the response of a map with a control parameter P, so that

$$y = F(x,P)$$

As the control parameter is varied, various fixed points will trace out paths in the (x, P) phase-control space, and it is the bifurcation of these path that we would like to address.

In order to study the singularity at the bifurcation point $P = P^c$, it is useful to expand F as a Taylor series in both the variable x and the change in P from its critical value, i.e., $p = P - P^c$, as follows

$$y = B + Cx + Dx^2 + Ex^3 + \dots$$
$$+ p(B_1 + C_1x + D_1x^2 + E_1x^3 + \dots)$$
$$+ p^2(B_2 + C_2x + D_2x^2 + E_2x^3 + \dots) + \dots \quad (2.16)$$

2.3 Folds and saddle-node bifurcation

To examine a fold in the fixed points, we measure x from the fixed critical point itself. In other words, the critical point is positioned at the origin. Since $x=p=0$ is a fixed point, we must have, from equation (2.16), B=0. This point is also critical; therefore C must be equal to 1. Because the path is a path for a fixed point we can set y=x and consider the typical case in which D and B_1 are non-zero. Then the local first-order approximation for the path is

$$Dx^2 + B_1 p = 0$$

Hence the local form of a fold bifurcation is a parabola, an example of which is shown in Figure (12). Here, the lower branch of the parabola represents a stable path while the upper branch is unstable. The left hand diagram shows that any iteration starting with a negative value of p diverges monotonically to infinity. While for positive p, all iterations converge to the stable branch. On the right hand diagram, any iterations start under the unstable path converge to the stable path while iterations starting above the unstable path diverge to infinity. Hence the unstable path is a separatrix between the catchment regions of the attracting path and the attractor at infinity.

The stability coefficient corresponding to C along the path can be found by differentiating the function F(x, p) to give F_x, where

$$F_x = C + 2Dx + 3Ex^2 + \dots + C_1 p + \dots$$

giving the first order solution

$$F_x = 1 + 2Dx$$

Hence, as x changes from negative to positive, the coefficient changes from less than 1 which is stable, to greater than 1 which is unstable as x changes sign *along* the path.

Other normal forms of saddle node bifurcations can be obtained using various constraints but will not be discussed here as they are not typical with only one control parameter. Interesting readers could consult the literatures listed in the reference list[34-36] which give an excellent and thorough treatment on this topic.

2.4 The flip bifurcation

The flip bifurcation is characterised by the coefficient C=-1. This time, we shall measure x from the path so that

$$B = B_1 = B_2 = ... = 0$$

Refering to equation (2.16), for a most typical loss of stability with increasing p, we can set C_1 non-zero and negative.

Since the oscillatory response indicates an n=2 path will bifurcate from the primary n=1 path, we can focus our attention on the second iterate

$$z = F^2(x) = T(x)$$

Therefore, at the origin (0, 0), i.e. the critical point, we have

$$T_x = (F_x)^2$$

At this point, the map F is at incipient flip with F_x=-1, so that the map T is at incipient divergence, since T_x=1. However, the second iterate of an n=1 fixed point is still the same fixed point, i.e., y=x implies z=x, we can therefore expect the n=2 solutions to include the primary n=1 path. In fact the primary path becomes an unstable path.

The first few terms of the Taylor series expansion of the map F^2 are

$$z = C(Cx + Dx^2 + Ex^3 + C_1xp) + D(Cx + Dx^2 + C_1xp)^2 + E(Cx)^3 + C_1p(Cx)$$

For an n=2 solution, $z=x$, and since C=-1, the z cancels with the C^2x so the first order n=2 solution will be given by

$$Ex^3 + D^2x^3 + C_1px = 0$$

At the critical point, i.e., the origin, $x=0$ or

$$C_1p + x^2(E + D^2) = 0$$

Notice that the continuous existence of the primary path excludes the possibility of a n=2 saddle-node bifurcation. With C_1 negative, a supercritical flip bifurcation occurs with $(E + D^2)$ positive and a subcritical flip bifurcation with $(E + D^2)$ negative.

Numerical examples of both type of bifurcations are shown in Figure (13). Convergence or divergence along the paths are as indicated by the arrows. Refering to Chapter 1, the subcritical bifurcation is thus classified as a dangerous bifurcation as there is no indication of the imminent catastrophe.

For a simple three dimensional flow problem, we may hope that most attractors and bifurcations will give rise to either a fold or flip bifurcation. However at certain value of the control parameter, a sudden onset of chaotic motions may occur and this will be the topic of Chapter 3.

3 Chaotic Dynamics

Dynamical systems with irregular, nonperiodic, 'chaotic' time evolutions are frequently encountered in physics, chemistry, and biology. One famous example is the rising of smoke in still air from a cigarette. Random oscillations appear at a certain height in the smoke column, and they are so complicated as to apparently defy understanding. Although the time evolution obeys strict deterministic laws, this system seems to behave according to its own free will. Physicists, chemists, biologists, and also mathematicians have tried to understand this situation. In fact a great deal of excitement in nonlinear dynamics today is centred around the hope that this transition from ordered to disordered flow may be explained or modelled with relatively simple mathematical equations. It is the recognition that chaotic dynamics are inherent in all of nonlinear physical phenomena that has created a sense of revolution in physics today. The constituents of a strange or chaotic attractor involve two apparently paradoxical phenomena. Namely, it has a steady attracting set but not an attracting fixed point, and within this attracting set, neighbouring orbits separate or diverge exponentially fast.

The long held belief that given an initial condition, we know what a deterministic system will do far into the future, has now proved to be false. Because even with the simplest conceivable equation of motions, almost any non-linear system will exhibit chaotic behaviour; and given any infinitesimally different starting conditions they often end up with widely different outcomes.

Since the pioneering works of Lorenz, later strengthened by Ruelle and Takens, the concept of strange attractor or chaos has provided a new way of thinking about the aperiodic behaviours observed in dissipative dynamical systems as well as in experiments. The sensitivity to small deviation has important consequences from a physical point of view, since due to some initial uncertainties, the information about the original state of the system is lost in a finite amount of time and so the system is effectively unpredictable. While chaotic dynamics exhibit random like phenomena , the discovery of an underlying order holds out the promise of being able to predict certain properties of noisy behaviour.

We must distinguish here between the so-called random and chaotic motions. The former is reserved for problems in which we truly do not know the input forces or we only know some statistical measures of the parameters. The term chaotic is reserved for those deterministic problems for which there are no random or unpredictable inputs or parameters.

3.1 Criteria for chaotic vibrations

The search for theoretical criteria to determine under what set of conditions a given dynamical system will become chaotic has tended to be ad hoc. The strategy thus far has been for theorists to find criteria for specific mathematical models and then use these models as analogs or paradigms to infer when more general or complex physical systems will become unpredictable. An example is the period-doubling bifurcation sequence discussed by May[37] and Feigenbaum[38].

Their investigations concern the bifurcational behaviour of the one dimensional map given by:

$$x_{n+1} = \lambda x_n (1 - x_n) \qquad (3.1)$$

They discovered solutions whose periods double as the parameter λ is varied. One of the important properties of equation (3.1) that Feigenbaum discovered was that the sequence of critical control parameters λ_m at which the period of the orbit doubles satisfied the relation

$$\lim_{m \to \infty} \frac{\lambda_{m+1} - \lambda_m}{\lambda_m - \lambda_{m-1}} = \frac{1}{\delta} \quad , \quad \delta = 4.6692..$$

This important discovery gave experimenters a specific criterion to determine if a system was about to become chaotic by simply observing the pre-chaotic periodic behaviour. The importance of Feigenbaum's work was that he showed how all period doubling behaviour satisfies the above relationship. Thus, for a mapping relationship parameterized by a control λ, the sequence of critical values, λ_m, of this parameter at which the orbit's period doubles satisfies the same relationship as that for the quadratic map. Thus, the period-doubling phenomenon has been called universal and δ has been called a universal constant, now known as the Feigenbaum number.

Another theoretical technique that has led to specific criteria for chaotic vibrations is a method based on the search for horseshoe maps and homoclinic orbits in mathematical models of dynamical systems.

In 1899 Poincaré[27] remarked on the complexity of the behaviour of dynamical systems having what he called a homoclinic point. Using his mapping technique, he realized that for phase space with more than two dimensions, invariant manifolds can cross without actually coinciding. Once the invariant manifolds cross, then they must intersect each other an infinite number of times due to recurrence. The consequence of these transverse intersections (homoclinic points or heteroclinic points) is a complex recurring structure called a tangle.

A tangle due to the intersection of the invariant manifolds of two different saddles is called a heteroclinic tangle. When the invariant manifolds belong to the same saddle point, it is called a homoclinic tangle. Each intersection point is called a heteroclinic or homoclinic point. A tangle contains an infinite number of secondary intersection points and was described in detail by Birkhoff[39].

Perhaps the most important concept of chaos is best illustrated by Smale's construction of a horseshoe map. Basically, this involves mapping a square onto itself. The dynamics behind this mapping is such that the square is stretched in the vertical direction and compressed in the horizontal direction. It is then folded or bent into a horseshoe like shape and placed over the original square. Overlapping regions are then retained and the rest are considered lost. By continuing this process, original neighbouring cluster of points gets dispersed to all sectors of the square. This is the same as a loss of information as to where a point originally started from. Smale was able to demonstrate some remarkable properties of this mapping. Namely: infinitely many periodic orbits, (all unstable), uncountably many aperiodic orbits and at least one point in the *cantor* set whose orbit comes arbitrarily close to every point in the set, i.e. the set is transitive. These properties are in fact identical to those found by Birkhoff when he looked at the problem of a tangle. Furthermore these properties are precisely those that describe chaotic motions and can be found in all known chaotic attractors of dissipative dynamical systems. Smale's horseshoe-type

dynamic is in particular related to the homoclinic trajectory of an inverting saddle because of the necessity of mapping back onto itself. All these theoretical aspects will be demonstrated in our application described in Chapter 7.

The appearance of horseshoe-like dynamics is directly related to the occurrence of homoclinic orbits. To see why homoclinic orbits lead to horseshoe maps, we recall that for a dissipative system, areas are mapped into smaller areas. However, near the unstable manifold (i.e. the outset of a saddle), the areas are also stretched. Since the total area must decrease, the areas must also contract more than they stretch. This is schematically illustrated in Figure (14). It can be observed that areas near homoclinic points also get folded. It is believed by some mathematicians that horseshoe maps are fundamental to most chaotic differential and difference equation models of dynamical systems. This idea is the centre piece of a method developed to find a criterion for when chaotic vibrations are possible in a dynamical system.

The Melnikov method is used to measure the distance between unstable and stable manifolds, (i.e. the inset of a saddle) when that distance is small. Hence it is possible to calculate the critical control parameter in which homoclinic tangency occurs. However, homoclinic orbit is only a necessary but not sufficient condition for chaotic vibrations to occur as we shall demonstrate in Chapter 7.

Folding and mixing actions are well known criteria for chaos. These actions can be graphically illustrated by the Poincaré maps or phase plane portraits. For low dimensional dynamical systems, this qualitative technique has become the de facto standard to present a chaotic attractor. To demonstrate the folding and mixing actions of a chaotic attractor, we shall briefly discuss our earlier work on the Birkhoff-Shaw chaotic attractor.

This chaotic attractor was reported by Shaw[40] working on a variation of the Van der Pol equation. The dynamical system investigated by Shaw is described by the equations

$$\dot{x} = 0.7y + 10x(0.1 - y^2)$$

$$\dot{y} = -x + 0.25\sin(1.57t)$$

To obtain a Poincaré section of the chaotic attractor, an arbitrarily chosen initial condition was computed over many forcing cycles until the transient died away. Thereafter, from this single trajectory, the next 1000 return points were recorded, i.e., the coordinates (x, y) after every forcing cycle. This produces a Poincaré section of the chaotic attractor at $\phi = 0$ where ϕ is the phase angle. If we now perform numerical integrations on these 1000 points in 10 degree steps for a whole forcing cycle, a sequence of 36 successive Poincaré sections can be obtained as shown in Figure (15). This can be described as a cylindrical model of the Birkhoff-Shaw chaotic attractor in full three-dimensional phase space.

At the 'front' section corresponding to $\phi = 0$, we have labelled 41 points which approximately spread evenly on the attractor at this phase angle. By integrating these initial conditions forward for exactly one forcing cycle, these points reach the 'back' of the 'cylinder'. Using these numbers for identification, it can be observed that after one forcing cycle, these points have already been 'mixed' together so that it is impossible to identify the number sequence. This mixing action can easily be demonstrated by unwrapping the cylindrical model to obtain the projection of the trajectories onto a two-dimensional phase space as shown in Figure (16). On the right hand diagram, the trajectories are obtained by numerical integrations and their position are now a function of the phase angle, ϕ, and the angle θ with respect to the x axis. Although not very obvious because of the heavy ink, the trajectories did cross if examined closely. The reason for this mixing action to happen is because part of the chaotic attractor folded onto itself as demonstrated in the series of Poincaré sections shown in the middle of Figure (16). The solid dots on the left hand diagram mark the apparently completed folding of the 'wing' (DE and AF) and immediately thereafter, this part of the chaotic attractor begins to stretch and a new 'beak' starts to emerge. Eventually, the beak becomes the wing and the whole cycle repeats ad infinitum so that a complete mixing of any sequence of initial conditions is possible. Obviously this gives rise to the exponential divergence and unpredictability of nearby starts.

3.2 Quantifying Chaos

Chaos has been discovered both in the laboratory and in the mathematical models that describe a wide variety of systems. In common usage, chaos is taken

to mean a state in which chance prevails. To the nonlinear dynamicist, the word 'chaos' has a more precise and rather different meaning. A chaotic system is one in which long term prediction of the system's state is impossible because the omnipresent uncertainty in demanding its initial state grows exponentially fast in time. The rapid loss of predictive power is due to the property that orbits (trajectories) that arise from nearby initial conditions diverge exponentially fast on the average. Nearby orbits correspond to almost identically prepared systems, so that systems whose differences we may not be able to resolve initially soon behave quite differently. In non-chaotic systems, nearby orbits either converge exponentially fast or at worst exhibit a slower than exponential divergence: long term prediction is at least theoretically possible.

Rates of orbit divergence or convergence, called Lyapunov exponents[41,42], are clearly of fundamental importance in studying chaos. Positive Lyapunov exponents indicate orbit divergence and chaos, and set the time scale on which state prediction is possible. Negative Lyapunov exponents set the time scale on which transients or perturbations of the system's state will decay.

The exponential divergence of adjacent starts can be demonstrated by a divergence study on the chaotic attractor originated from our investigations of the impact oscillator. This system is a limiting case of the bilinear oscillator described in Chapter 6. Results of such a study are shown in Figure (17). Here, starting at a point $(x_0, \dot{x}_0)$ and then a point $(x_0 + 10^{-r}, \dot{x}_0 + 10^{-r})$. We have observed the distance R between two subsequent motions for four different choices of $(x_0, \dot{x}_0)$ on the located steady state chaotic attractor. For each of these four choices we have taken r=3, 5, 7 and plotted -log R against the number of cycles completed. Here R is taken as the shortest distance between the two adjacent starts after each cycle, hence:

$$R = \sqrt{\Delta x^2 + \Delta \dot{x}^2}$$

The noisy straight lines on these logarithmic plots confirm that the adjacent solutions diverge exponentially before becoming completely uncorrelated. The slope of these noisy lines are then averaged to produce the Liapunov exponent, 0.16, which is positive, indicating a chaotic response.

In fact, this was only an ad hoc approach. The divergence of chaotic orbits can only be locally exponential. Since if a system is bounded, the distance between two adjacent starts cannot go to infinity as suggested. Thus to define a measure of this divergence of orbits, we must average the exponential growth at many points along a trajectory. Wolf[43,44] suggested that one began with a reference trajectory and a point on a nearby trajectory and measured their rate of divergence. When this became too large, one should look for a new 'nearby' trajectory. However, our ad hoc approach served as an easy and computational inexpensive effort to identify a chaotic phenomenon.

Both 'chaotic' and 'strange attractor' have been used to describe the nonperiodic, random like motions. Whereas chaotic is meant to convey a loss of information or loss of predictability, the term strange is meant to describe the unfamiliar geometric structure on which the motion moves in phase space. We have described a quantitative measure of the chaotic or informational loss aspect of these motions using Lyapunov exponents. We shall now describe a quantitative measure of the strangeness of the attractor. This measure is called the fractal dimension.

To understand the term 'fractal', the simplest example will be the Cantor Set discovered by George Cantor in 1883. An example of the construction of a Cantor Set begins with a line segment with unit length. This line is subdivided into three sections. By removing the middle segment of points, the total number of segments is increased to two and the total length is reduced to 2/3. This process is continued for the remaining line segments and so on. At each stage one discards the middle segments of points creating twice as many line segments but reducing the total length by 2/3. In the limit, the total length approaches zero but we are left with a set with an infinite number of points. Since a line is one dimensional and a point has zero dimension, this set of points has thus a 'fractal' dimension between zero and one, i.e., a fractional dimension. The property of this set of points is that when one keeps enlarging any part of the line segment, the same structure will be repeated ad infinitum which is just the same geometric structure that occurs in a chaotic attractor. Thus we can expect that a chaotic attractor has fractional dimension[45].

Various mathematical techniques have been used to calculate the fractal dimension of strange attractors such as the capacity dimension[46], point-wise

dimension[47], correlation dimension[48] and information dimension[49]. The practical use of all the dimensions in measuring and characterizing chaotic vibrations has yet to be settled. In many cases, it is sufficient to establish that the dimension is not integer or that the attractor is indeed strange.

In addition to the application of fractal ideas to a description of the chaotic attractor itself, boundaries between competing attractors, not necessary chaotic, may also have fractal properties. This so called fractal basin boundary has been discovered in the ship-capsize problem and will be discussed in Chapter 7.

Fractal dimensions and Lyapunov exponents have been widely used by scientists working with numerical models. For experimentalists, a spectral analysis is by far the most popular measure, because the idea of decomposing a nonperiodic signal into a set of sinusoidal or harmonic signals is widely known especially among engineers. The assumption made in this method is that the periodic or nonperiodic output can be represented as a synthesis of sine or cosine waves:

$$f(t) = \frac{1}{2}\pi \int_\Gamma F(\omega)e^{i\omega t} d\omega \qquad (3.2)$$

where

$$e^{i\omega t} = \cos \omega t + i \sin \omega t$$

In general, the function $F(\omega)$ is a complex function of ω and to represent certain classes of output $f(t)$, the integration of equation (3.2) must be performed along a path Γ in the complex ω plane. Numerical calculation of $F(\omega)$, given $f(t)$, can often be very time consuming even on a fast computer. However, a more efficient algorithm called the fast Fourier transform (FFT) can be used. Given a set of data sampled at discrete even time intervals, the discrete time FFT is defined by the formula

$$T(J) = \sum_{i=1}^{N} f(I)e^{-2\pi i(I-1)(J-1)/N}$$

where I and J are integers.

When an output signal is periodic or quasiperiodic, the power spectrum will show a set of narrow spikes indicating that the signal can be represented by a discrete set of harmonic functions. Near the onset of chaos, a continuous distribution of frequency appears and in the fully chaotic regime, the continuous spectrum may dominate the discrete spikes. Illustrated in Figure (18) is a typical power spectrum of a steady-state chaotic motions, showing a white noise type power spectrum which confirmed the existence of chaotic motion.

Quantitative measures of chaotic dynamics are essential tools when qualitative techniques such as the Poincaré map is impossible. This is especially true for systems with extreme frequencies ($10^6 - 10^9$) (as in laser systems) in which Poincaré maps may be difficult or impossible to capture. In addition, there are systems with many degree of freedom where the Poincaré map will not reveal the fractal structure of the attractor section: or the damping may be so low that the Poincaré map shows no structure but looks like a cloud of points. However the above three techniques will provide us with hard evidence on the existence of chaotic dynamics.

3.3 Bifurcation of Chaotic Attractors

We have seen in Chapter 2 that periodic attractors can bifurcate via the fold or the flip bifurcation. These two bifurcations are of the 'local' type. A chaotic attractor can suddenly be destroyed via the Chaotic Blue Sky catastrophe when it is tangent to the invariant manifolds so that this is classified as a global bifurcation. We shall now discuss a type of bifurcation of chaotic attractors which has a local character but involves invariant manifolds nevertheless. Therefore we can classify it as a local-global bifurcation after Thompson and Stewart[11].

In Chapter 1, Figure (7), we have shown a table for the bifurcation of attractors. For a chaotic attractor, there are the intermittency and chaotic explosion that we have not discussed. In fact these two types of chaotic bifurcations are of the local-global type and they often appear as a pair in a periodic window within a chaotic regime.

In the case of intermittency, bursts of chaotic or noisy motions occur between periods of regular motions. Such behaviour was even observed by Reynolds in pipe flow preturbulence experiments in 1883. Hence such a dynamical system is close

to a periodic motion but experiences short bursts of chaotic transients. An explanation of this behaviour has been proposed by Manneville and Pomeau[50] in terms of one dimensional maps.

From their numerical experiments, they investigated the statistical behaviour on the duration of the periodic motions between each burst of chaotic transients. They found that the mean time interval of periodic motions was proportional to the control parameter and established the relationship:

$$\tau \sim \frac{1}{|\lambda - \lambda_c|^{1/2}} \tag{3.3}$$

where λ is a control parameter and λ_c is the critical value at which chaotic motion occurs. As $\lambda - \lambda_c$ increases, the chaotic time interval increases and the periodic interval decreases. To measure λ_c, one must measure two average times τ_1 and τ_2 at corresponding values of the control parameter, that is λ_1 and λ_2. This should determine the proportionality constant in equation (3.3) as well as λ_c. Once λ_c is obtained, one should then measure other values of (τ, λ) to validate the scaling relationship of equation (3.3).

In Figure (19), part of the bifurcation diagram of the quadratic map is greatly enlarged along the parameter axis to show a period three window. The abrupt appearance of the period three solution near C=1.75 is due to a saddle-node bifurcation. To the left of this control parameter, we can see a higher concentration of points near the impending period three orbit which indicate the appearance of intermittency.

At the end of this period three window, just past c=1.79, it can be observed that the three bands of a 'period three' chaotic attractor bifurcate to another chaotic attractor and fill the entire interval. This is the chaotic explosion or in Grebogi's[51] terminology, an interior crisis. In this one dimensional case, the bifurcation is caused by the unstable saddle, generated by the saddle node bifurcation, touching the chaotic attractor. The path of the saddle is represented schematically by the dash line. However, in phase space of more than one dimension, this explosion can happen as a chaotic attractor touches the inset without touching the saddle itself.

The mechanism for chaotic explosion is similar to the Chaotic Blue Sky Catastrophe: however there is no jump to a remote attractor in this case. We can infer that there must exist a chaotic attractor which is non-attracting before the periodic attractor vanishes. Therefore, chaotic transients must exist prior to this transition and in fact this phenomenon also applies to the intermittency explosion. Because of the existence of chaotic transients, typically the result of intersecting invariant manifolds, we can expect that a local bifurcation will trigger a global transition to chaos. Hence the name local-global bifurcation.

4 Qualitative analysis of dynamical systems

In the theory of nonlinear oscillations, dealing with strongly nonlinear systems is always a very difficult task especially when the global behaviour of the systems becomes important. This chapter presents several efficient and practical ways of examining the global behaviour of nonlinear dynamical systems. Global bifurcations are associated with a profound change in the topological configuration of the invariant manifolds of a saddle point. A variety of types of global bifurcation exists, depending on the particular topological configuration of invariant manifolds involved. In general, any topological change in the configuration of invariant manifolds can be expected to cause some qualitative change in behaviour. In some cases, like the homoclinic connection in the Lorenz[20] system, this change dramatically affects the basin structure of the phase portrait without changing the attractors. Other global bifurcations create or destroy attractors, for example a heteroclinic connection. With such change, the domain of attraction or catchment region corresponding to different attractors can be drastically altered (fractal basin boundaries[52,53]), reduced (competing coexisting solutions) or even suddenly disappear (Blue Sky Catastrophe[54]).

To an engineer, the main motivation to examine the global phase space is whether these catchment regions of various coexisting attractors change when a control parameter is varied. Catchment regions are always separated by the stable manifold or inset of a saddle: therefore the latter is sometimes called a basin boundary. To understand these phenomena, it is inevitable that the global phase space must be thoroughly explored.

One common but important feature when modelling nonlinear dynamical systems is the possibility of multiple coexisting solutions. One obvious example is the bending over of the resonance response curve associated with a softening or hardening spring. This folding of the resonance response curve results in the familiar hysteresis due to two fold bifurcations as well as the coexisting high and low amplitude solutions seperated by unstable saddle point. The final or steady state solution thus depends crucially on the chosen initial conditions given to the system. As the control parameter is varied, the area of the catchment region changed so that there is no guarantee that a chosen initial condition can always settle onto the same steady state solution. This dependence on initial conditions has practical importance to engineers. As will be

seen later in this chapter, a high amplitude subharmonic resonance can easily be missed due to a coexisting fundamental response This is in contrast to a damped linear dynamical problem where a unique solution means that the whole phase space of initial conditions acts as a basin of attraction.

During the course of the research, various methods have been developed to investigate the global behaviour of dynamical systems. In this chapter we shall discuss these methods using various mathematical example as well as practical model of engineering problems.

Mathematical examples will be of the form:

$$\ddot{x} + \dot{x} + B(x) = F(t)$$

$$F(t) = F(t+T)$$

The three dimensional phase space for this equation is defined by $(x, \dot{x}, t)$, and the Poincaré section is defined by the $(x, \dot{x})$ plane at t equal to multiples of the forcing period. Notice that when a system is autonomous, i.e. time invariant, it is possible to obtain a picture of the phase portrait of the flow, by considering an ensemble of trajectories. Trajectories in flow phase portraits are effectively governed by the position of the attractor. For example we can observe trajectories defining the catchment regions of two coexisting limit cycles separated by an unstable saddle cycle as shown in Figure (20). This simplifies the task of evaluating the set of initial conditions. For a forced (nonautonomous) system as we shall consider here, the phase portrait is a collection of Poincaré sections so that we can only observe a series of dots approaching the attractor and no information is available between each step. Thus to obtain the catchment regions we need to consider every point of the phase space and it is this seemingly impossible task that we would like to address.

4.1 Interactive Graphical technique

As we have mentioned earlier, global bifurcation is directly linked to the changes in the topological configuration of the invariant manifolds. Furthermore the catchment regions are separated by the inset of a saddle. Therefore it is obvious that the first step should be taken to locate the saddle point so that inset of the saddle can be traced and hence the global structure of the phase space can be obtained. However,

-44-

this is not an easy task since the saddle is an unstable point. One of the techniques we have developed to locate a saddle point is based on its linear mapping characteristic. As we sample a three-dimensional flow problem using a Poincaré mapping technique, we reduce the dimension of the system by one so that all the equilibrium solutions become points in the two dimensional section. Close to an equilibrium point the trajectories of the mapping (Poincaré) points resemble a linear system. These trajectories can be represented pictorially by a straight line joining two consecutive Poincaré points. The characteristics of the trajectories are governed by the saddle's local eigenvalues. Figure (21) shows some typical trajectories of a two dimensional linear map with different eigenvalues. In the same way, we can identify a typical equilibrium point for a nonlinear system by these characteristics if we are close enough to the solution.

To locate a saddle point through an interactive graphical technique, the unforced, i.e. autonomous, counterpart of the forced equation under consideration can be used to analytically determine the coordinates of the saddle equilibrium point. For small forcing we can expect that the location of the corresponding unstable cycle will remain nearby. A set of starts in the form of a circle encompassing the estimated saddle point is then initiated. The system is then run forwards and backwards in time for one forcing cycle. For each start, a line is drawn joining the Poincaré points and a series of vectors is established. Since an inset or outset will separate vectors pointing in opposite directions, as shown in Figure (22b), an estimate can be made of the location of the saddle by guessing the intersection point of the inset and outset. This operation is then repeated with a sequence of progressively smaller circles so that each estimate will be improved until the required accuracy is reached.

Having approximately located the saddle point, this point can be used as an initial condition such that by running time backwards and forwards, the inset and outset can be traced out in the phase projection. However, we found that the sequence of Poincaré points along the inset always has a very large step size, so that we cannot obtain a well defined curve. The only way to obtain a pseudo-continuous curve which represents the locus of this separatrix is to consider a number of initial conditions close to the saddle point and use the so called ladder method.

The estimated saddle point is first used as an initial condition to run backward in time for one cycle; as the initial point is very close to the saddle, after one cycle, the two points obtained are still very close together so that we can approximate this section of the inset as a straight line. By subdividing this line into 'rungs' and iterating each rung backwards in time systematically, an almost continuous curve can be achieved. Figure (22c) illustrates this procedure schematically, where the points $P_0, P_1, P_2.....$ and Q_0, Q_1, $Q_2....$ represent Poincaré points along the inset and outset respectively. P_0 and Q_0 are chosen to be very close to the saddle point and the sections corresponding to one iteration of the map are denoted B_0, $B_1,.....$ etc. along the inset (A_0, $A_1,.....$ along the outset).

Hence by using an interactive graphical routine to locate a saddle point and applying the ladder method we are able to trace the path of an inset to determine the domain of attraction for a particular periodic solution. We shall see an illustration of this technique later with a practical application concerning the oscillations of an articulated mooring tower. The ladder method has also been used in more detailed studies in the ship-capsize problem where the basin boundary seperating two attractors become extremely complicated and is indeed fractal in nature.

4.2 Grid of starts technique

The grid of starts technique is the easiest to implement computationally. As we have mentioned earlier, in order to investigate the global bifurcational behaviour, we need either to locate the saddle and trace the inset or examine every point or state in the Poincaré section. The second method is rather impossible, since there are infinite number of point in the section. However, in practice the phase space can be divided into a grid covering the region that is of interest and we can record the final steady state of every point on the grid. By using different symbol to distinguish between different steady state attributed to each point on the grid, the catchment regions and the global characteristics can be obtained. This method is computationally very demanding and the resolution depends on the grid size so that when a system becomes complicated with, for example the occurence of fractal basin boundaries, this method becomes impractical.

The importance of grid of starts technique however should not be undermined by its expensive computational time. Consider the case when homoclinic intersection occurs. This special type of global bifurcation involves crossing of the invariant manifolds giving rise to fractal basin boundaries. Once this occurs, the catchment regions are so fragmented that a small perturbation can lead to dramatically different coexisting attractors. The advantage of grid of starts technique is that it can zoom into specific region and made a high resolution study as will be seen in later chapter.

Figure (23) is the catchment regions of the Duffing's equation presented earlier with k=0.1 obtained by Ueda[55,56] with a smooth boundary. This is produced by the grid of starts technique. After the appearance of homoclinic tangency at k=0.05 the smooth boundary has become fractal and this is highlighted in Figure (24) by enlarging different area of the original phase space.

Later in this chapter we shall introduce a method which is similiar to the grid of starts technique but which eliminates the need to obtain the steady state solution of every point on the grid.

4.3 Variational equation and the Van der Pol plane

The first mathematical example is a nondimensionalised form of Duffing's equation, namely:

$$\ddot{x} + 2\frac{\zeta}{\eta}\dot{x} + x + \alpha x^3 = F_0 \cos\frac{1}{\eta}t \qquad (4.1)$$

in which the parameter η is chosen to be the control variable and the remaining values are fixed as the constants,

$$\zeta = 0.1 \quad \alpha = 0.05 \quad F_0 = 2.5.$$

This equation has been extensively studied in the mathematical literature and also, has been used to model large amplitude vibrations of a buckled beam, the behaviour of elastic strings, and large forced motions of a pendulum[11,13].

Solutions of this seemingly simple equation are still not completely understood with new phenomena which govern the behaviour of the response still coming to light. Subharmonic resonances and regimes of chaotic motions have been identified.

But here we shall restrict our attention to the area in which there is a jump to resonance along the fundamental solution as the parameter η is varied. This equation, can be solved immediately by numerical method but instead we shall derive a variational equation using a method which assumes a slowly varying amplitude and phase of the harmonic solution (Hayashi[16]). If we assume that the solution of the system is close to a harmonic response then we may let

$$x(t) = u(t)\cos t - v(t)\sin t \qquad (4.2)$$

The amplitude of the nonsinusoidal response can be usefully and appropriately defined by

$$A = \sqrt{(u^2 + v^2)} \qquad (4.3)$$

and a corresponding phase,

$$\phi = -\tan^{-1} v/u \qquad (4.4)$$

Effectively we are looking at transient motions close to the periodic steady state. The new coordinates (u, v) now define the Van der Pol plane in which the primary rotation of the solution has been eliminated. Solution curves are plotted now in the (u, v) plane where trajectories do not cross; the (u, v) plane being termed the Van der Pol plane (Thompson[57]). If the Duffing equation was solved numerically and trajectories plotted as usual on the $(x, \dot{x})$ plane then trajectories cross and mingle causing the phase portrait to be unclear. This is of course due to the fact that the original system has a full three dimensional phase space spanned by $(x, \dot{x})$ and time. Here the (u, v) axes rotate with respect to the (x, y) axes so most of the cross overs on the two-dimensional phase are eliminated. Now provided that the response of the system is predominantly harmonic then under our assumptions, the transformation 'unscrews' the fibre of trajectories at the corresponding rate of rotation. This can be seen in Figure (25).

For our nonlinear oscillator described by Duffing's equation in the range of parameters under discussion, we can finally make an approximation by averaging the exact equation in u,v and t following the methods of Krylov and Bogoliubov as

given, for example, by Hale[58], assuming that the new variables u and v are slowly varing functions of time. We may ignore terms involving $\ddot{u}, \ddot{v}$ and any cross product terms. Using this form of solution we differentiate to yield

$$y = \dot{x} = (\dot{u} - v)\cos t - (u + \dot{v})\sin t$$

$$\dot{y} = \ddot{x} = -(u - 2\dot{v})\cos t + (-2\dot{u} + v)\sin t \tag{4.5}$$

and

$$x^3 = \frac{3}{4}u(u^2 + v^2)\cos t - \frac{3}{4}v(u^2 + v^2)\sin t \tag{4.6}$$

Substitution of the equation from (4.2) to (4.6) into equation (4.1) and matching the coefficients of *cos t* and *sin t*, yields the approximating system

$$\dot{u} = \frac{1}{2\eta^2}\left((\eta^2 - 1)v - 2\zeta\eta u - \frac{3}{4}\alpha v(u^2 + v^2)\right)$$

$$\dot{v} = -\frac{1}{2\eta^2}\left((\eta^2 - 1)u + 2\zeta\eta v - \frac{3}{4}\alpha u(u^2 + v^2) + F_0\right) \tag{4.7}$$

One immediate advantage of this new system is that it is autonomous so that the phase space is now only two dimensional. Therefore we can obtain the catchment regions by considering an ensemble of trajectories. Trajectories in the new (u, v) coordinates system will not cross and the cusping feature of the exact trajectories will also be eliminated as shown in Figure (25). Since these cusp like features and subharmnonic responses are smoothed out by the approximate system, equation (4.7) is referred to as the smoothed variational equation. A complete amplitude response diagram can be obtained for Duffing's equation for various levels of damping, as shown in Figure (26). We note that the bending over of the response curve which creates two alternative stable states depend on the damping level as well as the restoring function. The point at which this system jumps to a remote state is of course due to a fold bifurcation with the unstable path denoted here by a dotted line.

With $\zeta = 0.1$ hysteresis occurs for values of η between approximately 1.45 and 1.73. The final steady state motion of the system depends entirely upon the initial conditions. The system's phase portraits in the Van der Pol plane are plotted for six values of η in Figure (27).

In these diagrams, initial conditions are given equally spaced around a circle and then the smoothed variational equation is solved using a Runge-Kutta integration routine. The points marked along the trajectories represent Poincaré points taken at multiples of the period of the forcing. The flow in these diagrams can be interpreted in polar coordinates as the continuous adjustment by the system of its amplitude A and phase ϕ. The catchment regions for the two competing stable steady state oscillations, represented in this Van der Pol plane as two sinks, are bounded by the separatrix passing through the unstable saddle solution; one of the domains of attraction is shown dotted whilst the other is left blank. As the variable η is reduced the catchment region for the small amplitude solution decreases until it vanishes at just below 1.452, after which all trajectories are attracted towards the large amplitude resonant motion. The disappearance of this small amplitude solution is due to a fold bifurcation of the response curve at the point Q. By examining the beat frequency of the transient responses it is possible to make predictions of this incipent folding action as Q is approached. (Bishop and Franciosi[59], Thompson and Virgin[60]).

4.4 Analogue computer simulation

The analogue computer is a device that is naturally suited for the study of the dynamical behaviour of oscillating systems. This computer essentially comprises a set of units able to perform certain mathematical operations, which when properly coupled together, may be used to solve differential equations or, systems of differential equations. These basic units and the mathematical relationships obeyed by their input-output variables are shown in Figure (28). All variables are represented by voltages; system inputs are represented by voltages, as well as system outputs or responses.

The behaviour of the system may be observed and recorded using oscilloscopes and electromechanical recorders. The accuracy of the analogue computer however is limited by the precision of the components in the machine, and the ability to measure the voltage accurately.

The advantages of using analogue computer simulation are the speed and the ease in programming. Essentially, this involves connecting various units using a piece of wire. Its flexibility is due to the development of a wide range of easily applicable nonlinear function-generating components. Thus in many cases an analogue simulation of a nonlinear problem may be the most practical and economical approach. Indeed, Ueda's work on nonlinear dynamical systems has been assisted by a hybrid of a large analogue and digital computer.

For problems involving the use of the analogue computer, it is necessary to scale properly the system variables (or inputs) so that the voltages that represent the variables do not exceed the full dynamic range of the components in the computer. Here, the 'normalized variable' magnitude scaling technique[61,62] and the time scale factor method[63,64] have been applied throughout. A thorough algebraic presentation of the scaling technique can be found in Ghaffari[65].

Our analogue computations were performed on an EAI-1000 Analogue computer supplemented by an external wave generator. The resulting system allows quick approximate results to be obtained under, for example, different values of initial conditions.

The example we have used in our studies is again a version of Duffing's equation with no linear stiffness; namely

$$\ddot{x} + k\dot{x} + x^3 = B \cos t$$

This equation has been considered by Hayashi[16] and extensively studied by Ueda[66]. For variation of the two parameters k and B a wealth of nonlinear behaviour has been charted by Ueda, including coexisting periodic and chaotic solutions. In the absence of a natural, linear frequency the usual resonance response diagram can be drawn by plotting $B^{-1/3}$, a measure of the forcing-frequency/system-frequency ratio, against $B^{-1/3}$ multiplied by the amplitude which in turn gives an appropriate amplitude/static-response measure.

With the coefficient of damping held constant at $k=0.2$ the familiar form of an engineering resonance response curve is shown in Figure (29) obtained by digital time simulations and confirmed by analogue studies. If the variable B is increased, i.e. $B^{-1/3}$ is decreased, a jump to resonance can be initiated. The hysteresis implied

by this jump leads to two alternative harmonic solutions onto which the system may settle, depending upon the initial conditions. The region of initial conditions on the $(x,\dot{x})$ plane which results in motion decaying onto the small amplitude solution has been obtained by analogue computer simulations using a grid of starts. To illustrate how this area of attraction diminishes as $(x,\dot{x})$ is decreased, this grid of starts method was carried out for seven values of B within the hysteresis loop. The results are displayed in Figure (30). The catchment region for the small amplitude solution is represented by a square while the catchment region for the large amplitude solution is left blank. As the control parameter is decreased to the fold point, just below 1.34, the shaded area diminishes indicating the respective dominance of the two relevant modes. To confirm our analogue study, also included in this Figure is a diagram obtained by Ueda when $B=0.3$ ($B^{-1/3} = 1.49$) which compares favourably with our own result shown here in the Figure where ($B^{-1/3} = 1.50$).

The Poincaré points (shown in small squares) and trajectories of the stable steady state oscillations are also given in the diagrams of Figure (30). It should be remembered though that the phase portrait shown here is really a two dimensional projection of the solution from the three dimensional phase space. In the diagram by Ueda, the saddle point, denoted by the number 1 lies on the unstable path, correspondingly indicated by the dashed line in Figure (29).

We have detailed several ways in which the domains of attraction for competing harmonic solutions can be evaluated. In the next section we shall see how these and further methods may be applied to mathematical models in the field of offshore mechanics.

4.5 Examples in Offshore Mechanics

In this section we shall present some examples in offshore engineering when nonlinearity in the restoring force leads to coexisting fundamental and subharmonic solutions with a sensitivity to initial conditions. The major practical implication for engineers is the possibility of relatively large amplitude subharmonic oscillations of compliant and offshore structures in parameter regions well away from the natural frequency in what might otherwise be considered 'safe' conditions.

4.5.1 Subharmonic resonance of an articulated mooring tower

The first example involved an articulated mooring tower used in the North Sea to load oil into tankers. This mooring tower has a discontinuity in the restoring force such that it's behaviour is essentially nonlinear in nature. This dynamical system is defined mathematically as follows:

$$\ddot{X} + 2\frac{\zeta}{\eta}\dot{X} + K_iX = \frac{1}{\eta^2}\sin\tau$$

where a dot denotes differentiation with respect to time (τ), X represents displacement, ζ is the damping factor, η is the frequency ratio, K_i is used to denote whichever of K_1, for positive displacement, or K_2, for negative displacement, is appropriate for the domain under consideration and:

$$K_1 = (1+\sqrt{\alpha})/4\alpha\eta^2$$

$$K_2 = (1+\sqrt{\alpha})/4\eta^2$$

where $\alpha = k_2/k_1$ is the stiffness ratio while k_1 and k_2 are the stiffnesses for positive and negative displacement respectively.

A detailed description of this dynamical system will be presented in a later chapter.

Because of the underlying nonlinearity, the existence of coexisting subharmonic solutions is possible. This has been extensively charted by Thompson[67] for a range of the control parameter η. We shall concentrate here on the parameter range such that the n=1 fundamental solution coexists with the larger amplitude n=4 subharmonic, which occurs well away from the fundamental resonance at $\eta = 1$. An enlargement of this region on the amplitude response diagram is shown in Figure (31e). The dangerous implications for design engineers is clearly seen in this figure, in which the subharmonic solution can have a maximum displacement considerably greater than that of the harmonic solution.

To illustrate the differences in the two alternative solutions we detail here some results where the control parameter is fixed at $\eta = 3.95$.

Figure (31c) shows a study of the transient decay of the system as a time history of the displacement, while the corresponding phase projection is given in Figure (31d). Two alternative starts are used, S_1, converging onto the smaller amplitude n=1 solution, and S_4 decaying onto the larger n=4 subharmonic. If the system is allowed to oscillate at the lower amplitude state then as η is *slowly* varied, some transients will decay onto this harmonic solution. However given a different initial condition, for example caused by some sudden external loading, the higher amplitude state can be achieved. To safeguard against this, we must chart the catchment regions for the n=4 subharmonic solution. The problem now centres on the location of the separatrices which form the boundaries of the domains of attraction, Figure (31f), and the determination of the stability of the system under normal environmental conditions.

In order to uncover the catchment regions, the location of the period four saddle was first obtained by graphical technique and then the ladder method was applied to trace out the inset of this saddle. Figure (32a) shows this result displaying both the inset and outset to each of the four saddle points (since we are sampling at every forcing cycle instead of every fourth forcing cycle). In this Figure each dot represents a Poincaré point but it should be remembered that the collection of points which form a curve will be from a set of different starts (rungs) and not a single start. From these data, one can immediately access the probability of the mooring tower attaining subharmonic oscillations under environment loading.

Alternatively, a grid of starts could be used to evaluate the catchment regions. Such a task was also completed for the same parameters and included here is the equivalent diagram for comparison with Figure (32b). Starting conditions leading to the small amplitude n=1 solution are indicated by the hatched region, which is composed of small crosses showing each trial. Starting conditions leading to the large amplitude resonant n=4 solution are indicated by the blank region, trials in this region having been made on the same resolution as the crosses.

4.5.2 Surge motion of a moored semi-submersible platform

A second brief example from the field of offshore mechanics concerns the surge motions of a floating semi-submersible platform chained to the sea bed by catenary mooring lines. These chains exert a nonlinear restoring force on the structure shown

schematically in Figure (33a). Here the stiffness function K(X) and the local restoring force *k(x)*, are obtained by curve-fitting design data using third order polynomials, as shown in Figure (33b): note the analogy to a hardening spring restoring force. The simplified equation of motion used to model this system is of the form:

$$m\ddot{x} + b\dot{x} + k(x) = F_0 \sin\left(\frac{2\pi t}{T}\right)$$

Again, this problem has been the subject of a detailed parametric study and the relevant coefficient values can be found in Bishop and Virgin[68]. We shall focus our attention on a region of parameter values where it has been shown that stable, coexisting n=1 and n=2 motions persist. Figure (33c) shows the maximum amplitudes and the position of the Poincaré points as a function of the wave period, while Figure (33d) shows the time series and the corresponding phase portraits of the two competing steady states when *T*=19.7 seconds.

For fixed values of the forcing wave period the catchment regions enclosing these alternative solutions can be mapped out as shown in Figure (33e) by tracing the inset of the saddle points. A sweep through resonance given in Figure (34) shows the relative dominance of the two modes. This clearly bears some resemblance to the catchment regions for Duffing's equation as illustrated in Figure (24). Again the subharmonic oscillation has the greater amplitude so that care must be taken when investigating this, or any other nonlinear system. Of special concern is that we are considering here regions of wave period that might very well coincide with design wave conditions away from the fundamental resonance at approximately T=44.9 seconds, and yet still achieving dangerously large amplitude motions.

4.6 Simple cell mapping technique

So far we have met several methods which can explore the phase space so that the global behaviour of the dynamical system can be explored. However, it is also true that they are quite tedious to implement. Like the graphical technique and the smoothed Van del Pol plane, they are only practical for simple systems. When we deal with problems like fractal basin boundaries, the only real possibility is the grid of starts technique. However even for a really coarse grid with 100x100 starts, we had 10,000 points, and for each starting point, 50 forcing cycles are required so that

we can be reasonably sure that it has attained a steady state. Then the total number of forcing cycles needed to be simulated will be 500,000. This is tremendously expensive even with a high speed super computer such as the Cray. It is with this in mind that we have employed the simple cell mapping technique.

Using the grid of starts technique, we have to follow the trajectory of each intial condition until a steady state is reached. Thus, on the two dimensional phase projection, we can observe a series of dots or Poincaré points moving across the plane until the Poincaré point is repeating in a cycle, i.e. a periodic solution. Obviously, if we want to uncover the catchment regions, we can cover this phase space with as many points as possible and strike a balance between computational efficiency and resolution. However, we have no information about points which do not fall on this grid so that the final result on the catchment regions will still be an approximation, although all the computed points are exact within the numerical accuracy of the computer and the integration routine employed.

Since it is impossible to define each and every point of the phase space on the grid and then obtain the final steady state of each point as accurately as possible, we divide the two dimensional phase space into cells, each cell being a square instead of a point. This square covers an area of the phase space, and we assumed that every point within this cell would have the same steady state behaviour. Then the Poincaré map will map one cell into another cell rather than from one point to another point. Again, a steady state periodic solution will be obtained when a cell is repeatedly mapped onto itself. The advantage of this method can be easily understood. When one trajectory is defined on this phase plane leading to a steady state, whenever we encounter a cell which lies on this trajectory, we know immediately the final steady state of this cell and it is not necessary to apply the Poincaré map again. Therefore each cell need only be mapped one step forward and the final steady state can be determined. Using the same resolution as the grid of starts technique mentioned above, we are 50 times faster than the grid of starts technique and consequently we can afford to increase the resolution by defining a smaller cell.

This simple cell mapping technique is similiar to Hsu's cell-to-cell and generalized theory of cell to cell mapping but is simplified to enhance efficiency.

While the generalized theory can deal with more complicated global behaviour, it sacrifices computational speed by incoporating probability techniques which defeat the origin aim of improving efficiency.

4.7 Computational algorithm of simple cell mapping technique

In this section we describe the basic idea of the algorithm which allows us to determine the periodic cells and their domain of attraction in a very effective manner. We shall use the same terminlogy as Hsu so that the interested reader can get to grip with Hsu's[69-73] generalised theory much more easily.

Periodic motions and periodic cells. Let C^n denote the cell mapping C applied n times to form a sequence of K distinct cells Z(j), j=1,2,...K which satisfy

$$Z(n+1) = C^n(Z(1)), n = 1, 2, ..., K - 1$$

$$Z(1) = C^K(Z(1))$$

This is said to form a periodic motion of period K. Hence each of the sequence's elements Z(j) is a periodic cell of period K or simply a P-K cell. A P-1 cell thus have the same period of the forcing frequency.

Sink cell and regular cell. When a cell is mapped outside the region of interest, say to a remote attractor, the sequence of mapping is stopped and the cells are said to map to a sink cell. This is arbitrarily ssigned as a P-1 cell. Cells within the region of interest are called regular cells.

The evolution of the system starting with any regular cell Z can lead only to three possibilities:

(i)   Cell Z is itself a periodic cell of a periodic motion. The evolution of the system is simply a periodic solution.

(ii)   Cell Z is mapped onto the sink cell after r-steps. Then this sequence of cells belongs to the domain of attraction of a remote attractor.

(iii)   Cell Z is mapped into a periodic cell of a certain period after r-steps. Thereafter, the evolution is locked into that periodic motion. Then this sequence of cells belongs to the domain of attraction of that periodic motion.

In order to differentiate different domains of attraction, it is useful to introduce two numbers to delineate the properties of each cell. They are the group number G(Z) to distinguish coexisting attractors and the periodicity number P(Z) to identify the period of the attractor. To each periodic motion obtained, a group number is assigned to every periodic cell of that periodic motion and also to every cell in the domain of attraction. A periodicity number equal to this period is assigned to all the cells in this group. Hence, the problem presents itself as to determine these two numbers for every regular cell when a cell mapping is given.

The algorithm involves processing the cell by applying the mapping systematically. For example, for a two dimensional problem, we can use a two dimensional array where each element's position in the array reflects the coordinates of the centre of the cell on the phase plane. During this process, we must also be able to distinguish three kinds of cells. The first ones are those which have not been processed, they can be called virgin cells. The group number of these cells can be conveniently set to 0. Therefore a virgin cell Z is characterized by having G(Z)=0. The second kind of cells are those which are under processing but the steady state solution has not been identified either as a sink cell or a periodic cell. These cells can be characterized as having a group number of -1. The third kind are those whose group and periodicity numbers have been assigned. Thus G(Z) is characterized by a positive integer. Hence, the group number is serving as a flag in computational terms.

Starting with a cell Z, we have a sequence of cells produced by the mapping; in our problem, this sequence of cells is derived from numerical integration of the original differential equation. We have:

$$Z \rightarrow C(Z) \rightarrow C^2(Z) \rightarrow .... \rightarrow C^m(Z)$$

For each mapping sequence, there are three possibilities for each cell which is under processing:

(i)   The newly generated element $C^i(Z)=Z'$ is such that its group number $G(C^i(Z))=0$ indicating that the cell $C^i(Z)$ is a virgin cell. In this case we continue

-58-

to apply the mapping and locate the next cell $C^{i+1}(Z)$ in the sequence. Before doing that, we must now set $G(C^i(Z))=-1$ in order to indicate that $C^i(Z)$ is no longer a virgin cell but one which has been processed.

(ii)   The newly generated cell $C^i(Z)=Z''$ is found to have a positive integer as its group number $G(Z'')$. This indicates that Z' has already been processed in a previous sequence. Since the current processing sequence has been mapped onto a cell with known final motion this sequence of processing can be stopped. Obviously all the cells of the present processing sequence will have the same group number as well as the periodicity number as that of Z''. We can then assign the same numbers to the current processing sequence and go back to pick the next virgin cell to begin a new processing sequence.

(iii)   The newly generated cell $C^i(Z)=Z'''$ is found to have -1 as its group number. This indicates that $C^i(Z)$ has appeared before in the present sequence. Therefore, there is a periodic motion contained in the current sequence. In this case the processing sequence is again terminated. The whole sequence of cells is then assigned a group number which is one larger than the number of groups which have already been determined. The periodicity of the sequence can now be calculated easily. Let $C^i(Z)$ reappear in the (j+1)th position of the sequence, i.e., $C^i(Z)=C^j(Z)$, j<i. The periodicity of the motion is thus i-j, and all the cells in the sequence will have the same periodicity number. Once these numbers have been assigned, we go back and pick up another virgin cell to begin a new processing sequence.

Using these processing sequences starting with virgin cells, the whole phase space is covered and the global characteristic is determined in terms of the group number and periodicity number. Given a set of parameters, even if we do not know of any coexisting solutions, or any global characteristic, the whole phase space can be uncovered in a fast and efficient way.

In our program implementation, since we deal only with a two dimensional phase space, a two dimensional array has been used. For example, if 100x100 cells are used to cover the phase space, the array will have the same dimension. Using the position of the element in the array, the coordinates of the centre of the cell are calculated and put into the numerical integration routine and run for one forcing cycle. The result is then checked and the position of the cell which contains this

point is found and hence the position of the element in the array. The procedure is then repeated and a group number is assigned to the elements of the array. To reduce the number of arrays required, the decimal part of the number can be used to denote the periodicity number and the integer part for the group number.

While the Simple Cell Mapping technique is easy to implement as well as efficient, it does has a disadvantage. Once a cell is mapped outside the region of interest, it is considered to map onto the sink cell and no information will be availiable as to its final behaviour. It can either go to infinity or to an attractor outside the region. Therefore, the region under investigation must contain at least one attractor so that the corresponding domain of attraction can be located. Now, suppose we want to investigate part of a region in detail with an attractor outside this region; using a grid of starts technique we can fire off as many points as required and record all of their final motions. However, using the Simple Cell Mapping technique this is impossible because all the cells will eventually be mapped outside the region and considered to be mapped onto the same sink cell. Therefore this method is suitable only to investigate the global phase space rather than the global behaviour of a local region.

Using the Simple Cell Mapping method we have made extensive studies into the global behaviour of the ship-capsize model. It will be seen in a later chapter that as this dynamical system evolves, complicated phenomena such as fractal basin boundaries appear and the Simple Cell Mapping technique contributes signigicantly to the understanding of this type of behaviour.

5 Steady state solution path-following technique

From an engineering point of view, one of the most useful ways to look at the behaviour of a dynamical system is by way of the control phase space diagram. For example, given the damping and stiffness, at what forcing parameter will a structure undergo resonant vibrations? This type of question can only be answered by a thorough parametric study.

In the past engineers have used linear theory and analytical techniques to obtain approximate solutionsof nonlinear systems However, large scale compliant structures such as an oil platform have inherent large amplitude vibrations so that nonlinear effects can no longer be ignored. Typically, a nonlinear equation has no analytical solution. The behaviour of the system can only be obtained by a numerical technique. A parametric study would then involve varying a control parameter, such as the damping, stiffness or forcing amplitude and obtaining the steady state solutions. The control phase space diagram can be constructed when the effect of the variation of each parameter is obtained. One can see that even for a simple system, parametric studies are computationally very expensive. Therefore, engineers tend to extrapolate the effect of a control parameter or operate within the range which is thought most likely to be encountered. This is perhaps very dangerous as we have observed in the examples shown in Chapter 4.

This deficiency has led us to look at the way in which mathematicians and theoretical dynamists deal with this type of problem. The introduction of a Poincaré map and two-dimensional linear mapping theory are just two examples of this cross pollination between engineers and theoreticians. In this chapter, we shall introduce a steady state solution path-following[74,75] technique so that for a given range of a single control parameter, the steady state solutions and their stability can be obtained with great computation efficiency.

5.1 Formulation of residual map

Consider a dynamical system defined by a Poincaré map P; if $P(U_p) = U_p$ is a fixed point of the system, then

$$P(U_p) - U_p = 0 \qquad (5.1)$$

We can formulate this problem as a zero point problem by defining the residual map Q as

$$Q(U_i) = P(U_i) - I(U_i) \qquad (5.2)$$

where I is the identity map, i.e.,

$$I(U_i) = U_i$$

Then if U_p is the fixed point, we have

$$Q(U_p) = P(U_p) - I(U_p)$$

$$= 0$$

Hence, we shall be looking for a solution such that the residual Q becomes 0.

This zero point problem can be solved using the Newton Raphson method. For a one-dimensional system this iterative scheme is given by the equation

$$x_{n+1} = x_n - \frac{f(x_n)}{f'(x_n)} \qquad (5.3)$$

Let

$$\Delta = (x_{n+1} - x_n) \qquad (5.4)$$

where Δ is the correction needed for the next trial solution . Then from equation (5.2) we have

$$Q'(U_i) = P'(U_i) - I \qquad (5.5)$$

where I is now the identity matrix and we need the first directive of P.

Consider a two-dimensional phase space with a point (u_1, u_2) mapped to (v_1, v_2) as shown in Figure (35a). Then

$$v_1 = P_1(u_1, u_2)$$

$$v_2 = P_2(u_1, u_2)$$

This is an implicit functional relationship. In our case, the two functions, P_i (i=1,2), can only be found numerically by time integration. To obtain the derivative of P, we consider two adjacent maps as shown in Figure (35b). Hence

$$\delta v_1 = \frac{\partial P_1}{\partial u_1}\delta u_1 + \frac{\partial P_1}{\partial u_2}\delta u_2 \equiv P_{11}\delta u_1 + P_{12}\delta u_2$$

$$\delta v_2 = \frac{\partial P_2}{\partial u_1}\delta u_1 + \frac{\partial P_2}{\partial u_2}\delta u_2 \equiv P_{21}\delta u_1 + P_{22}\delta u_2$$

Or

$$\begin{pmatrix} \delta v_1 \\ \delta v_2 \end{pmatrix} = \begin{pmatrix} P_{11} & P_{12} \\ P_{21} & P_{22} \end{pmatrix} \begin{pmatrix} \delta u_1 \\ \delta u_2 \end{pmatrix} \tag{5.6}$$

Definition[76]. If $f(u_0 + h) - f(u_0) = Mh + e(h)$, where M is a bounded linear operator and $||e(h)||/||h|| \rightarrow 0 \quad as \quad ||h|| \rightarrow 0$, the function f is called Fréchet-differentiable at the point u_0 and we define $f'(u_0) = M$.

Therefore the derivative $P'(U_i)$ can be linearly approximated by the matrix P_{ij}. To obtain the coefficients of P_{ij}, a small increment h is taken in the direction x such that

$$\delta u_1 = h \qquad \delta u_2 = 0$$

$$\delta v_1 = P_{11}h \quad \Rightarrow P_{11} = \frac{\delta v_1}{h}$$

$$\delta v_2 = P_{21}h \quad \Rightarrow P_{21} = \frac{\delta v_2}{h} \tag{5.7}$$

Similarly, an increment in the direction y gives the coefficients P_{12} and P_{22}. We are now ready to apply the Newton Raphson method to find a fixed point.

Substituting equations (5.4) (5.5) and (5.2) into equation (5.3) we obtain

$$Q_i + Q_{ij}\Delta_j = 0 \tag{5.8}$$

where

$$Q_i = v_i - u_i$$

and

$$Q_{ij} = \begin{pmatrix} P_{11} - 1 & P_{12} \\ P_{21} & P_{22} - 1 \end{pmatrix}$$

After solving for Δ_j, the trial solution (u_i) is then corrected by the amount Δ_j and the iteration proceeds until $Q_i = 0$. When the fixed point is found so that

$$u_{i+1} = P(u_i)$$

then the fixed point's stability can be examined by obtaining the eigenvalues of the matrix P_{ij}, see Chapter 2, or from equation (5.5)

$$P_{ij} = Q_{ij} + I$$

The position of the eigenvalues in the complex plane belonging to this two-dimensional matrix then determines the stability of the fixed point.

5.2 Path following algorithm

When a system of ordinary differential equations has only one control parameter, the steady state solution can be obtained using the residual map as defined above. We can proceed in the following manner: having found the periodic solution; let that be (U_0, C_0), where U_0 is a fixed point with the control parameter fixed at C_0. We can take this as an initial estimate and increase the control parameter C_0 to C_1. If C_1 is close to C_0, we have already a good estimate, and we then apply the Newton Raphson method again.

This method can be improved if we know how U_0 changes when C_0 is varied in the direction C_1. Furthermore, this improvement is absolutely necessary when we want to follow the solution path when it goes through a saddle node bifurcation, see Figure (36a). Therefore, we must formulate a path following strategy and this leads to a new formulation of the residual map.

We could do as follows: for a specific value of parameter, the periodic solution is found as described in the last section. Suppose we find (U_0, C_0). We then increase or decrease the parameter a little (of the order h) and keeping the parameter fixed at the new value, a new periodic solution is obtained. Say (U_1, C_1). The vector $t_p = (U_1, C_1) - (U_0, C_0)$ then provides an estimate of the direction of the solution path. t_p is then converted into unit vector and a step h_p is taken in the direction of t_p. We then come to a point $v = (U_1, C_1) + h_p t_p$. If v turns out to be a point on the solution path, then the process is completed. If this is not the case, we must force the Newton Raphson iteration scheme to move in a direction orthogonal to t_p. Using this method, we shall not have any difficulty passing through a saddle node bifurcation as t_p has no component in the control parameter direction, see Figure (36b). By going orthgonal to t_p, the control parameter becomes a variable within the Newton Raphson scheme and is no longer fixed, i.e. an increment h does not mean an increment in the control parameter. What is kept fixed is the linear combination of U and C. In order to satisify this condition, the zero point problem must be reformulated which amounts to a reformulation of the residual map.

Suppose with a step length h_p, we have obtain a point v in the direction of t_p from a given point (U_0, C_0). We want to find the periodic solution by going orthogonal to t_p. These two vectors can be obtained conveniently by forming the cross product between t_p and e_1 as well as t_p and e_2. Here e_1 and e_2 are the base vectors of $(x, \dot{x})$. Let these two vectors be f_1 and f_2 respectively. Then the new basic, i.e. a set of linear independent unit vectors defining the vector space, becomes (f_1, f_2, t_p). Therefore v will now be varied in the direction f_1 and f_2 rather than $(x, \dot{x})$. Notice that the control parameter C is an independent variable, therefore the matrix Q_{ij} is essentially unchanged: what has changed is the interpretation of the matrix Δ_j. The coefficients in Δ_j are now the amount that we must change in our original estimate in the direction f_i, i.e., we must resolve the corrections needed in x, $\dot{x}$ and the control parameter, C, directions.

The steplength h_p should be adjusted automatically in the following manner. Suppose i iterations are allowed for the convergence to the periodic solution using the Newton Raphson method. If exactly i iterations are needed, the steplength is reduced in the next step. If less than i-1 iterations, then the steplength is increased.

Otherwise, h_p stays the same. Furthermore, h_p is controlled by lower and upper bound limits, i.e., $h_{min} \le h_p \le h_{max}$. If Newton's method does not converge in i steps, then h_p is again reduced.

Once we find the periodic solution, we can determine its stability by finding P_{ij}. This is done by running the iteration one more step but using (e_1, e_2) as the basis.

5.3 Validation of the path following algorithm

The periodic solution obtained from the path following technique can be checked by comparing the solution using time integration. The results have been found to be the same within seven significant figures. One of the important feature of the path following technique is that it can calculate the local linearized eigenvalues of the periodic solution. The accuracy of this feature is very important since it directly affects the result of the periodic solution as well as prediction of any imminent bifurcation. This again can be checked indirectly by comparing the numerically obtained Jacobian with the analytical solution.

Consider now a two-dimensional flow given by:

$$\dot{x} = f(x, y)$$

$$\dot{y} = g(x, y)$$

Expanding locally at any given point using Taylor series and neglecting any high order terms, we have:

$$\dot{x} = L + Ax + By$$

$$\dot{y} = M + Cx + Dy$$

hence

$$\frac{\partial \dot{x}}{\partial x} = A$$

$$\frac{\partial \dot{y}}{\partial y} = C$$

-66-

If we look at the flow of a small triangle in time Δt as shown in Figure (37a), we can obtain the rate of change of its area in the following manner.

$Original \quad area = J\,L\,M = \dfrac{1}{2}\delta x \delta y$

$Final \quad area = J'\,L'\,M'$

$$= \frac{1}{2}\{(\delta x + A\,\delta x \Delta t)(\delta y + D\,\delta y \Delta t) - (B\,\delta y \Delta t)(C\,\delta x \Delta t)\}$$

$$= \frac{1}{2}\{1 + AD\Delta t^2 + D\Delta t + A\Delta t - BC\Delta t^2\}\,\delta x \delta y$$

By dropping the second order terms, we have:

$$Final \quad area = \frac{1}{2}\delta x \delta y(1 + A\Delta t + D\Delta t)$$

The rate of change of area is therefore:

$$\frac{\partial area}{\partial t} = \frac{Final \quad area - Original \quad area}{\Delta t}$$

$$= \frac{1}{2}\delta x \delta y(A + D)$$

$$= (area)\left\{\frac{\partial \dot{x}}{\partial x} + \frac{\partial \dot{y}}{\partial y}\right\}$$

Generalizing this to three dimensions we have:

$$\frac{\partial Volume}{\partial t} = (Volume)\left\{\frac{\partial \dot{x}}{\partial x} + \frac{\partial \dot{y}}{\partial y} + \frac{\partial \dot{z}}{\partial z}\right\}$$

where the term

$$\frac{\partial \dot{x}}{\partial x} + \frac{\partial \dot{y}}{\partial y} + \frac{\partial \dot{z}}{\partial z}$$

is the divergence of the three dimensional flow. The divergence of the escape equation can be calculated as follow:

$$\ddot{x} + \beta\dot{x} + x - x^2 = F\sin\omega t$$

$$\dot{x} = y$$

$$\dot{y} = -\beta y - x + x^2 + F\sin\omega t$$

$$\dot{z} = t = 1$$

which gives

$$\frac{\partial\dot{x}}{\partial x} = 0$$

$$\frac{\partial\dot{y}}{\partial y} = -\beta$$

$$\frac{\partial\dot{z}}{\partial z} = 0$$

Hence the divergence is found to be

$$div = -\beta$$

Therefore the divergence in this case is independent of x and y or any control parameter except β, the damping. The volume of flow at any time t with respect to the flow at $t = t_0$ can now be obtained by integration, i.e.,

$$\frac{\partial Volume}{\partial t} = -\beta Volume$$

$$\Rightarrow Volume = (Volume)_0 e^{-\beta t}$$

Since all trajectories keep step in time, a disc of thickness δt remains a disc of thickness δt: therefore volumes can be interpreted as areas:

$$(New \quad Volume) = (Old \quad Volume)\, e^{-\beta t}$$

or

$$Area_{i+1}\delta t = Area_i \delta t\, e^{-\beta t}$$

$$\frac{Area_{i+1}}{Area_i} = e^{-\beta t}$$

As we sample the flow using Poincaré mapping technique, the integration can be performed over a length equal to the period of the forcing frequency. Hence the area ratio is given by

$$\frac{Area_{i+1}}{Area_i} = e^{-\beta T}$$

where
$$T = \frac{2\pi}{\omega}$$

Consider now the area ratio of a two-dimensional mapping defined by

$$x_{i+1} = F(x_i, y_i)$$

$$y_{i+1} = G(x_i, y_i)$$

Again, we can expand the functions and retain the linear terms at any point to obtain

$$x_{i+1} = l + a x_i + b y_i$$

$$y_{l+1} = m + c x_i + d y_i$$

where

$$a = \frac{\partial x_{i+1}}{\partial x_i} \qquad b = \frac{\partial x_{i+1}}{\partial y_i}$$

$$c = \frac{\partial y_{i+1}}{\partial x_i} \qquad d = \frac{\partial y_{i+1}}{\partial y_i} \qquad\qquad (5.9)$$

Mapping of a triangle JLM shown in Figure (37b) leads to

$$Area_{i+1} = \frac{1}{2}\{a\delta x_i d\delta y_i - b\delta y_i c\delta x_i\}$$

$$= \frac{1}{2}\delta x_i \delta y_i\{ad - bc\}$$

$$= Area_i\{ad - bc\}$$

$$\frac{Area_{i+1}}{Area_i} = ad - bc$$

Comparing equation (5.9) with equation (5.6), we see that the term (ad-bc) is just the linearized Jacobian of the functions F and G, and a, b, c and d are the coefficients of P_{ij}. If this is evaluated at a fixed point the eigenvalues of the matrix

$$\begin{bmatrix} a & b \\ c & d \end{bmatrix}$$

describe the stability of the fixed point. Furthermore, by letting

$$T = a + d$$

$$D = ad - bc$$

The product of the eigenvalues can be expressed as

$$\lambda_1\lambda_2 = \frac{1}{2}(T + \sqrt{T^2 - 4D})\frac{1}{2}(T - \sqrt{T^2 - 4D})$$

$$= \frac{1}{4}\{T^2 - (T^2 - 4D)\}$$

$$= D$$

We can now equate the area ratio of the map which we can obtained numerically, with the area ratio of the flow, which has been obtained analytically by integration over a period of time equal to the period of the forcing.

$$\frac{Area_{i+1}}{Area_i} = e^{-\beta\frac{2\pi}{\omega}} = D = \lambda_1\lambda_2$$

Therefore, for a given value of β and ω, the product of the eigenvalues of a fixed point is a constant. Furthermore

If
$$\lambda_1 = \alpha + i\beta \quad \lambda_2 = \alpha - i\beta$$

$$\lambda_1 \lambda_2 = \alpha^2 + \beta^2$$

$$= (radius)^2$$

Hence if the fixed point's eigenvalues are complex, they describe a circle in the complex plane with a radius equal to

$$radius = \sqrt{D}$$

$$= \sqrt{e^{-\beta \frac{2\pi}{\omega}}}$$

For $\beta = 0.1$ and $\omega = 0.85$ the value of D is 0.4775 and the radius would be 0.691. This is confirmed by the path of the eigenvalues on the complex plane as shown in Figure (38) obtained numerically using the path following technique.

5.4 Application

The path following algorithm not only allows us to explore the control phase space of the ship capsize problem presented in Chapter 7. The residual map also helps us to locate the saddle point with ease such that the global characteristic of the state space can be investigated by tracing the inset of the saddle. One of the great advantages of the path following technique is that it can also calculate the local linearized eigenvalues automatically and any imminent bifurcation can be noticed in advance.

Some of the path following works are shown in Figure (39). This series of diagrams is one of many that we have done in order to construct the control phase space with the forcing frequency and forcing amplitude as the control parameters. For these diagrams, the computer is instructed to stop the algorithm once a flip bifurcation occurs, i.e., one of the eigenvalues becomes -1. The program then automatically increases the forcing amplitude slightly and runs until a steady state solution is obtained. Hence a period doubling cascade and the whole path of the

saddle solutions are obtained. The two diagrams in the middle have in fact a casade of period doubling close to one end of the unstable path, but the ranges are just too small to be visible in this scale.

Notice the solution paths at $\omega = 0.4$ and $\omega = 0.5$ are widely different and studies at finer increments of ω are shown in Figure (40). It is precisely this capability of the path following technique to produce the whole solution path with ease that is so valuable in our work. Instead of taking weeks to get the same path it now takes only hours. In Chapter 7, we shall show that this technique has *helped* us to locate special features like the remerging Feigenbaum tree as well as contruction of part of the control phase space.

6 Predicting an incipient jump to subharmonic resonance

When designing structures to withstand dynamic loadings such as wind or wave action, the major concern is to avoid resonance. To simplify design, engineers often use linear dynamical theory to ensure that fundamental resonance can be avoided. However structures of compliant type such as those designed to operate in the North-Sea have inherent large amplitude vibration so that their behaviour is nonlinear in nature. This nonlinearity means that coexisting solutions and subharmonic resonances are possible. The high amplitude subharmonic response is especially dangerous so that any method to predict this type of behaviour must be considered valuable to engineers. We explore in this chapter some possible prediction techniques for a jump to subharmonic resonance. These techniques have been shown to work extremely well under a variety of computational situations, when applied to the simulation of an oscillating articulated mooring tower approaching the potentially dangerous subharmonic resonance.

Studies of the behaviour of compliant offshore structures are well suited to the Poincaré mapping technique when one assumes that the exciting force is periodic. A steady state of stable, periodic oscillation will manifest itself as a fixed point on the displacement-velocity plane, or the phase plane. A jump from the fundamental response to subharmonic resonance corresponds to a flip bifurcation in dynamical systems theory. After the bifurcation there will be two fixed points in the phase plane. This type of bifurcation is easily modelled locally by a discrete two-dimensional linear map of the type discussed in Chapter 2. Our prediction techniques are based on the fact that when this steady state solution bifurcates from an n=1 fundamental response, where n is the periodicity of the response, to a n=2 subharmonic solution, it must do so via the *flip* bifurcation in accordance with the mapping theory. While we cannot construct a mapping equivalent for our flow problem, nevertheless, the transient response of the structure produced by numerical integration can be sampled using the Poincaré mapping technique. Hence one can observe the local two-dimensional linear map's eigenvalues going through the unit circle and passing

-1 in the complex plane as the bifurcation occurs. By monitoring the eigenvalues, we can predict the imminent bifurcation as well as the critical control parameters by extrapolation.

In practice, the only information available from a dynamical system is its time history. Therefore we must look for a way in which the information needed for analysis can be extracted from the transient response rather than the steady state solution. In a practical situation, any dynamic loading is more likely to be irregular in nature and the structure is less likely to have any chance to settle into a steady state oscillation. In our investigations we have attempted to create this effect by including a random slam load on top of a regular sine wave. Therefore any equilibrium state will be perturbed to produce a transient motion. This transient motion is then analysised quantitatively to produce a prediction. A further complication in a real life situation is the possibility of an ever changing dynamic loading, typically in the form of a gradual increase in the forcing amplitude, i.e., an evolving state. Therefore, we should also take into account this type of situation.

6.1 The articulated mooring tower

The articulated mooring tower is essentially an inverted pendulum, pinned to the sea bed and standing vertically in still water due to its own buoyancy. It is used for loading oil products to tankers from the deep offshore installations, as sketched in Figure (41). A massive tanker moored to such a tower is essentially a fixed object during the tower's oscillation. Periodic slackening of its mooring line generates a discontinuity of stiffness providing the necessary ingredient for the existence of subharmonic resonance typical of a nonlinear system. Notice that we shall only consider the case of just-tight mooring. The more typical tensioned and slack moorings bring with them greater complexity, and will be ignored in the present investigation. The restoring force on the tower during oscillation is thus due to 'buoyancy plus mooring line' in one direction, and just buoyancy in the other. In each half of the phase plane separated by the stiffness discontinuity, the behaviour is linear, hence we shall refer to our mathematical model as the bilinear oscillator. Comprehensive studies of the bilinear oscillator leading to the discovery of continuous coexisting

small amplitude solutions under all subharmonic resonances as well as chaotic non-periodic motions can be found in references listed[67,77,78]. Analytical studies of Shaw and Holmes[79,80,81] on the bilinear and impact oscillator should also be mentioned.

It has been shown that the bilinear oscillator can be modelled in a non-dimensionalised form as:

$$\ddot{X} + 2\frac{\zeta}{\eta}\dot{X} + K_i X = \frac{1}{\eta^2}\sin\tau$$

where a dot denotes differentiation with respect to time (τ), X represents displacement, ζ is the damping factor, η is the frequency ratio, K_i is used to denote whichever of K_1, for positive displacement, or K_2, for negative displacement, is appropriate for the domain under consideration and:

$$K_1 = (1 + \sqrt{\alpha})/4\alpha\eta^2$$

$$K_2 = (1 + \sqrt{\alpha})/4\eta^2$$

where $\alpha = k_2/k_1$ is the stiffness ratio while k_1 and k_2 are the stiffnesses for positive and negative displacement respectively.

For each domain, the solution of the non-dimensionalized equation of motion can be written in the form

$$X = X_a + X_b \tag{6.1}$$

where X_a and X_b are the complementary and the particular solutions, respectively. The particular solution is of the form

$$X_b = M\sin\tau + N\cos\tau \tag{6.2}$$

where

$$M = \frac{K_i - 1}{\eta^2[(K_i - 1)^2 + (2\zeta/\eta)^2]}$$

and

$$N = \frac{-2\zeta/\eta}{\eta^2[(K_i - 1)^2 + (2\zeta/\eta)^2]}$$

The complementary function X_a can be written as

$$X_a = e^{-\zeta\tau/\eta}(A \sin \omega_d\tau + B \cos \omega_d\tau) \qquad (6.3)$$

where the damped circular frequency, appropriate to either domain, is

$$\omega_d = \sqrt{[K_i - (\zeta/\eta)^2]}$$

and the coefficients A and B, dependent on the initial conditions $(X_0, \dot{X}_0, \tau)$, are reset at every switchover from one domain to the other.

Substituting equation (6.3) and (6.2) into (6.1) and assuming the initial conditions to be $(X_0, \dot{X}_0, \tau)$, the two coefficients can be evaluated as

$$A = e^{\zeta\tau/\eta}\{(X_0 - M \sin\tau - N \cos\tau) \sin \omega_d\tau$$

$$+ \frac{1}{\omega_d}[\dot{X}_0 + \frac{\zeta}{\eta}X_0 + \left(N - \frac{\zeta}{\eta}M\right)$$

$$\sin\tau - \left(M + \frac{\zeta}{\eta}N\right)\cos\tau]\cos\omega_d\tau\}$$

$$B = e^{\zeta\tau/\eta}\{(X_0 - M \sin\tau - N \cos\tau) \sin \omega_d\tau$$

$$- \frac{1}{\omega_d}[\dot{X}_0 + \frac{\zeta}{\eta}X_0 + \left(N - \frac{\zeta}{\eta}M\right)$$

$$\sin\tau - \left(M + \frac{\zeta}{\eta}N\right)\cos\tau]\cos\omega_d\tau\}$$

The digital computer program was written to detect the stable steady-state solutions of the bilinear oscillator given the initial conditions $(X_0, \dot{X}_0, \tau)$, the frequency ratio η, the damping ratio ζ, and the stiffness ratio α. In this particular study, the following parameters will be kept constant at; $\alpha = 10, \zeta = 0.1$, while η will be the control parameter that will be varied.

The program uses the exact solution $X(\tau)$ for each half of the phase space, and evaluates this at very small increments of time. It then determines accurately the state at which the switch from one stiffness to the other occurs by solving a transcendental equation numerically. In doing so, it initializes a new set of initial conditions for the next half of the phase space. This process is repeated until a periodic solution is detected.

In the case of an evolving sea-state, the parameter η is put as a function of the non-dimensionalised time τ in the form

$$\eta = \eta_0 + r\tau$$

where r is the evolution rate and η_0 is the initial frequency ratio.

As we sample the transient periodically, any excitation introduced will be at the beginning of a cycle. This will be in the form of a sudden increase in the velocity. A random number generator is used to produce the effect of an excitation with irregular amplitude as well as the time when this excitation occurs.

A typical resonance response curve for this dynamical system with the above control parameters is shown in Figure (42). We shall now focus our attention on the transition from the fundamental response to the subharmonic resonance via the flip bifurcation in the region where the control parameter η is approximately equal to 1.5.

6.2 Poincaré maps and mapping techniques

Due to the periodicity of the forcing, transient responses of the bilinear oscillator are sampled using the Poincaré mapping technique and analysed using two-dimensional linear mapping theory. Making use of the fact that when a flip bifurcation occurs, one of the corresponding local linearized eigenvalues will go *through* -1, the problem presents itself as follows; for a given set of control parameters, find the eigenvalues from its transient response.

While our flow problem has no explicit mapping equivalent, our sampling method produces a sequence of points (Poincaré points) in the $(x,\dot{x})$ phase plane which will converge to a fixed point corresponding to a periodic steady state if the

system is stable, or diverge if the system is unstable. The relationship between two successive Poincaré points may be governed by complex nonlinear behaviour, but close to the fixed point we can approximate the dynamics by a two-dimensional linear map of the form:

$$x_{i+1} = a x_i + b y_i$$

$$y_{i+1} = c x_i + d y_i \qquad (6.4)$$

where x_i and y_i are coordinates in the phase plane such that the fixed point is centred at the origin. We shall not repeat here the stability criteria of a two-dimensional map as discussed in Chapter 2. The problem here is to calculate the four coefficients; a, b, c and d such that the eigenvalues of the Jacobian matrix:

$$H = \begin{pmatrix} a & b \\ c & d \end{pmatrix}$$

can be found.

We have assumed that the sampled points are described by equation (6.4). Therefore, using three successive mapping points from a transient trajectory, the four coefficients of the linear matrix can be found by solving a set of simultaneous equations:

$$x_{i+1} = a x_i + b y_i$$

$$y_{i+1} = c x_i + d y_i$$

$$x_{i+2} = a x_{i+1} + b y_{i+1}$$

$$y_{i+2} = c x_{i+1} + d y_{i+1}$$

where x_i (i=1,2,3...) are known from the transient trajectory using numerical integration technique. Noticed that the origin of the coordinate system must always be moved so that it coincides with the fixed point. This is done here by first obtaining the steady state Poincaré point before any perturbation is given. After the elements of the linear matrix have been found, the eigenvalues and eigenvectors can be obtained. This method involves three Poincaré points, hence we shall refer to this technique of tracking the transient as the three-point method.

The three-point method is a somewhat theoretical approach since it is unusual to know, a priori, the exact location of the fixed point. We can go around this problem by using one extra Poincaré point. Assuming the steady state Poincaré point is (x_e, y_e), then the coordinate system can be displaced so that the point (x_e, y_e) becomes the origin. Since x_e and y_e are unknowns, we need to introduce two more equations into the system of simultaneous equations as shown below:

$$x_{i+1} - x_e = a(x_i - x_e) + b(y_i - y_e)$$

$$y_{i+1} - y_e = c(x_i - x_e) + d(y_i - y_e)$$

$$x_{i+2} - x_e = a(x_{i+1} - x_e) + b(y_{i+1} - y_e)$$

$$y_{i+2} - y_e = c(x_{i+1} - x_e) + d(y_{i+1} - y_e)$$

$$x_{i+3} - x_e = a(x_{i+2} - x_e) + b(y_{i+2} - y_e)$$

$$y_{i+3} - y_e = c(x_{i+2} - x_e) + d(y_{i+2} - y_e)$$

This technique of approximation, which we shall refer to as the four-point method, would be used for instance when considering the transient motion of the articulated mooring tower under an evolving sea-state. In this situation, there is no steady state although the system will oscillate very close to a corresponding locus.

After evaluating the linear map we can determine the nature of the stability of the system by calculating the eigenvalues of the Jacobian matrix, H. The eigenvalues can be conveniently found in terms of the trace and determinant of H given respectively by:

$$T = a + d$$

and

$$D = ad - bc$$

so that

$$\lambda_{1,2} = (T \pm \sqrt{T^2 - 4D})/2$$

Now suppose that under the action of a changing sea-state, the coefficients of the linear map in equation (6.4) vary so that the eigenvalues describe a path in the complex plane. If the eigenvalues are both real, one of them can cross the unit circle at -1, producing the flip bifurcation or a jump to subharmonic resonance of order 2. The other possible routes to instability will not concern us here[82].

As the dynamical system tends to exhibit its bifurcational behaviour on the eigenvector associated with the critical eigenvalue, i.e., the eigenvalue with the largest absolute value, it seems reasonable to further simplify our approach and reduce the system to one dimension that also preserves all the qualitative properties of the two dimensional map. This can be achieved through the center manifold idea[60], rather like the principle of eliminating any passive coordinates. The reason why multidimensional dissipative systems become effectively one-dimensional is due to the difference in the rate of convergence in different directions. The direction of the slowest convergence defines a one-dimensional line which will contain the attractor. Physically, this suggests that the transient response of the system in the two-dimensional phase space is being rapidly sucked close to the critical eigenvector, i.e., the center manifold, which is one-dimensional. After this, the convergence is slowed down. In this way, we can view the transient as predominantly one-dimensional.

However, one must realize that when the control parameter is varied, the eigenvalues of the two-dimensional linear map can start off as being a pair of complex conjugates and then change into to a pair of real values. In Figure (43), the Poincaré points are joined together by a straight line to show the trajectory. It can be observed that these trajectories change gradually from a spiral to an oscillatory fashon when the control parameter approaches the bifurcation point. In fact one can also notice this characteristic from their time histories. Figure (44) compares the difference between a spiraling and an oscillating trajectory. Notice that the time history is obtained from the Poincaré points and not the trace for a complete cycle. The time history on the top diagram shows that each cycle took three steps corresponding to a triangular spiraling orbit shown on the right. In the bottom diagram, each cycle took only two steps corresponding to an oscillatory orbit. If we look at the time history of a complete cycle rather than using the Poincaré points, this characteristic will not be observable.

From a computational point of view, this rapid convergence creates problems. When the Poincaré points are oscillating close to the centre manifold, or the critical eigenvector, the equations for the solution of the two-dimensional linear map becomes singular. So whenever the transient comes near the centre manifold, the system of simultaneous equation becomes ill-conditioned. However, if we approximate the behaviour of the Poincaré map to be linear and one-dimensional, we can expect the critical eigenvalue calculated using the transient response to vary and then settle into a steady state when the oscillations occur near the centre manifold. Hence, we can say:

$$x_{i+1} = \lambda_1 x_i$$

We require $|\lambda|_1 < 1$ for stability, and a sequence of values for λ_1 using successive Poincaré points can be found. We shall refer to this technique of approximation as the 'centre manifold' method. This technique is shown to work extremely well in getting a steady value of the critical eigenvalue as summarized in Figure (45).

To eliminate any doubt as to whether the Jacobian matrix H calculated using the three or four-point method does correspond to our flow problem, a simple test is devised. For a value of the control parameter we can calculate the coefficients of the matrix and obtain the equation of the eigenvector. Since any initial start on the eigenvector will oscillate along that vector only, we can then use the eigenvectors to calculate two initial conditions on both the eigenvectors and look at the transient trajectory that is produced. Figure (46) shows our results: the oscillation remained essentially on a line, revealing the eigenvector and implying that our two-dimensional discrete model provides a good simplification of our non-linear flow problem close to the fixed point.

6.3 Predicting subharmonic resonance

Figure (47) shows both the three-point and the centre manifold methods for two chosen values of the control parameter, η. The three-point method gives solutions for both eigenvalues. When the control parameter is close to the flip bifurcation point (this is indicated by the eigenvalue getting closer to -1) the estimates can be seen to diverge. This is because the difference between the two eigenvalues becomes large and the trajectory is rapidly attracted to the centre manifold so that

ill-conditioning of the equations occur as explained earlier. When this problem occurs, it is possible to use the centre manifold method to estimate the critical eigenvalue as shown in the figure. It can be observed clearly that the approximation of the critical eigenvalue settles down into a steady value as predicted.

A peculiarity of the equations used in the three-point method is that, while λ_2 diverges as expected, the critical eigenvalue restabilizes after initial divergence to those obtained using the centre manifold method. In fact, a similar problem is also encountered when using the four-point method. Figure (48) shows the estimate of the eigenvalues using the four-point method with the same control parameters. Again λ_2 diverges as expected, and λ_1 is restablized after the divergence.

Let us now consider the bilinear oscillator subjected to a sequence of random impulsive loads with variable amplitude and at random times. Using the three and four-point methods we can expect that far away from fixed point it will be possible to detect easily both of the eigenvalues. While relatively close to the fixed point it will be more difficult to detect the non-critical eigenvalue, λ_2 as discussed above. However, it may still be possible to obtain an approximation of the eigenvalues using mapping points which are not close to the centre manifold, as we can see in Figure (49).

Using either the three or four-point method it is thus possible to compute eigenvalues for increasing increments of the control parameter as the dynamical system approaches the bifurcation. Bifurcation from the fundamental n=1 path to the subharmonic n=2 paths at $\eta = \eta^c$ is shown in the top diagram of Figure (50). This bifurcation can be observed equivalently by the movement of the critical eigenvalue λ_1 on the T-D plane as shown in the bottom diagram of Figure(50). Variation of the eigenvalues with the control parameter, η, in the middle diagram shows that when the eigenvalues become real the dynamical system moves quickly towards the flip bifurcation at $\eta^c = 1.5486$.

To simulate a practical situation, it is necessary to consider an evolving system in which the frequency, η, becomes a function of time. To analyse such a situation, the four-point method must be used since there is now no information regarding the steady state solution. In fact, there is strictly no steady state solution under an evolving state. Figure (51) shows the results using this method with two different

evolution rates, r, as indicated. The top diagram shows the impulsive load introduced in a deterministic manner. Using the transient produced after each impulsive load, the four-point method seems to produce a satisfactory result in calculating the critical eigenvalue. It can be observed that the path of the critical eigenvalues cuts the $\lambda_1 = -1$ line at $\eta=1.5486$, exactly the same as the result we have observed earlier.

The bottom diagram is perhaps a more realistic case where an impulsive load is generated at random in terms of both amplitude and frequency. Although the calculated eigenvalues are more irregular, the result for both evolution rate gives the same η value.

From our investigation, it can be seen that given such information as the movement of the eigenvalues in the complex plane, it is possible to predict at what control parameter the bilinear oscillator will bifurcate from a fundamental to a subharmonic response. Hence, if one can extract the relevant information from the transient response of a "structure", for example; obtaining the Poincaré sampling points, it is possible to predict the incipent bifurcation.

The techniques introduced in this chapter form the early stage of research into the application of dynamical system theory to the problems encountered in modern compliant offshore structures. They are intended to provide a means of extracting useful information so that the onset of potentially dangerous oscillation can be predicted and even avoided. Obviously in a complex real life situation, more sophisticated methods should be employed. Nevertheless, these theoretical studies clearly can be useful when, for example, guiding laboratory or computer simulations.

7 Chaotic dynamic of ship rolling response under beam sea

In Canada during the seventies, it was reported that several fishing vessels had capsized unexpectedly in sea conditions that were not thought to be particularly hazardous. Artec Canada Ltd. were consulted, and asked by the Canadian Government to prepare a report on the dynamic stability characteristics of typical hull shapes, to see if advanced computer simulations could help in the formulation of new design regulations for these small vessels. Two 150 ton fishing boats of different hull forms were studied[83], with 'hard chine' and 'round bilge' characteristics respectively.

The AQWA suite of hydrodynamic programmes employed were those developed by Atkins R&D of the United Kingdom for the offshore energy resources industry. These treat each boat as a rigid body with its full six degrees of mechanical freedom. Typical forms of hydrodynamic analysis being developed by the Atkins group can be seen in the work of Rainey[84].

While the physical aspect such as the hull shape is important in the design of a vessel to withstand capsize, the dynamic phenomenon which triggers the capsize has not yet been fully investigated. In order to understand the basic underlying principles, we shall start by formulating the simplest possible model so that it would give us a better insight into the problem and from then on a more sophisticated model can be developed.

In the simplest possible way, the capsize of a ship in lateral ocean waves can be modelled by an equation[85-87] of the form:

$$m\ddot{x} + b\dot{x} + GZ = F\sin\omega t$$

where x is a measure of the roll angle. The constant mass here is taken to include the added mass in roll, b is an equivalent linear damping coefficient usually evaluated empirically in still water conditions, and GZ is the restoring force provided by the stiffness of the vessel: in an ideal situation the GZ curve will be a symmetrical

function of the roll angle but in reality a vessel is usually biased in some way so that it has a propensity to capsize in one particular direction. This bias term, B, is incorporated into the GZ curve such that:

$$GZ = B + g(x)$$

This bias could possibly be due to a shifted or unevenly distributed cargo, environmental loading, or perhaps even damage.

Excitation of the vessel by wave action is clearly irregular or stochastic in nature. However, an alternative approach is by way of the so called design wave method. In this method, a regular or sinusoidal wave having an amplitude F assumed to be the worst possible occurrence in 100 years of sea-state is employed. This type of analysis coincides with our simplistic approach which takes the excitation as purely sinusoidal. As the fishing vessels capsized in sea conditions which at the time were not thought to be rough or hazardous, the forcing amplitude will here be increased slowly from a small value until criticality so as to observe the dynamical behaviour of the system.

The governing potential energy function, V, for typical unbiased and biased systems, found by integrating the stiffness curve GZ, has been schematically drawn in Figure (52). In this figure a stable equilibrium point is envisaged as a ball shown blacked-in resting in a *potential well,* and similarly with a white ball on the *hill-top* depicting an unstable point. Also shown in the figure is the $(x, \dot{x})$ phase portrait for the undamped unforced counterpart to this problem. In this simplistic situation, capsize of the vessel can be thought of as the ball being forced by the excitation to oscillate, such that it surpasses the unstable position and rolls out of the potential well to infinity.

To examine a probable mechanism which triggers the capsize, the biased system's GZ curve local to the capsize region is approximated by a quadratic expression. The main reason for this approximation is computational expedience since many thousands of integrations will be performed in the computer simulation. After a rescaling of the time and roll angle, we shall focus our attention on an equation in the form:

$$\ddot{x} + \beta\dot{x} + x - x^2 = F \sin \omega t$$

which we shall refer to as Thompson's single potential well model.

The global behaviour of Thompson's capsize model without forcing for a lightly damped system is sketched in Figure (53). The catchment region is the white area where all motions flow onto the equilibrium point as time evolves. If we now consider the system to be excited by a small amount of external force, then the equilibrium point becomes a periodic solution and the saddle point now becomes a saddle cycle. In this case, where the forcing is non-zero, the dynamical behaviour is examined via the Poincaré sampling technique and so the phase portrait shown in the figure is now not that for a flow but a map. It should be noted that, because of the need for continuity, for arbitrary small forcing F, the qualitative structure of the phase portrait of the map must be the same as that of the flow.

7.1 Pilot studies of the ship capsize model

For a given value of damping, in our model, at what value of forcing will the ship capsize and furthermore by what mechanism? To answer these questions, we shall keep the damping a constant and put the forcing amplitude F as a slowly varying function of time. Physically, this represents a changing or evolving sea-state and the slowly evolving forcing also serves as a reasonable indicator for the situation in which the exciting force is kept constant.

Investigations using this technique are shown in Figure (54) with the linear damping, β, constant at 0.1. This diagram shows the time histories of the roll motion of the vessel at various values of the forcing frequency, ω. Notice that, following the rescaling procedure the point at which $x = 1$ is when capsize occurs.

From Figure (54), it can be observed that below $\omega = 0.83$, capsize happens well before x reaches 1. The phenomenon occurs as a jump in the response of the system and there is no warning of the impending disaster. Above $\omega = 0.83$, this jump is restabilized at a higher amplitude and the response again increases steadily until another phenomenon occurs. This time, capsize happens after an irregular rolling motion has developed and again there is no warning. Although the amplitude of the rolling motion is higher, it is still below $x = 1$. Thus any attempt to predict capsize based on the increasing amplitude would surely overestimate the time to capsize by a considerable amount.

To understand these phenomena, the resonance response diagram of the dynamical system must be investigated. Here, the path of the fixed point in the phase plane, corresponding to a periodic solution at a fixed value of the forcing amplitude is followed with increasing forcing amplitude until the ship is capsized. Some typical examples are given in Figure (55) where the displacement of the Poincaré points are plotted against the forcing F. (Note: the displacement of a Poincaré point is not the same as the maximum amplitude of the response).

From this figure, it is clear that capsize can be caused by one of two mechanisms. If the forcing frequency, ω, is at or below 0.8, the jump to capsize is due to a fold catastrophe where there ceases to be a local attractor or stable solution. At higher values of forcing frequency, a stable region has emerged. The jump phenomenon due to the fold catastrophe is restablized because of the presence of this stable solution. Further increase in the forcing amplitude leads to a cascade of period doubling and eventually a chaotic attractor emerges. However, the chaotic attractor disappears quickly, i.e. the ship capsizes, without any indication whatsoever. In the case where $\omega = 0.8$, the chaotic attractor coexists with the stable n=1 periodic solution. When the chaotic attractor is destroyed the motion is restablized onto the periodic solution. Other features we have observed in this stage is the pulling apart of the solution path so that the hysteresis feature disappeared at $\omega = 0.95$. This explains the disappearance of the jump phenomenon on the last two diagrams of Figure (54) where $\omega = 0.93$ and 0.94 respectively. Also, it is not true that below the critical forcing amplitude where capsize occurs, any perturbation given to the system will restablize to the steady state periodic solution. We have observed that even a small perturbation can lead to capsize when F is well below critical as we shall see in later sections.

7.2 Predicting Escape using analytical and statistical methods

As our simple mathematical model for the capsize of a ship can be visualized as a ball rolling out of, or escaping from the potential well, we shall refer to capsize as escape from now on.

Our attention will for the moment focus on the parameters where $\omega = 0.85$ and $\beta = 0.1$. At these values of parameters the system exhibits all the interesting phenomena, namely the fold catastrophe and chaotic attractor just before capsize or

escape occurs. We shall not concern ourself when the escape is caused by the fold catastrophe where no local attractor exists, since this type of dynamical behaviour can be predicted using the local linearized map of the dynamical system and research has been conducted by our colleague L.N. Virgin[60]. Our main concern here will be to find out the mechanism which triggers the capsize after a chaotic attractor is developed.

Figure (56) shows the path of the fixed points (displacement of the steady state Poincaré points) with increasing forcing amplitude together with the unstable fixed points or direct resonant saddles. At these values of parameters, escape occurs at $F = 0.109...$: the cascade of period doubling leading to a chaotic attractor is not observable at this scale. Further enlargement of the cascade is shown in Figure (57). Here, the unmistakeable hallmark of chaotic attractors, namely, period doubling and periodic windows can be observed clearly. To further substantiate our claim that this is indeed a chaotic attractor, the Poincaré sections will be plotted at different phase angles, ϕ, to examine how its topological structure varies with changing phase angle. Figure (58) displays a sheared Van der Pol plane showing 80 Poincaré sections at 4.5 degree interval. It can be seen from the figure that the attractor is a two band or period two chaotic attractor, (i.e. any initial start on one band of the attractor will return to the same band after two forcing cycles). The typical folding and mixing actions can be observed clearly. If we follow the progress of any one point for a duration of two forcing cycles, we find that the trajectory will form a Möbius band. This is in fact not accidental but a feature of a flow problem. Since the inset of the period two inverting saddle forms a virtual separatrix between the two band chaotic attractor, and its local two-dimensional linearised map has a pair of negative eigenvalues, each point will be *mapped* across the inset and outset as shown schematically in Figure (59a). However, in a flow problem we cannot have crossing trajectories, so the three dimensional phase space must be twisted in such a way that the flow is able to cross the inset and outset without the trajectories actually crossing each other. This is shown schematically in Figure (59b), which is in fact a Möbius band.

7.2.1 Blue Sky Catastrophe and Melnikov's method

Let us now investigate how a chaotic attractor can disappear suddenly. Returning to Chapter 1 for the bifurcation diagram classified by Thompson et al, Figure (7) shows clearly that the only possible way for a chaotic attractor to disappear is via the chaotic Blue Sky Catastrophe[24,88]. It is called Blue Sky Catastrophe simply because the original attractor (not necessarily chaotic) suddenly disappears into the *blue*. The simplest example which occurs in a flow problem has been discussed in Chapter 1 and illustrated in Figure (6): this shows schematically a sequence of phase portraits leading to the bifurcation. Below the critical value there exists a limit cycle, the shaded region is the catchment region for this periodic solution. The inset of the saddle is the separatrix. As the control is varied, the saddle moves closer to the limit cycle until they touch and form a homoclinic orbit. This *homoclinic connection* may be though of as a limit cycle of infinite period; by increasing the control further, the limit cycle has ceased to exit since the inset is no longer a separatrix and all motion goes to the remote attractor.

In a one dimensional map such as the quadratic map studied by Grebogi[51], the separatrix is the saddle itself, therefore the Blue Sky Catastrophe occurs when the saddle collides with the attractor. This is in fact what happens in Grebogi's interior and boundary crises where a chaotic attractor collides with a saddle. However, in a phase space of more than one dimension, the basin boundary is the inset, not just the saddle itself. Thus a Blue Sky Catastrophe can happen as an attractor touches the inset without touching the saddle itself.

To understand this type of bifurcation, a good example can be found in Abraham's paper[24]. In his paper, he demonstrates that the Birkhoff-Shaw strange attractor is destroyed when the inset of the saddle cycle touches the chaotic attractor. Since in this case, the inset also touches the outset of the saddle cycle, this bifurcation coincides with the homoclinic tangency of the invariant manifolds.

Tangency giving rise to transverse intersections between manifolds can occur between the inset and outset of two different saddles or the same saddle (as the case above), and is known as heteroclinic and homoclinic tangency respectively. Carles Simö[89] also distinguishes between inner and outer heteroclinic tangency. This will become clear later in our investigations. After the tangency, there begins an extensive

and complicated interweaving between the inset and outset, giving rise to the famous homoclinic or heteroclinic tangle. Because of the tangle, points which are originally inside the catchment area bounded by the inset are no longer guaranteed to map onto the steady state periodic or chaotic solution. The basin boundary has changed from smooth to being fractal[52,90-92]. Points which are trapped by the tangle would be mapped chaotically in the phase space before they can emerge from the tangle, thus the term 'chaotic transients'. The long term behaviour can no longer be predicted in a short time.

An initial approach here is then to determine whether the disappearance of our chaotic attractor is due to the homoclinic tangency of the global (hilltop) saddle. To this end, we use the Melnikov method. In simple terms, Melnikov's method provides an analytic expression for the parameter values at which homoclinic tangency occurs, i.e., when the outset and the inset of the saddle first touch. If the controlling parameter is varied still further, a homoclinic tangle ensues in which the inset and the outset must now intersect an infinite number of times due to recurrence.

Using the Melnikov's[93] method, an analytical expression for the critical value of the parameters in which homoclinic tangency occurs is given by the relationship:

$$F_c = \frac{\beta \sinh(\pi\omega)}{5\pi\omega^2}$$

for the global saddle. When $\omega = 1.0$, the critical value in which homoclinic tangency occurs is found to be $F_c = 0.0735$. This compares favourably with the computational evidence in Figure (60), where $F = 0.074$ must be just after the tangency has occurred. The shaded region in this diagram depicts the area of the phase plane which leads to escape. However we find that the homoclinic tangency of the global saddle at these control parameters does not coincide with the escape where $F = 0.203052...$

A summary of the values of forcing F at which various bifurcations occur between $\omega = 0.5$ and $\omega = 1.8$ is given in Figure (61). If we look at the position of the Melnikov curve (M) in relation to the period doubling (D) and subsequent escape (E), it appears that the homoclinic tangency of the global saddle does not trigger the escape.

7.2.2 Predicting Escape using Chaotic Transients

When the chaotic attractor is destroyed, it is replaced by chaotic transients[53]. An orbit which originally lies on the attractor does not move off to a remote attractor instantly but is attracted towards the vicinity of the chaotic attractor. After bouncing around in a chaotic way, such an orbit then rather suddenly moves off towards the distant attractor. This phenomenon can be observed in Figure (62) where at $F = 0.109046$ the chaotic attractor still exists. However, at $F = 0.109047$ the same initial conditions give rise to a chaotic transient which resembles the original attractor but moves off to infinity after a while. The length of the chaotic transients vary, depending on the initial conditions as well as the control parameters. This shows clearly that it is very difficult to determine if a particular initial condition would lead to escape if it is not run for a sufficiently long period of time. The unpredictable length of chaotic transients can be highlighted by Figure (63).

In this diagram, we show seven different initial conditions all taken from the attractor at $F = 0.1090$. The bottom diagram shows that no escape occurs. As the forcing is increased, the length of chaotic transient varies and depends only on the initial conditions. This is of significant importance to engineers who build complex numerical models, and because of computational expedience only do a small number of simulation cycles using previously located steady state solutions as the initial conditions for a new set of parameters. They could then pick up a long transient and since this type of transient resembles a stable solution, they would surely overestimate the safety margin, perhaps even by a considerable amount.

The length of a chaotic transient depends sensitively on the initial conditions. However Grebogi[94] on studying a one dimensional map has shown that the transient life time has an exponential probability distribution:

$$\phi(E) = \frac{\text{Exp}(-E/M)}{M}$$

where E is the length of chaotic transient, measured here in forcing cycles. M is the expected (mean) value of E.

He showed that the *mean* lifetime, M, of the chaotic transients is related to the control parameter in the following relationship:

$$M \propto \mu^{\gamma}$$

where μ is a small change from the bifurcation or the critical value of control parameter where the chaotic attractor is destroyed, i.e., $\mu = F - F^E$. The parameter γ is termed the critical exponent.

The critical exponent calculated by Grebogi was 1/2 and hence a plot of $1/M^2$ against μ should reveal a straight line such that linear extrapolation could be used to *predict* the critical value. Unfortunately, for the problem in hand, the results are less than convincing, see Figure (64). This can be due to the following factors: firstly, a critical exponent of 1/2 implies that to observe transients longer than 100 cycles requires the control parameter to be within 0.01% of the critical bifurcation value. However, if we look at the probability density function in the accompanying diagram of Figure (64), the probability density function becomes very flat for larger values of M, that is to say we need to consider a greater number of transients than is practical. Secondly, Grebogi's calculation was based on a one dimensional map and therefore we could not expect the same degree of correlation in our flow problem.

Another study using 300 steady state Poincaré points on the chaotic attractor at *F=0.109* as initial conditions is shown in Figure (65). The top right hand diagram shows M plotted directly against F, with M clearly going to infinity at about 0.109. To give some idea of the relative F values involved, this diagram is preceded at the top left by a sketch of the earlier period doubling cascade on the same F axis, and we see that chaotic transients with means of 10 to 20 forcing cycles persist for quite an appreciable F interval beyond F^E.

By not assuming the critical exponent as *1/2,* we have plotted in the lower right-hand diagram M^{-1} against F, from which we conclude that F^E is very close indeed to 0.109. Finally, to determine the scaling critical exponent γ, the lower left-hand diagram plots *ln(M)* against *ln(F-0.109)* and the fitted straight line yields the value of $\gamma = 0.87$, compares with Grebogi's value of $\gamma = 0.5$.

7.3 Fractal basin boundaries

To understand the numerically determined bifurcations in the (F,ω) control space, it is convenient to consider the steady states of the system under slowly incremented F at a series of constant ω values as shown in Figure (66). For $\omega > \omega^P$, there exists a monotonic trace of fundamental (n=1) oscillations originating at $x = y = F = 0$ and terminating in a Feigenbaum cascade (with first and second period doubling at F^C and F^D say). This leads to a chaotic folding-band attractor, see Figure (58), and finally escape is triggered by the blue sky disappearance of this attractor at F^E as illustrated in the right-hand insert (d) of the figure. The fundamental solution has a cusp point at P, so for $\omega < \omega^P$ the trace of n=1 cycles exhibits a resonant hysteresis in the regime $F^B < F < F^A$ between two cyclic folds at F^A and F^B, as in the left-hand inserts (a-c).

The value of F^E decreases steadily with decreasing ω, and at ω^Q it becomes less than F^A. The escape is now associated with the simple cyclic fold at F^A, although the coexisting end of the trace is still stable up to F^E where a blue sky event carries the system back to the non-resonant state. It can be seen that as ω is decreased past ω^Q towards 0.6, the values of F^B, F^C, F^D and, F^E all seems to approach one another, but we have not explored this regime in detail at this stage.

Because the folds at A and B evolve from the cusp at P, we expect the jumps from the fold A to always re-stabilize on the coexisting trace for $\omega^Q < \omega < \omega^P$, rather than to over-shoot and escape. Thus escape is at F^A for $\omega < \omega^Q$ and at F^E for $\omega > \omega^Q$ with the minimum F necessary to escape given by F^Q.

We have also drawn on this figure the Melnikov curve, thus F^M denotes the appearance of a homoclinic tangency between the invariant manifolds of the saddle cycle close to the $x = 1$ hill-top. This homoclinic tangency signals the appearance of a fractal basin boundary defined by the hill-top saddle inset, between containment and escape. Notice that this tangency is essentially *unrelated* to the eventual escape, F^M offering no useful estimate of any of the other curves in the figure. This is in contrast to the Birkhoff-Shaw chaotic attractor mention above where the homoclinic tangency *triggers* the blue sky event.

Although the homoclinic tangle of the global saddle is unrelated to the eventual escape, it plays an important part in the global topology of the two-dimensional phase projection as well as the *creation* of the chaotic attractor as we shall see. Once the tangle occurs, the catchment region has a very complicated appearance. Figure (67) shows a small catchment region around the chaotic attractor using a grid of 100x100 starts. Each dot denotes escape within 7.1 cycles with control parameters: $\omega = 0.85, \beta = 0.1, F = 0.109$. The intricate nature of the catchment region can be realized by enlarging the little picture 'behind' this diagram as shown in Figure (68). This diagram shows the length of transients before escape occurs across the region where $x = 0$. The length of the white region represents the length of the transient. It can be observed clearly that by increasing the number of forcing cycles and the resolution of the grid of starts, we can expect that more dots will appear in the white area of the catchment region and hence more complication.

To understand the formation of the so called fractal basin boundary, let us look at what happen when the invariant manifolds of a saddle cross. The inset and outset can originate from the same saddle point (*homoclinic* tangle), or from different saddle (*heteroclinic* tangle). Figure (69) is an illustration of a homoclinic tangle when the inset and outset cross at the point H, a homoclinic point. Consider mapping this point forward, this point must again map onto the inset (H^+) by recurrence. However since H also lies on the outset, the outset must also go through H^+. To preserve the orientation, the outset must cut through the inset by doubling back in the manner as shown. The two complete segments joining H and H^+ is called Birkhoff's signature[10]: more complicated signatures are possible and can be found in Abraham and Shaw's book. By mapping forward again, more and more homoclinic points can be observed and more densely the closer the distance to the saddle. By mapping backward in time, the same thing happens. In other words, there are infinitely many, infinitely long sequences of homoclinic points implied by a single one. A collection of all homoclinic points is the homoclinic orbit with infinite periodicity. Once a homoclinic tangle occurs, the catchment region formerly defined by the inset becomes exceedingly complex. Furthermore some areas within the original catchment region can now be mapped outside and never return, thus leading to fractal basin boundary.

The exceedingly complicated catchment region can be traced in the following manner. Starting near the saddle cycle on the outgoing eigenvector, a point is chosen and is mapped forward once. Since these two points are still very close together, we can approximate the path between these two points by a straight line and divide the line into a ladder of points. By mapping this ladder of starting points forward the outset would be filled with points and has the appearance of a continuous curve. The same procedure can then applied to the inset but this time we have to map the points on the incoming vector backward in time. This method is easy to implement in computational terms: however we do encounter some difficulties in our problem. Because of our single potential well characteristic, any point mapped outside the catchment region is quickly mapped to infinity, these point are thus *lost* and a continuous curve becomes broken. Therefore we have to keep increasing the number of starting points in order to *fill the gap*.

Using the above method, a homoclinic tangle of the escape equation is shown in Figure (70). The non-uniform spread of points are due in part to the choice of starting points. Although this method is successful in tracing the tangle, when the tangle is as complicated as shown in the figure, it is not possible to determine which part of the region will map onto the attractor and which part will lead to eventual escape. A simpler picture without the tangled outset but with the same control parameters is shown in Figure (71). The white region is the stable region where any point will eventually be mapped on to the chaotic attractor. The insert is a grid of starts approach and it can be seen that as the resolution is increased, more white region is eroded by the black. In between, thin *whiskers* of white region also appear. This *brute force* approach is very effective in establishing the complicated catchment region. The result of another study is shown in Figure (72). This is an enlargement of a region close to one band of the chaotic attractor with the same control parameters as above but with a different phase angle at $\phi = 180°$. This picture is composed of a quarter of a million coloured squares centred on the grid points, the colours represent how many forcing cycles were substained before escape. The black central region denotes points on the starting grid that have not escaped before 25 forcing periods. The white points forming an arc within the black zone represent the chaotic attractor, and the black region represents the basin of attraction of this stable attractor. We have only followed each trajectory for 25 forcing periods for obvious reason of computational economy.

As can be observed from the complexity of the colouring, the boundary of this basin has a fractal nature, making practical prediction of whether or not a given start will lead to escape quite impossible in the more highly tangled regions. It should be noted that a simple cyclic attractor can also exhibit a fractal basin boundary, the type of boundary being essentially unrelated to the type of attractor within it. In fact, for some ω values, we can see from the Melnikov curve that homoclinic tangency occurs when the attractor is a simple fundamental (n=1) solution.

After the occurrence of homoclinic tangency, the tangle becomes progressively more and more complicated as the control parameter is varied. As the tangle develope , more and more of the catchment region is eroded away. We have traced the development of the catchment region with equal increments of the forcing until just before escape using Simple Cell to Cell mapping as shown in Figure (73). Just before escape occurs, the stable region is so small that the resolution used can no longer give us a well defined curve. Notice the catchment region at $F = 0.0872$; although the Blue Sky event occurs at $F > 0.109$, the stable region has already been so badly eroded that practically it can be considered unsafe. This rapid erosion of the stable region can be observed again in Figure (74). Here, the stable solution is *not* a chaotic attractor. The escape sequence in the last diagram shows how a point seemingly trapped by the tangle is mapped outside the previously stable region. In fact, a look at the full three dimensional phase space generated by a plot of the catchment regions at different phase angles shown in Figure (75) revealed that every *fractal layer* is an image of the previous one. Thus, for every forcing cycle, a point in this tangled catchment region *jumps* across one layer until it leaves the original catchment region and shoots to infinity.

Another phenomenon which facilitates the rapid erosion of the catchment region, first identified by Grebogi[92], is the sudden changes in the *accessible orbit* due to the appearance of a saddle node bifurcation. This can be observed as a sudden inwards jump of the boundary and the bifurcation suddenly creates a catchment region of its own, coexisting with the original catchment region of the periodic solution. However this coexisting solution is soon destroyed together with the catchment region. Such a sequence of events occurs in our system in association with the n=3 saddle-node

bifurcation. Figure (76) shows the difference in appearance in the catchment region before and after the appearance of the n=3 periodic solution. Clearly, this is yet another significant way in which the catchment region can be eroded.

7.4 The Dollar sign map

The importance of homoclinic tangles lies in the Smale-Birkhoff homoclinic theorem, which stated that transverse homoclinic intersections imply the existence of horseshoes[29,95]. The proof of this theorem is basically a precise specification of the mapping action associated with tangles, and can be found in Guckenheimer and Holmes. Further examples of tangles can be found in Hayashi[96]. Because of the Smale-Birkhoff theorem, one could expect complex behaviour like the existence of horseshoes whenever the inset and outset of a saddle have transverse homoclinic intersections. In fact Moon[97] has suggested the occurrence of homoclinic orbits as a precursor to chaos. (However we did locate a chaotic attractor before the global saddle had its homoclinic tangency at low values of ω .) Therefore homoclinic tangency is not a sufficient condition for the appearance of a chaotic attractor.

As a further indication of the importance of horseshoes and transverse homoclinic intersections, a theorem of Katok[98] should be mentioned. This involves the concept of *topological entropy*, which is a mathematical formulation of the notion of exponential separation of nearby initial conditions. Katok showed that a large class of Poincaré mappings with positive topological entropy must have transverse homoclinic points. In other words, the exponential spreading of nearby starts is linked to the existence of transverse homoclinic trajectories and horseshoes. However, a horseshoe may correspond to either a chaotic attractor or a pre-chaotic behaviour in which aperiodic final motions exist but are observed with probability zero. Thus folding and mixing can only be observed in transients. The condition that a folding action could lead to a chaotic attractor is that observed trajectories which fall off the invariant set I in Smale's[95] construction must somehow be *re-inserted* into the square S.

From the above theorems, it is clear that a homoclinic tangle does not necessarily mean the existence of a chaotic attractor. However it does imply a fractal basin boundary as shown in the last section as well as chaotic transients. On the other hand, the existence of a chaotic attractor implies a homoclinic tangle. Thus the

connection between chaotic behaviour and homoclinic tangles depends on whether trajectories that fall off the invariant manifolds (the horseshoe created by the homoclinic tangle), can be re-inserted into the invariant set.

Before we go any further, we shall follow Hayashi's[99] example and call any saddle point produced by a saddle-node collision as a direct saddle and label it as 'D^n'. The superscript will indicate the periodicity of the saddle. Similarly a saddle produced by a flip bifurcation will be denoted by 'I^n', because of the nature of its mapping action, it will be called an inverting saddle. All stable periodic solutions will be denoted by 'S^n'.

While a homoclinic tangle of the global saddle, (D^1), gives rise to a very complicated basin boundary, we shall now consider the implication of an inverting saddle having transverse homoclinic intersections.

The term 'dollar sign map' was first introduced by Rössler[100-102]. This term was used because of the topological nature of the map. Figure (77a) shows a homoclinic tangle of an inverting saddle from the escape equation. Unfortunately, the outset is so compressed that the layered structure is impossible to observe. However a topological equivalent structure is drawn in Figure (77b), making it clear why it is called a dollar sign map. Notice that the outset of I^4 and the period 4 chaotic attractor coincide with each other.

The interesting property of the dollar sign map is that it possesses not one but two ordinary horseshoe maps in the sense of Smale in its second iterate. This is because the inverting saddle has a pair of eigenvalues with negative sign. Each horseshoe uses the other as a sink so that the second iterate always *re-inserts* the trajectory back into the original closure of the outset. Thus, this characteristic is synonymous with the 'cap-shaped' map described by Rössler with its reinjection principle and Carles Simo's feedback property. This is with marked contrast with the homoclinic tangle formed by the global saddle in which there is only one horseshoe map. As the eigenvalues are both positive, no reinjection is possible. After a period of *transients* any point will be mapped either to an attractor within the fractal basin boundary or to the other side of the boundary and never return. Therefore, when the invariant manifolds of a direct saddle cross, we would not expect the formation

of a chaotic attractor just the appearance of fractal basin boundary. However, because of the reinjecting property, we can expect very different behaviour when an inverting saddle has a transverse homoclinic intersection.

Let us now look at the characteristics of a tangle. Once the invariant manifolds of a saddle cross, an infinite number of crossings occur. Since they all traverse at differing rates, those lines coming closer to the saddle being punctuated more densely there, the family is bound to comprise an infinite number of cases in which the self-intersection occurs in a periodic point. Therefore, each (transversal) homoclinic point implies an infinite number of periodic trajectories of different periodicity in its neighbourhood. Smale's unravelling of the tangle also shows that there are also an uncountable number of nonperiodic trajectories present. However, the definition of chaotic behaviour given by May and Yorke suggest precisely the same things; namely, infinite number of periodic solutions (fixed points) of repelling type; in between, there are uncountably many nonperiodic (wandering) solutions. Qualitatively, a chaotic attractor is characterized by its stretching, folding and mixing actions. All these characteristics can be accounted for when the invariant manifolds of an inverting saddle cross. Since the absolute value of one of the eigenvalues is larger than 1 while the other is smaller than one, trajectories are thus stretched along the repelling eigenvector and compressed orthogonal to the attracting eigenvector. The negative eigenvalues mean that all trajectories will be re-inserted into the invariant set and hence the mixing and folding actions appear. From these evidences one can conclude that chaotic motions are produced whenever the invariant manifolds of an inverting saddle cross. Furthermore, a chaotic attractor is in fact the outset of an inverting saddle when its invariant manifolds form a homoclinic tangle.

In our investigation, we shall assume a chaotic attractor will form when the above conditions are satisfied. Therefore we would expect that before a chaotic attractor appears, the corresponding inverting saddle's invariant manifolds do not cross, and right after the attractor is formed, homoclinic tangling occurs: while at the bifurcation point we have homoclinic tangency. To sum up, in order to have a n-piece chaotic attractor, the inverting saddle with period n (i.e., I^n) must be homoclinically tangled. From now on we shall refer the n-piece chaotic attractor as having period n. The loss of stability of a period $2^{(n+1)}$ chaotic attractor to a period 2^n chaotic attractor will be discussed in the next section.

Figure (78) is a period doubling cascade with the control parameters as shown in the diagram. Notice that the data is sampled at 2 times the forcing period so that only the band with positive displacement is plotted. Therefore the chaotic attractor at $F = 0.20249$ is actually a period 8 chaotic attractor. Bifurcation of the chaotic attractor with period 8 to period 4 is at $F = 0.202532$. By plotting the invariant manifolds of the period 8 inverting saddle before and after this value we can test the validity of the above assumption. Figure (79) shows this result: the top diagram shows the invariant manifolds of the inverting saddle (I^8) at $F = 0.202530$ and the bottom diagram shows the same invariant manifolds at $F = 0.202534$. It is clear that before the bifurcation occurs, i.e., before the period 8 chaotic attractor changed into a period 4 chaotic attractor, the invariant manifolds of I^4 do not touch. After the bifurcation, the invariant manifolds have crossed.

Therefore we conclude that a chaotic attractor is the closure of a homoclinically tangled outset of an inverting saddle. We also expect that chaotic attractors with different periods formed under this condition are topologically equivalent. Hence there must exist a scaling factor just like Feigenbaum's[38] universal number. If this is true, it also implies that this type of chaotic attractor is universal. Figure (80) is a series of period doubling cascades; each window is enlarged as shown and the bifurcation points indicated have been further enlarged so that a good approximation can be determined. The results are tabulated below:

$$F_8 = 0.202532 - 0.2024653 = 6.670 x 10^{(-5)}$$

$$F_{16} = 0.2024653 - 0.2024504 = 1.490 x 10^{(-5)}$$

$$F_{32} = 0.2024504 - 0.202447214 = 3.186 x 10^{(-6)}$$

$$F_{64} = 0.202447214 - 0.202446532 = 6.820 x 10^{(-7)}$$

$$F_{128} = 0.202446532 - 0.202446386 = 1.460 x 10^{(-7)}$$

$$\frac{F_8}{F_{16}} = 4.4765..$$

$$\frac{F_{16}}{F_{32}} = 4.6767..$$

$$\frac{F_{32}}{F_{64}} = 4.6715..$$

$$\frac{F_{64}}{F_{128}} = 4.6712..$$

It can be observed that the number approaches the *same* Feigenbaum constant, $\delta = 4.6692016...$ as the period of the chaotic attractor increases. This suggests rather surprisingly that period doubling of the *periodic* solution has a intimate relationship with the period doubling of the chaotic attractors.

7.5 The effect of Heteroclinic Tangency and Stability Transfer

Looking back to the Blue Sky event at the end of the period doubling cascade, we have determined that escape is triggered when the chaotic attractor touches the basin boundary. Since the invariant manifolds of D^1 have already intersected before escape occurs, this can not be a homoclinic event. However, as the chaotic attractor is the outset of the period 2 (noting that the chaotic attractor has two bands) inverting saddle; it means that this is in fact a heteroclinic event. In this case, the inset of D^1 touches the outset of I^2. Since the chaotic attractor or the outset of I^2 touches the boundary of another attractor causing escape; (here, the "other attractor" being at infinity) we can say that we have a stability transfer.

Notice that as the invariant manifolds of D^1 cross, the inset of any periodic saddle point must have a heteroclinic connection with the outset of D^1. Stability transfer will not appear in this case because the attractor has not touched the inset of D^1. Therefore, to distinguish the two cases, we shall follow Carles Simó's example and call the former case with stability transfer an outer heteroclinic tangle, and the latter case an inner heteroclinic tangle.

We have observed that when an inverting saddle forms a homoclinic tangle, its outset changes into a chaotic attractor. But how does a higher period chaotic attractor lose its stability to a lower period chaotic attractor? We suspect the above mechanism applies, i.e., an outer heteroclinic tangency occurs. Thus the sequence of events can be deduced as follows: the inset of I^{2^n} touches the outset of $I^{2^{n+1}}$, since the closure of the outset of $I^{2^{n+1}}$ is the chaotic attractor, the chaotic attractor is destroyed. This is the case of an outer heteroclinic tangency. As the chaotic attractor is destroyed, the invariant manifolds of I^{2^n} develop into a homoclinic tangle, thus forming the chaotic attractor with the same period as the inverting saddle and hence a stability transfer occurs. Since the destruction of the period 2^{n+1} chaotic attractor and the creation of the period 2^n chaotic attractor happens simultaneously, we also expect the outer heteroclinic tangency and the homoclinic tangency to happen simultaneously.

This phenomenon can be demonstrated again in Figure (79). Clearly, it can be observed that when I^4 has a homoclinic tangency, it also means that the inset of I^4 touches the period 8 chaotic attractor. Since the closure of the outset of I^8 is the period 8 chaotic attractor, an outer heteroclinic tangency occurs and the stability of the period 8 chaotic attractor is transferred to the period 4 chaotic attractor. As the two events happen simultaneously we can only conclude that the closure of the outset of I^8 is a subset of the closure of the outset of I^4. In fact this explains why the two types of tangency can happen simultaneously.

Consider again the ultimate destruction of the chaotic attractor at $\omega = 0.85$. The system jumps to infinity at F^E, just above 0.109. We have in fact found that the attractor collides with D^6 as shown in Figure (81). This directly unstable n=6 subharmonic is the saddle of a very recent saddle-node that generates over a very short F interval a complete n=6 cascade: notice that the figure corresponds to sampling at 2iT (at phase $\phi = 180°$), so that only half of the full picture is observed. At the end of the n=6 cascade, when the n=6 chaotic attractor collides with D^6 at $F \doteq 0.1077$, the system jumps back to the main sequence S^4 as indicated by J.

The final collision at F^E is shown in Figure (82) in the phase projection (x,y), with sampling again at 2iT and phase $\phi = 180°$. The path of three points of D^6, in equal F steps, is shown relative to one band of the chaotic attractor at $F = 0.109$, this representation being useful because the chaotic attractor is not moving significantly over the F range involved. Notice that the apparent crossing of the path and the attractor is illusionary, because the attractor had not yet formed at the lower F values.

This type of destruction of the chaotic attractor seems to be of different type to that discussed earlier concerning the outer heteroclinic tangency type of bifurcation. However, as pointed out by Grebogi et al[92], the period 6 direct saddle at this point lies on the basin boundary of the global saddle D^1 and therefore we can consider the chaotic attractor to be touching the basin boundary.

7.6 Mathematical constraint on the Escape equation

No analysis will be completed without the use of analytical tools. It can be seen later that some interesting properties emerge due to mathematical constraint imposed on our dynamical system.

Consider again the escape equation which has been reduced to the standard form:

$$\ddot{x} + \beta\dot{x} + x - x^2 = F \sin \omega t$$

we shall write

$$y = \dot{x}$$

$$\phi = \omega t \quad (\text{mod } 2\pi)$$

$$T = 2\pi/\omega$$

and can observe that the driven oscillator has a three dimensional phase space, R^3 spanned by x, y and t. Due to the periodicity this can be alternatively viewed toroidally using x, y and ϕ where the phase angle ϕ is a cyclic coordinate with $0 < \phi < 2\pi$ The oscillator can, moreover, be written formally as a set of three autonomous first-order nonlinear ordinary differential equations

$$\dot{x} = y$$

$$\dot{y} = -x + x^2 - \beta y + F \sin \phi$$

$$\dot{\phi} = \omega$$

with the three control parameters $(F \, \omega \, \beta)$. We have in fact set β=0.1 throughout our numerical studies, corresponding to a damping ratio ζ=0.05, leaving the two primary controls F and ω.

The divergence of the trajectories flowing in the three-dimensional phase space is governed by

$$\frac{\partial \dot{x}}{\partial x} + \frac{\partial \dot{y}}{\partial y} + \frac{\partial \dot{\phi}}{\partial \phi} = -\beta$$

so we have a *constant* exponential contraction of phase volume V, according to

$$\dot{V} = -\beta V$$

$$V(t) = V(0)e^{-\beta t}$$

Our numerical studies make continuous use of the Poincaré section defined by

$$t = t_p + it \qquad (i=1,2,\ldots\ldots)$$

$$\phi = \phi_p = \omega t_p$$

and we shall be concerned with the Poincaré map $P(\phi_p)$ that is generated by the flow,

$$P(\phi_p){:}[x(t_p), y(t_p)] \rightarrow [x(t_p+T), y(t_p+T)]$$

As indicated, the mapping depends on the chosen phase ϕ_p, and for most of our studies we use $\phi_p = 0$. This map takes us iteratively from a point (x_i, y_i) to a new point (x_{i+1}, y_{i+1}) according to an *implied* functional relationship

$$x_{i+1} = G(x_i, y_i)$$

$$y_{i+1} = H(x_i, y_i)$$

The functions G and H are of course not known analytically, but can always be evaluated numerically for any (x_i, y_i) by making a Runge-Kutta numerical time intergation of the governing differential equation through one forcing period of duration T.

Now since there is no stretching action along the time axis, the constant exponential contraction of volume for the flow ensure that for the map an area A in the Poincaré section contracts according to the relation

$$A_{i+1} = e^{-\beta T} A_i$$

which implies that the Jacobian determinant D of the map is a constant, since

$$D = \begin{pmatrix} \dfrac{\partial G}{\partial x} & \dfrac{\partial G}{\partial y} \\[2mm] \dfrac{\partial H}{\partial x} & \dfrac{\partial H}{\partial y} \end{pmatrix}$$

So any fixed point of the map, corresponding to a fundamental n=1 oscillation with period T, will have mapping eigenvalues λ_i *(i=1,2)* constrained by the condition

$$\lambda_1\lambda_2 = D = e^{-\beta T} = e^{-\beta 2\pi/\omega}$$

In a similar way, the eigenvalues $\lambda_i^{(n)}$ of the n-map P^n corresponding to a subharmonic of any order n (with period nT) are constrained by the equation

$$\lambda_1^{(n)}\lambda_2^{(n)} = e^{-n\beta T}$$

These constraints place strong restrictions on the sequences of folds ($\lambda = +1$) and flips ($\lambda = -1$) that can be generated by our escape equation. They also exclude the possibility of a Neimark bifurcation (the mapping equivalent of the Hopf bifurcation for a flow) in which a pair of complex conjugate eigenvalues leaves the stable unit disc away from the real axis.

7.6.1 Re-merging Feigenbaum trees

The consequence of mathematical constraint on the eigenvalues leads to the formation of re-emerging Feigenbaum trees[103], and degenerated period doubling. To look at how the underlying mathematical constraint affects our dynamical system, we shall concentrate on a *typical* response curve with hysteresis, i.e. two cyclic folds, as well as a period doubling cascade. With ω just less than ω^p the behaviour is thus as sketched in Figure (83). This schematic diagram relates to the phenomena at $\omega = 0.85$ and $\beta = 0.1$ and shows the paths represented by the stroboscopically sampled $x_i = x(iT)$ under the variation of F. To understand the stability transitions of the fundamental n=1 path in this constant ω (and constant T) cross-section, we recall that the product of the mapping eigenvalues is a constant. The eigenvalues are therefore either real with geometric mean

$$\sqrt{\lambda_1\lambda_2} = e^{-\beta T/2} = \rho$$

or complex and constrained to lie on a circle of radius ρ centred on the origin of the Argand diagram.

From S^0, the path S^1 starts off as an attracting focus, becomes a directly attracting node at a where the complex eigenvalues become real and positive, and folds at A as λ_1 penetrates the unit circle at +1. From fold A to fold B we have the directly unstable saddle D_R^1 (where the R for resonant serves to distinguish this from the hill-top saddle D^1), and the primary n=1 path restablizes at fold B as λ_1 re-enters the unit circle at +1. Then λ_1 becomes complex at b, passing completely around the circle of radius ρ to give an inversely attracting node with real and negative mapping eigenvalues between c and C. At C, λ_1 passes out of the unit disc at -1, and we have a super-critical flip bifurcation into a stable n=2 subharmonic as shown. This is followed by a supercritical flip from n=2 to n=4, and a complete period-doubling cascade leading to a two-band chaotic attractor, which quickly becomes unstable at a blue sky instability at E leaving no attractor and an inevitable jump to escape.

The unstable n=1 solution meanwhile continues to the fold G where it turns back to become the hill-top saddle cycle D^1. Before doing so, however, it is clear from the constraints on λ_i that we must have a reversed flip at F, since the eigenvalues must yet again go through the unit disc thereby pass through -1, changing from negative eigenvalues to positive eigenvalues and emerge from the unit disc again through +1. This is confirmed by our numerical studies. There is, indeed, a complete reversed period-doubling cascade and chaos as illustrated schematically in the diagram. Figure (84) is the result of our numerical studies showing the solution path and the changing eigenvalues for the whole path. It can be noticed that the reversed flip F is however very close to G, so that the stable n=1 regime F-f-g-G is in reality very short at these control parameters. Path D^1 finally returns to the hill-top equilibrium D^0.

7.6.2 Response surface of escape equation

The response surface, deduced from extensive numerical studies is sketched in Figure (85), a schematic diagram in which the 'response amplitude' might loosely be thought of as the maximum value of the displacement, x_M, during a steady state oscillation. The surface represents the steady-state solutions, with x_M and the forcing

frequency in the base plane, with the second control F plotted vertically for ease of visualization. The damping is held constant at $\beta = 0.1$ throughout as mentioned before. Bifurcations on the response surface can be projected back onto the (F, ω) control plane to give the final bifurcation diagram.

The main n=1 (fundamental solution) surface cuts the $F = 0$ base plane in two straight lines, $x_M = 0$ corresponding to the system resting in the stable equilibrium S^0 and $x_M = 1$ corresponding to the system resting in the unstable hill-top state D^0.

To explore the surface, it is convenient both computationally and descriptively to focus attention on the $x_M(F)$ paths at prescribed ω values. At the highest value of forcing frequency represented in the diagram, for which ω is approximately 2.5, the two equilibria are joined by a simple path of n=1 solutions: it can be observed that the solution paths of S^1 and D^1 grow, merge, and annihilate one another at the cyclic fold at G. Passing from S^1 to D^1 through this fold, one of the mapping eigenvalues, λ_1 say, passes through +1, so that after G the n=1 solution is directly unstable with both eigenvalues positive and $1 < \lambda_1 < \infty$, $0 < \lambda_2 < 1$. The physical system starting at S^0 under slowly increasing F is thus stable up to the fold G, from which a fast dynamic jump carries the system out of the well with x tending to infinity. So at high ω the fold line, G-G in the control space is the escape boundary. The numerical solution path at $\omega = 2.3$ is shown in the bottom diagram of Figure (86).

This simple folding response is preserved under decreasing ω until at ω^R (approximately 2.2) a flip bifurcation into an n=2 subharmonic is encountered. Thus at the value of ω drawn between ω^P and ω^R the n=1 path is cut by a closed n=2 curve after which the n=1 solution restablized as indicated, before finally losing its stability at fold G, this is demonstrated in the second diagram of Figure (86). Between the two opposing flips the n=1 solution is inversely unstable with both mapping eigenvalues real and negative, one inside the unit circle and the other outside, i.e. an inverting saddle where $-\infty < \lambda_1 < -1$, $-1 < \lambda_2 < 0$. These flips project into the boundary F-R-C in the control space. For the value of ω illustrated, the n=2 solution is everywhere stable, so our physical evolving system driven from S^0 would experience a brief regime of stable n=2 subharmonic oscillation between the two supercritical flips, before escape from the fold at G.

As ω is decreased, the n=2 solution next exhibits a pair of opposing supercritical flips into an n=4 solution, giving the second flip boundary D-D. The period-doubling scenario is repeated at diminishing scales, so that at $\omega = 2$, between ω^P and ω^R, there is an opposing pair of complete period-doubling cascades leading to a pair of chaotic attractors, separated by a region of no attractor, implying inevitable escape. This behaviour can be observed in the first diagram of Figure (86). On further reduction of ω to ω^P (approximately 0.9) the n=1 solution exhibits a cusp at P, generating a pair of folds on the early part of the $x_M(F)$ curve. This corresponds to the well known hysteresis in nonlinear resonance, which here is of the softening variety, the softening for $x > 0$ being more powerful than the hardening for $x < 0$: this resonance response aspect is highlighted by the sketched constant F lines on the n=1 surface.

Since the folds A and B are born at the cusp point P, they share initially the same basin of attraction, so the jump from A under a controlled physical increase of F will restablize on the attracting n=1 focus as indicated by the arrow E. So from the pulling apart of the two period-doubling cascades at ω just less than ω^R down to ω^Q (less than ω^P) the escape is triggered by the cascade-chaos-Blue-Sky scenario denoted by C (flip from n=1 to n=2), D (flip from n=2 to n=4) and finally E (escape).

Conclusion

One of the most interesting questions in chaotic dynamics is what constitutes a chaotic attractor? We have observed typically the appearance of chaotic attractors at the end of a period doubling cascade, but what determines that it is not a periodic attractor with a very high periodicity. The key to this question is the creation of inverting saddles during the course of a cascade of period doubling. When the invariant manifolds of an inverting saddle cross each other, the unstable manifold or more precisely the closure of the unstable manifold, i.e. the outset, becomes the chaotic attractor. This could possibly first occur at the Feigenbaum's limit point with an inverting saddle having a high periodicity. After this point, a cascade of destruction and creation of chaotic attractor occurs. A chaotic attractor with a period of 2^{n+1} will be destroyed by a chaotic attractor with a period of 2^n due to an outer heteroclinic tangency, simultaneously creating a chaotic attractor of period 2^n. In between, we could expect windows of coexisting steady periodic solutions because of the property of the 'horseshoe', namely, infinitely many periodic orbits and uncountably many aperiodic orbits. The reason that we cannot observe all of them is because some of the windows where they exist are small compared with the main period doubling event. The divergence action due to the unstable manifold and the attracting action due to the stable manifold constitute the stretching, folding and mixing actions. Together, they make a 'chaotic' attractor chaotic.

We also propose in Chapter 7 that if chaotic attractors are formed when the invariant manifolds of an inverting saddle cross, there is no reason why one chaotic attractor is different from another: hence they must be topologically the same. By topological, we mean that the geometric structure of all the chaotic attractors should belong to one master structure. The 'appearance' of a chaotic attractor is affected by the eigenvalues of the inverting saddle as well as the Birkhoff signature. Note that for a one dimensional discrete map, a saddle has no separatrix and hence we can only view it as a degenerate problem rather than a generic one.

While chaotic behaviour has not been considered dangerous by engineers, (dangerous in the sense that a high amplitude vibration can cause the collapse of a structure), nevertheless the research into chaotic phenomena has given us insight into problems such as fractal basin boundaries. To most engineers, a structure must

be designed within a safety margin. To dynamicists, this safety margin is the catchment region for a steady state solution which is acceptable in application. This would include the amplitude of vibrations and even the frequency during the vibrations, when fatigue and resonance are taken into account. If this stable region can be eroded so suddenly and unpredictably, this must be considered dangerous.

This unpredictability of the catchment region first started when the invariant manifolds of the global saddle crossed. This generates chaotic transients where chaotic-like behaviour is observed before the dynamical system is settled into a steady state or a remote attractor. This global saddle produces chaotic-like behaviour as well as separating different steady state solutions. We can thus classify it as a chaotic saddle. The problems of tangles and fractal basin boundaries are immensely complicated, partly because they are computationally expensive to explore and further research is in progress to unravel this complexity.

On a more practical note, the erosion of the catchment region is now under further research in the form of integrity curves so as to provide the design engineer with an indication of when the catchment region would become critical. This would serve as a lower bound type design curve in the design exercise.

While a tremendous amount of research has been conducted by the dynamical research group in the Civil Engineering Department of University College London, it is just the end of the beginning. We are confident that more fruitful and exciting results for both the engineers and scientists will emerge in the not so distant future.

References:

1. Clough R. W. and Penzien J.
    Dynamics of Structures.
    McGraw Hill (1982).

2. Beards C. F.
    Structural Vibration Analysis.
    Ellis Horwood Series in Engineering Science. (1983)

3. Coddington, E. A., and N. Levinson
    Theory of Ordinary Differential Equations.
    McGraw-Hill, New York, (1955).

4. Cunningham, W. J.
    Introduction to Nonlinear Analysis.
    McGraw-Hill, New York, (1958).

5. Andronov, E. T., Vitt, E. A. and Khaiken, S. E.
    Theory of Oscillators.
    Pergamon Press, Oxford, (1966).

6. Arnold, V. I.
    Mathematical Methods of Classical Mechanics.
    Springer-Verlag: New York, Hidelberg and Berlin, (1978).

7. Jordan, D. W. and Smith, P.
    Nonlinear Ordinary Differential Equations.
    Oxford University Press: Oxford, (1977).

8. Abraham, R. H., and Shaw, C. D.
    Dynamics: The Geometry of Behaviour, Part One, Periodic Behaviour.
    Aerial Press: Santa ruz, CA, (1982).

9. Abraham, R. H., and Shaw, C. D.
    Dynamics: The Geometry of Behaviour, Part Two, Chaotic Behaviour.
    Aerial Press: Santa ruz, CA, (1983).

10. Abraham, R. H., and Shaw, C. D.
     Dynamics: The Geometry of Behaviour, Part Three, Global Behaviour.
     Aerial Press: Santa ruz, CA, (1985).

11. Thompson J. M. T. and Stewart H. B.
     Nonlinear Dynamics and Chaos.
     John Wiley and Sons, Chichester, (1986).

12   Arnold, V. I.
     Geometrical methods in the Theory of Ordinary Differential Equations.
     Springer-Verlag: New-York, Heidelberg, and Berlin.

13   Thompson, J. M. T.
     Instabilities and Catastrophes in Science and Engineering.
     Wiley and Son, Chichester, (1982).

14   Thompson, J. M. T. and Hunt, G. W.
     A general theory of Elastic Stability.
     Wiley and Son, London, (1973).

15   Argoul, F. and Arneodo A.
     Lyapunov Exponents and Phase Transitions in Dynamical Systems.
     Lectures Notes in Mathematics, Ed. L. Arnold and V. Wihstutz,
     pp. 338-360, Springer-Verlag, Berlin Heidelberg, New-York, (1984).

16   Hayashi C.
     Nonlinear Oscillations in Physical Systems.
     Princeton University Press, Princeton, New Jersey, (1985).

17. Guckenheimer, J. and Holmes, P.
     Nonlinear Oscillations, Dynamical Systems, and Bifurcations of Vector
     Fields.
     Springer-Verlag: New York, Berlin and Heidelberg, (1983).

18. Golubitsky, M. and Stewart, I.
     Hopf Bifurcation in the presence of symmetry.
     Arch. Rat. Mech. Anal., 87, pp 107-165, (1985).

19. Marsden, J. E. and cCracken M.
The Hopf Bifurcation and its applications,
Applied Mathematical Science 19; Springer-Verlag, New York, (1976).

20. Lorenz, E.N.
Deterministic nonperiodic flow.
J. Atmos. Sci, (1963), 20, pp. 130-141.

21. Lorenz, E. N.
The problem of deducing the climate from the groverning equations.
Tellus, 16, pp. 1-11, (1964).

22. Stewart, H. B.
The Lorenz System (16mm film).
Aerial Press: Santa Cruz, CA.

23. Thompson, J. M. T., Bishop, S. R. and Leung, L. M.
Fractal Basins and Chaotic bifurcations prior to escape from a potential well.
Phys. Lett. A121, pp. 116-120, (1987).

24. Abraham, R. H. and Stewart, H. B.
A chaotic blue sky catastrophe in forced relaxation oscillations,
Physica D 21, pp 394-400, (1986).

25. Shilnikov, L. P.
Theory of bifurcation of dynamical systems and dangerous boundaries.
Sov. Phys. Dokl., 20, pp674-676, (1976).

26. Stewart, H. B. and Thompson J. M. T.
Towards a classification of generic bifurcations in dissipative dynamical systems.
Dynamics and Stability of Systems Vol. 1 No. 1, pp 87-96, (1986).

27. Poincaré H.
Les Methodes Nouvelles de la Mécanique Celeste, Vols 1-3.
Gauthier-Villars: Paris, (1899).

28. Birkhoff G. D.
     Surface transformation and their dynamical application.
     Collected Mathematical Papers, Vol 2, Dover, New York, (1966).

29. Smale, S.
     Differentiable dynamical Systems.
     Bull. Am. Math. Soc., 73, 747-817, (1967).

30. Arnold V. I.
     Small denominators. I. Mappings of the circumference onto itself.
     Am. Math. Soc. Transl., Ser. 2, Vol 46, (1965).

31. Henryk F., Hsu C. S.
     A study of nonlinear periodic systems via the point mapping method.
     Int. J. for Numerical Methods in Eng., Vol 19, (1983).

32. Thompson J. M. T., Bokainan A. R., Ghaffari R.
     Subharmonic and Chaotic motions of compliant offshore structures and
     articulated mooring towers.
     ASME, J. Energy Resources Tech., Vol 106, (1984).

33. Ueda Y., Akamatsu N.
     Chaotically transional phenomena in the forced negative resistance
     oscillator.
     IEEE, Trans. Circuits Syst., CAS-28, (1980b).

34. Thompson J. M. T., Hunt G. W.
     Elastic Instability Phenomena.
     Wiley and Son, Chichester, (1984).

35. Zeeman E. C.
     Bifurcation and Catastrophe Theory.
     Papers in Algebra, Analysis and Statistic, R. Lidl (ed.).
     American Math. Soc.: Providence, RI, (1982).

36. Holmes P. J., Whitley D. C.
     Bifurcations of one and two-dimensional maps.
     Phil. Trans. R. Soc. Lond. A 311; Erratum, 312, (1984).

37. May R. M.
     Simple Mathematical Models with Very Complicated Dynamics.
     Nature, 261, pp 459-467, (1976).

38. Feigenbaum M. J.
     Qualitative Universality for a class of Nonlinear Transformations.
     J. Stat. Phys. 19(1), pp 25-52, (1978).

39. Birkhoff, G. D.
     Proof of Poincaré's geometric theorem.
     *Trans. Am. Math. Soc., 14, pp 14-22, Collected Mathematical Papers, Vol.
     1, pp 673-681, (1913).*

40. Shaw R.
     Strange attractors, chaotic behaviour and information flow.
     Z. Naturf., 36a, pp 80-112, (1981).

41. Eckmann J. P. and Ruelle D.
     Ergodic theory of chaos and strange attractors.
     Rev. Mod. Phys. 57, pp 617-656, (1985).

42. Farmer J. D., Crutchfield J., Froehling H., Packard N. and Shaw R.
     Power Spectra and mixing properties of strange attractors.
     *In Nonlinear Dynamics. R. H. G. Helleman (ed.). N. Y. Academy of
     Sciences, N.Y., (1980).*

43. Wolf A.
     Quantifying Chaos with Lyapunov Exponents.
     *Nonlinear Sci. Theory Appl., A. V. Holden (ed.), Manchester Univ. Press,
     (1984).*

44. Wolf A., Swift J. B., Swinney H. L. and Vasano J. A.
     Determining Lyapunov Exponents from a Time Series.
     Physica 16D pp 285-317, (1985).

45. Mandelbrot B. B.
     Fractals, Forms, Chance and Dimension.
     W. H. Freeman, San Francisco, CA., (1977).

46. Farmer J. D., Ott E. and Yorke J. A.
     The Dimension of Chaotic Attractors.
     Physica 7D, pp 153-170, (1983).

47. Grassberger P. and Proccacia I.
     Characterization of Strange Attractors.
     Phys. Rev. Lett. 50, pp 346-349, (1983).

48. Moon F. C. and Li G-X.
     Fractal Dimension of the Two-Welled Potential Strange Attractor.
     Physical 17D, pp 99-108, (1985).

49. Shaw R.
     The Dripping Faucet as a Model Chaotic System.
     Aerial Press, Santa Cruz, CA., (1984).

50. Manneville P. and Pomeau Y.
     Different Ways to Turbulence in Dissipative Dynamical Systems.
     Physical 1D, pp 219-226, (1980).

51. Grebogi C., Ott E. and Yorke J. A.
     Crises, Sudden Changes in Chaotic Attractors and Transient Chaos.
     Physica 7D, pp 181-200, (1983).

52. Moon F.C. and Li G.X.
     Fractal Basin Boundaries and Homoclinic Orbits for Periodic Motion in a
     Two-Well Potential.
     Physical Review Letters, Vol. 55, No. 14, pp 1439-1442 (1985).

53. Thompson, J.M.T., Bishop, S.R. and Leung, L.M.
     Fractal basins and chaotic bifurcations prior to escape from a potential
     well.
     Phys. Lett. A121, (1987), pp. 116-120.

54. Abraham, R.H.
     Complex dynamical systems: selected papers.
     Aerial Press: Santa Cruz, CA. (1986).

55.   Ueda, Y., Nakajima, H., Hikihara, T. and Stewart, H.B.
       Forced two-well potential Duffing's oscillator.
       Proc. Conf. on Qualitative Methods for the Analysis of Nonlinear
       Dynamics, Henniker, New Hampshire, June (1986) (ed. F. Salam and M.
       Levi). Philadelphia: SIAM.

56.   Ueda, Y. and Yoshida, S.
       Attractor basin phase portraits of the forced Duffing's oscillator.
       European Conf. on Circuit Theory and Design. Paris, Sept. 1-4, (1987).

57.   Thompson, J.M.T.
       An introduction to Nonlinear Dynamics.
       Appl. Math. Modelling, June, Vol. 8, pp. 157-168, (1984).

58.   Hale, J.K.
       Ordinary differential equations.
       Wiley Interscience, New York, USA, (1969).

59.   Bishop, S.R. and Franciosi, C.
       Use of rotation numbers to predict the incipient folding of a periodic orbit.
       Appl. Math. Modelling, 11, pp. 117-126, (1987).

60.   Thompson, J.M.T. and Virgin, L.N.
       Predicting a jump to resonance using transient maps and beats.
       Int. J. Nonlin. Mech., 21(3), pp. 205-216, (1986).

61.   Jackson, A.S.
       Analogue Computation.
       New York, McGraw Hill,(1960).

62.   Paul, R.J.A.
       Fundamental analogue techniques.
       Blackie and Son Ltd, (1965).

63.   Blum, J.J.
       Introduction to analogue computation.
       Harcourt Brace and World, Inc., (1968).

64. Fiala, V.
Solutions of nonlinear vibration systems by means of analogue computers.
*Monographs and Memoranda of the National Research Institute for
Machine Design. Bechovice, Czechoslavakia, 19,134, (1976).*

65. Ghaffari, R.
Subharmonic resonance of bilinear marine systems.
Thesis, University College London, (1983).

66. Ueda, Y.
Steady motions exhibited by Duffing's equation: a picture book of regular
and chaotic motions.
*New approaches to nonlinear problems in dynamics, P.J. Holmes (ed.), pp.
311-322, SIAM: Philadelphia.*

67. Thompson, J.M.T.
Complex dynamics of compliant off-shore structures.
Proc. R. Soc. Lond. A387, pp. 407-427, (1983).

68. Virgin, L.N. and Bishop, S.R.
Catchment regions of multiple dynamic responses in nonlinear problems of
off-shore mechanics, (1988).
Presented at the 7th Int. Conf. OMAE, Houston, Feb., 7-12, (1988).

69. Hsu, C.S. and Guttalu, R.S.
An Unravelling algorithm for Global analysis of Dynamical Systems: An
Application of Cell-to-Cell Mappings.
Trans. ASME Dec., Vol. 47, pp. 940-948, (1980).

70. Hsu, C.S.
A generalized theory of Cell-to-Cell Mappings for Nonlinear Dynamical
Systems.
Trans. ASME Vol. 48 Sept., pp. 634-642, (1981).

71. Hsu, C.S., Guttaln, R.S. and Zhu, W.H.
J. App. Mech., Dec., Vol. 49, pp. 885-894, (1982).

72. Hsu, C.S. and Chiu, H.M.
     A cell mapping method for Nonlinear Deterministic and Stochastic
     Systems. Part I: the method of analysis.
     J. App. Mech., Sept., Vol. 53, pp. 695-701, (1986).

73. Chiu, H.M. and Hsu, C.S.
     A cell mapping method for Nonlinear Deterministic and Stochastic
     Systems. Part II: examples of application.
     J. App. Mech., Vol. 53, pp. 702-710, (1986).

74. Doedel,E.
     AUTO: Software for continuation and bifurcation problems in ordinary
     differential equations.
     *Report, Department of Applied Maths, California Institute of Technology,
     May (1986).*

75. Kass-Petersen, C.
     PATH: user's guide.
     Report, Leeds University: Centre for Nonlinear Studies, May (1987).

76. Sawyer W.W.
     A first look at Numerical Functional Analysis.
     Oxford University Press, (1978).

77. Thompson, J.M.T., Bokaian, A.R., and Ghaffari, R.
     Subharmonic resonances and chaotic motions of a bilinear oscillator.
     IMA J. Appl. Math., 31, pp 207-234 (1983).

78. Thompson, J.M.T., BokaiAn, A.R. and Ghaffari, R.
     Subharmonic and Chaotic Motions of compliant Offshore Structures and
     Articulated Mooring Towers.
     J. Energy Resources Tech., Trans. ASME, Vol. 106, pp 191-198 (1984)

79. Shaw, S.W., and Holmes, P.J.
     A periodically forced impact oscillator with large dissipation.
     ASME J. Appl. Mech., 50, 849-857 (1983a).

80.   Shaw, S.W., and Holmes, P.J.
        A periodically forced piecewise linear oscillator.
        J. Sound Vib., 90, pp 129-144 (1983b).

81.   Shaw, S.W., and Holmes, P.
        Periodically forced linear oscillator with impacts: chaos and long period
        motions.
        Phys. Rev. Lett., 51, 623-626 (1983c).

82.   Bishop S.R., Leung L.M. and Virgin L.N.
        Predicting incipient jumps to resonance of compliant marine structures in
        an evolving sea-state.
        Proc. 5th Int. Off. Mech. ASME Vol. III pp 179-185 (1986).

83.   Miller, D.R., Tam, G., Rainey, R.C.T. and Ritch, R.,
        Investigation of the use of Modern Ship Motion Prediction Models in
        identifying Ships with a larger than acceptable Risk of Dynamic Capsize.
        *Report prepared by Arctec Canada Ltd for the Transporation Development
        Centre of the Canadian Government. Report No. Tp7407E 1986).*

84.   Rainey, R.C.T.
        A new theory and its application for stability criteria covering
        wave-induced tilt phenomena on semi-submersibles.
        *Proc. Int. Conf. Stationing and Stability of Semi-submersibles, pp 41-59,
        Graham & Trotman, London (1986).*

85.   Wright J.H.G. and Marshfield W.B.
        Ship Roll Response and Capsize Behaviour in Beam Sea.
        Trans. R.I.N.A., Vol. 122, pp 129-148 (1980).

86.   Cardo A., Francescutto A. and Nabergoj R.
        Nonlinear Rolling Response in a regular sea.
        Int. Shiping Progress, Vol. 31, pp 204-208 (1984).

87. Robinson R.W. and Stoddart A.W.
An engineering Assement of the Role of Non-linearities in Transportation Barge Roll Response.
Paper No 8 Spring meeting (1986), to be published in Trans. R.I.N.A.

88. Stewart, H.B.
A chaotic saddle catastrophe in forced oscillator. Presented at Conf. on Qualitative Methods for the analysis of Nonlinear Dynamics (Henniker, NH, June 1986).
To be published by SIAM, eds, F. Salam and M. Levi.

89. Simó C.
On the Hénon-Pomeau Attractor.
Journal of Statistical Physics, Vol. 21, No. 4, pp 465-494 (1979).

90. Gwinn E.G. and Westervelt
Horseshoes in the Driven, Damped Pendulum.
Physica 23D pp 396-401 (1986).

91. Grebogi C., Ott E. and Yorke J.A.
Metamorphoses of Basin Boundaries in Nonlinear Dynamical Systems.
Physical Review Letter, Vol. 56, No. 10, (1986).

92. Grebogi C., Ott E. and Yorke J.A.
Basin Boundary Metamorphoses: Changes in Accessible Boundary Orbits.
Physica 24D, pp 243-262, (1987).

93. Thompson J.M.T.
Chaotic phenomena triggering the escape from a potential well.
Proc. Roy. Soc. Lond. A421, pp 195-225, (1989).

94. Grebogi C., Ott E. and Yorke J.A.
Critical Exponent of Chaotic Transients in Nonlinear Dynamical System.
Physical Review Letters, Vol. 57, No. 11, (1986).

95.   Smale, S.
      Diffeomorphisms with many periodic points. In Differential and
      Combinatorial Topology.
      S. Cairns (ed.), pp 63-80. Princeton Press: Princeton, NJ (1963).

96.   Hayashi, C.
      Nonlinear Oscillation in Physical Systems.
      McGraw-Hill, (1964).

97.   Moon F.C., Cusumano J. and Holmes P.J.
      Evidence for Homoclinic Orbits as a Precursor to Chaos in a Magnetic
      Pendulum.
      Physica 24D, pp 383-390, (1987).

98.   Katok, A.B.
      Lyapunov exponents, entropy and periodic points for diffeomorphisms.
      Publ. Maths. IHES, Vol. 51, pp 137-174, (1980).

99.   Hayashi C.
      The method of mapping with reference to the doubly asymptotic structure
      of invariant curves.
      *International Journal of Non-linear Mechanics. Vol. 15, No. 4/5,
      pp.341-348 (1980).*

100. Rössler, O.E.
      Chaos.
      *Structural Stability in Physics, W. Güttinger and H. Eikerneier (eds), pp
      290-309, Pub. Springer-Verlag (1979).*

101. Rössler, O.E.
      An Equation for Continuous Chaos.
      Physics Letters, Vol. 57A, No. 5, pp 397-398 (1976).

102. Rössler, O.E.
      Chaotic Behaviour in Simple Reaction Systems.
      Z. Naturf., Vol. 31A, pp 259-264, (1976).

103. Bier, M. and Bountis, T.C.
Remerging Feigenbaum Trees in Dynamical Systems.
Physics Letters, Vol., 104A, No. 5, (1984).
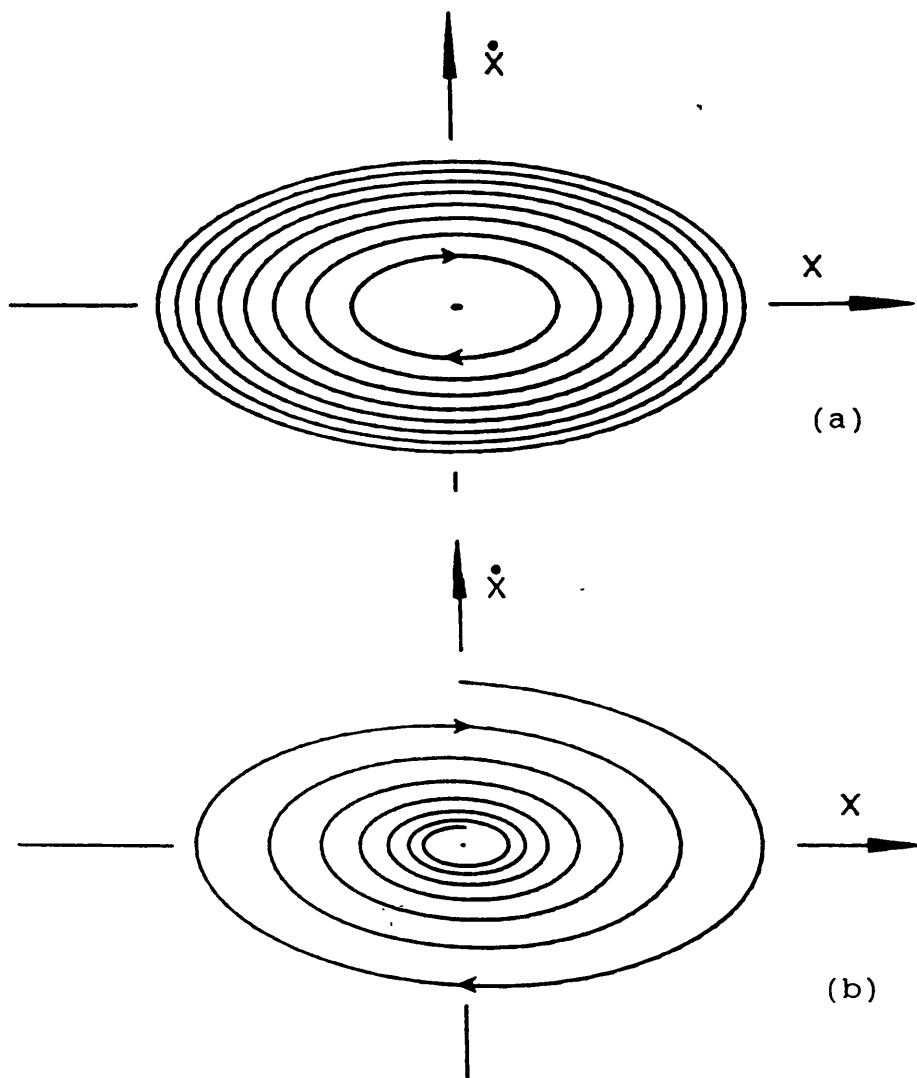
Figure 1. Undamped and damped phase trajectories of a linear oscillator.
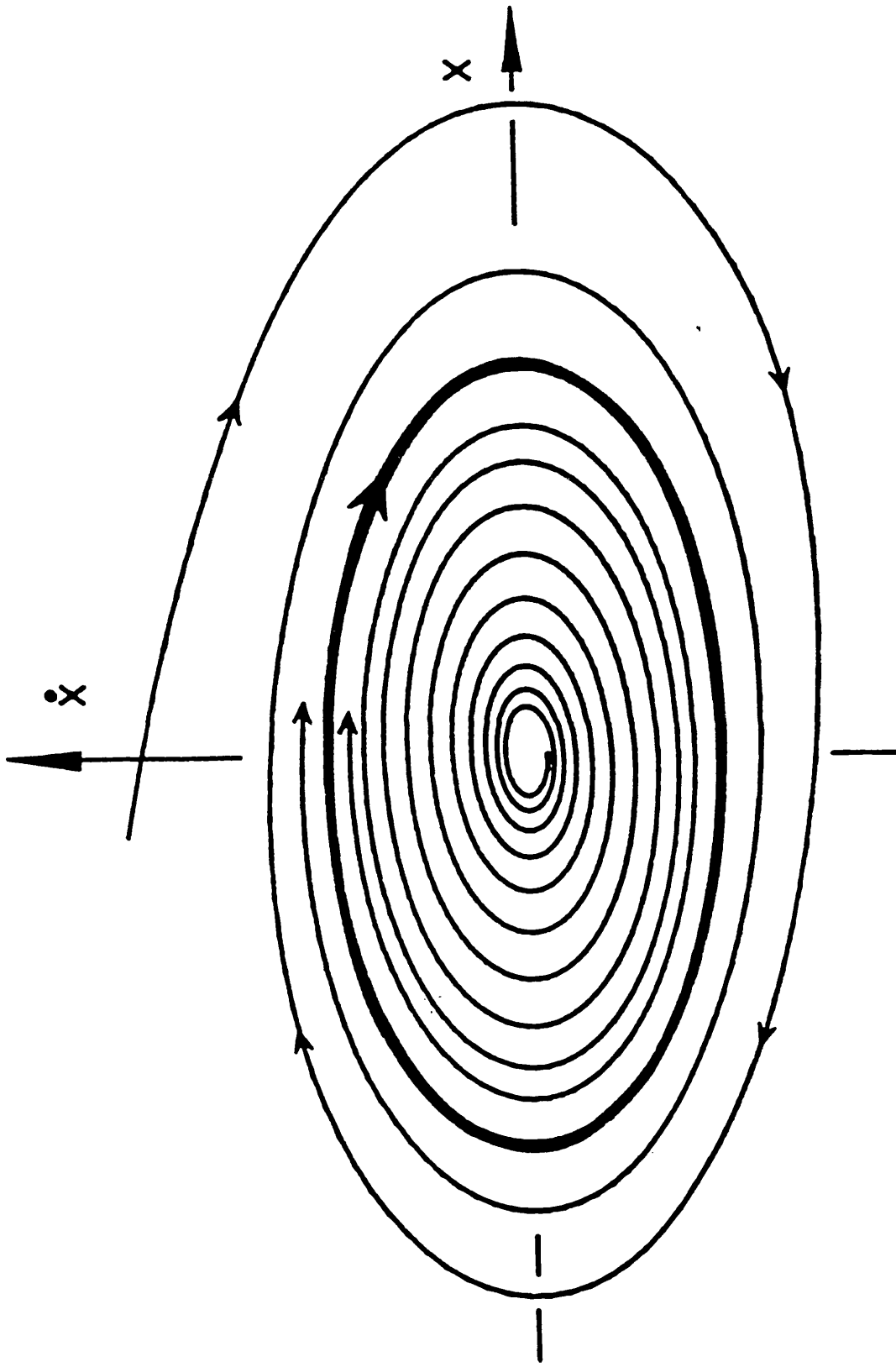
Figure 2. Phase trajectories of a non-linear oscillator with a single stable limit cycle.
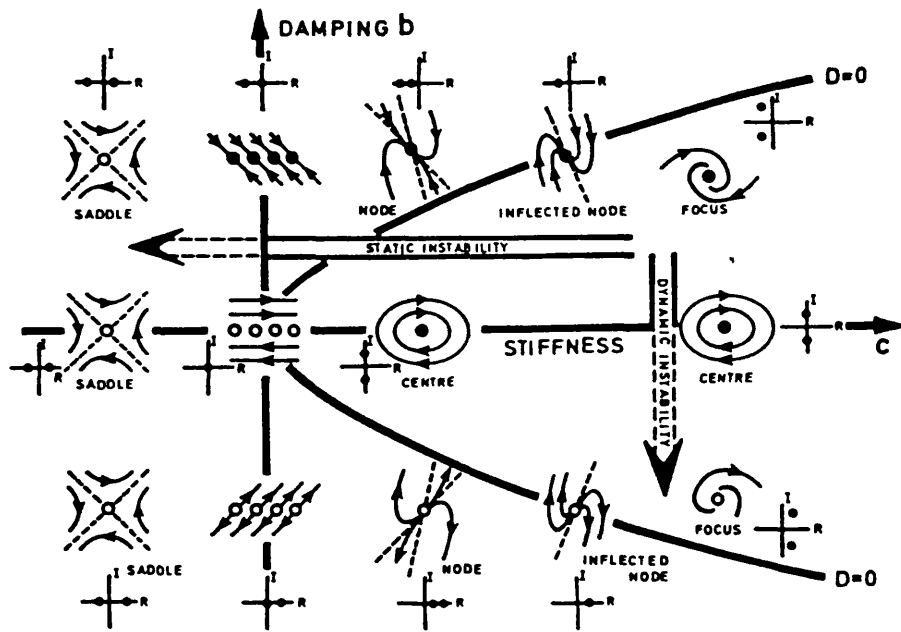
Figure 3. Root structure of a linear oscillator.
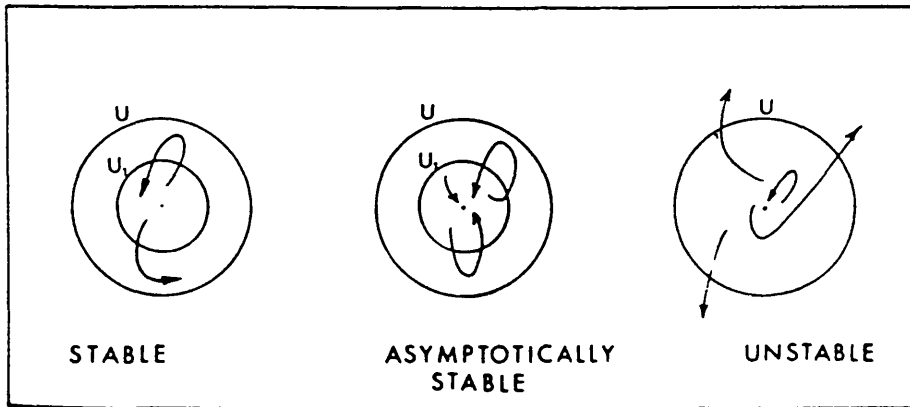
Figure 4. Liapunov stability for an equilibrium state.
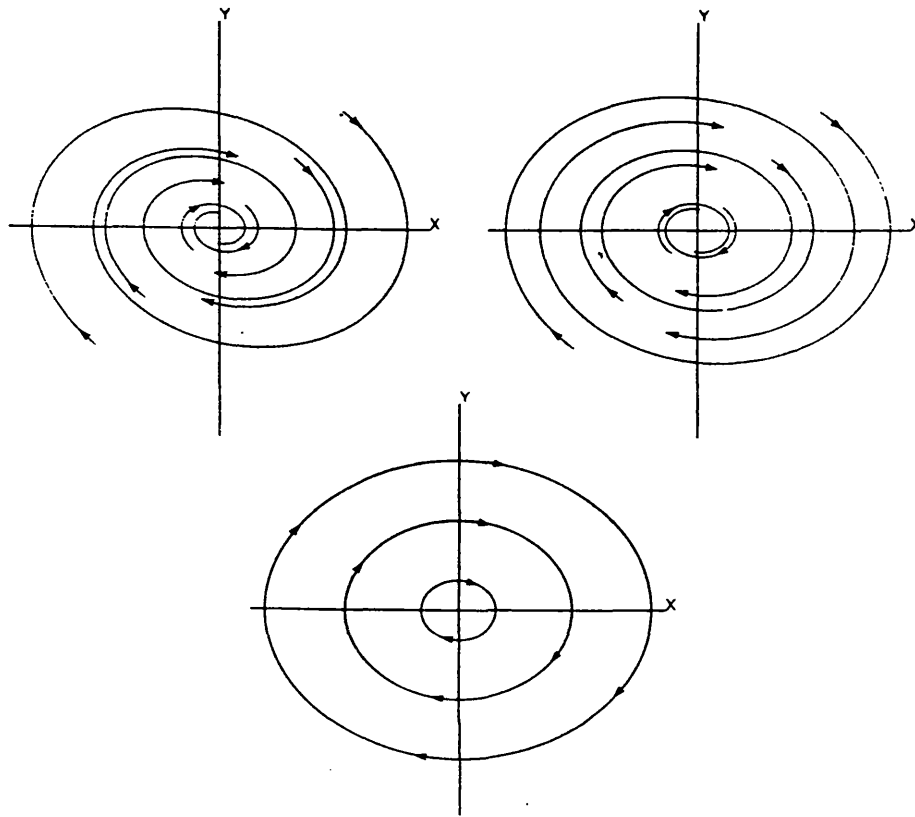
Figure 5. Dynamics near a focal point with varying characteristic exponents.
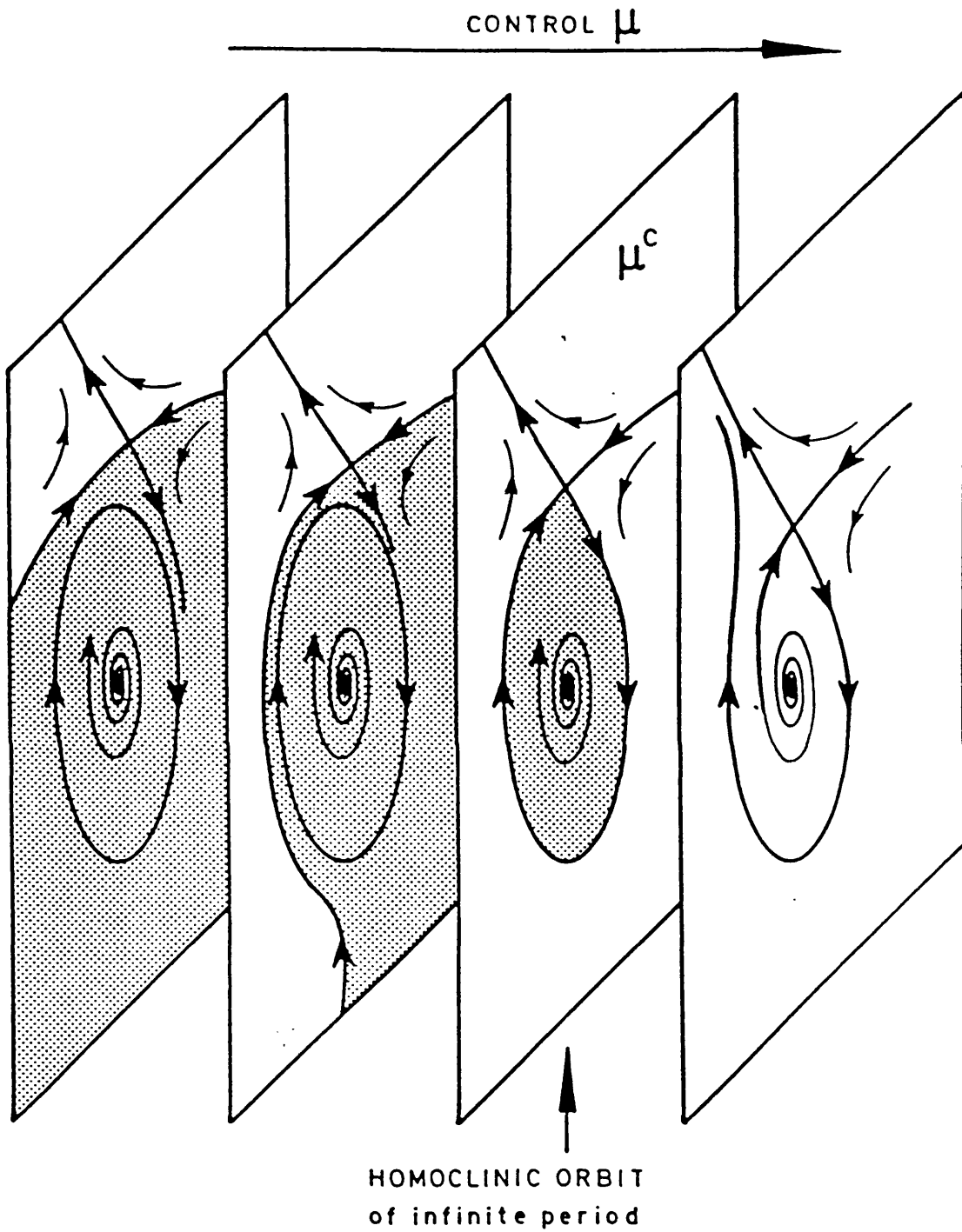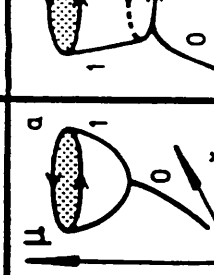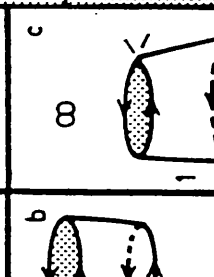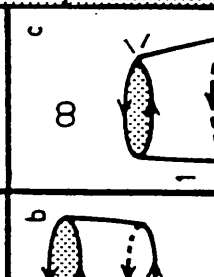
A SADDLE CONNECTION (BLUE SKY)
CATASTROPHE

Figure 6.   Schematic   diagram   showing   the   various   stages   of
a Blue Sky Catastrophe.

Figure 7.

Classification of co-dimension 1 bifurcation types.

ATTRACTOR DIMENSION AFTER THE BIFURCATION

	0 POINT	1 CYCLE	2 TORUS	3 CHAOTIC	∞ NO ATTRACTOR
0 POINT	(Stable-symmetric) (Asymmetric)	Super-crit. Hopf [a] FLOW EXPLOSION [b]		?	FOLD SUB-CRIT. HOPF (UNSTABLE-SYMMETRIC)
1 CYCLE		Super-crit. Flip	Super-crit. Neimark MAP EXPLOSION	[Flip cascade] INTERMITTENCY EXPLOSION	CYCLIC FOLD SUB-CRIT. FLIP SUB-CRIT. NEIMARK SADDLE CONNECTION [c]
2 TORUS					
3 CHAOTIC				CHAOTIC EXPLOSION	CHAOTIC BLUE-SKY CATASTROPHE

ATTRACTOR DIMENSION BEFORE THE BIFURCATION — SEVERITY

Terminology:

	Subtle i.e. Continuous (lower case)	CATASTROPHIC i.e. DISCONTINUOUS (UPPER CASE)	
	Safe	EXPLOSIVE	DANGEROUS
	a	b	c

- 130 -

$$\ddot{x} + f(\dot{x}, x) = F\sin\omega t$$

2D PHASE PROJECTION

POINCARE MAPPING: $\begin{bmatrix} x(t) \\ y(t) \end{bmatrix} \Longrightarrow \begin{bmatrix} x(t+T) \\ y(t+T) \end{bmatrix}$ $\begin{array}{l} x_{i+1} = G(x_i, y_i) \\ y_{i+1} = H(x_i, y_i) \end{array}$

3D PHASE PORTRAIT

STEADY STATES

TRANSIENTS

A → B → A   n=2 FIXED POINT (SUBHARMONIC)
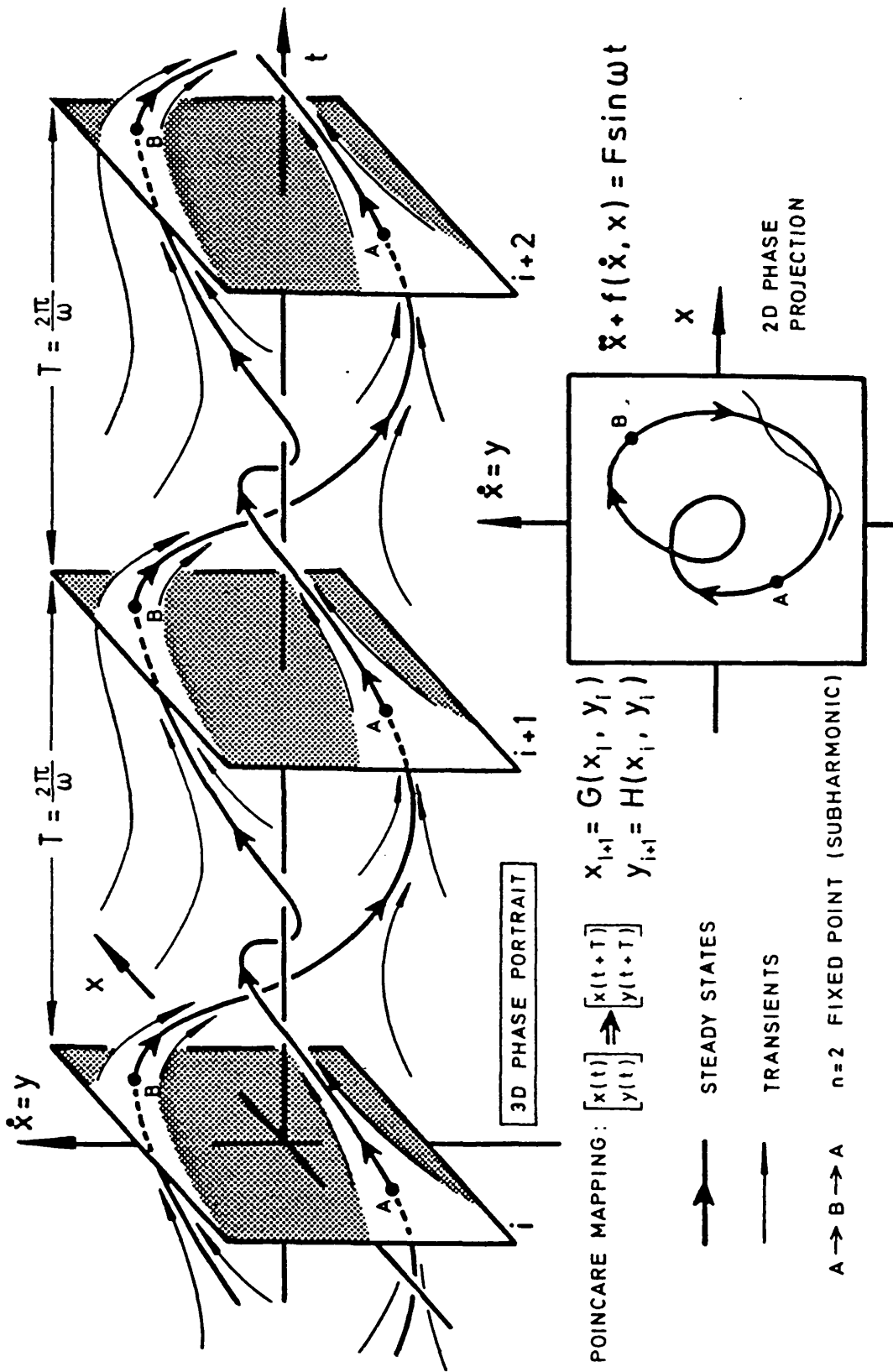
Figure 8. STROBOSCOPIC POINCARE SECTIONS FOR FORCED OSCILLATORS
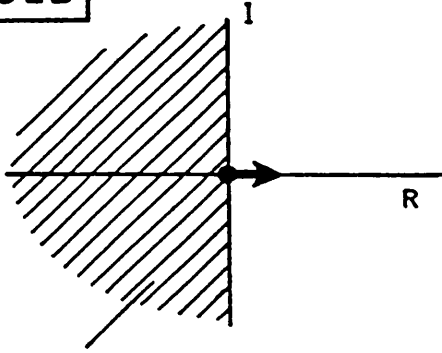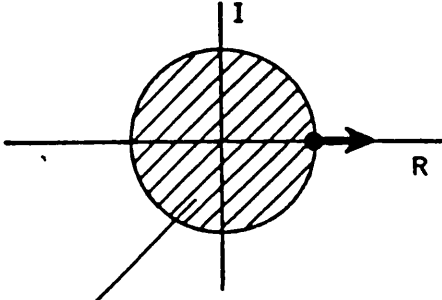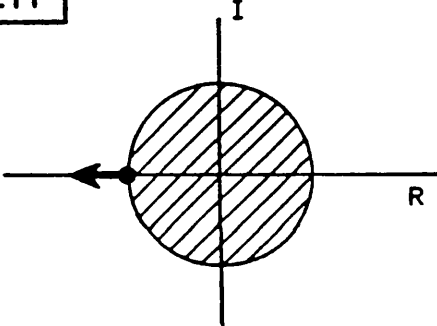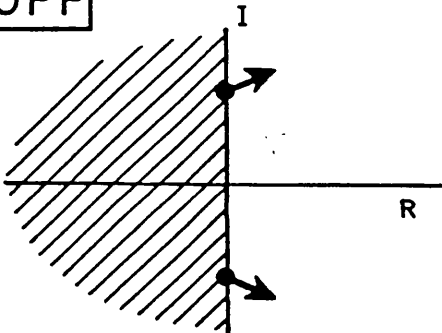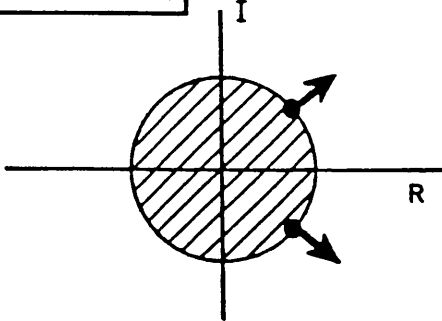
- 131 -

Figure 9. Stability boundary on the complex plane of a flow and a map.

Figure 10.

Stability criteria in the trace-determinant plane.
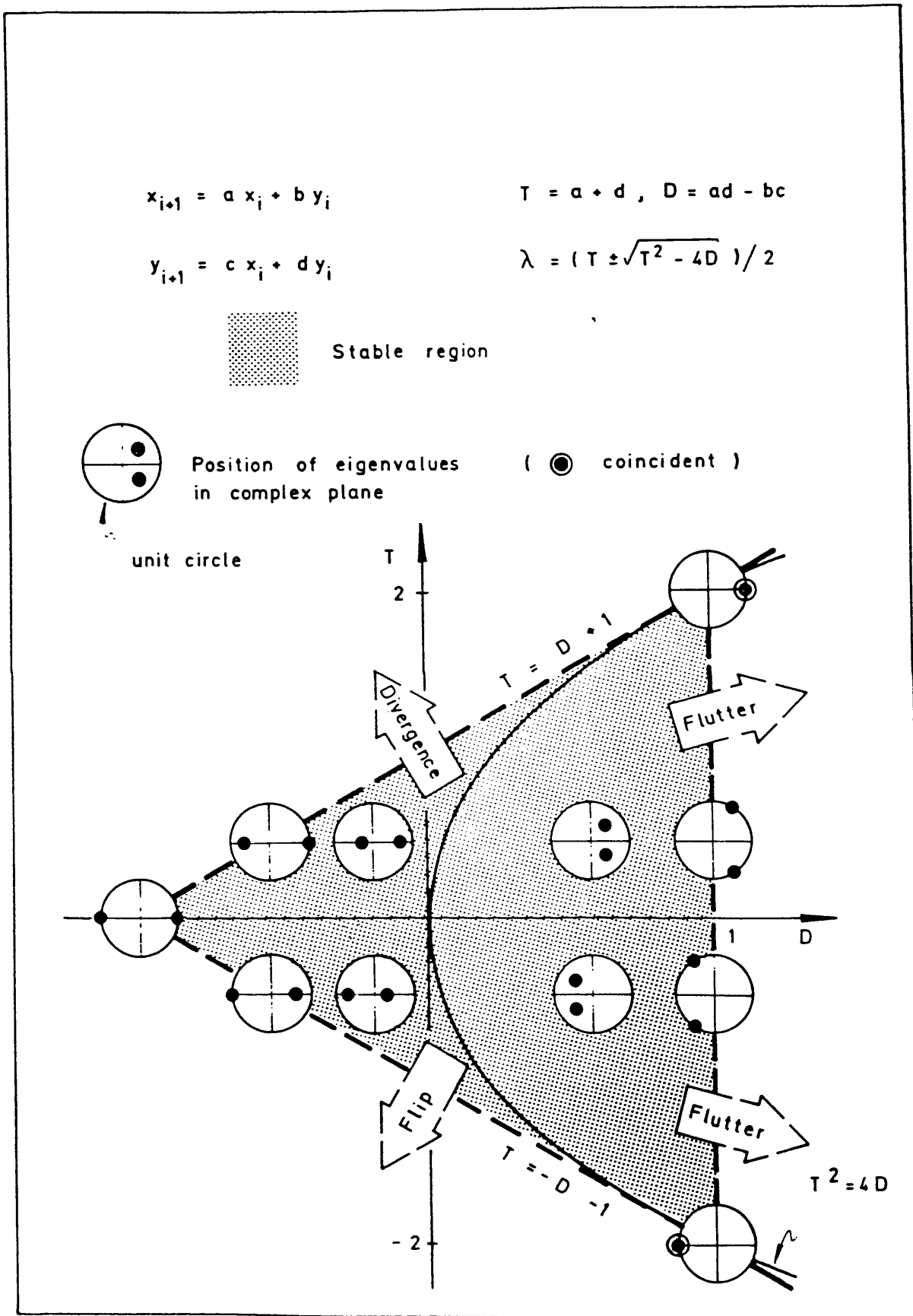
SECOND EIGENVALUE POSITIVE
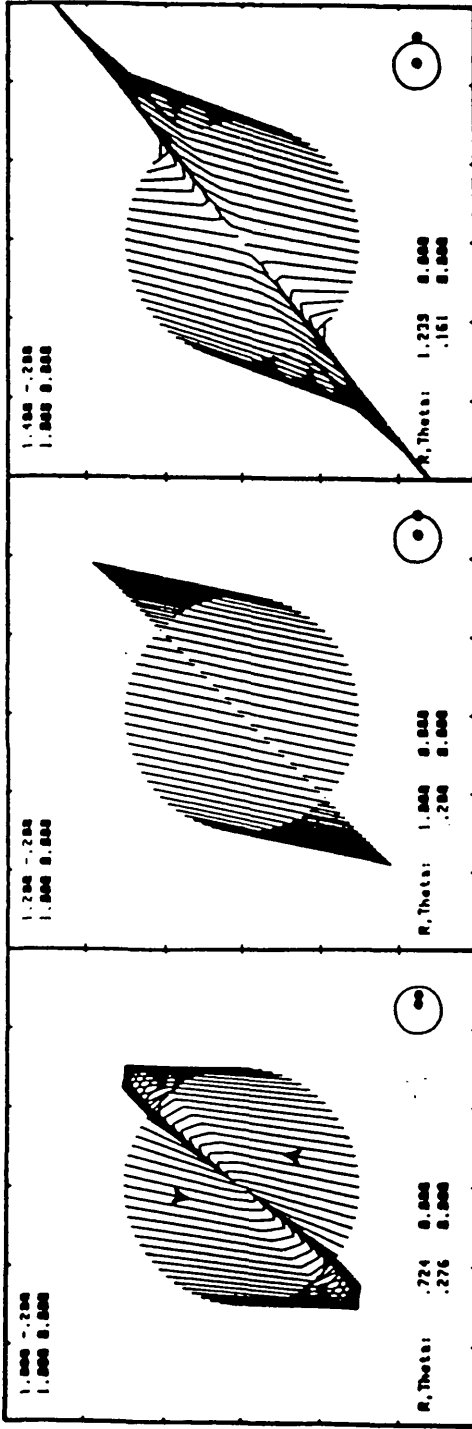
SECOND EIGENVALUE NEGATIVE
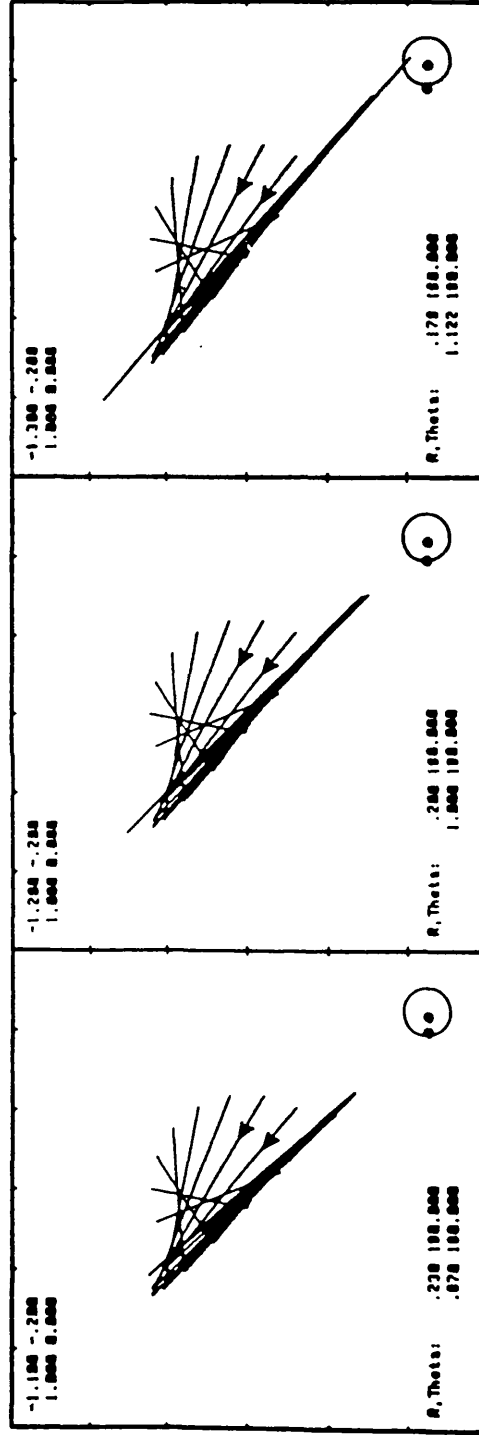
Figure 11. Two-dimensional map approaching a fold or a flip bifurcation.
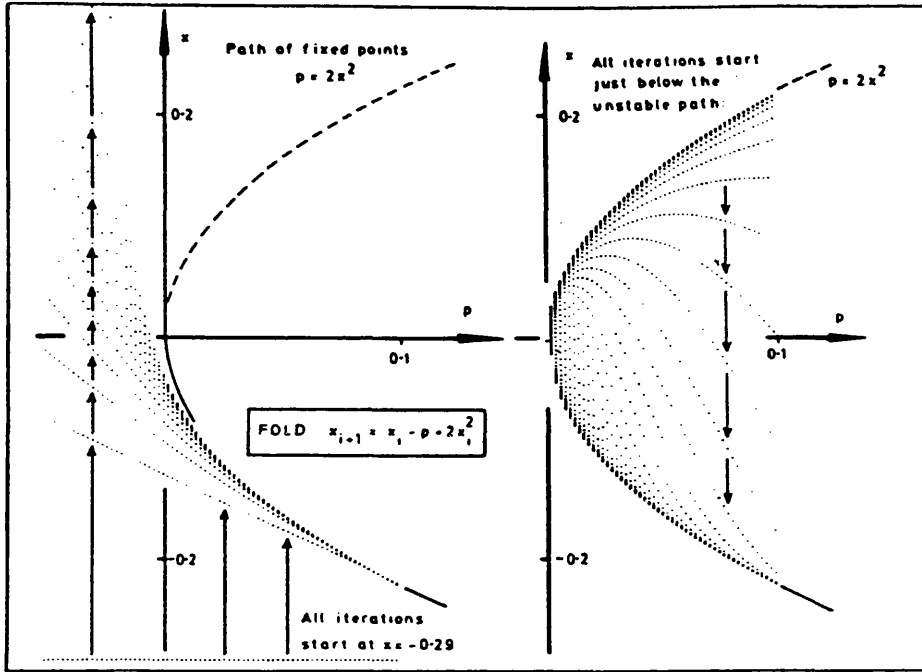
Figure 12. Saddle-node bifurcation of a map.

FLUTTER
MN 2

Perturbation solution
for n = 2

$y = -x(1+p) - 2x^3$

First-order perturbation
solution for n = 2 is

$p = 2x^2$

All runs start
$x = 0.4$ or $x = 0.01$
All iterations alternate in
$x, - - - - - -$ etc

Pert soln. n = 2

FLUTTER
MN 4

All starts indicated
All $x, - - - -$ etc

$y = -x(1+p) - 2x^3$
Perturbation soln. in n = 2 : $p = -2x^2$
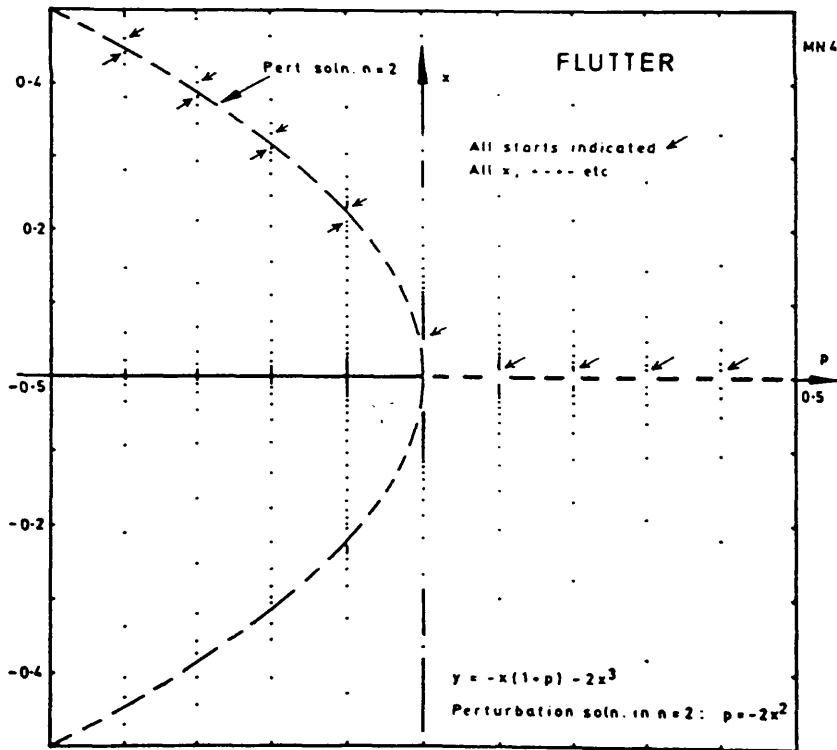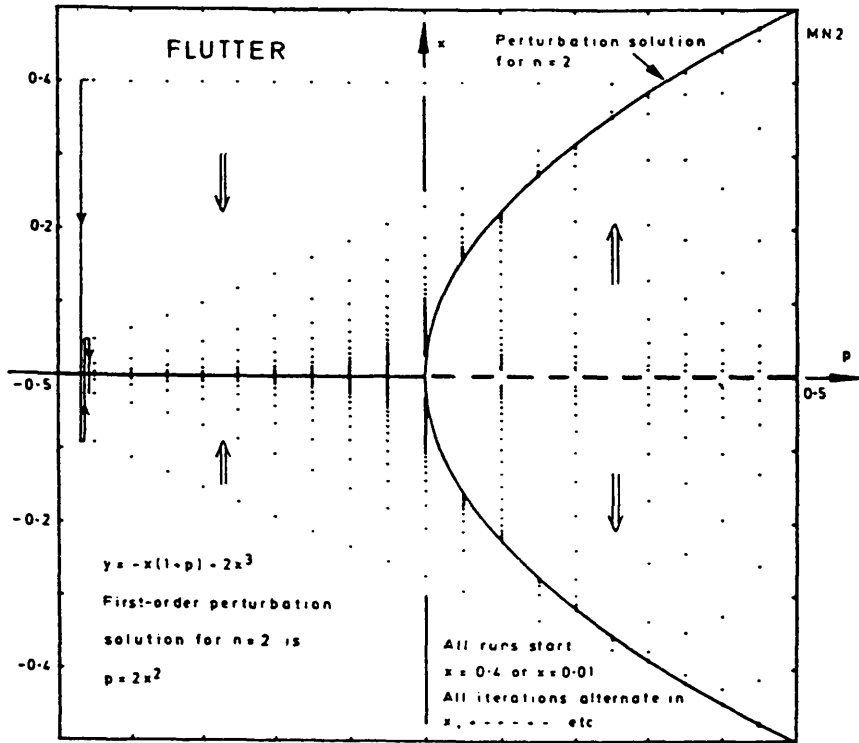
Figure 13. Flip bifurcation of a map.
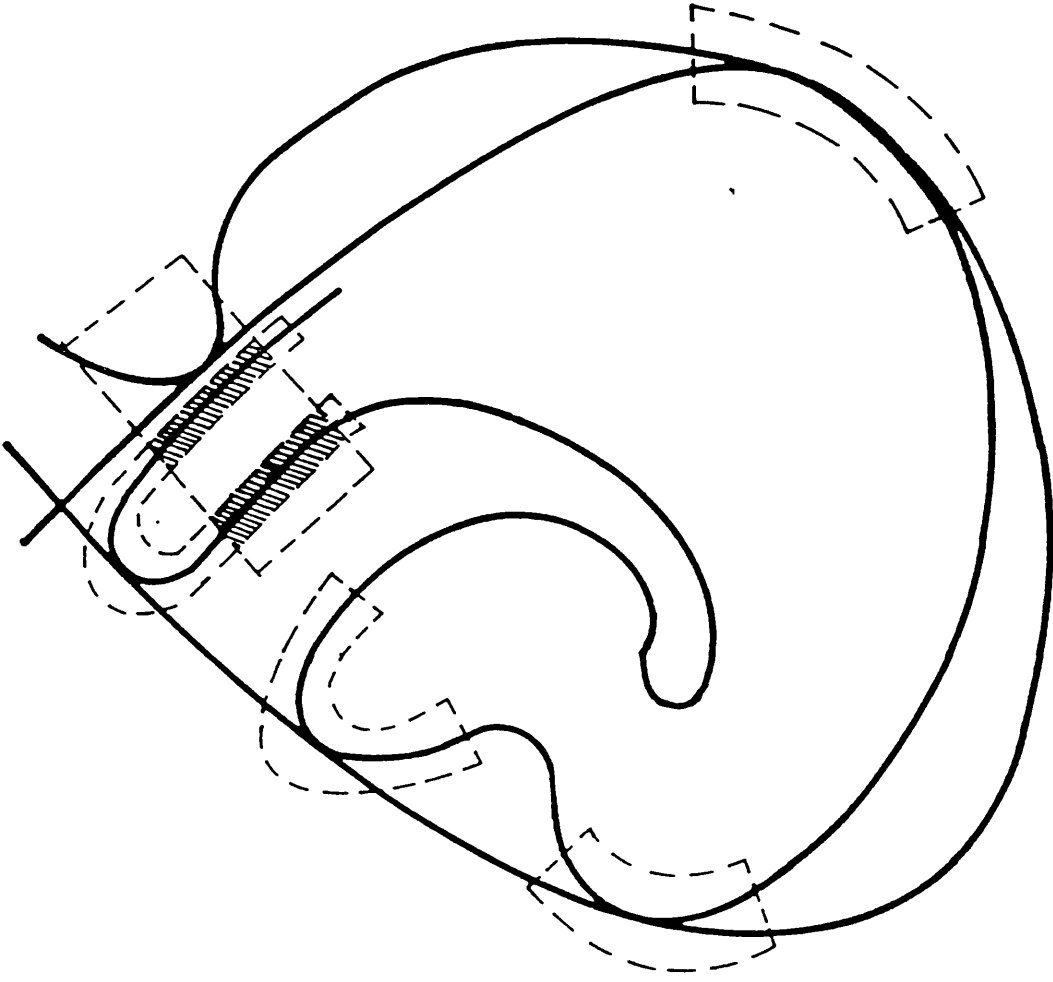
Folding and stretching action

Mixing action

Figure 14.

Schematic diagram illustrating the effect of Homoclinic Tangle
leading to horseshoe like dynamics

Figure 15. Two dimensional cylindrical model of the
Birkhoff-Shaw Strange Attractor

$$\dot{x} = 0{\cdot}7y + 10x(0{\cdot}1 - y^2)$$

$$\dot{y} = -x + 0{\cdot}25 \sin 1{\cdot}57\,t$$

Cross-sections
at 10° intervals

FC

- 138 -
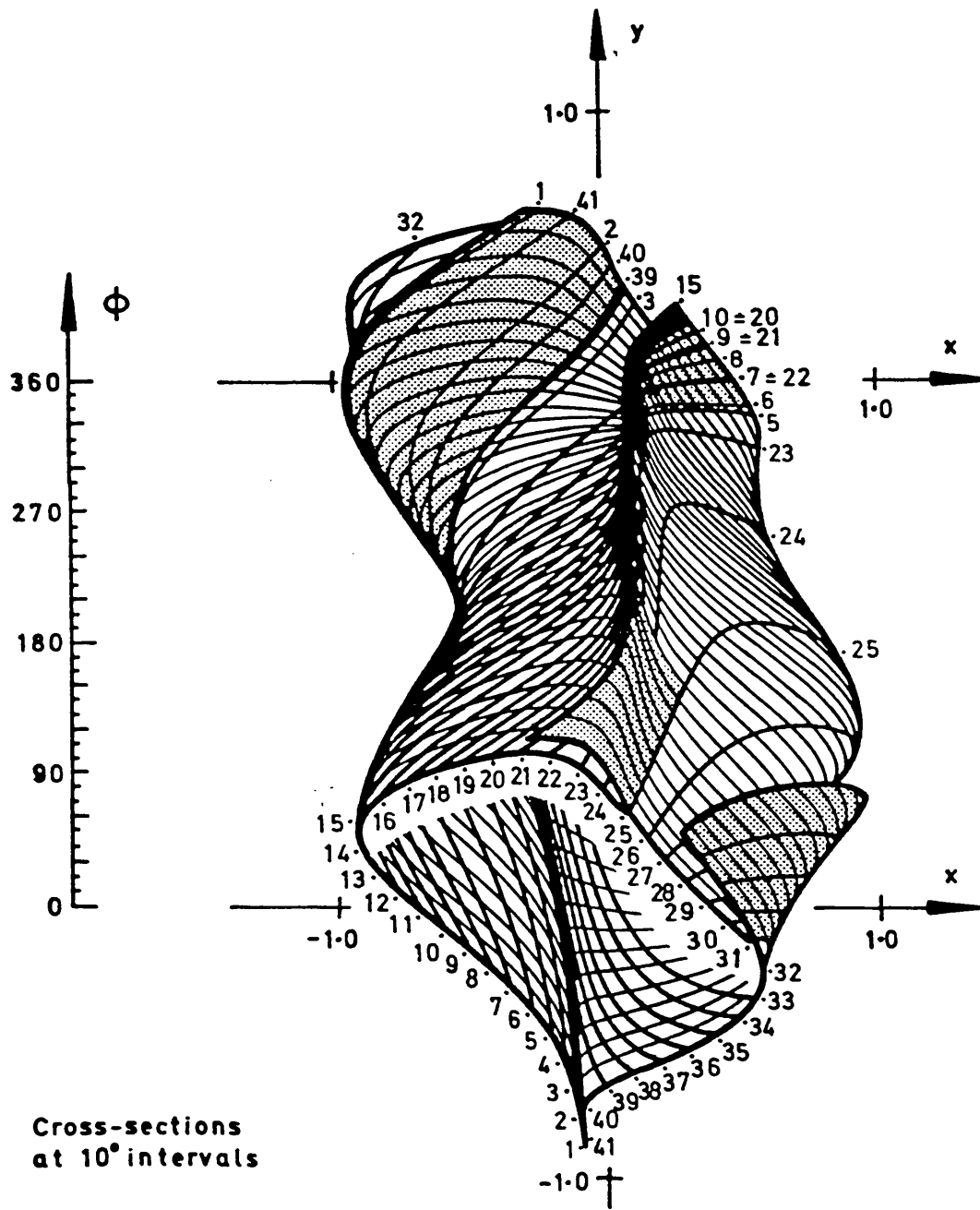
Figure 16. Unfolded cylindrical model of the Birkhoff-Shaw Strange Attractor

A single trajectory wandering
chaotically for 200 cycles after
settling on the Strange Attractor
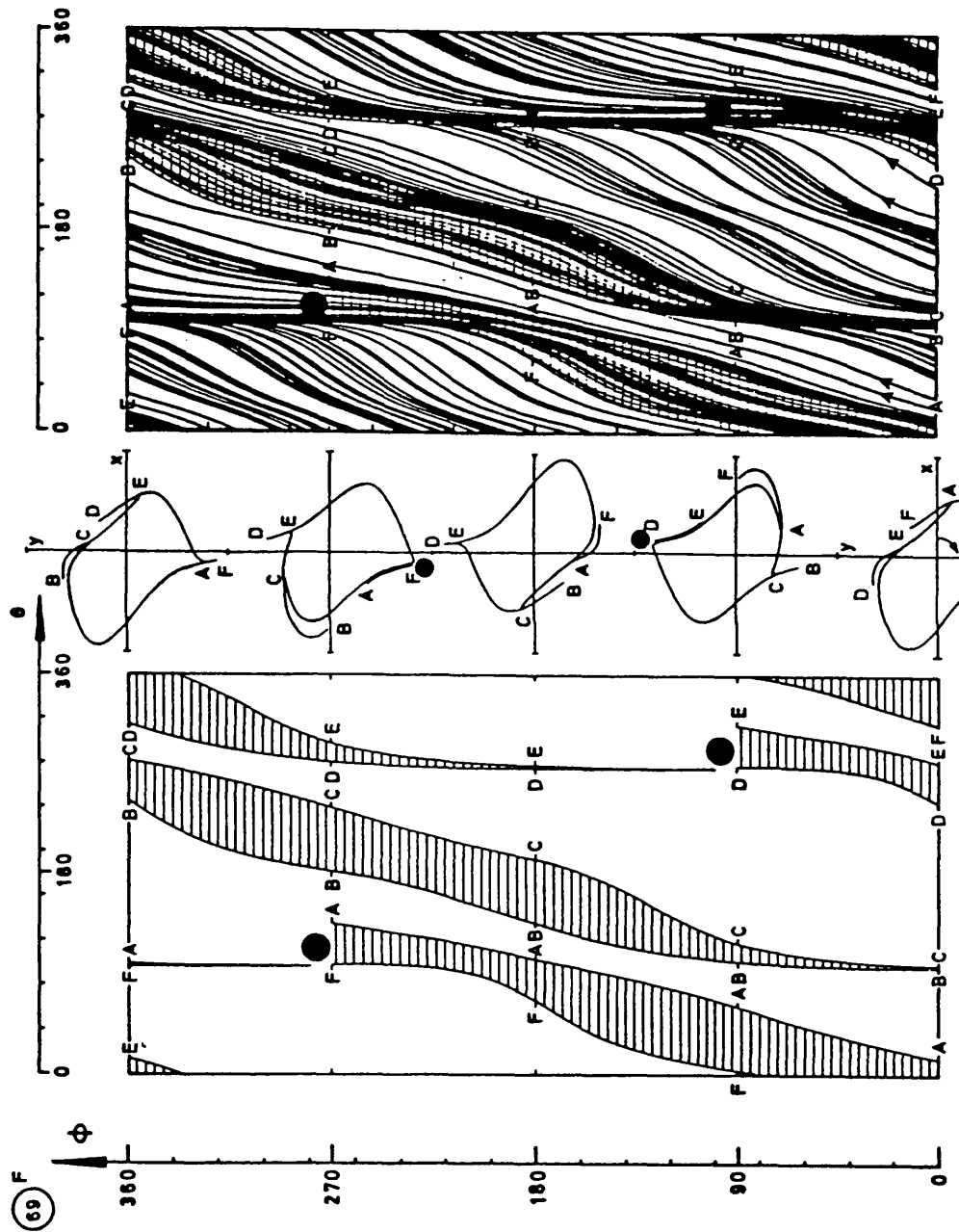
● Folding of a wing and creation of a beak

● Wing-beak structure winds like a subharmonic of order 3

- 139 -

Figure 17. Exponential divergence studies (Impact Oscillator)
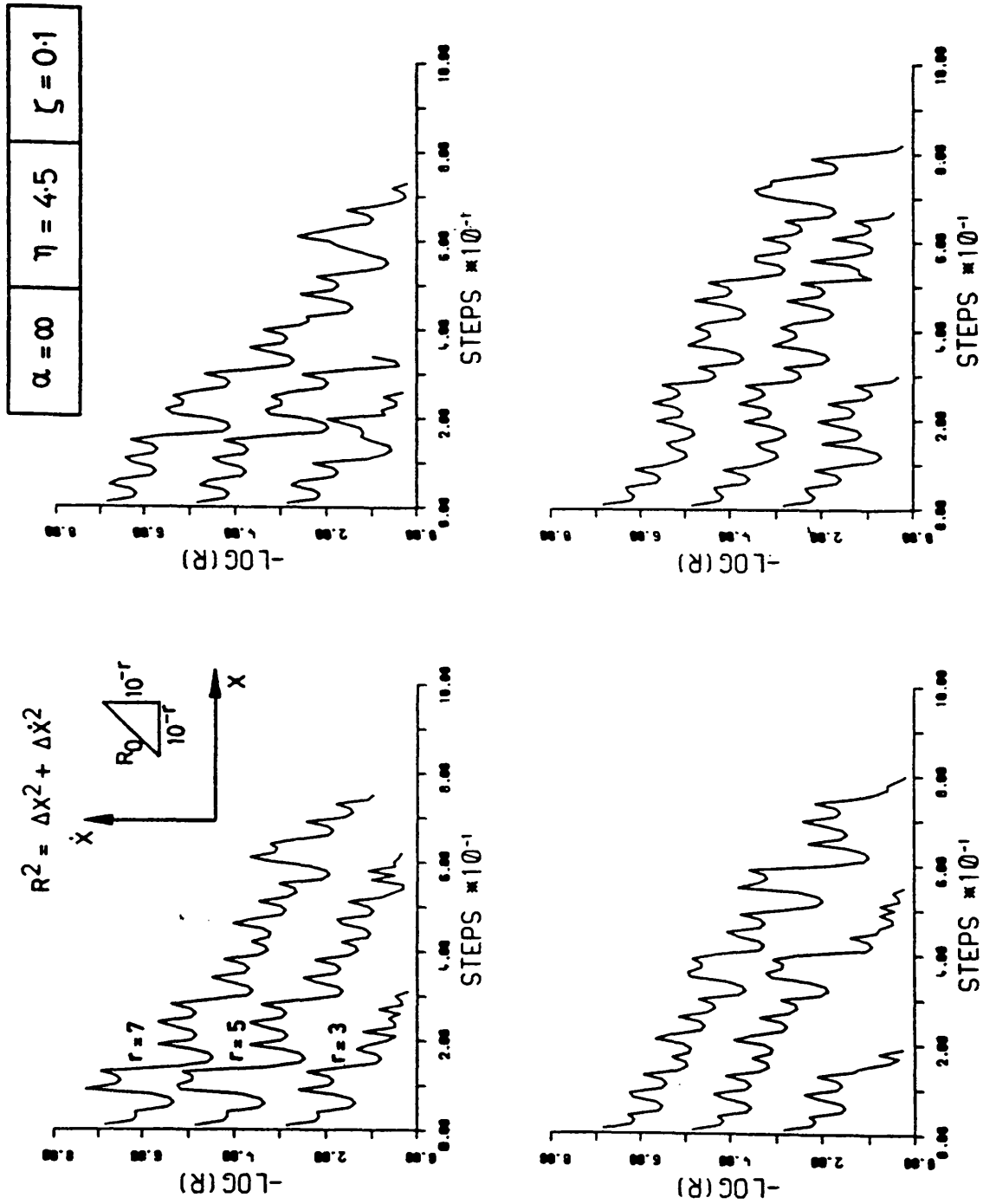
Figure 18. Typical Power Spectrum of Ueda's Strange Attractor

SET(5) ≡ UEDA(5)

$\ddot{x} + 0.05\dot{x} + x^3 = 7.5\cos t$

Damped
Forced
Nonlinear
Oscillator

Beam at buckling load

Transients to unique
STRANGE ATTRACTOR
governing steady state CHAOS
In the steady chaotic state
the positive x peaks
synchronize approximately
with the $t = 2i\pi$ sections

Power

Typical spectrum
$(k = 0.1, B = 12)$

ω

Steady state CHAOS

$\vdash_{2\pi}$

Transient from $x = 0, \dot{x} = 0$

100π

t

Ueda's solution (k) for $k = 0.05, B = 7.5$

High frequency transient from large de-synchronized start
at $x = -5, \dot{x} = 0$

60π

t

$\Delta t = 0.15$

Steady chaos
Poincaré
$2i\pi$ sections
(mapping points)
defining the
ATTRACTOR
(k)

FC

- 141 -

Figure 19. Enlarged view of the one dimensional Quadratic map.
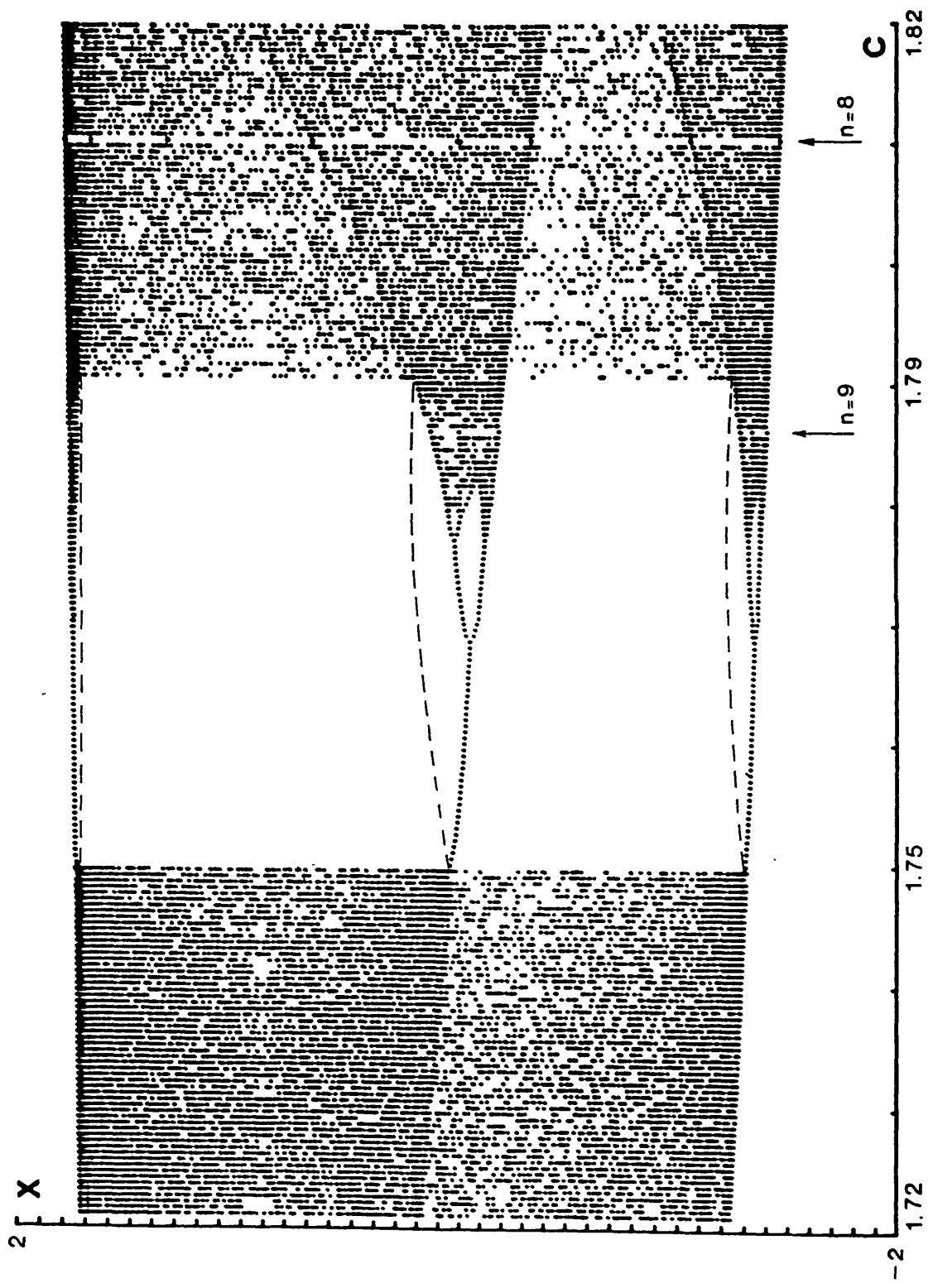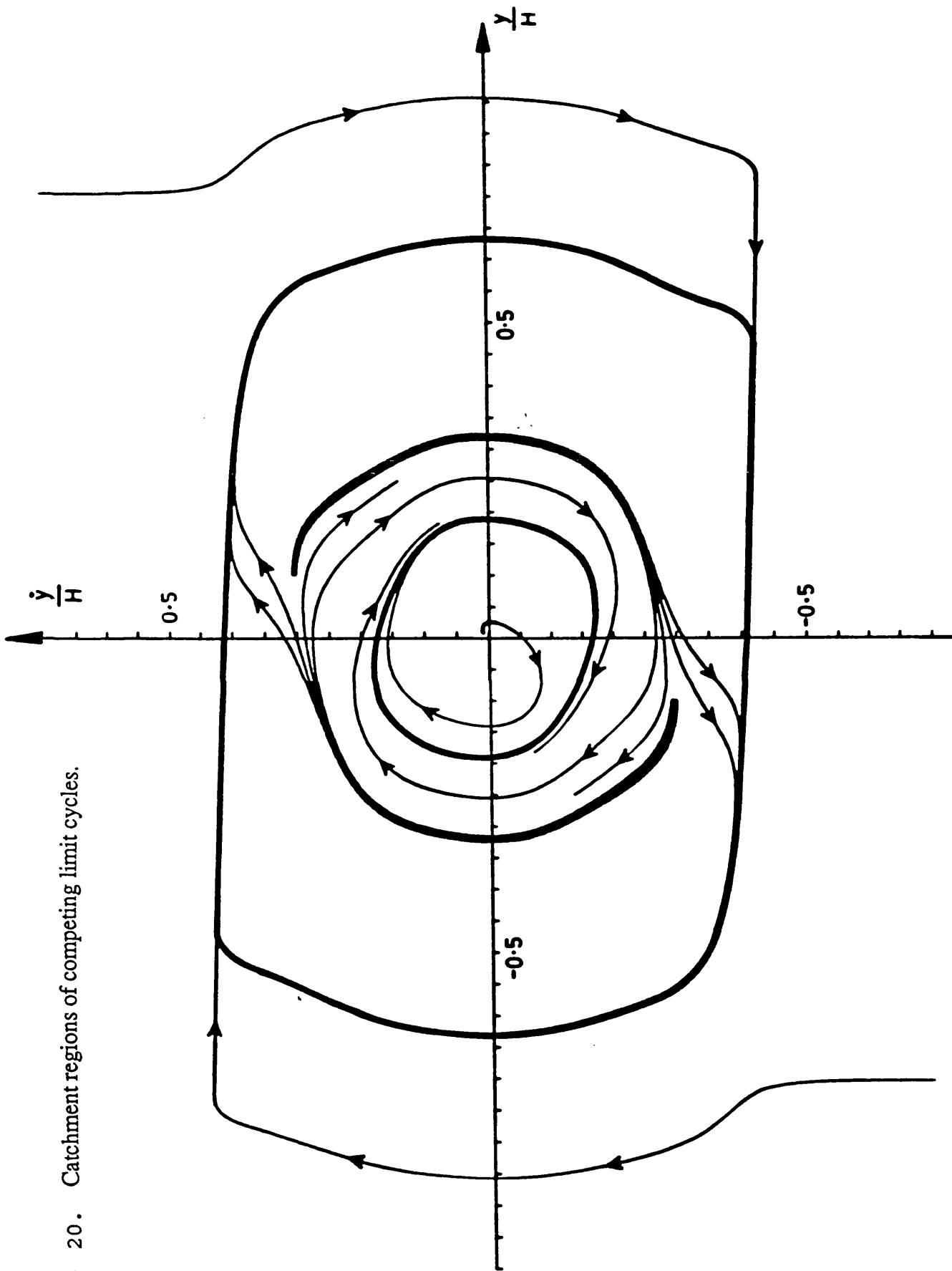
Figure 20. Catchment regions of competing limit cycles.

SECOND EIGENVALUE POSITIVE
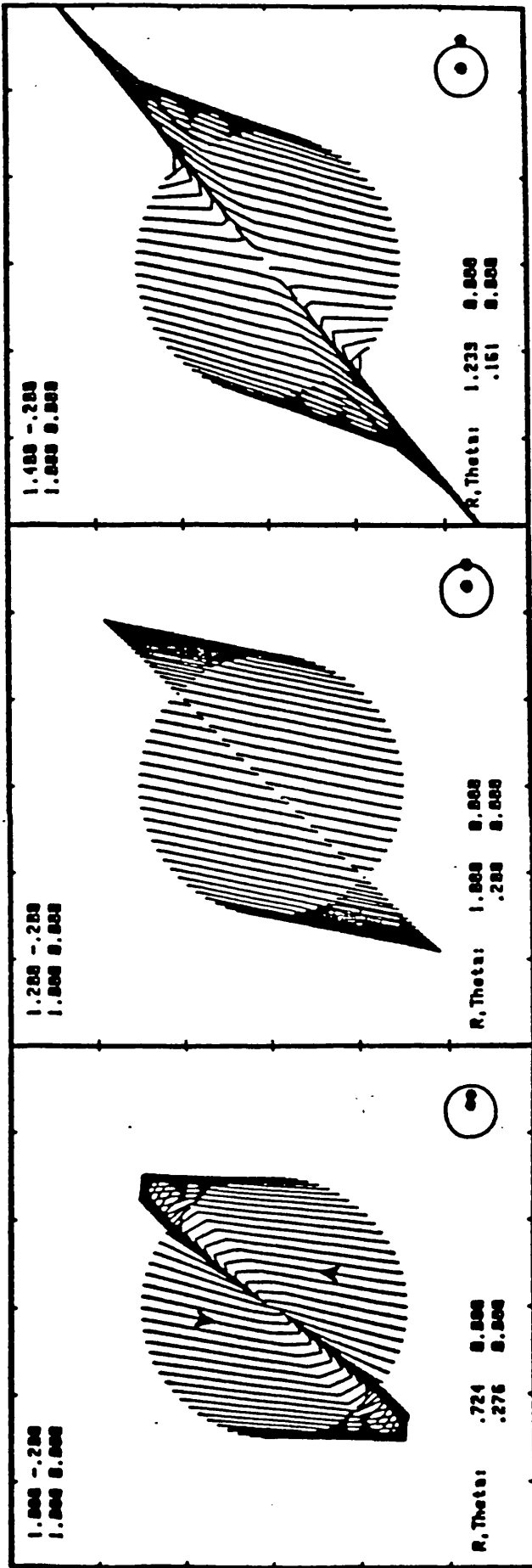
$$\begin{bmatrix} X_{i+1} \\ Y_{i+1} \end{bmatrix} = \begin{bmatrix} X_i \\ Y_i \end{bmatrix} \begin{bmatrix} a & b \\ c & d \end{bmatrix}$$

Figure 21.   Trajectories of a two dimensional linear map close to an equilibrium point.
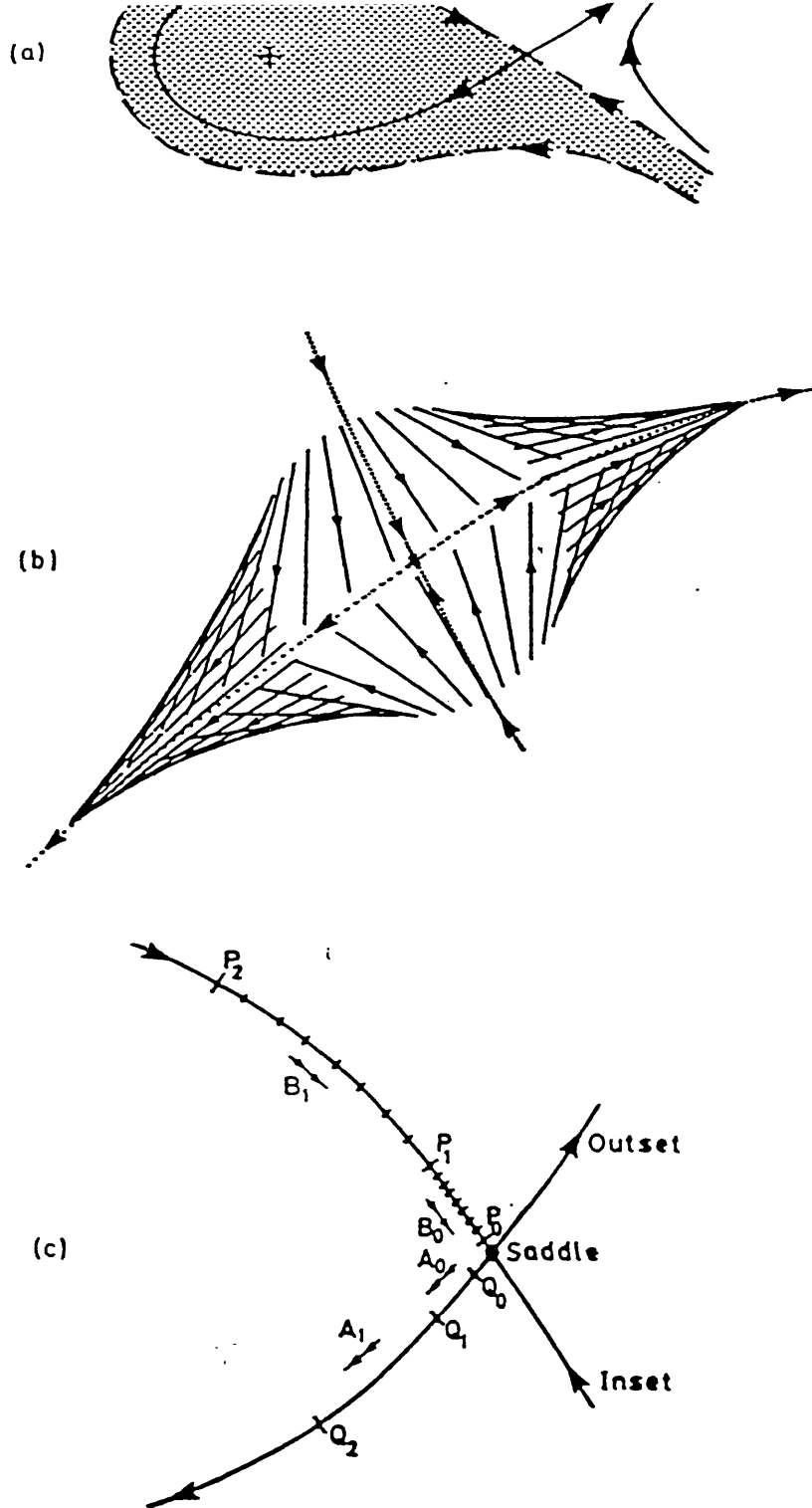
Figure 22. (a) Schematic phase portrait showing the invariant manifolds of a typical saddle point enclosing the catchment region of a steady state solution.

(b) Location of a possible saddle point when using the interactive graphical technique.

(c) Poincaré points stepping along the inset and outset of a saddle using the ladder method.
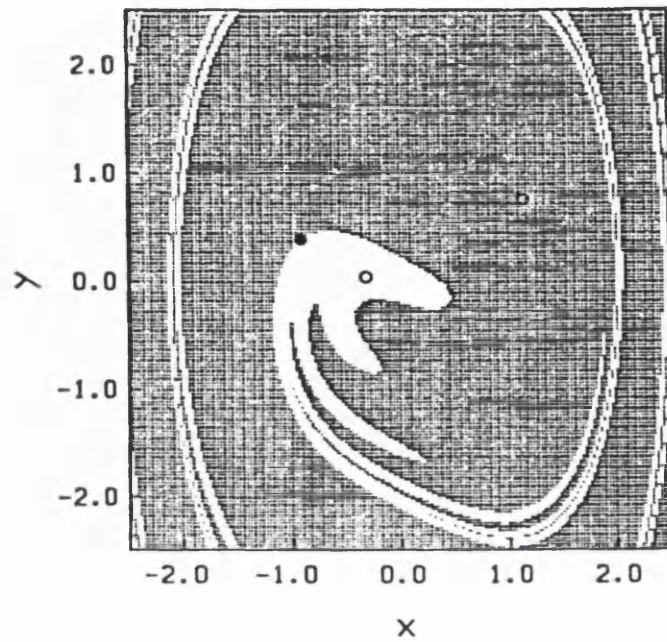
$$\ddot{x} + k\dot{x} + x^3 = B \cos t$$

$$k = 0.1 \quad B = 0.3$$

Figure 23. Catchment region of Ueda's equation showing smooth basin boundary.
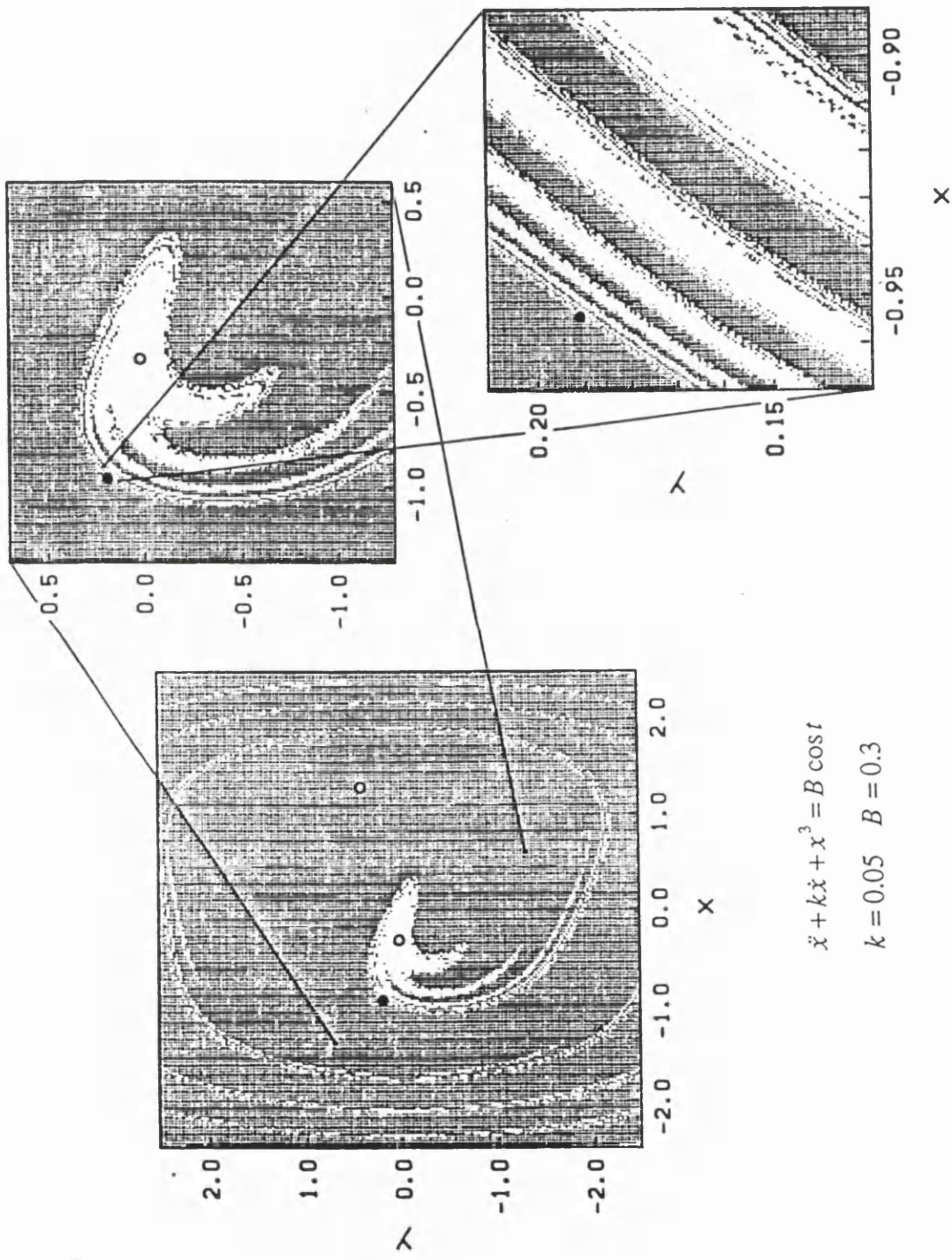
Figure 24. Catchment regions of Ueda's equation showing fractal basin boundaries.

$$\ddot{x} + k\dot{x} + x^3 = B\cos t$$

$$k = 0.05 \quad B = 0.3$$
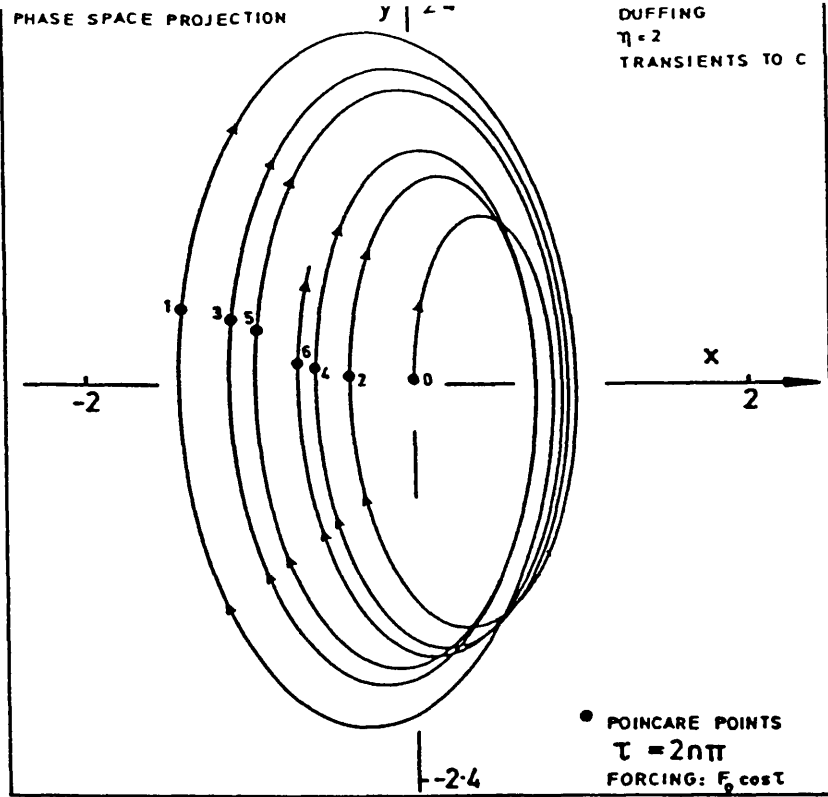
$$\eta^2 \ddot{x} + 2\eta\zeta\dot{x} + x + \alpha x^3 = F_0 \cos\tau$$

$$\eta = 1.6 \quad \zeta = 0.1 \quad \alpha = 0.05 \quad F_0 = 2.5$$
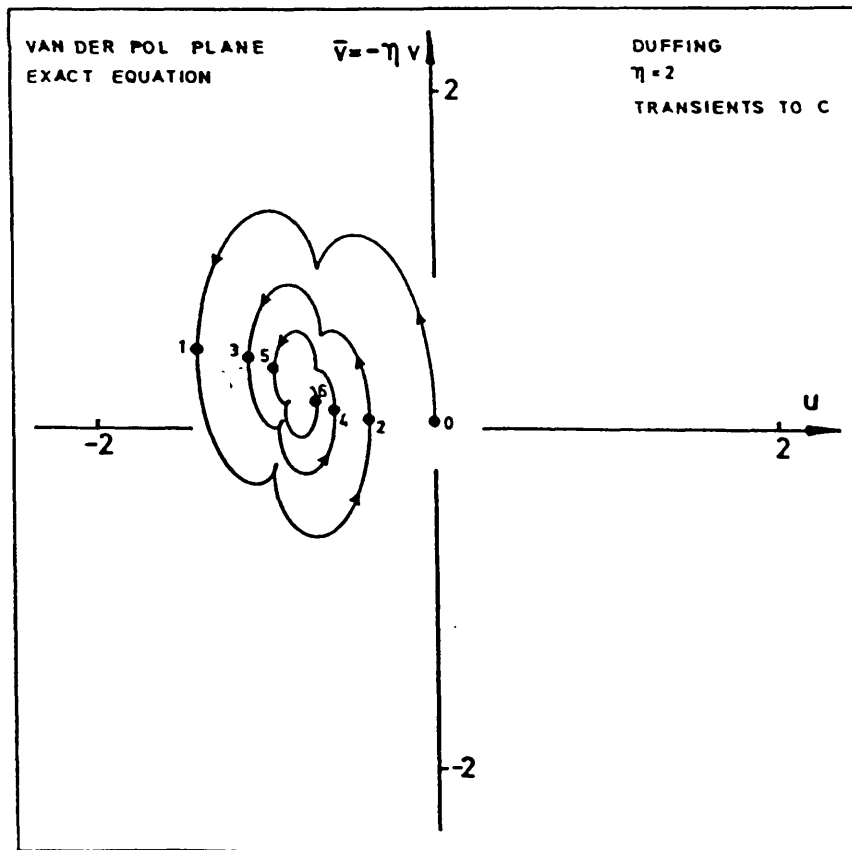
Figure 25. Transient trajectory on the phase space projection and on the Van Der Pol plane.
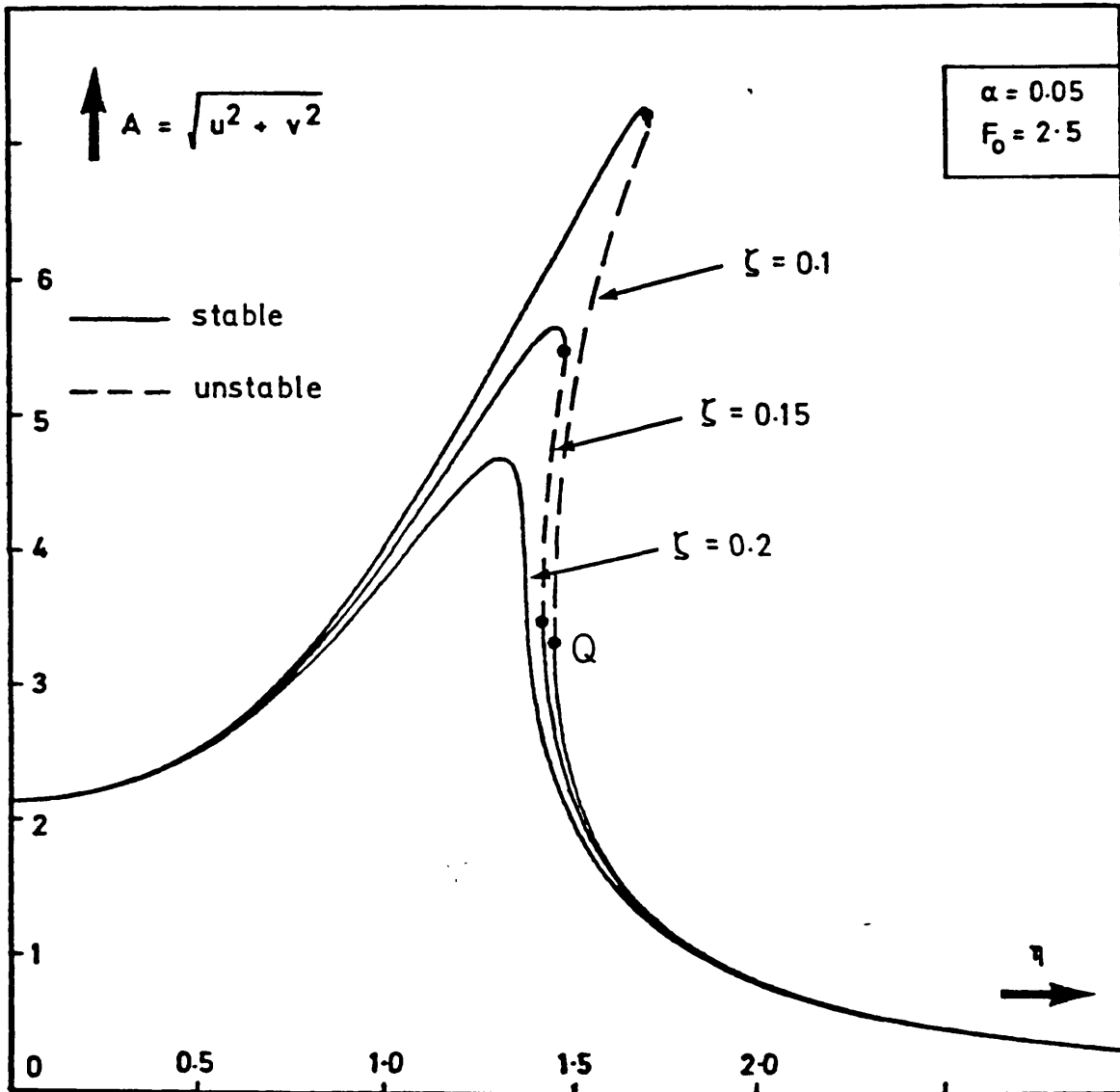
Figure 26. Amplitude response diagram of Duffing's equation at resonance with different damping ratios.
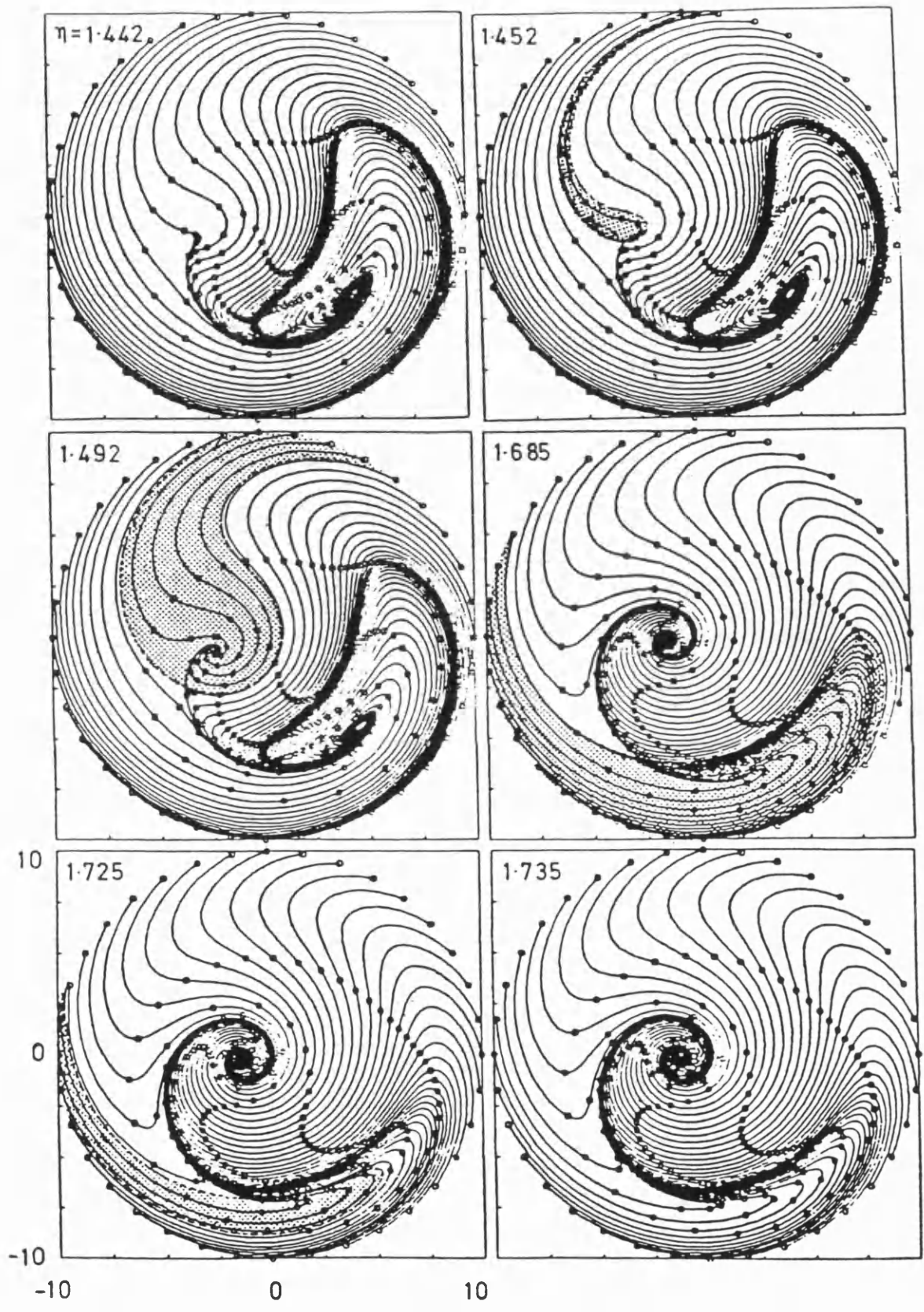
Figure 27. Six phase portraits of the smoothed variational equation of Duffing's equation on the Van der Pol plane during a transition through resonance.
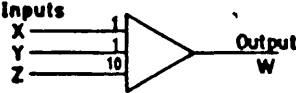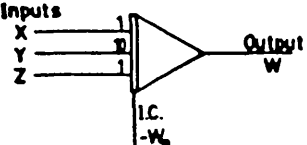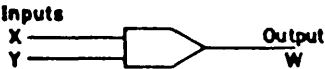
UNIT	USE	SYMBOL	EQUATION
Potentiometer	Multiplication of a variable by a positive constant coefficient <1	Input X — (K) — Output KX	Output=Kx where $0 < K < 1$
Invertor	Sign reversing	Input X — ▷ — Output W	Output= - Input $W=-X$
Summer	Summation of member of variables including multiplication by 'gains' 1 or 10	Inputs X 1 Y 1 Z 10 ▷ Output W	Output= -'Sum of Inputs' $W=-(X-Y+10Z)$
Integrator	Integration of a variable with respect to the computer independent variable 'time t'	Input X — ▷ — Output W I.C. -W₀	$$Output=-\int_{0}^{t} input\ dt$$ $$W=-\int_{0}^{t} X\ dt$$ Initial value of output $= W_0$
Summer Integrator	Summation with Integration	Inputs X 1 Y 10 Z 1 ▷ Output W I.C. -W₀	$$W=-\int_{0}^{t}(X-10V+Z)dt$$
Multiplier		Inputs X Y — Output W	Output=product of inputs $W=XY$

Figure 28. Analogue computer components' symbols and operations.

- 151 -
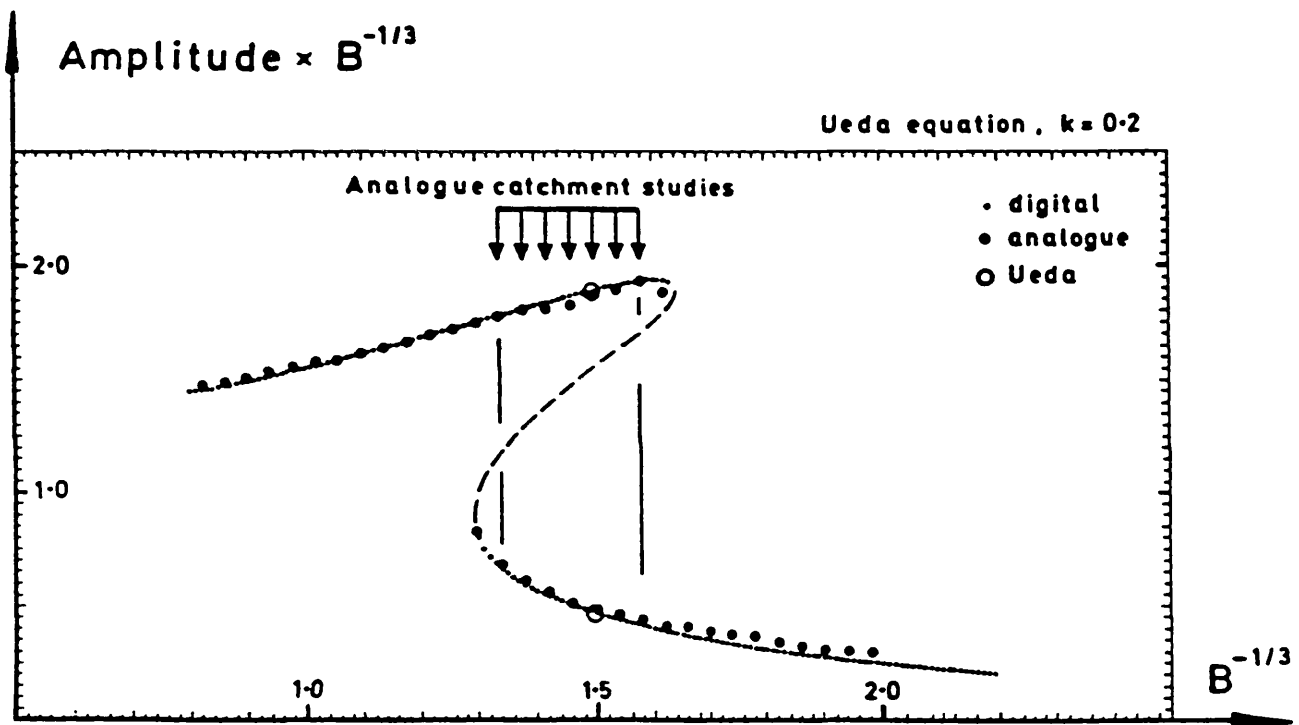
Figure, 29. Resonance response diagram for Ueda's version of Duffing's equation using digital and analogue simulations.
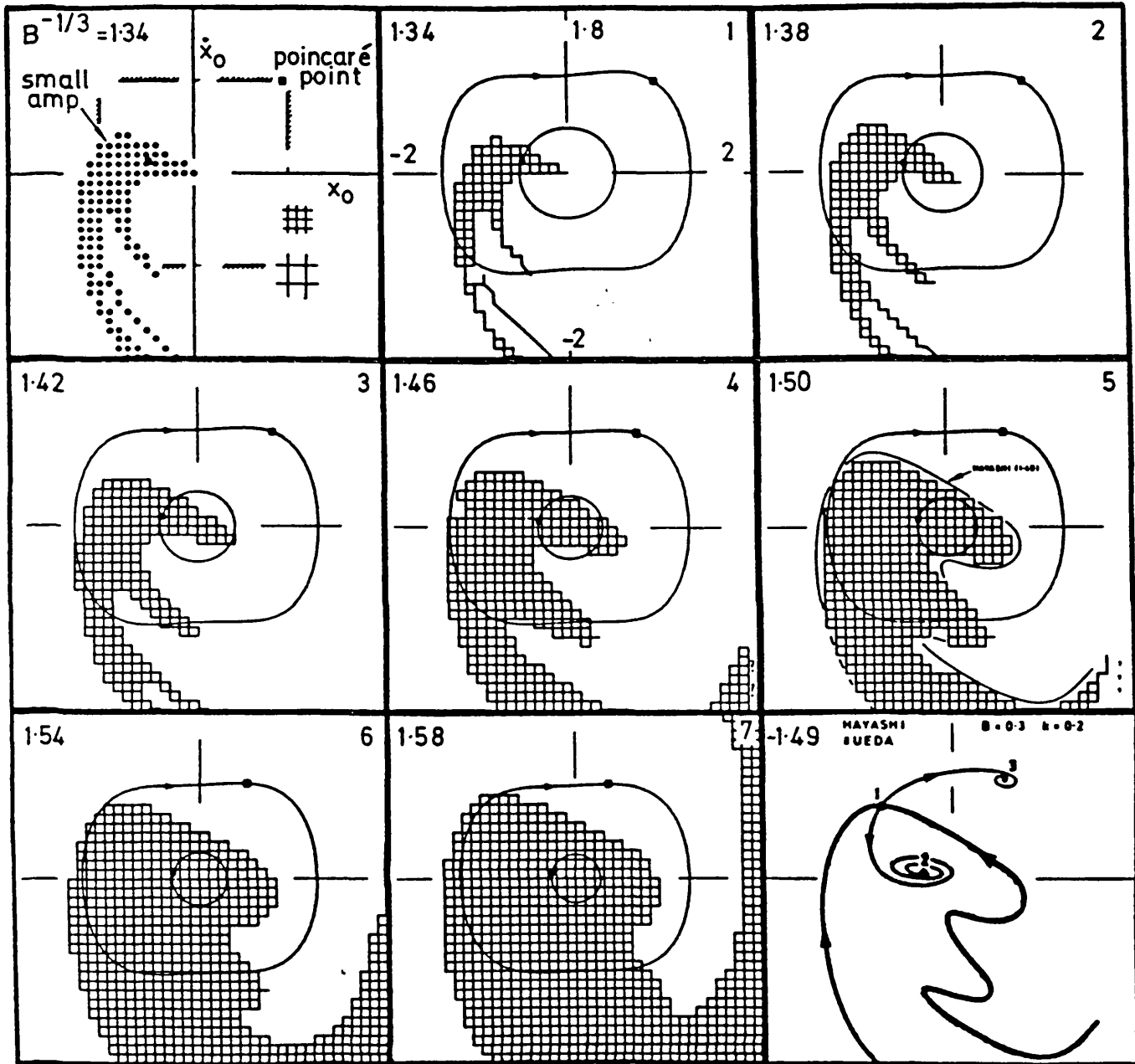
Figure 30. Catchment regions within the hysteresis loop of Ueda's equation as indicated in Figure 29. Analogue simulations are based on a grid of starts.
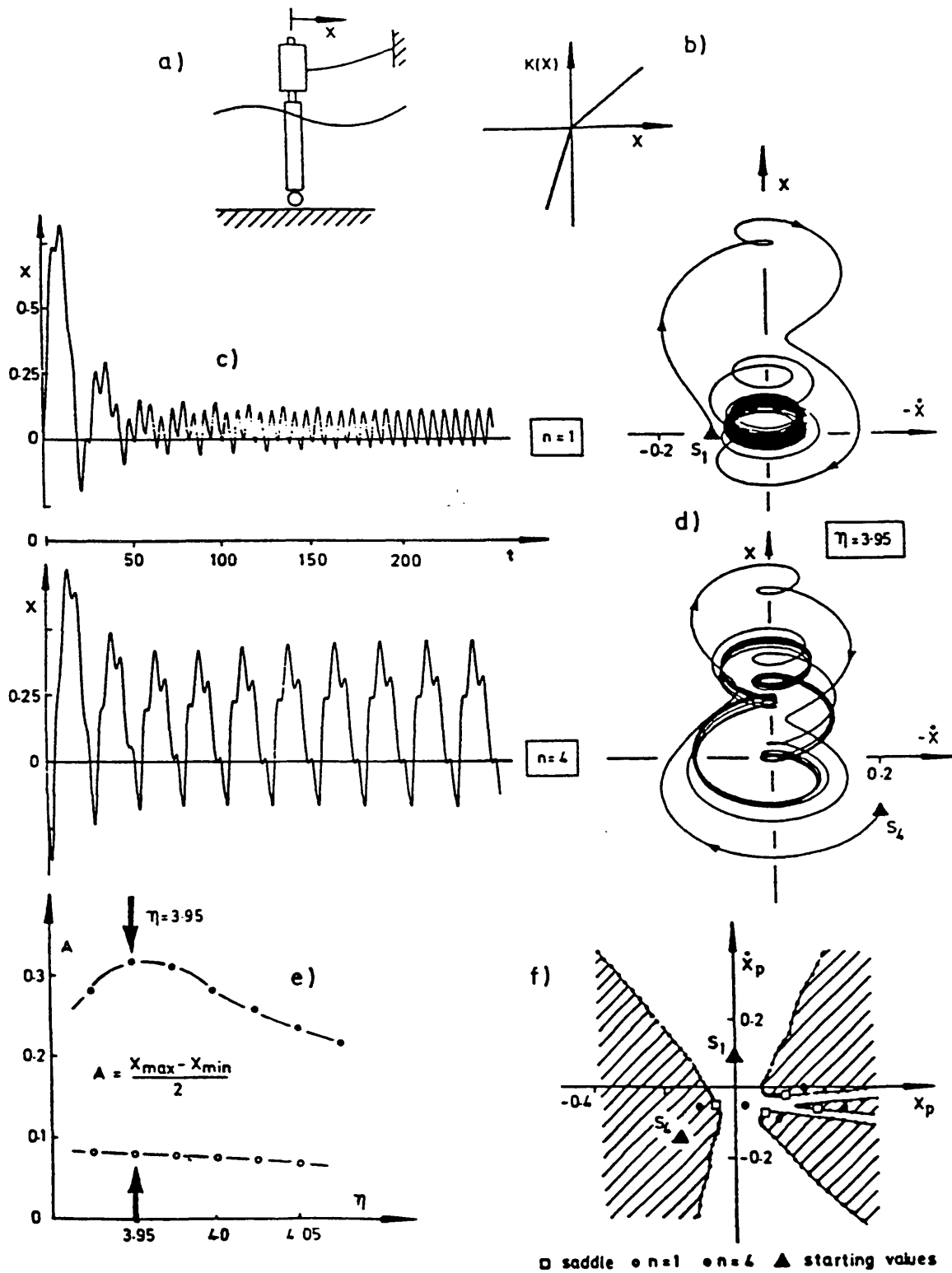
(a) Schematic diagram of the mooring tower.

(b) Stiffness curve illustrating discontinuity at the origin.

(c) Two time histories of displacement using different initial conditions.

(d) Corresponding phase diagrams.

(e) Amplitude response diagram in the neighbourhood of competing n=1 and n=4 response.

(f) Catchment regions for the two co-existing solutions.

- 154 -
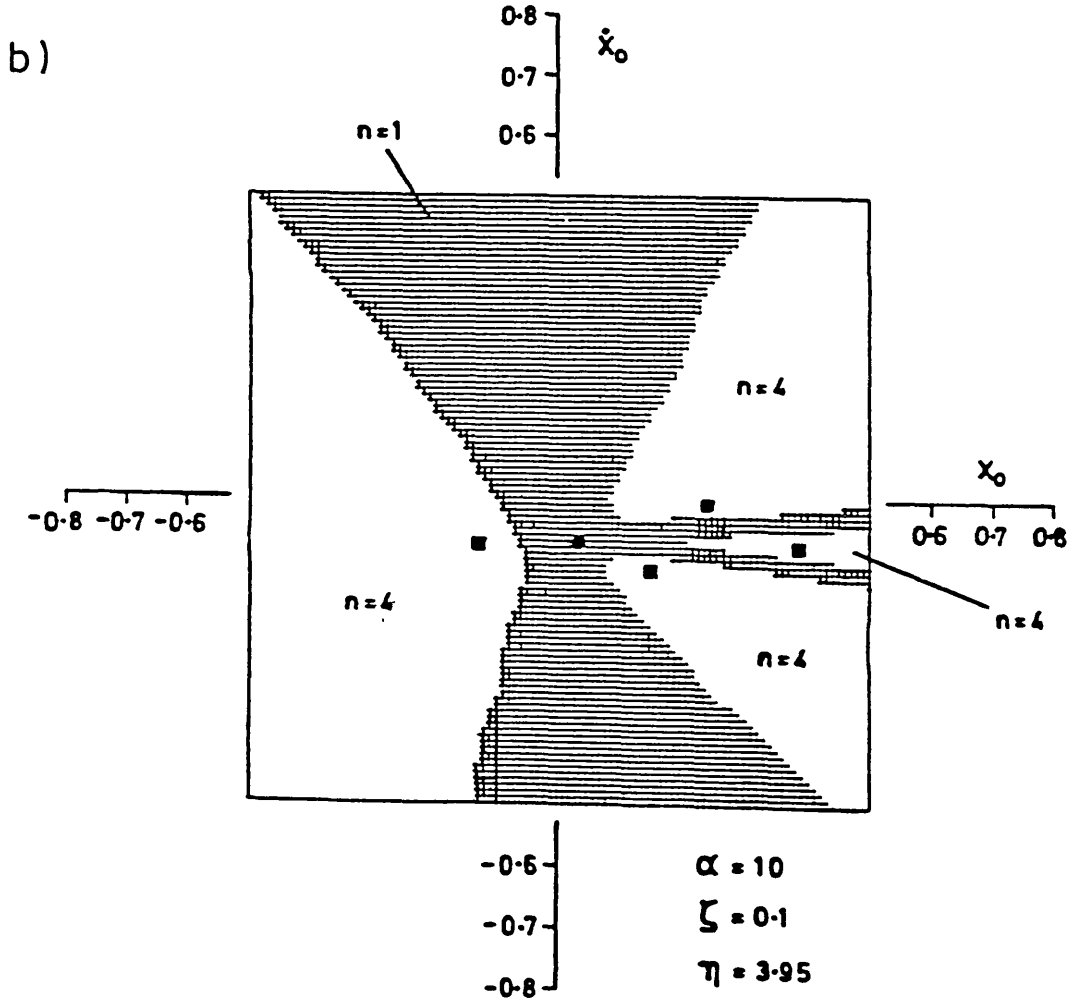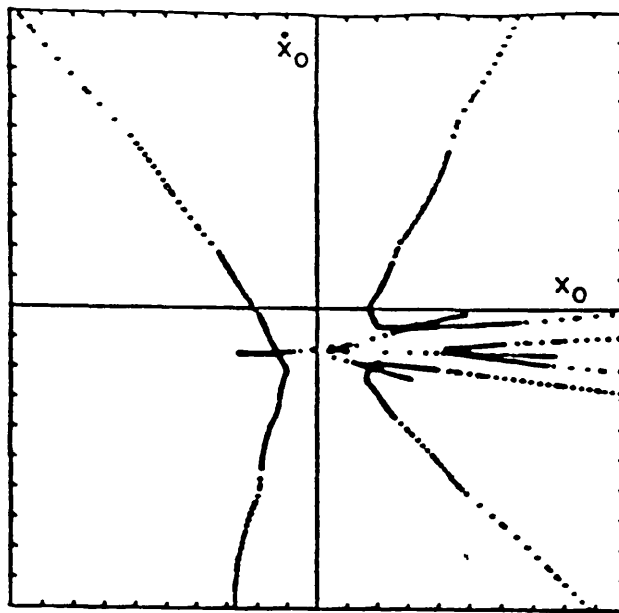
Figure 32. Catchment regions for the n=1 and n=4 solutions for the bilinear oscillator.

(a)   Inset tracing using ladder method.

(b)   Digital simulations base on grid of start technique.
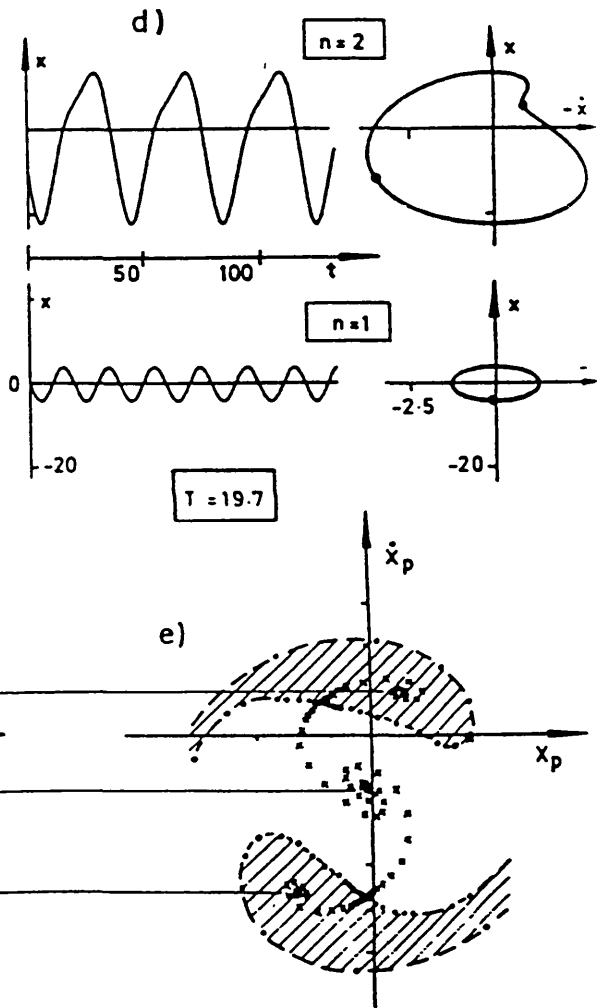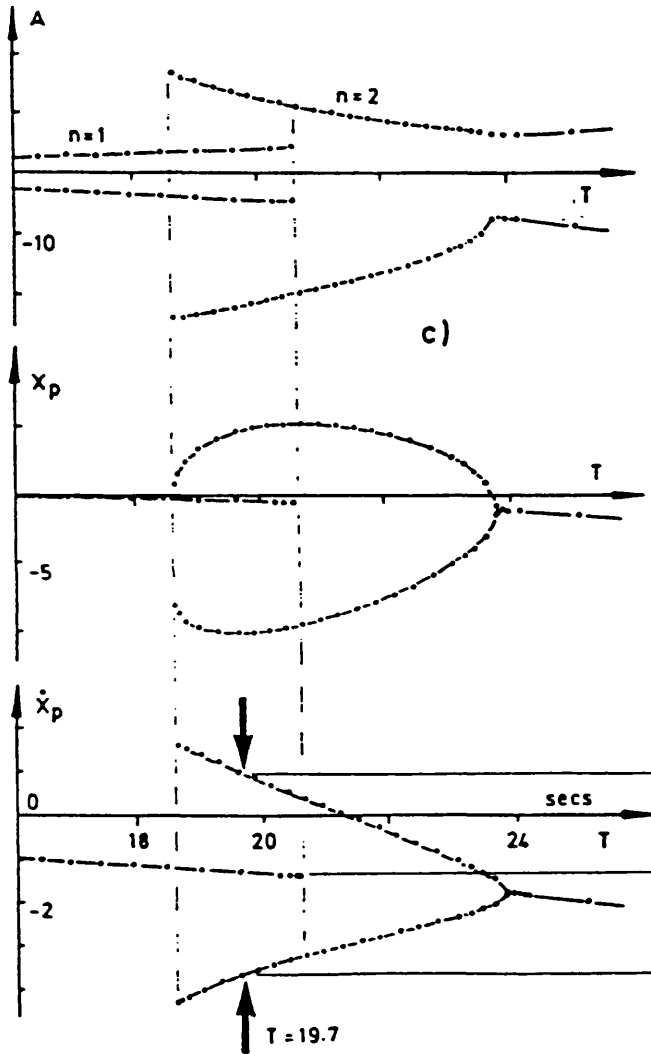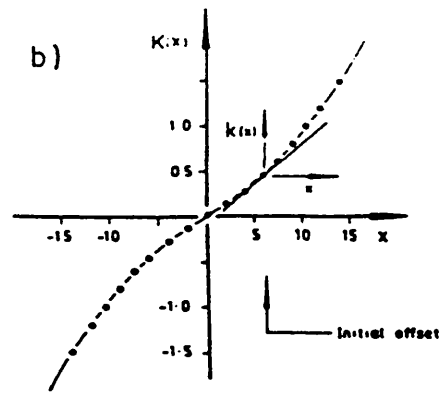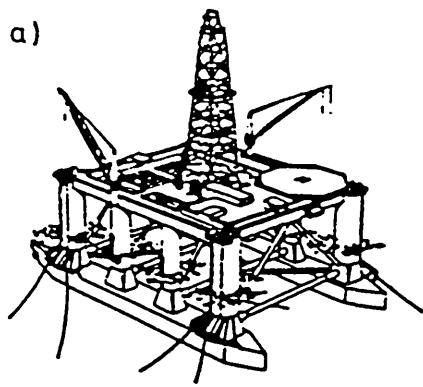
(a) Schematic diagram.

(b) Nonlinear restoring force of the catenary mooring chains.

(c) Maximum amplitudes of motion, displacement and velocity of the Poincaré

points as a function of forcing period illustrating hysteresis.

(d) Two stable steady-state solutions with different initial conditions.

(e) Catchment regions for a wave-period of T=19.7 seconds.
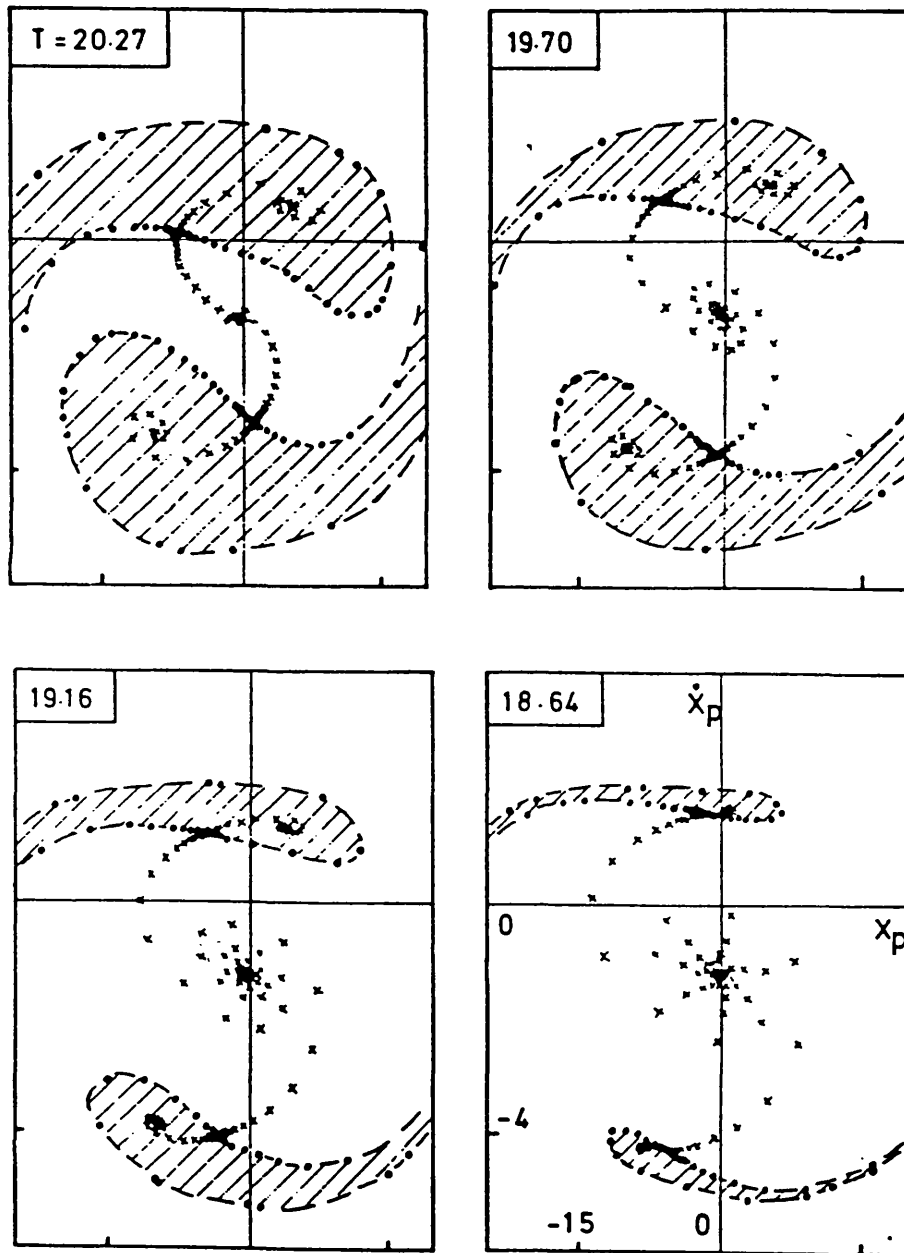
Figure 34. A closer look at the relative dominance of catchment regions during a transition through subharmonic resonance.
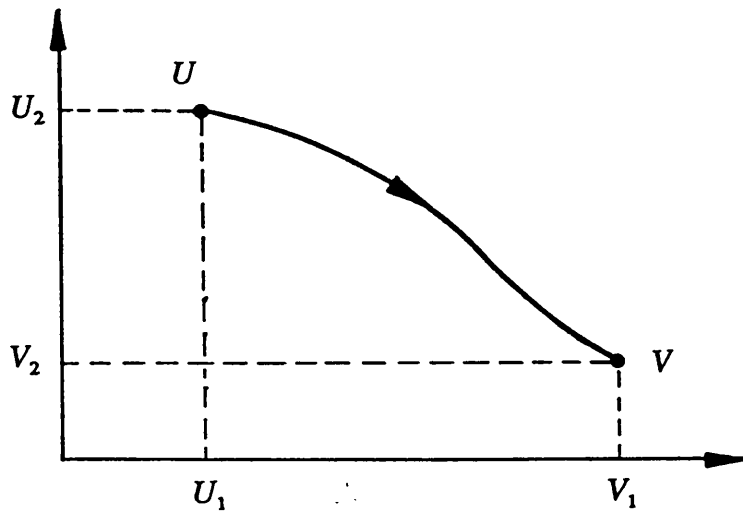
Figure 35a
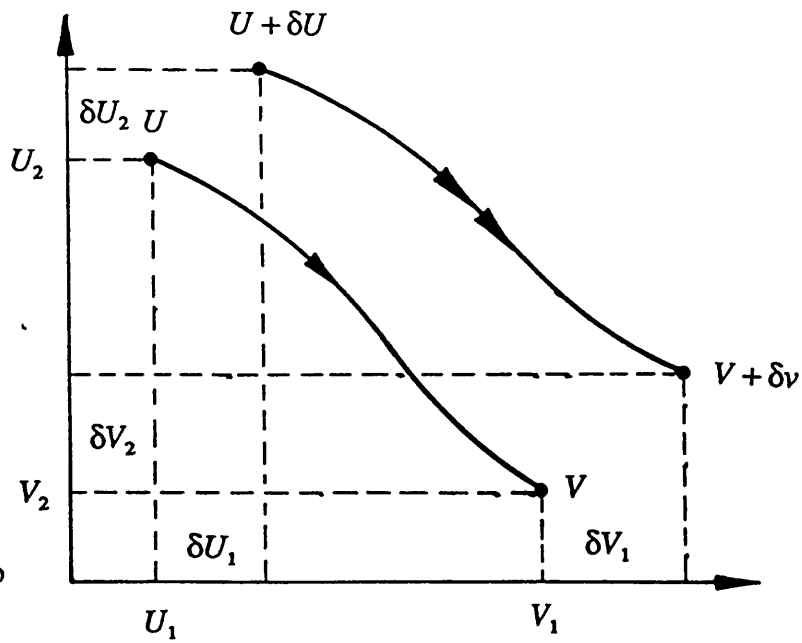
Figure 35b

Poincare map of a point in two-dimensional phase space.

Figure 36a
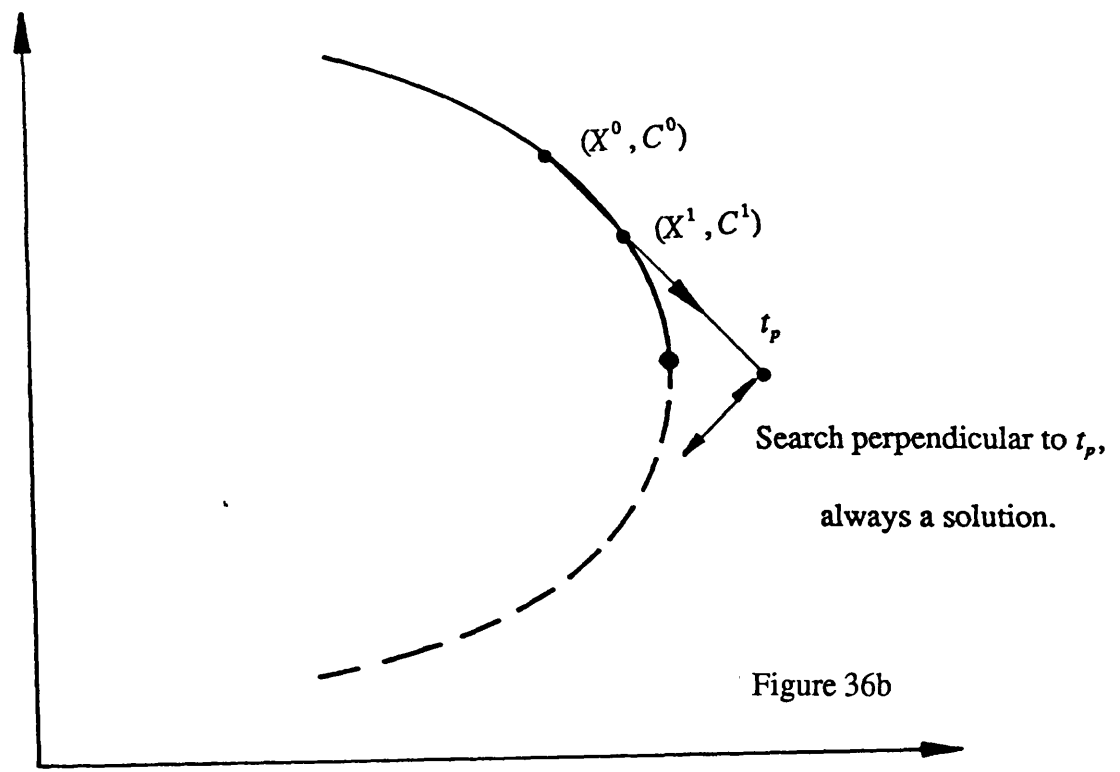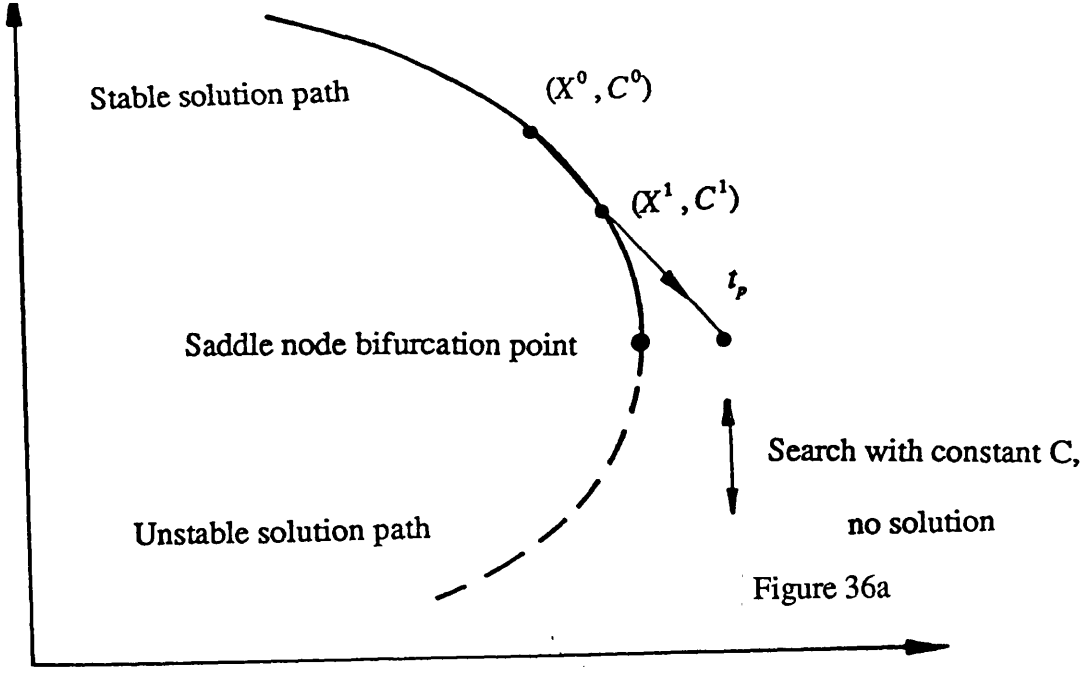
Figure 36b

Schematic diagrams of path following technique.
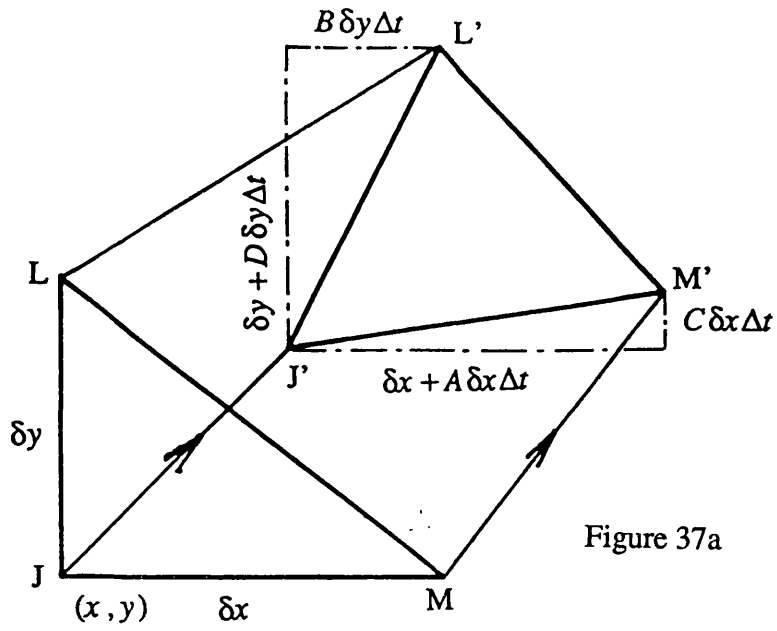
Figure 37a

Rate of change of area in a flow.
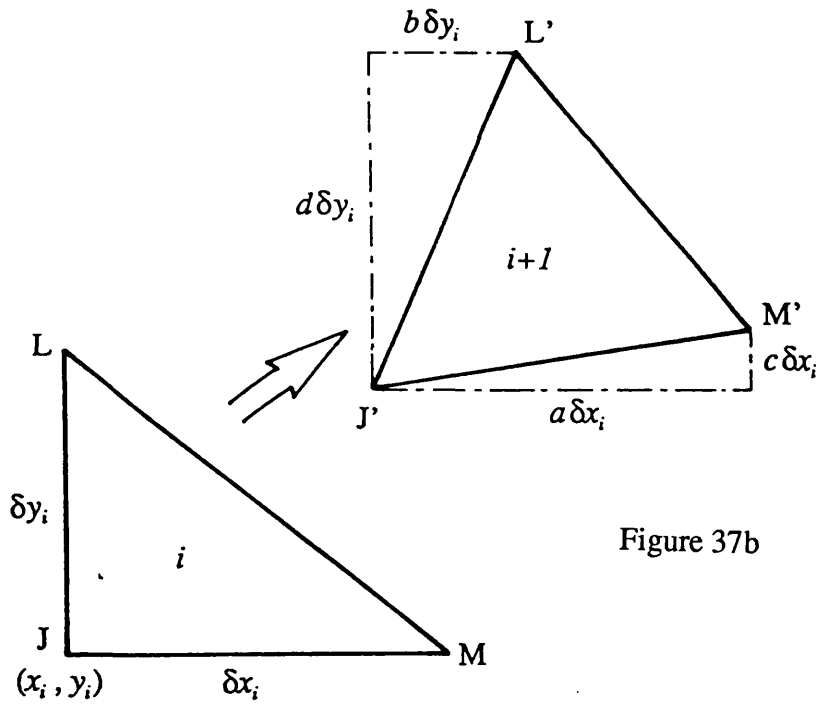
Figure 37b

Rate of change of area in a map.

$$\ddot{x} + \beta\dot{x} + x - x^2 = F \sin \omega t$$
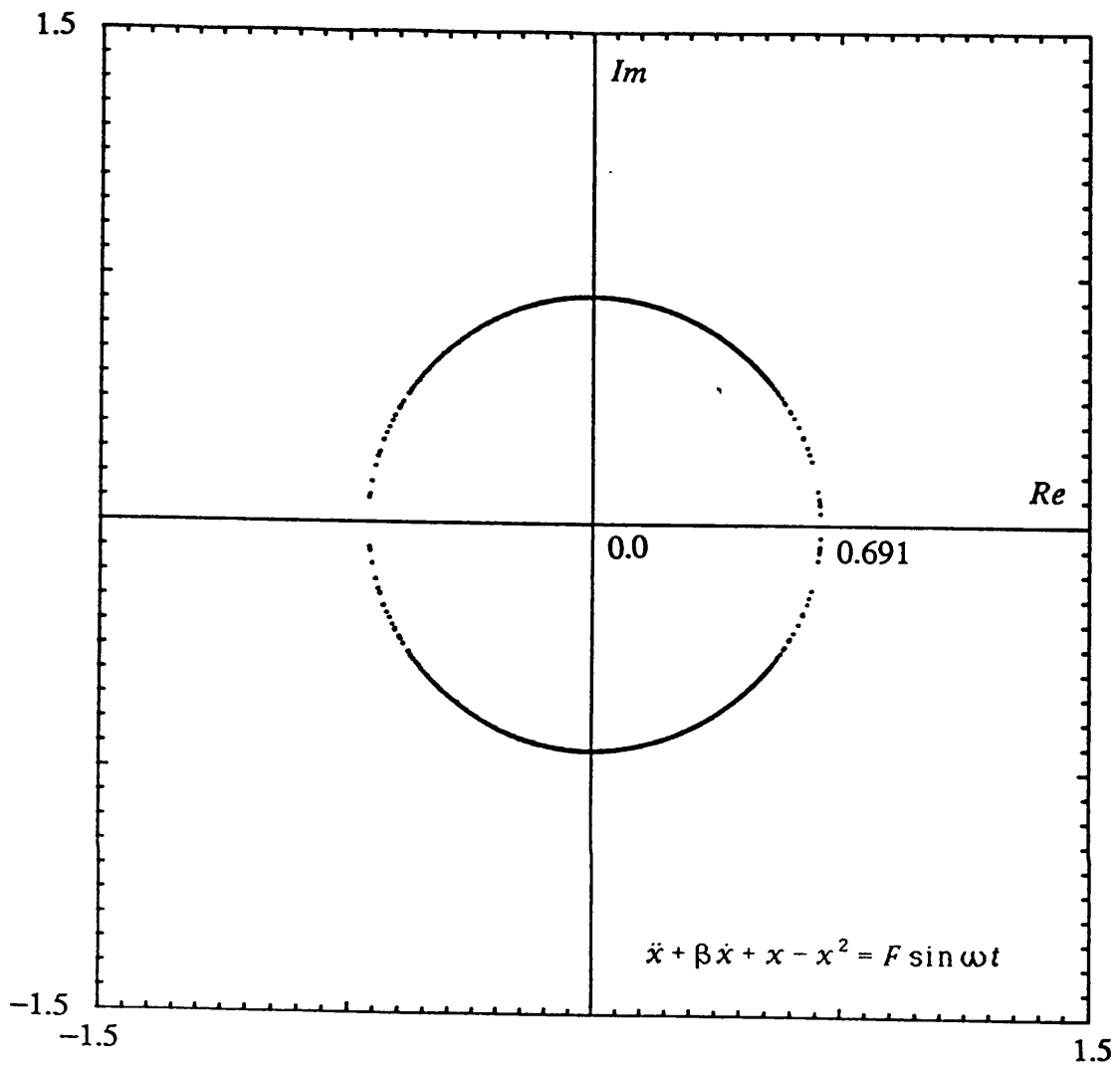
Escape equation $\beta = 0.1$

Figure 38. Path of eigenvalues in the complex plane.

$$\ddot{x} + \beta \dot{x} + x - x^2 = F \sin \omega t$$

Escape equation $\beta = 0.1$

$\omega = 0.4$

$\omega = 0.5$

$\omega = 0.6$

$\omega = 0.7$

F

0.6

−0.6

0.0

0.4
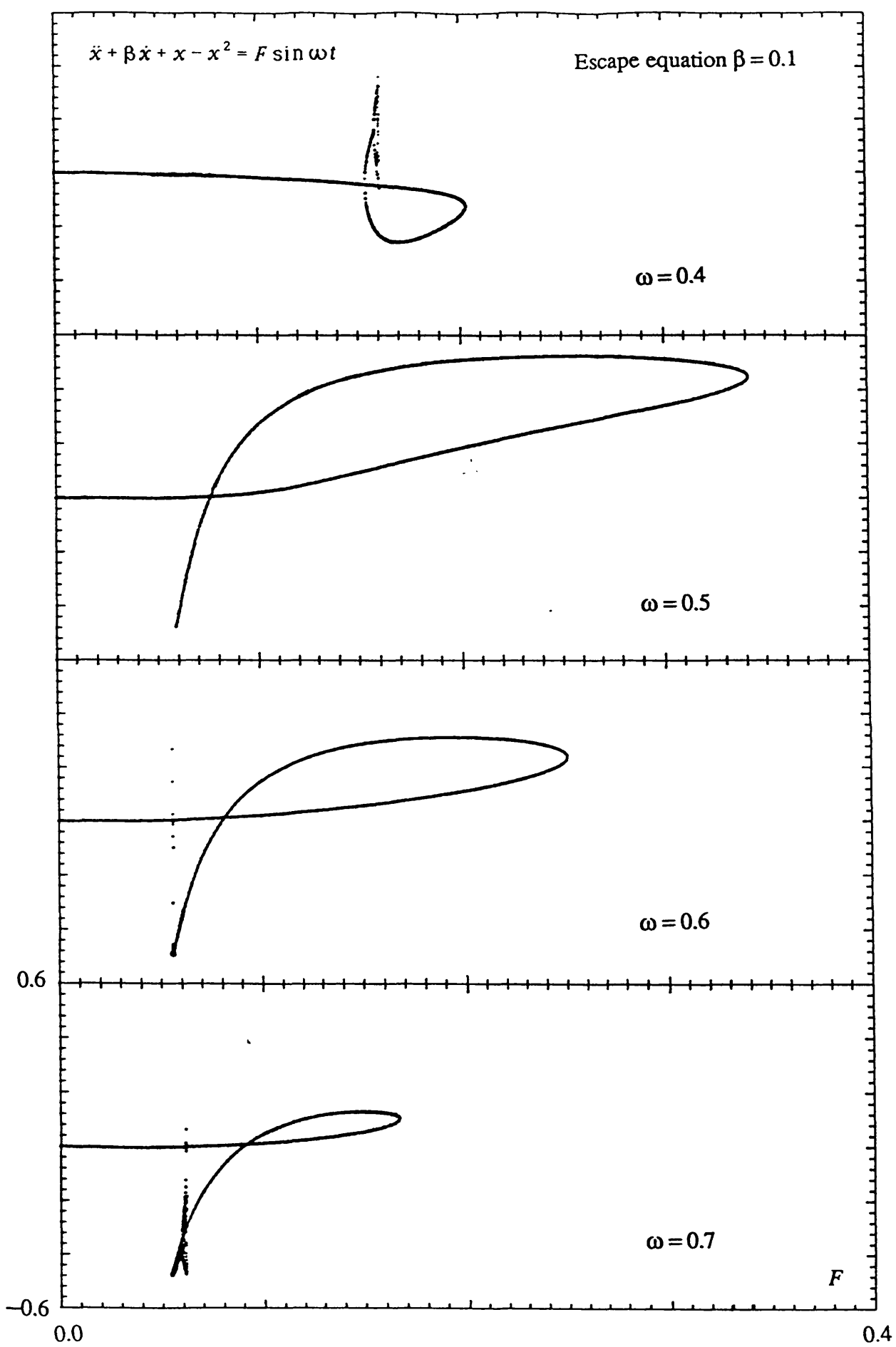
Figure 39. Solutions obtained using path following technique, a.

$$\ddot{x} + \beta\dot{x} + x - x^2 = F\sin\omega t$$

$\omega = 0.3$

Escape equation $\beta = 0.1$

$\omega = 0.35$

$\omega = 0.4$

$\omega = 0.45$

F

0.4

-0.4

0.0

0.3
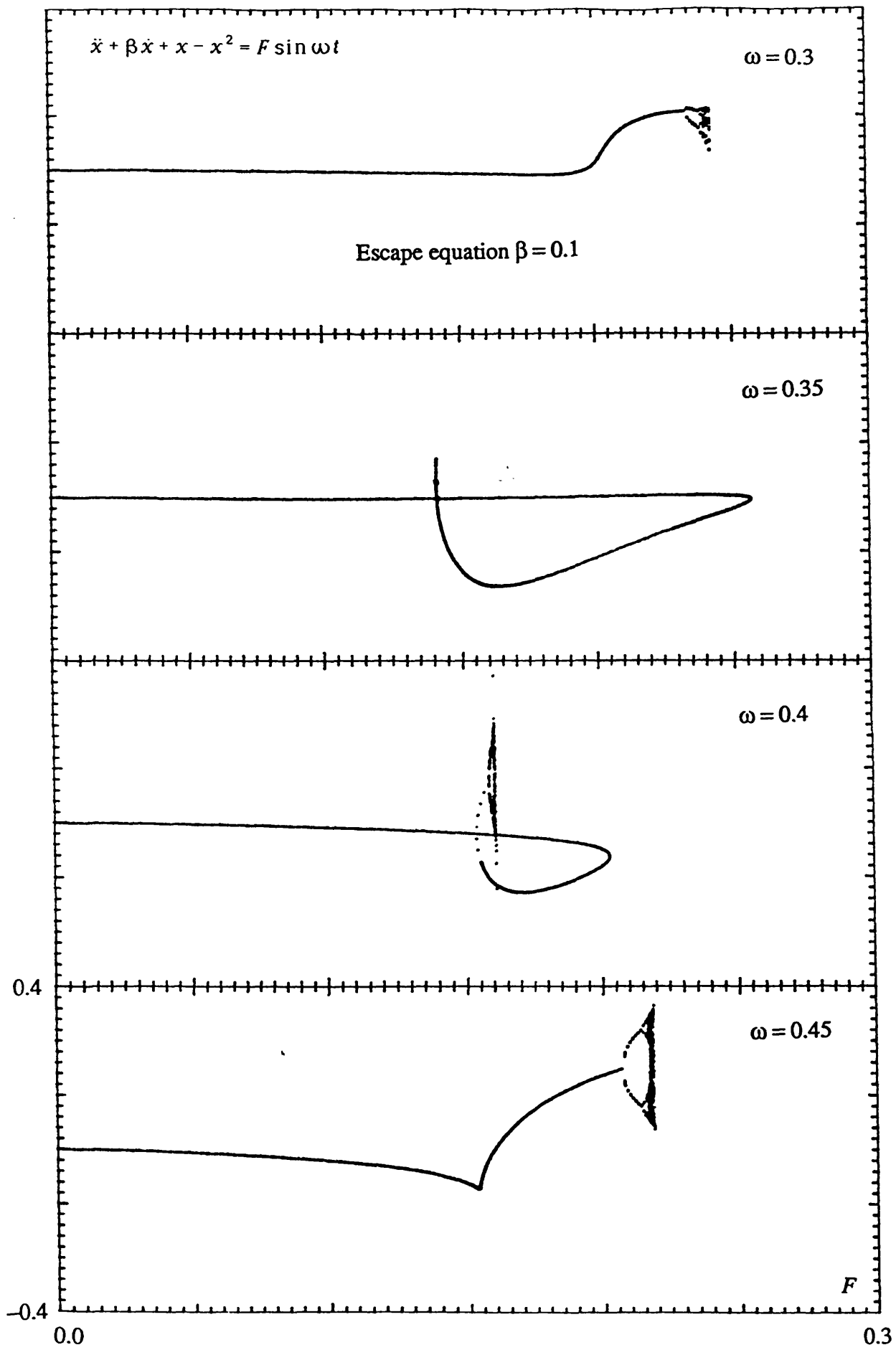
Figure 40. Solutions obtained using path following technique, b.

Figure 41. Schematic diagram of an Articulated Mooring Tower and Floating Vessel.

VESSEL

PROCESS PLANT

TRANSFER HOSE

ARTICULATED MOORING TOWER
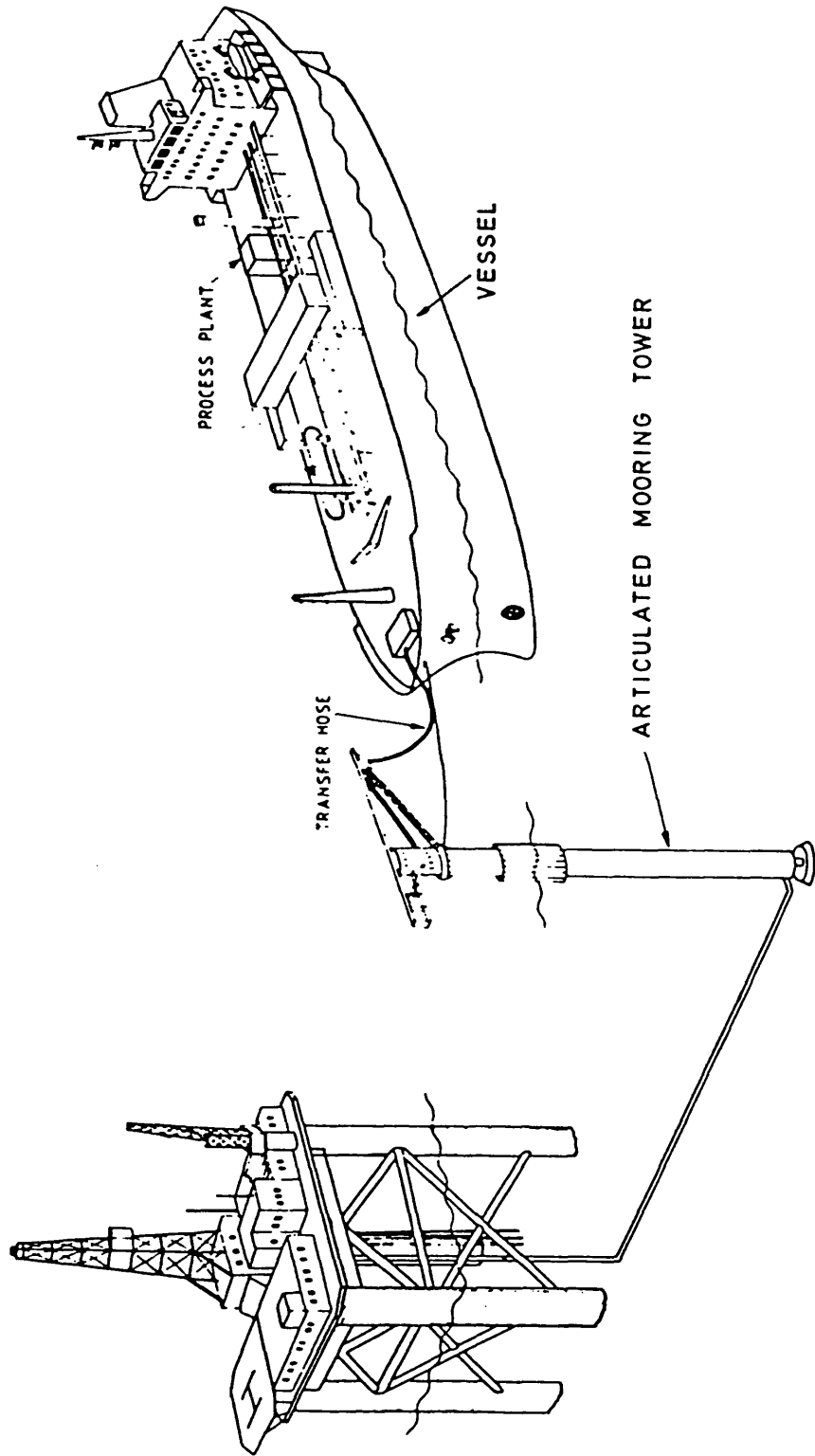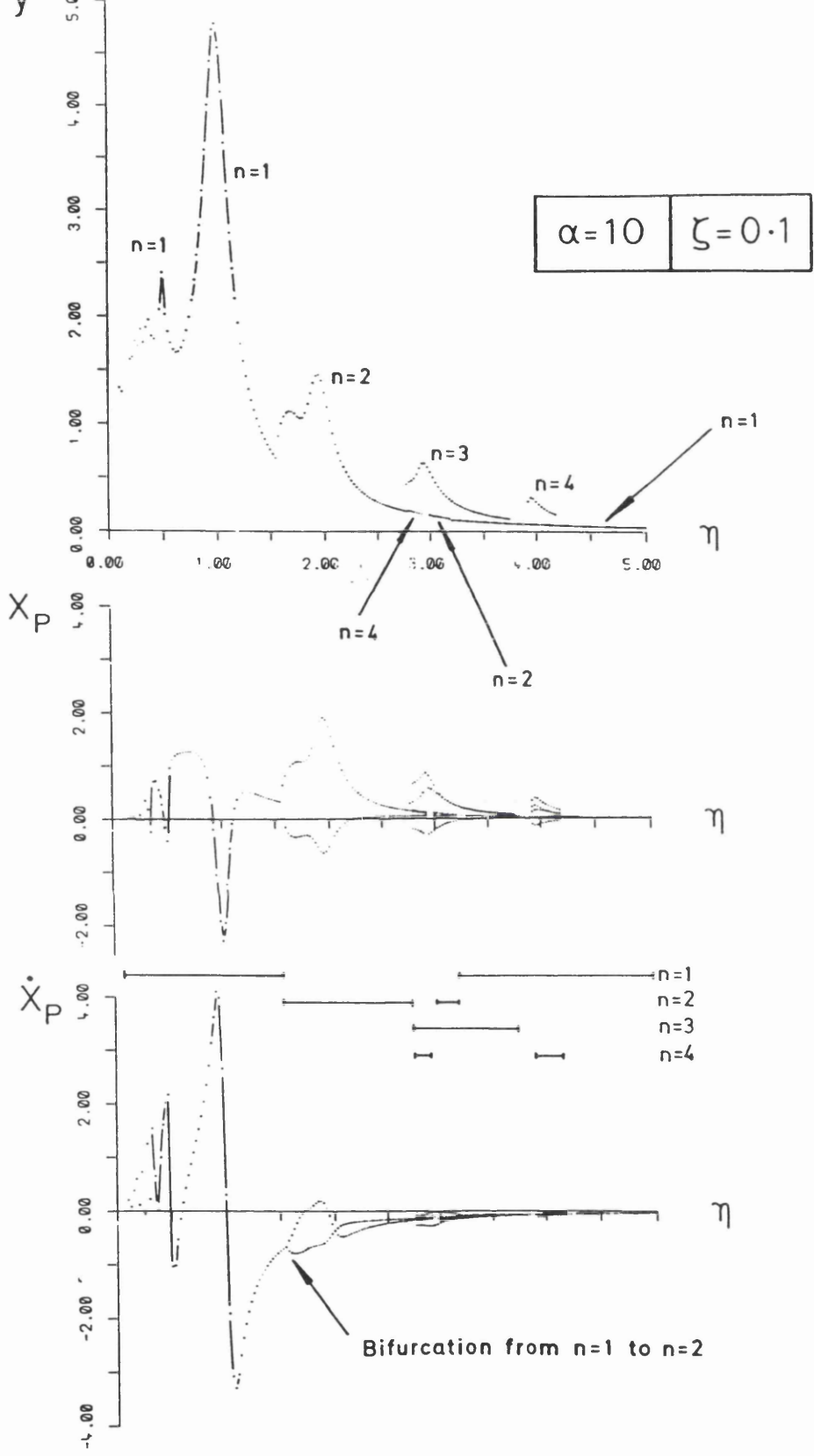
Bilinear Oscillator : α=10 ζ=0.1

Figure 42.   Resonance response diagram of the Bilinear Oscillator.

Figure 43. Poincaré maps of the Bilinear Oscillator.

Bilinear Oscillator : $\alpha=10$ $\zeta=0.1$
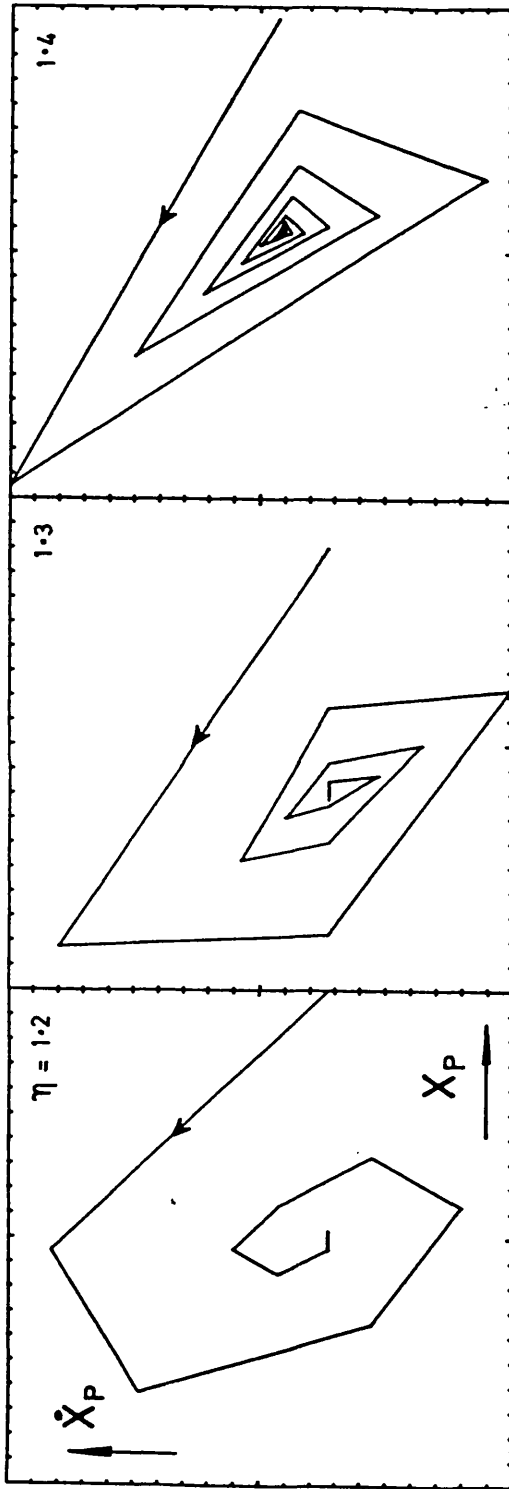
Sample Poincaré maps (all to the same arbitrary scale)
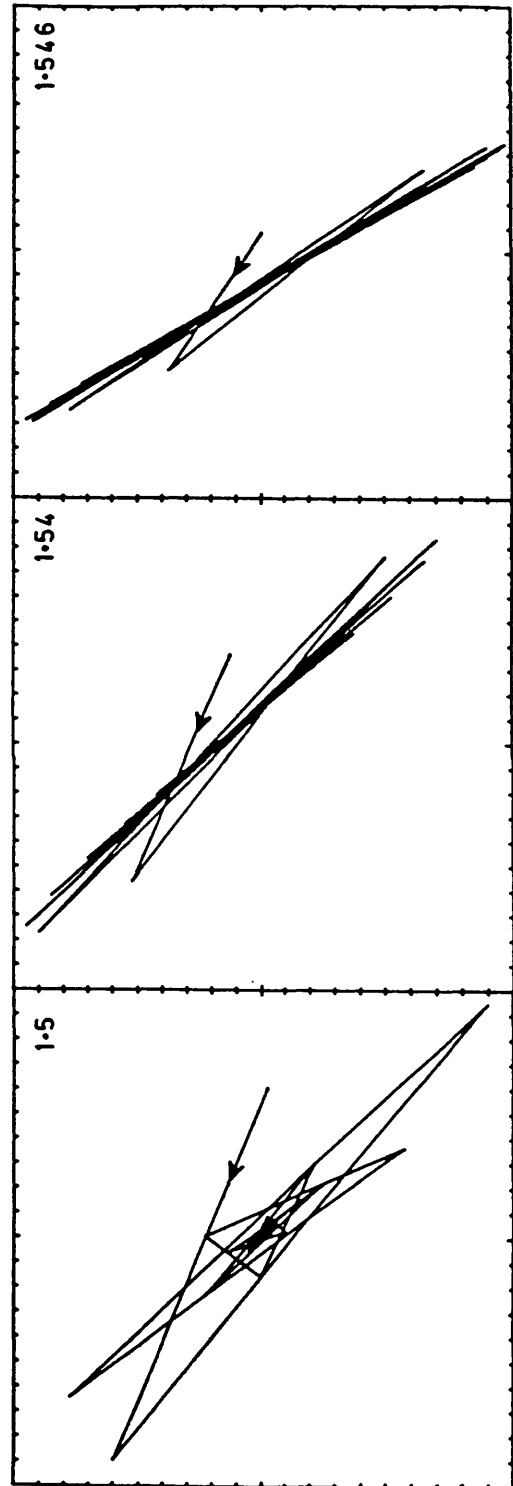
FC

Bilinear Oscillator : α=10 ζ=0.1
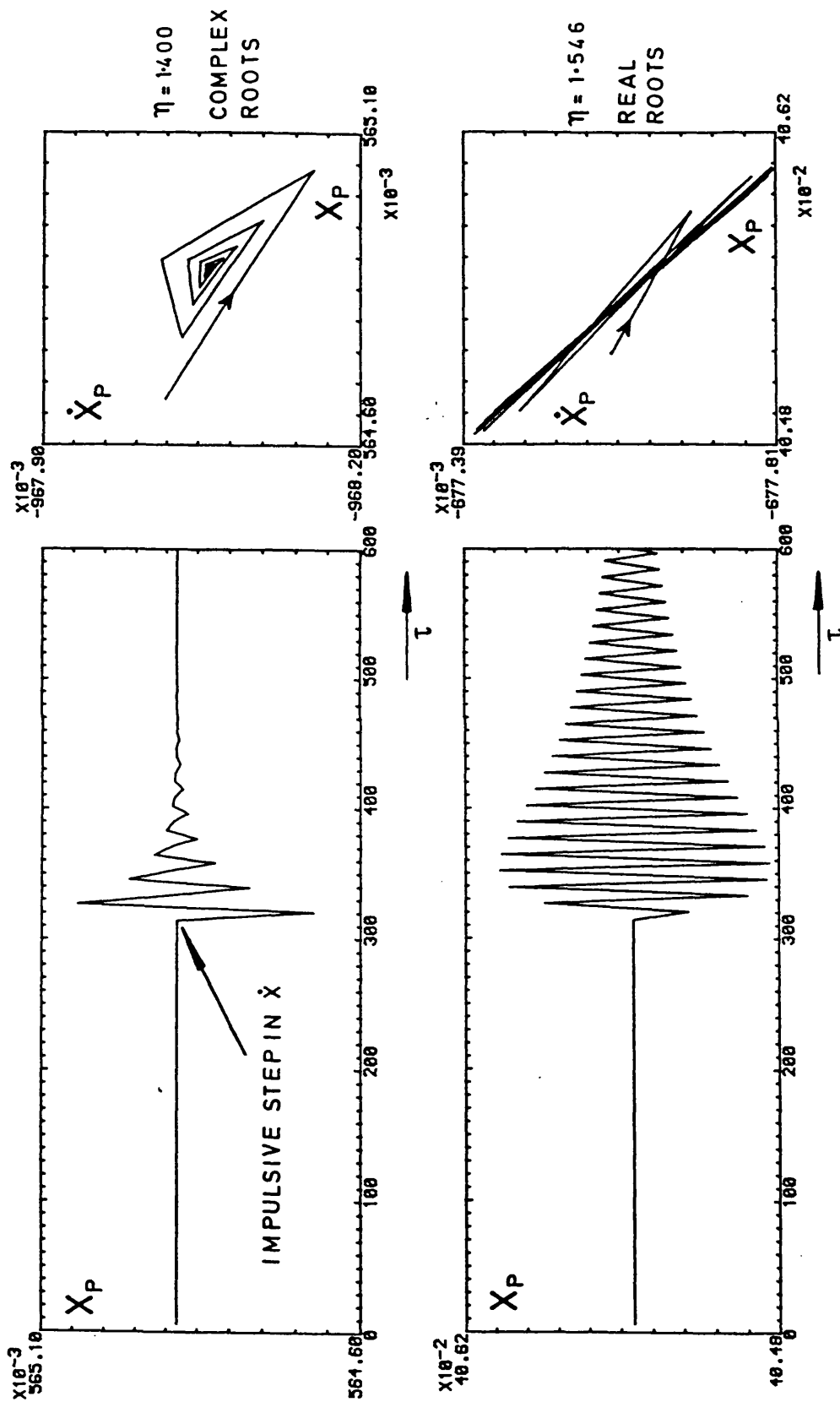
Figure 44. Comparision of two Poincaré maps and their time histories.

FC

- 167 -

Bilinear Oscillator : α=10 ζ=0.1
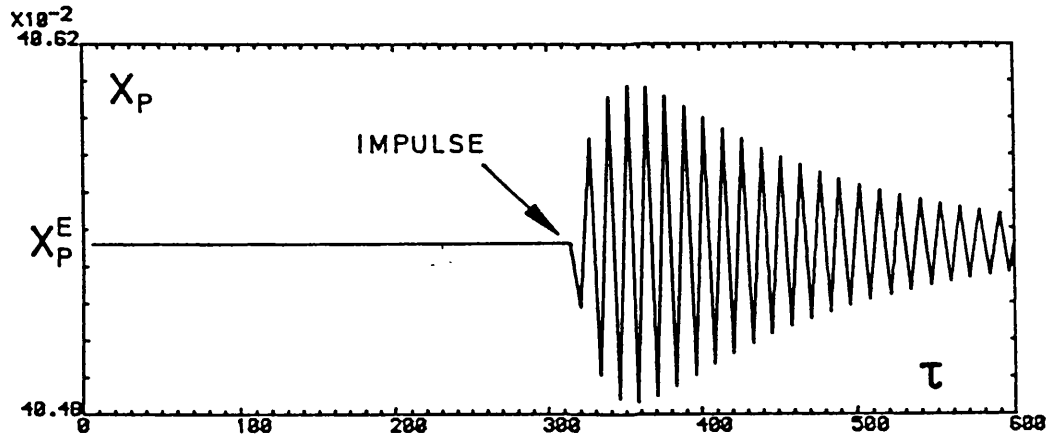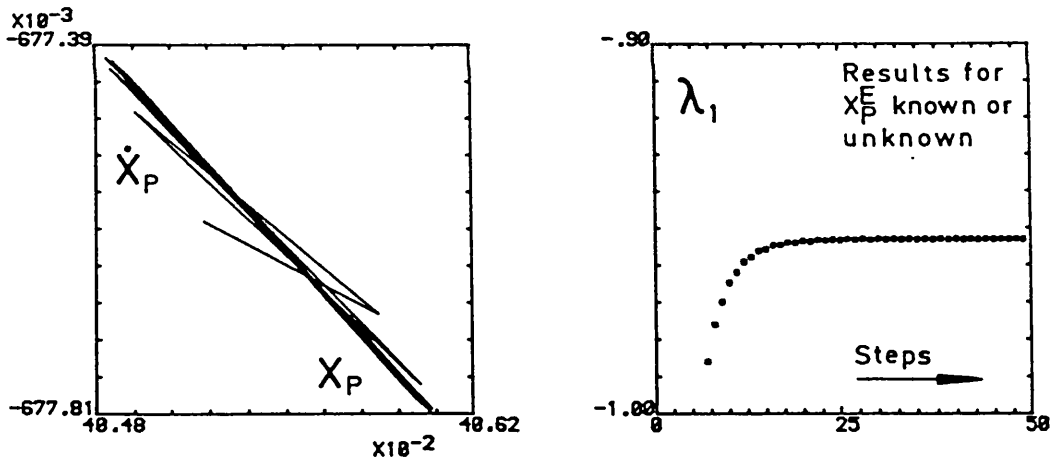
$$\eta = 1{\cdot}546$$

CENTRE MANIFOLD METHOD

$$\lambda_1 = \frac{(X_P - X_P^E)_{i+1}}{(X_P - X_P^E)_i}$$

FC

Figure 45.   Summary of the Centre Manifold technique.
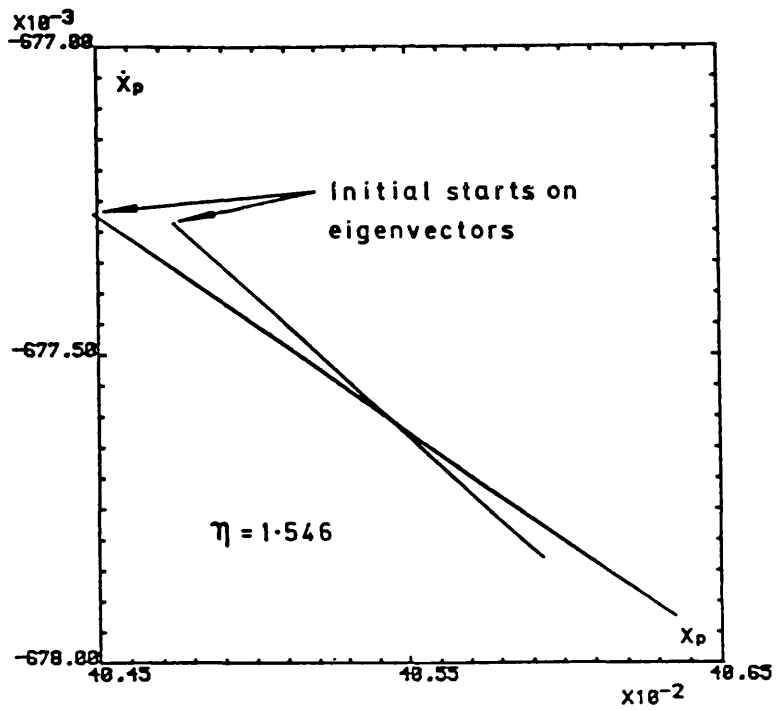
$$\eta = 1.546$$

$$H = \begin{pmatrix} -1.795 & -2.404 \\ 0.3842 & 0.1435 \end{pmatrix}$$

$$\lambda_1 = -0.953$$

$$\lambda_2 = -0.698$$

Figure 46. Numerically calculated eigenvector.

FC

- 169 -

THREE-POINT METHOD FOR LINEAR MAPPING

MATRIX (compared with C.M. results)

Bilinear Oscillator : $\alpha=10$ $\zeta=0.1$ FC
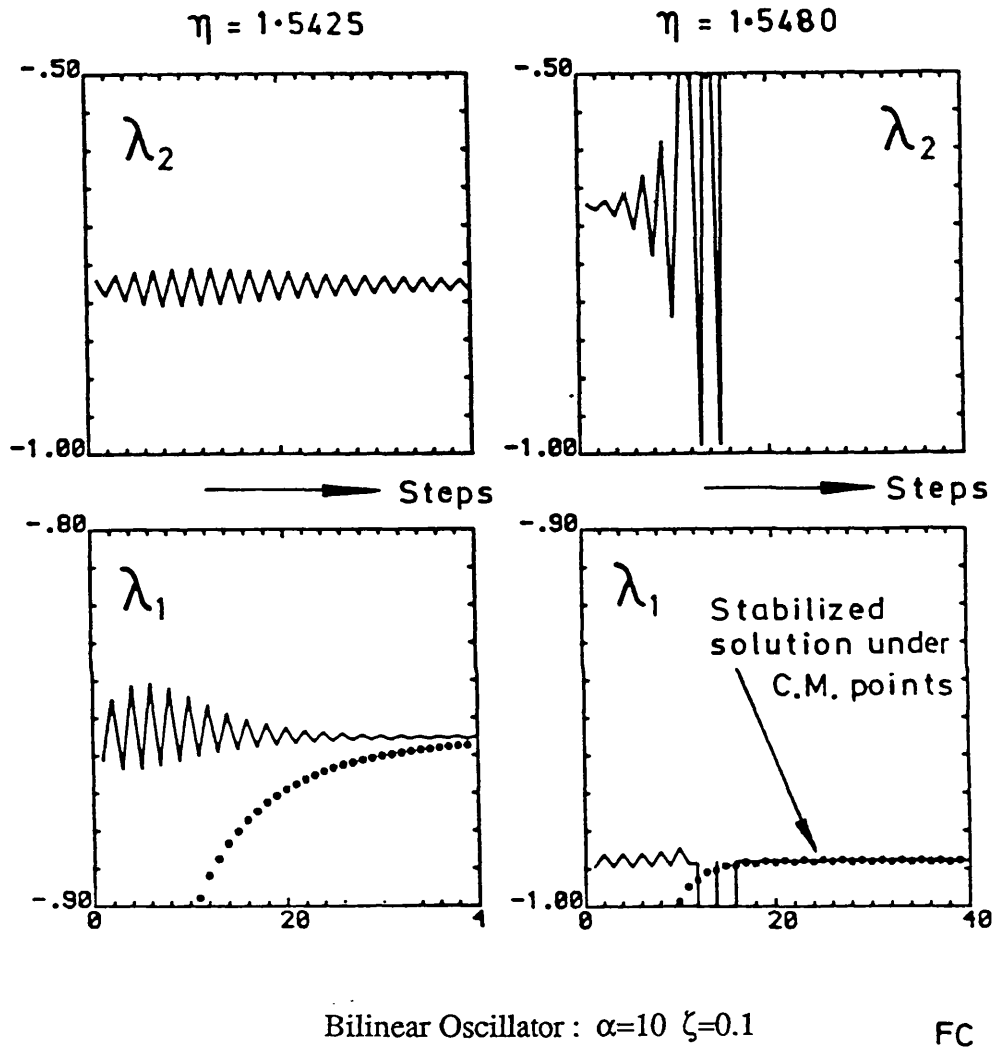
Figure 47. Three-point method for linear mapping matrix.

FOUR-POINT METHOD FOR LINEAR MAPPING
MATRIX AND EQUILIBRIUM FIXED POINT
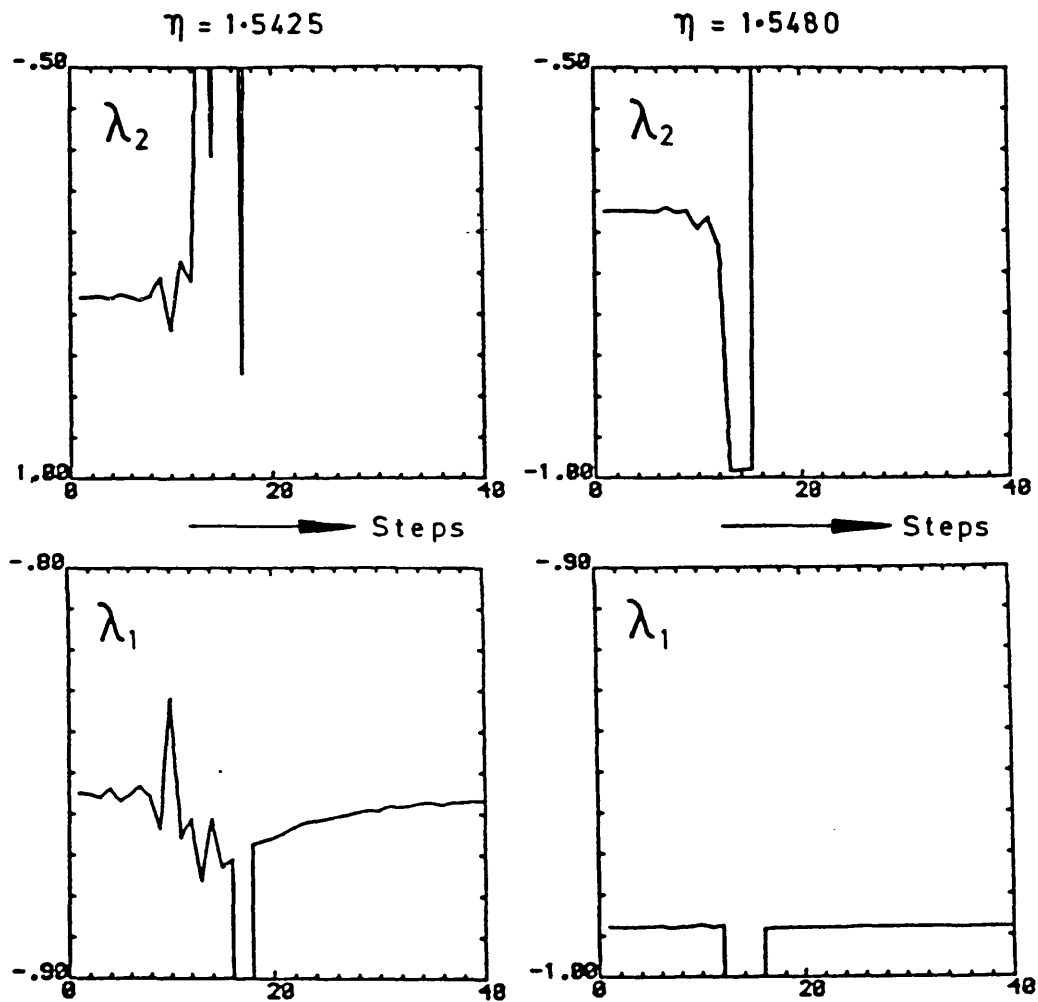
Figure 48. Four-point method for linear mapping matrix and equilibrium fixed point.

RANDOM LOADING for $\eta = 1.546$
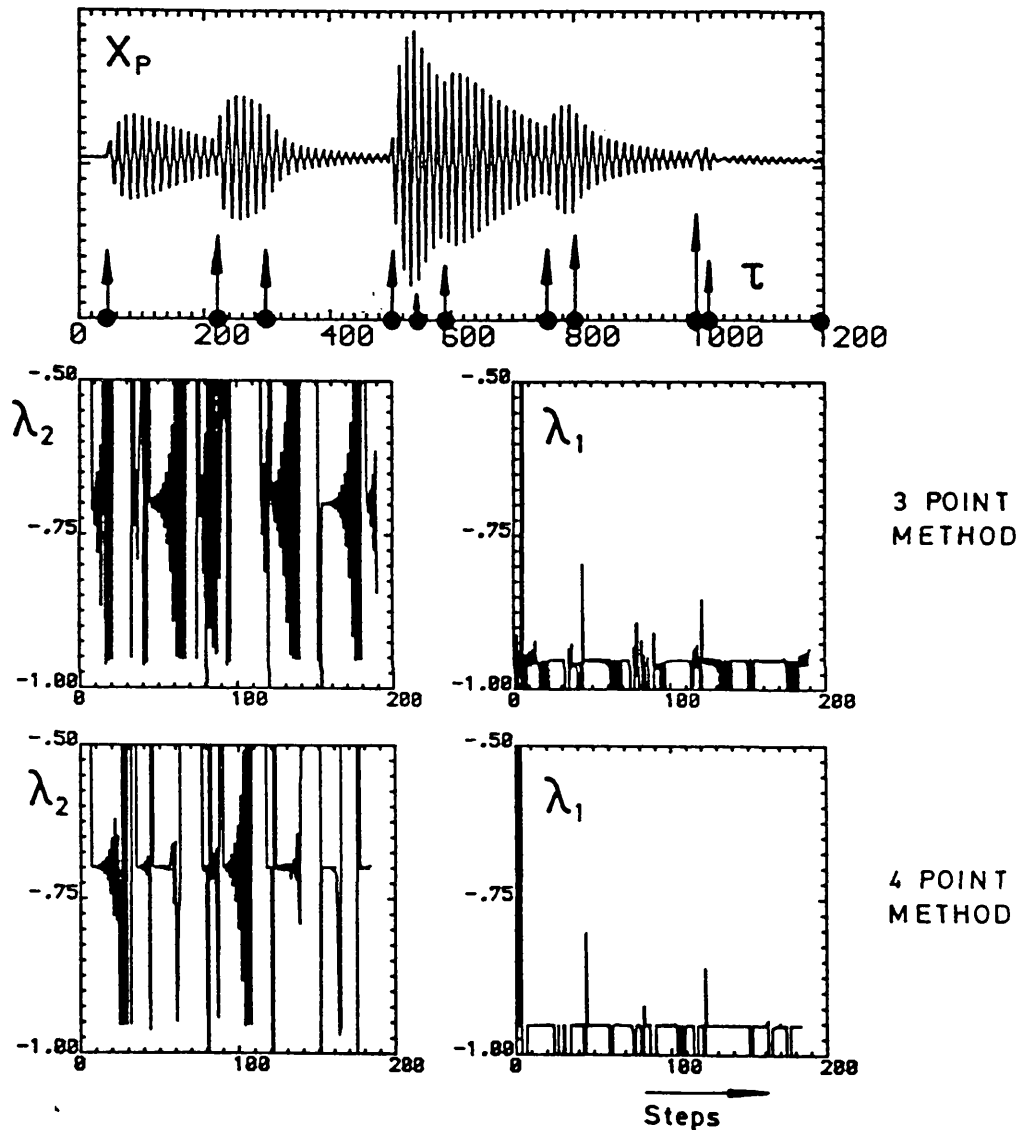
Impulses random in magnitude and timing
Displayed magnitudes are purely schematic

Bilinear Oscillator : $\alpha=10$ $\zeta=0.1$ FC

Figure 49. Impulsive and random loading on the Bilinear Oscillator.

Figure 50. Movement of the eigenvalues on the Complex Plane.
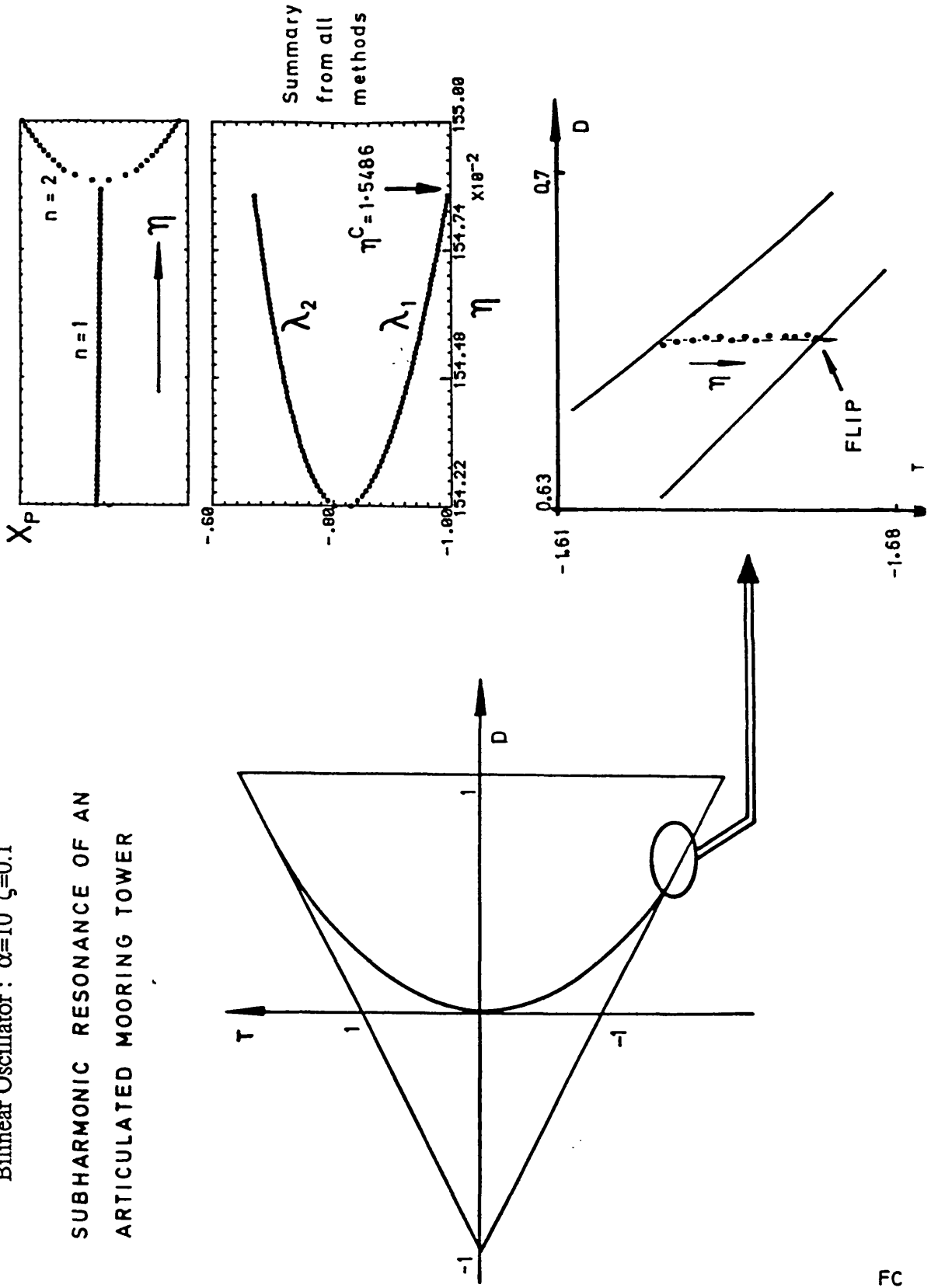
Bilinear Oscillator : $\alpha=10$ $\zeta=0.1$

FOUR-POINT METHOD FOR AN EVOLVING SYSTEM WITH $\eta = \eta_0 + r\tau$

$r = 5 \times 10^{-6}$ $r = 1 \times 10^{-6}$
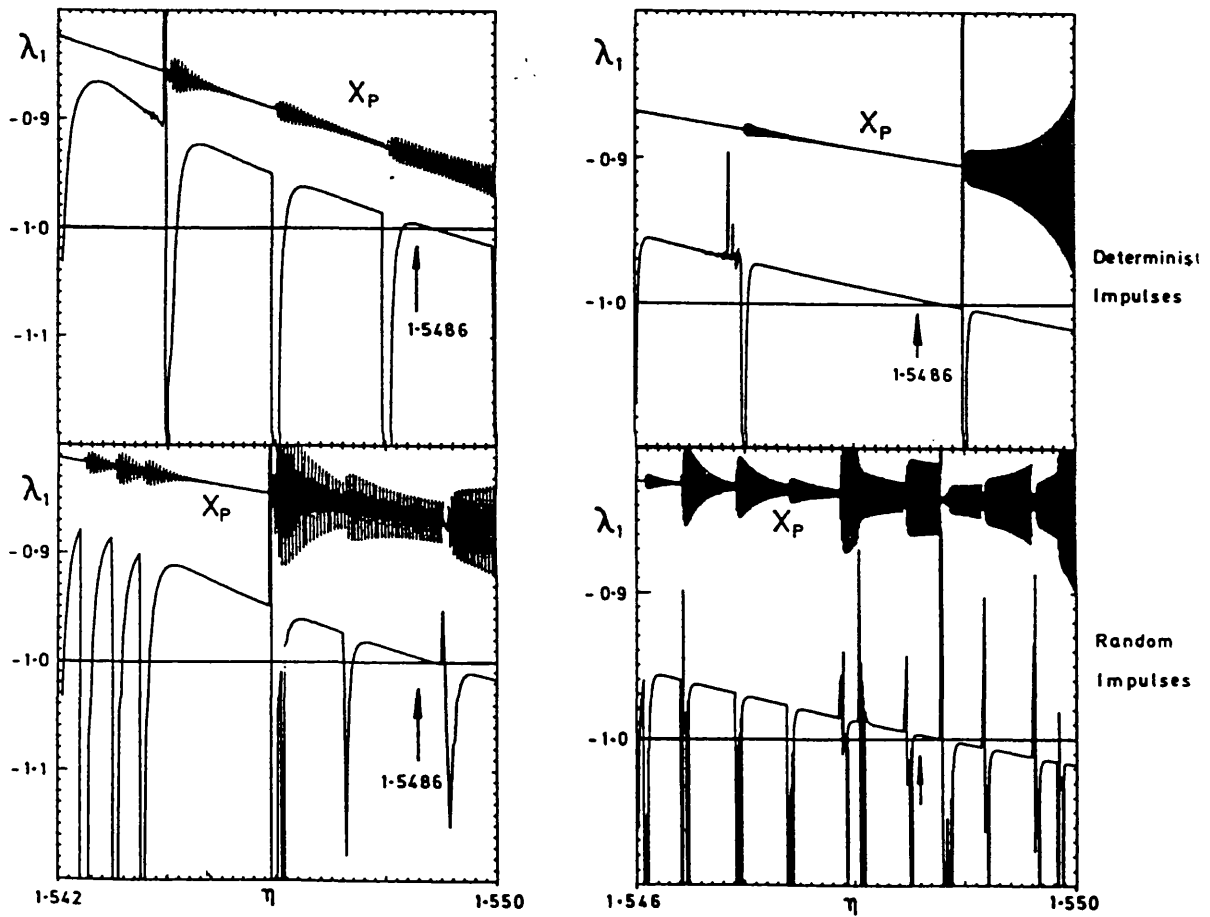
Figure 51. Four-point method for an evolving system.

- 174 -

Figure 52. Schematic diagrams illustrating the differences between two systems with a biased and an unbiased restoring force.
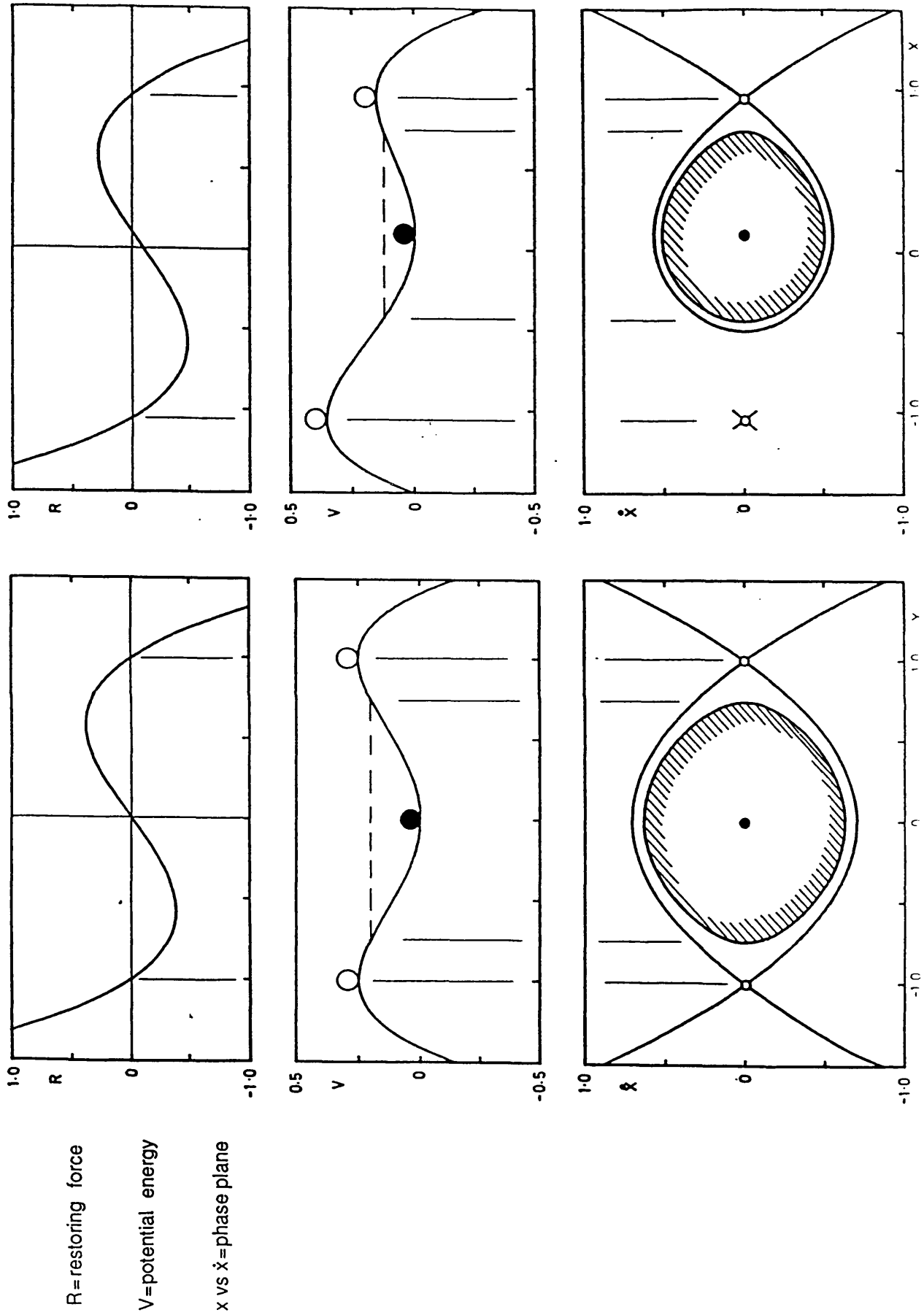
R = restoring force

V = potential energy

x vs ẋ = phase plane

Figure 53. Schematic diagram illustrating the catchment region of the Escape equation.

$$\ddot{x} + \beta\dot{x} + x - x^2 = F\sin\omega t$$

$$V = \tfrac{1}{2}x^2 - \tfrac{1}{3}x^3$$

F = 0   β = 0·1 :———
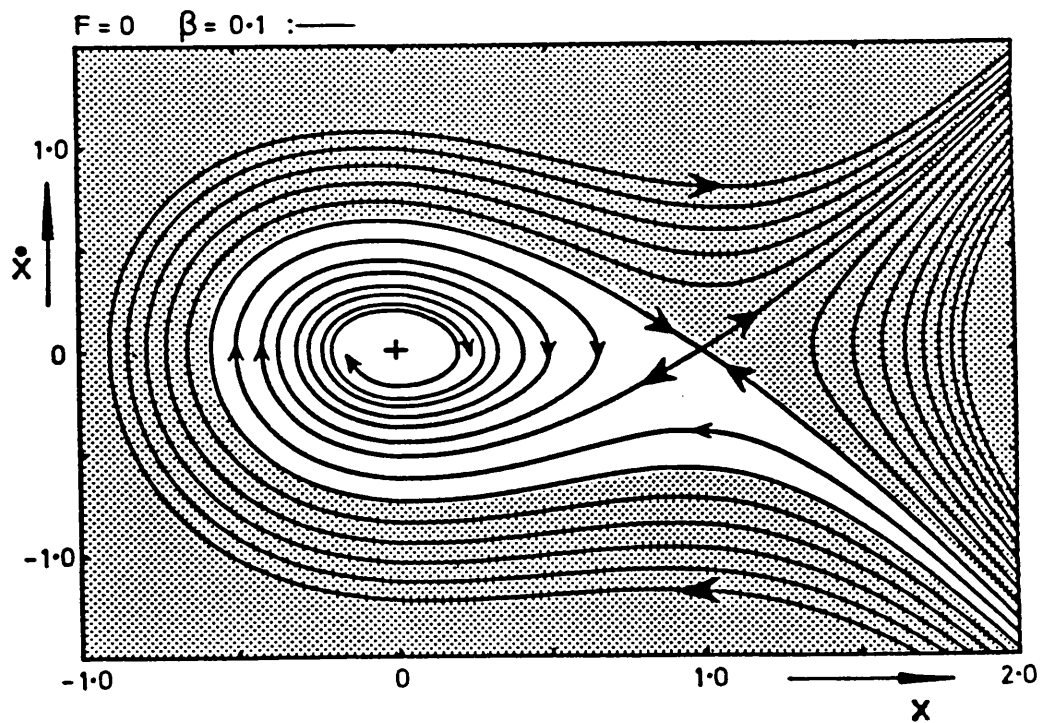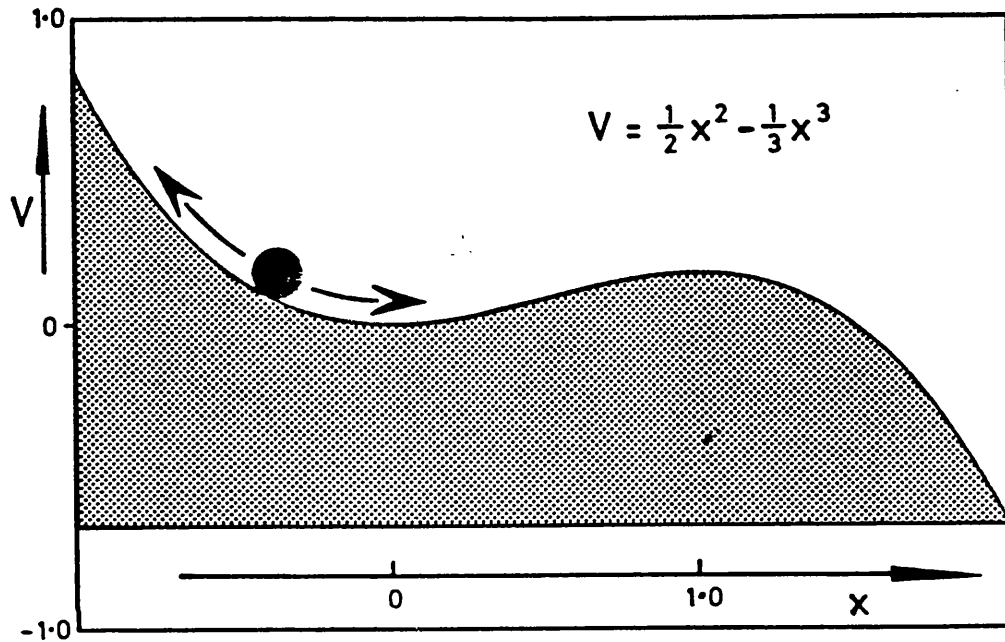
Figure 54. Roll motion time histories under evolving
forcing frequency.

CHAOTIC ESCAPE FROM A WELL $\ddot{x} + \beta\dot{x} + x - x^2 = F\sin\omega t$ $F = \alpha + \gamma t$ $\zeta = \beta/2$ $A = x_{MAX}$ Saddle at $x = 1$ A:170

$\beta = 0.1$ $\alpha = 0$ $\gamma = 5 \cdot 10^{-5}$ $x_0 = \dot{x}_0 = 0$ Fourth order Runge-Kutta: 20 steps per forcing cycle   RUN: Escape (E)

- 177 -
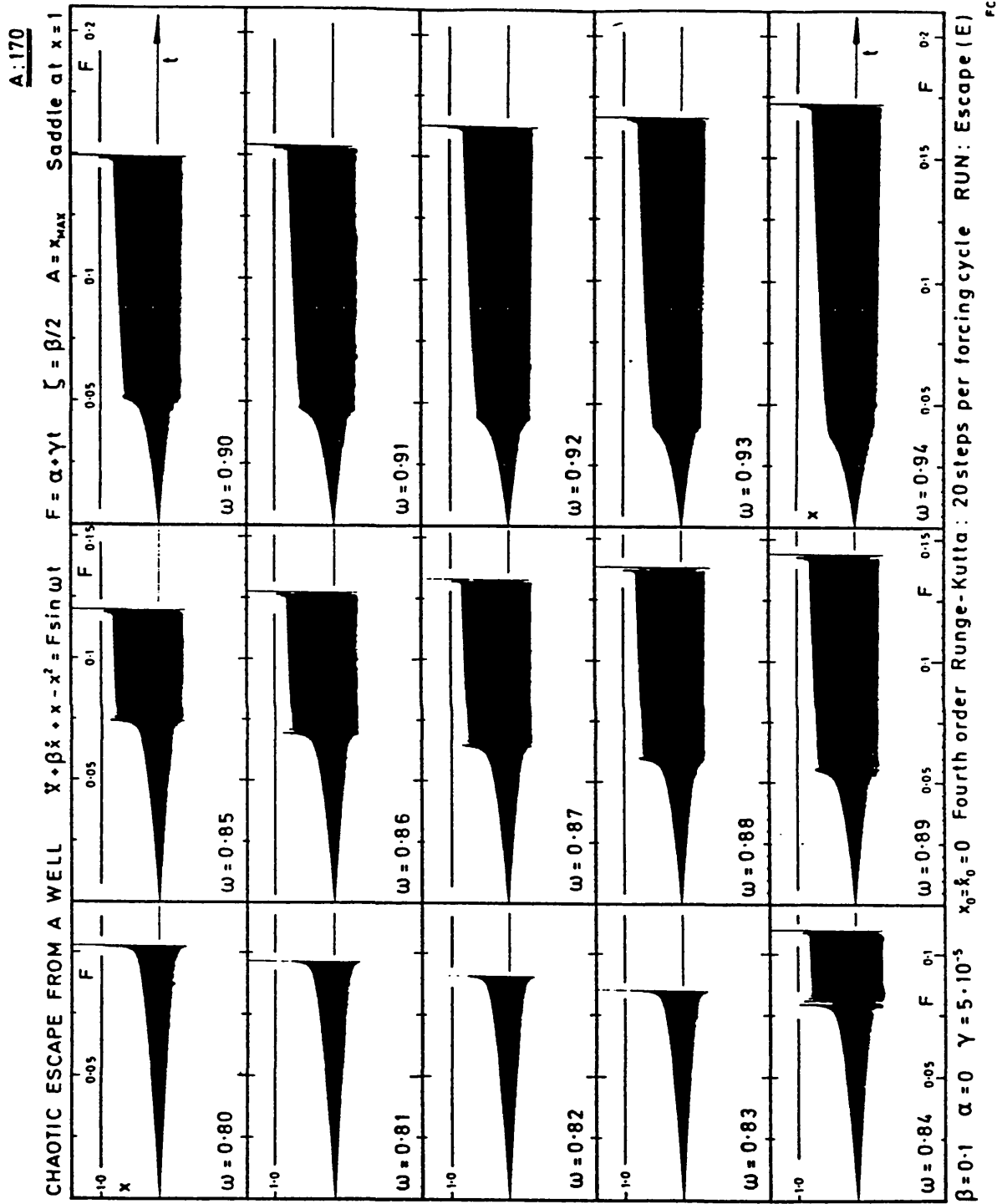
Figure 55. Chaotic escape from a well $\beta = 0.1, \Delta F = 0.001$
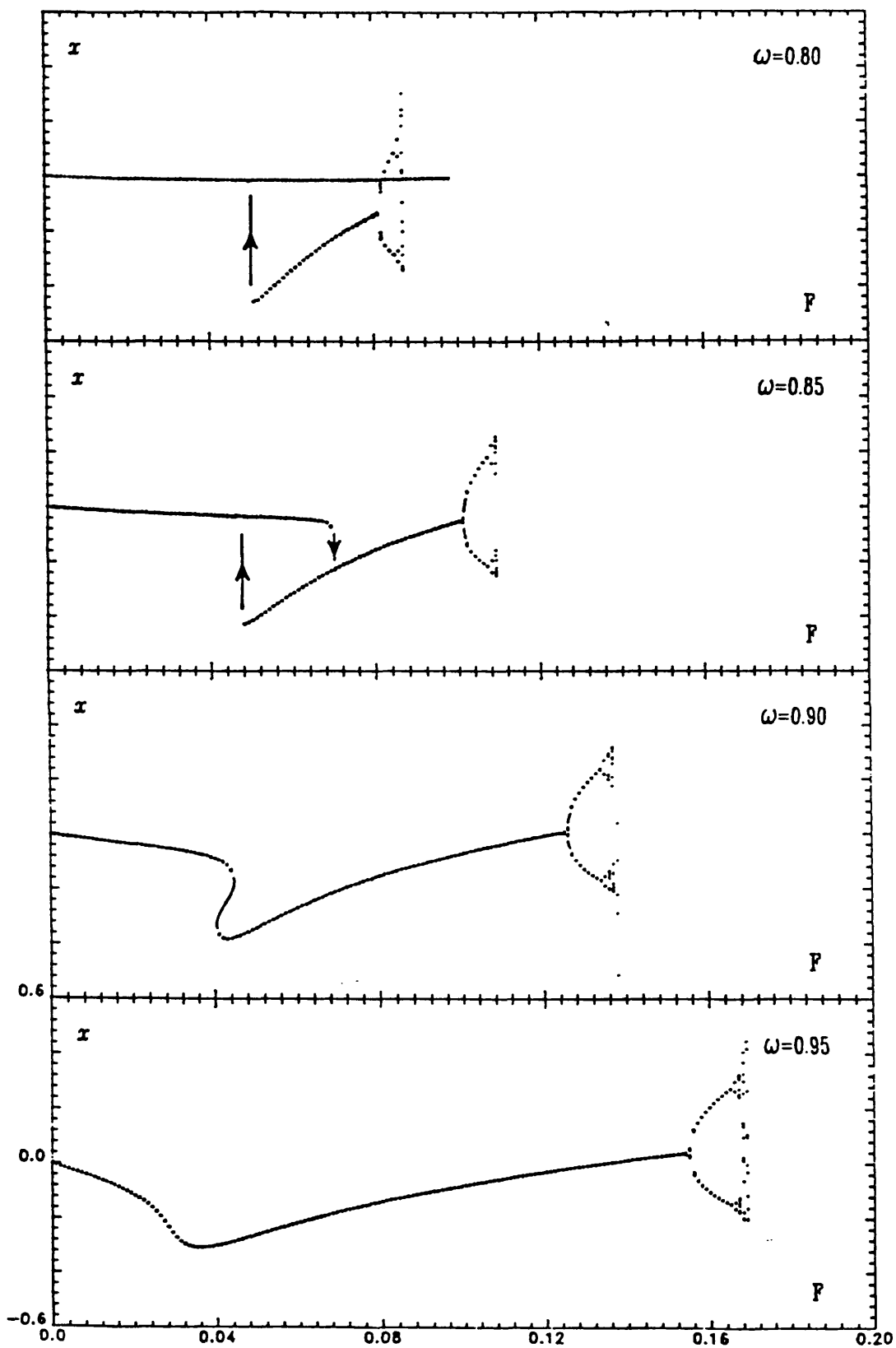
FC

Figure 56. Poincaré response diagram of the Escape equation.
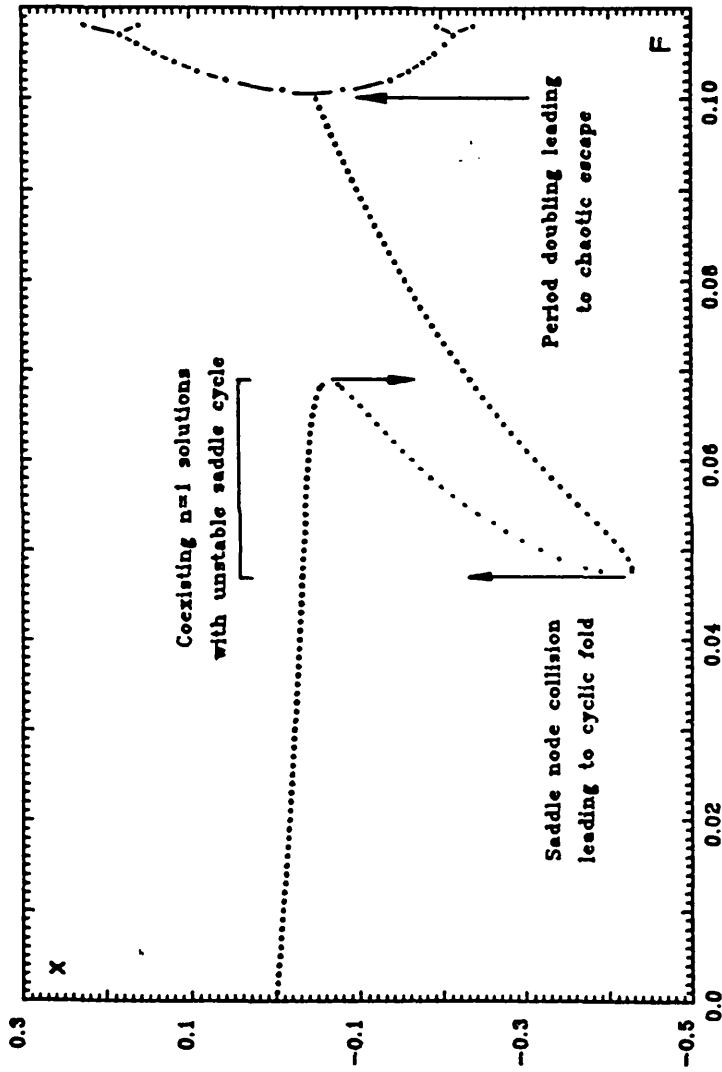
CHAOTIC ESCAPE FROM A POTENTIAL WELL

$$\ddot{x} + \beta\dot{x} + x - x^2 = F\sin\omega t$$

$$\beta = 0.1 \quad \omega = 0.85 \quad \Delta F = 0.001$$

FC

- 179 -

Figure 57. Period-doubling and chaotic response diagram of the Escape equation.
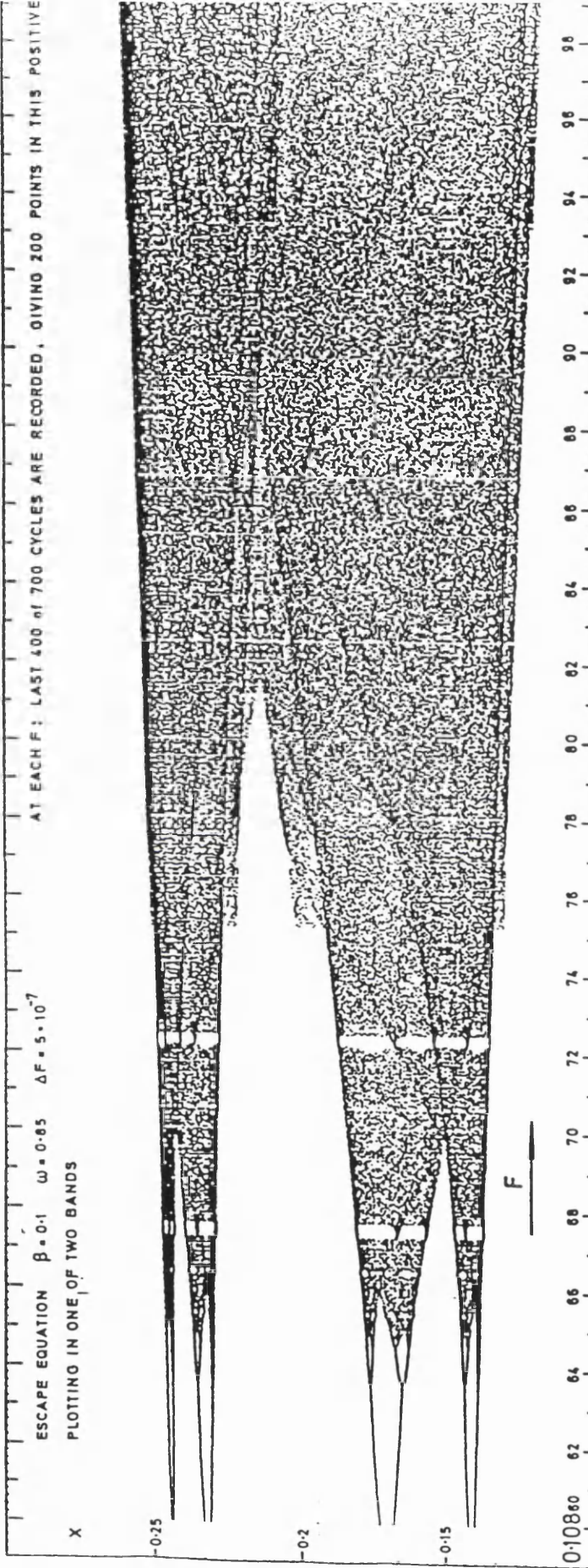
Figure 58. Chaotic attractor shown in a sheared Van Der
Pol plane.

ESCAPE EQUATION   SHEARED VAN DER POL PLANE

x(0) = 0·120414869994   ẋ(0) = – 0·577999778433

Run : BANGLE. 4–RK(80s/c), 50mins. Last 160 of 200 cycles plotted

FOLDING MOBIUS BAND with 80 Poincaré Sections, every 45° of phase φ

β=0·1   ω = 0·85   F=0·109

u = x Cos ωt – ẋ Sin ωt + 0·15 Sin ωt   v = x Sin ωt + ẋ Cos ωt + 0·15 Sin ωt
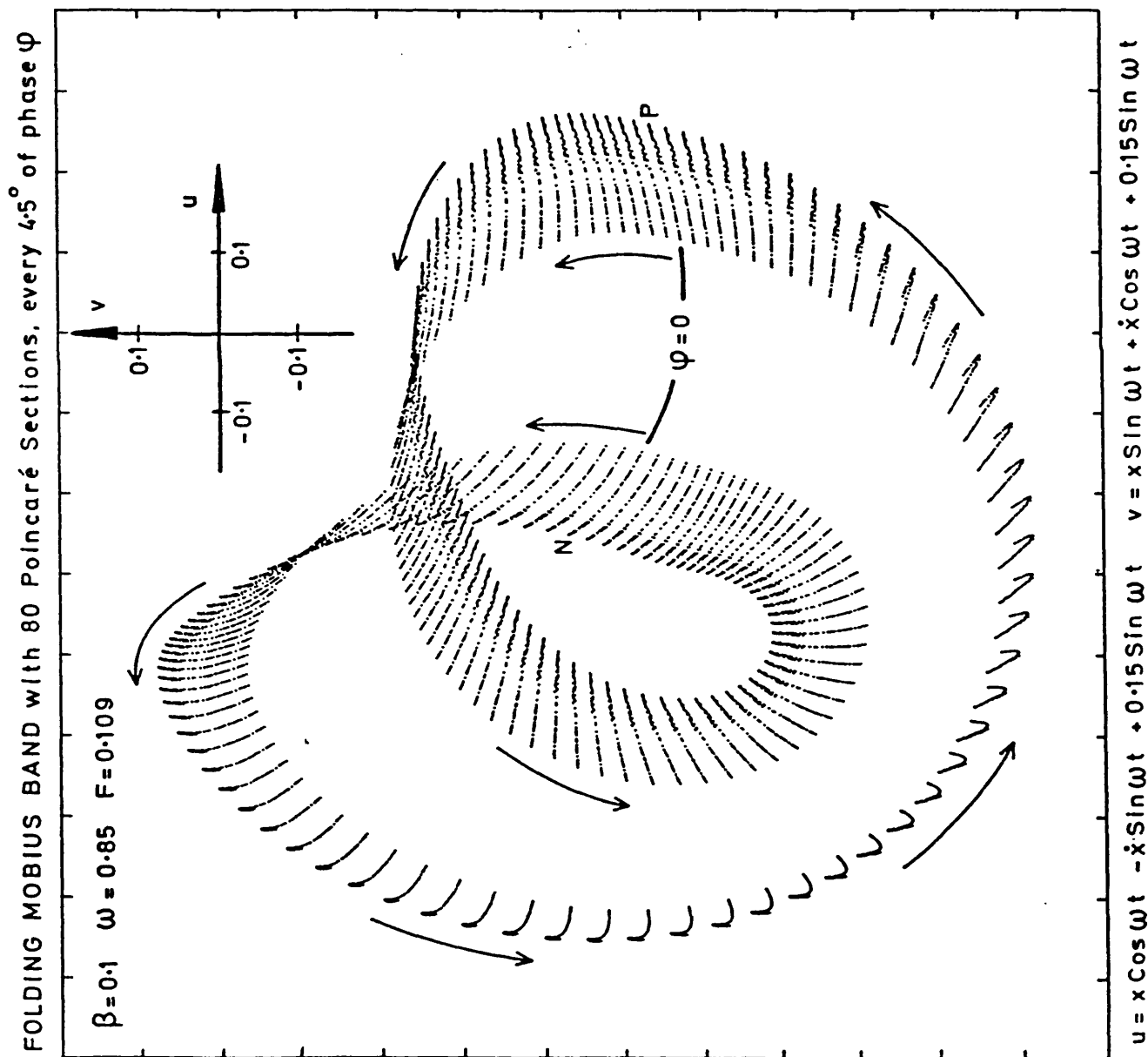
FC
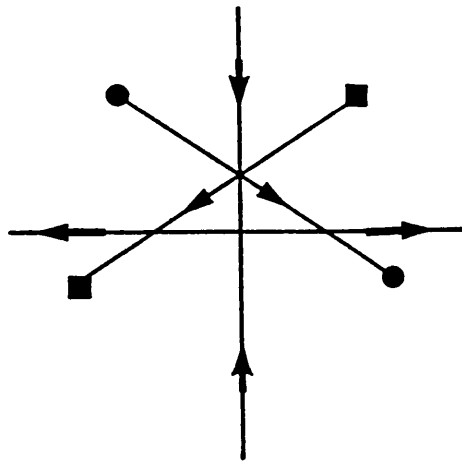
Apparent crossing of trajectories in a two dimensional
projection.
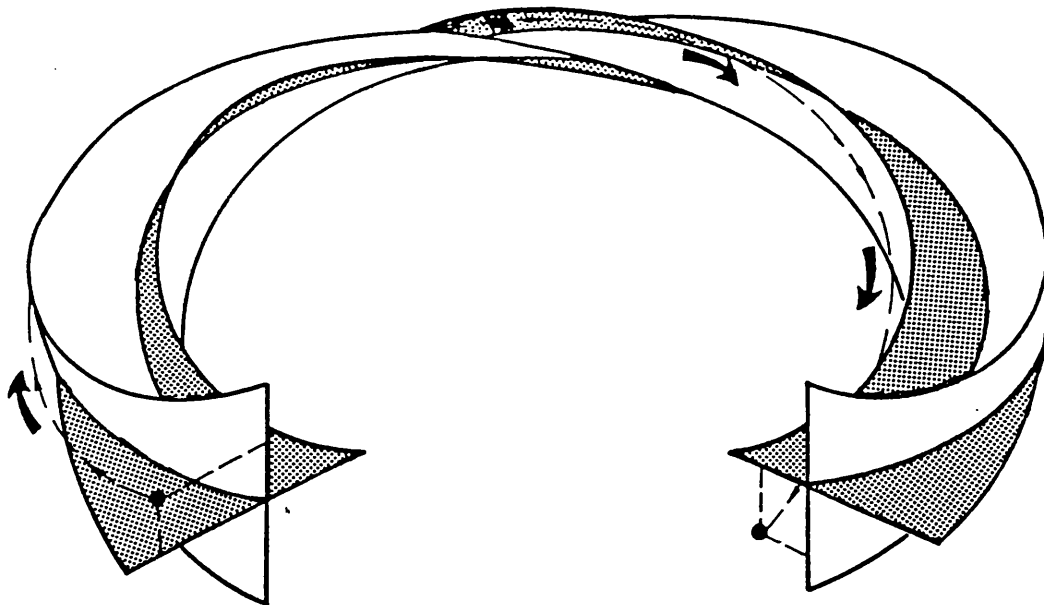
Three dimensional view of a twisted invariant manifolds:
the dotted line shows a typical trajectory

Figure 59. Schematic diagram of a Möbius band showing the
apparent crossing of trajectories.

Figure 60. Numerical evidence of homoclinic tangency of the Escape equation.

HOMOCLINIC TANGENCY: escape equation   F = 0·074   β = 0·1   ω = 1·0
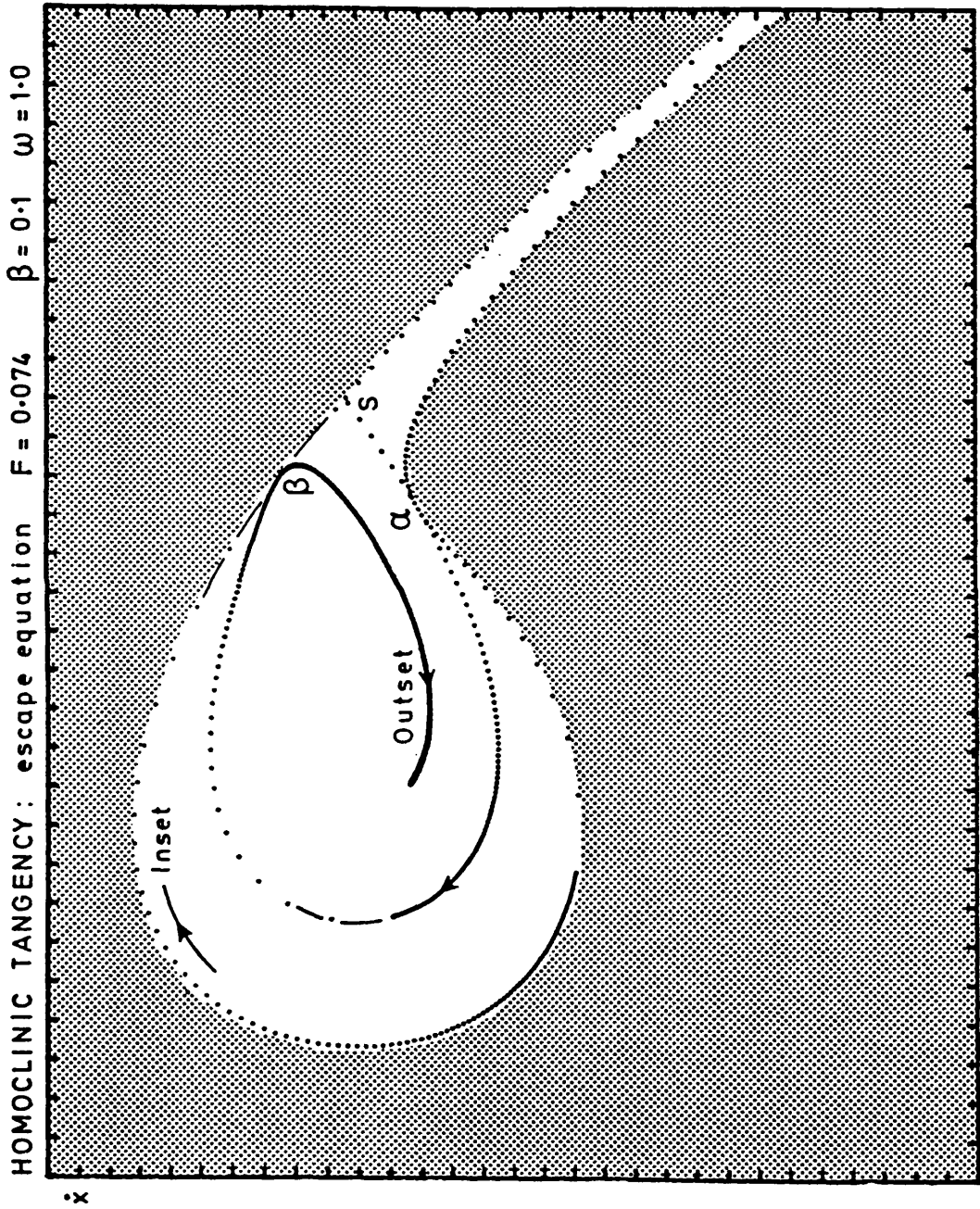
Phase φ = 180°. Inset and outset from complete eigenvector ladders.
−1 < x < 2 : −2 < ẋ < 1.

Run: HOMOCLINIC TANGENCY
4 - RK (40 s/c)   FC

- 183 -

$$\ddot{x} + \beta\dot{x} + x - x^2 = F \sin\omega t$$

$$\beta = 0.1$$
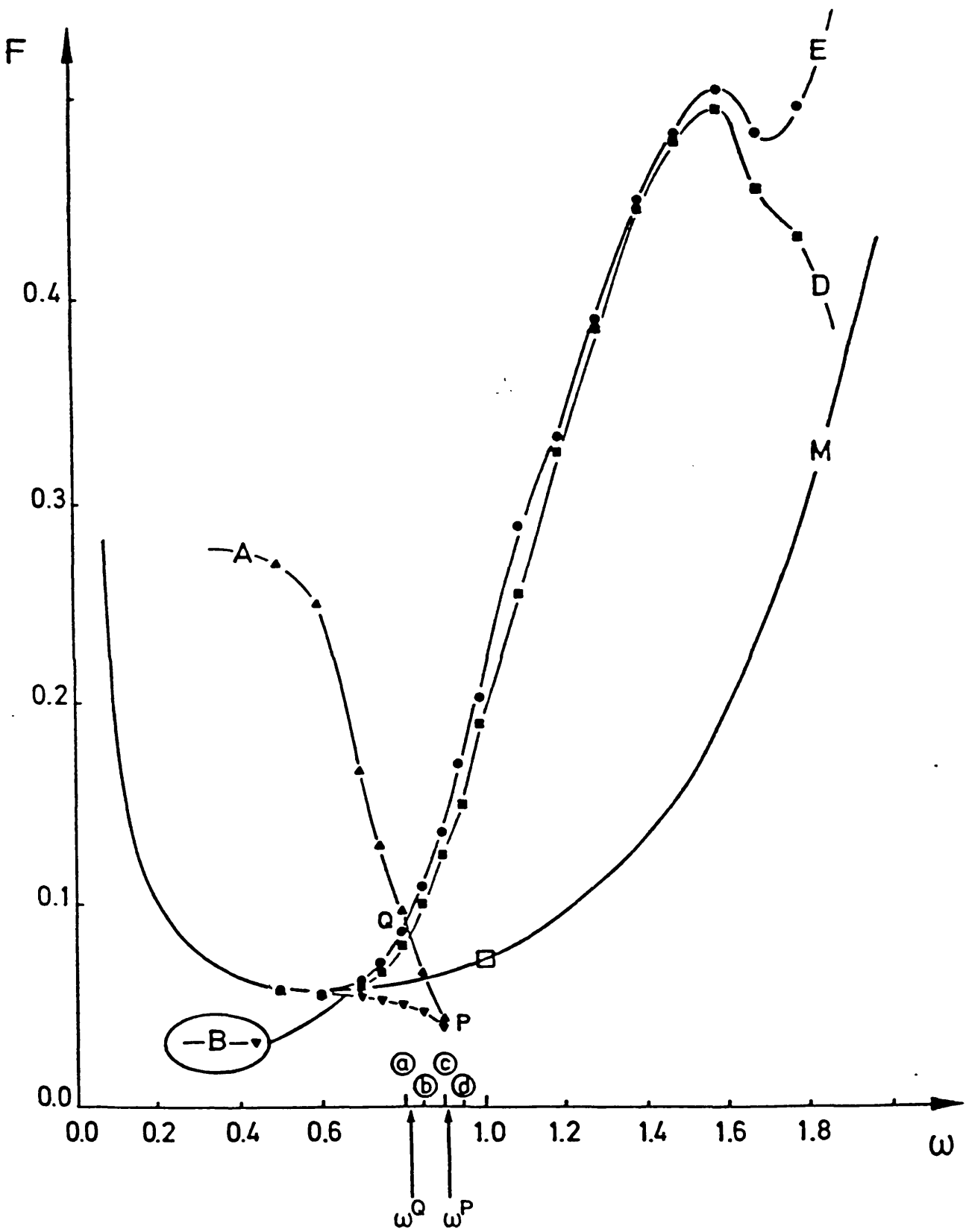
Figure 61. Two dimensional control space of the Escape equation, (I).

Figure 62.   Time histories before and after the Blue Sky
Catastrophe showing the effect of chaotic
transients.

β = 0·1   ω = 0·85   x(0) = 0·160048303704   ẋ(0) = −0·570398353278

Eight Poincaré Sections   (1,1)

ẋ

Phase φ

A

B

C

D

F = 0·109046   (−1,−1)   F = 0·109047

Steady state chaotic solution x(t). Poincaré points at φ = 0.

Chaotic transient leading to escape
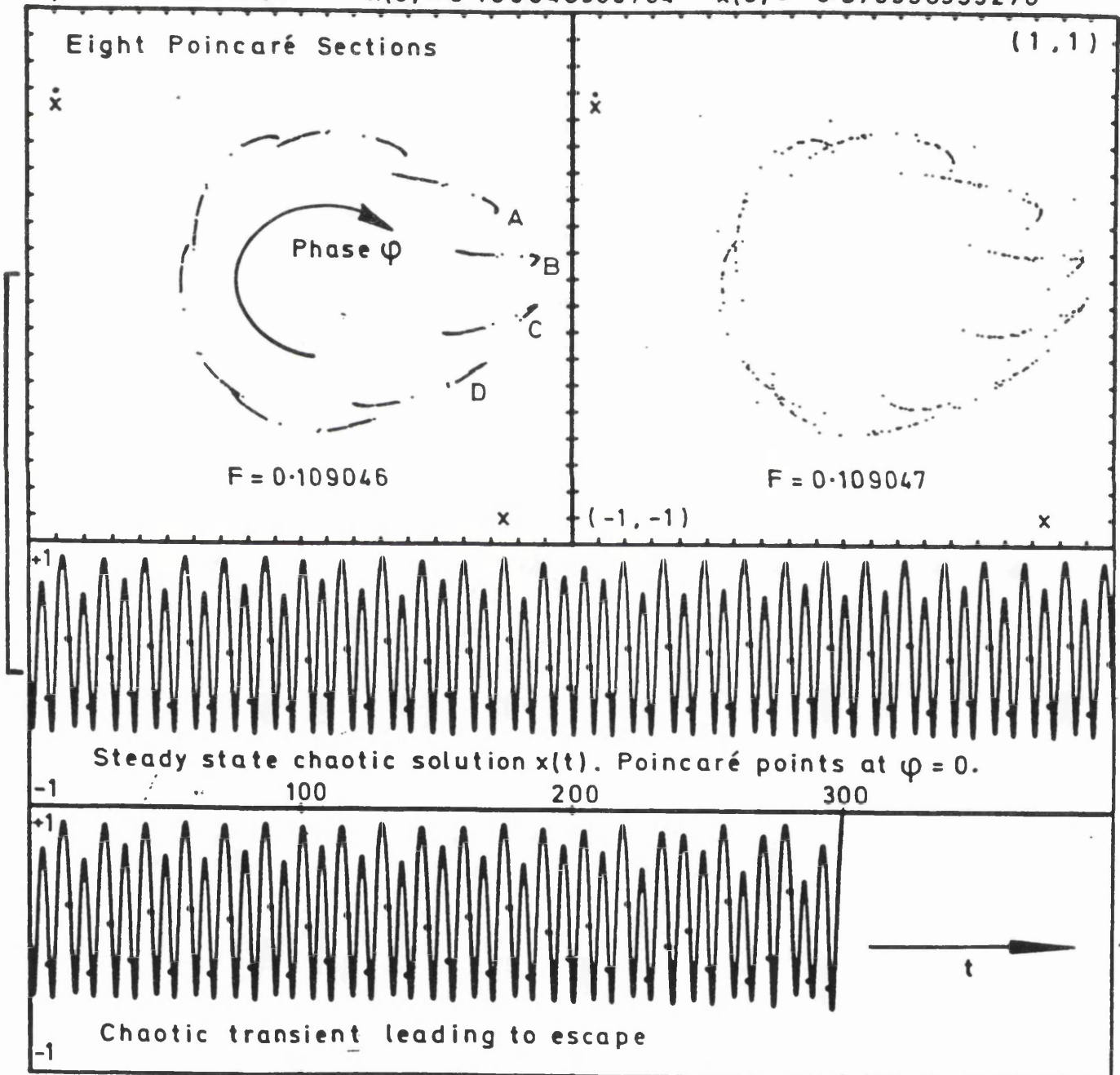
RUN: H−21   40s/c

FC

Figure 63. Numerical evidences showing the unpredictability of the chaotic transients.

CHAOTIC TRANSIENTS LEADING TO ESCAPE (x)1) FROM 7 STARTS, ALL TAKEN FROM THE ATTRACTOR AT F = 0·1090, RUN AT 6 DIFFERENT VALUES OF F.
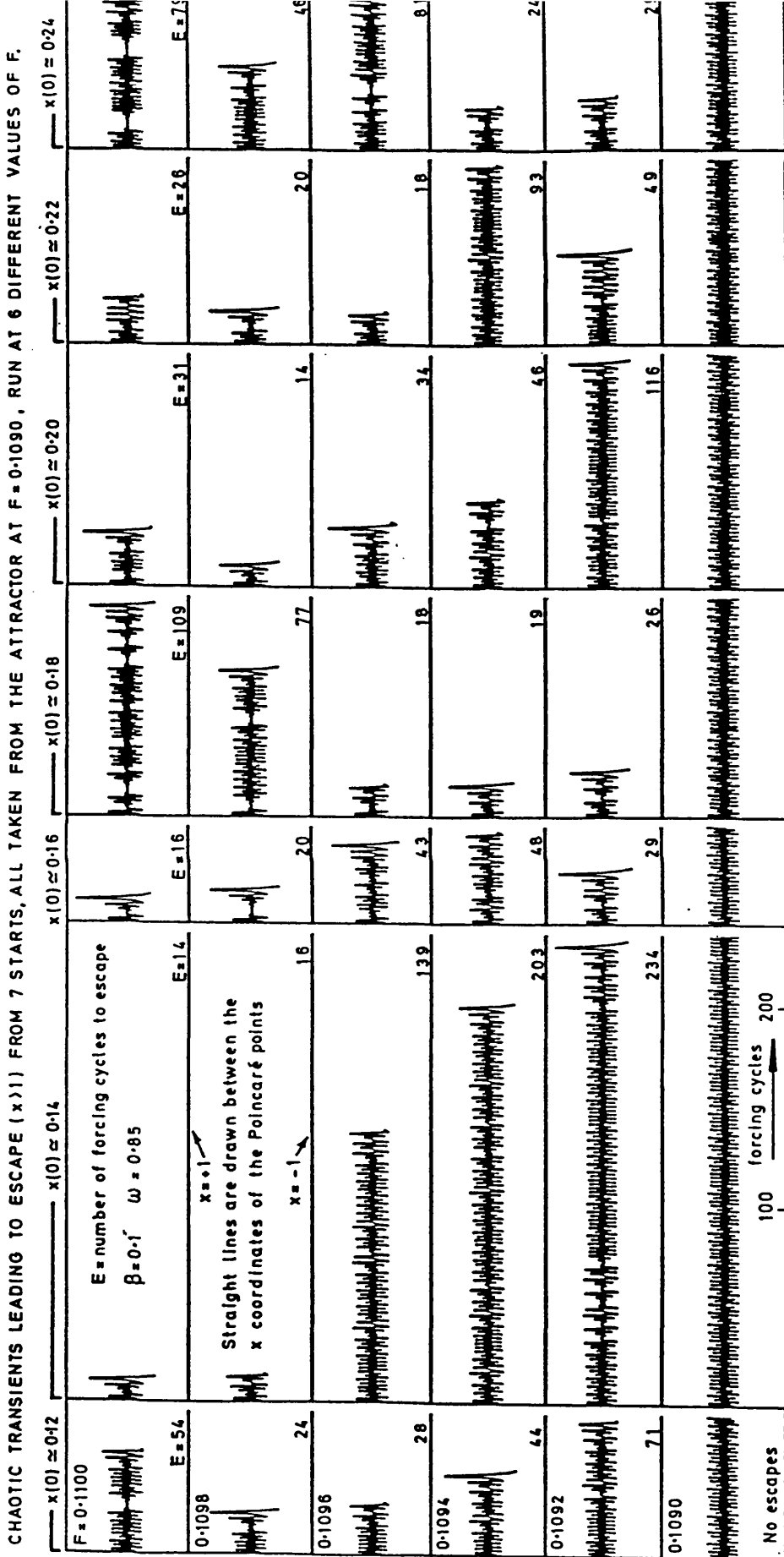
SCALING OF CHAOTIC TRANSIENTS BEYOND A CHAOTIC BLUE-SKY CATASTROPHE

Length of a chaotic transient = E (measured here in forcing cycles)

Expected (average) value of E = M (mean)

Probability density function $\phi(E) = \dfrac{Exp(-E/M)}{M}$

If μ is the change in control from the bifurcation value, then for small μ,

we have $M \propto \mu^{-1/2}$
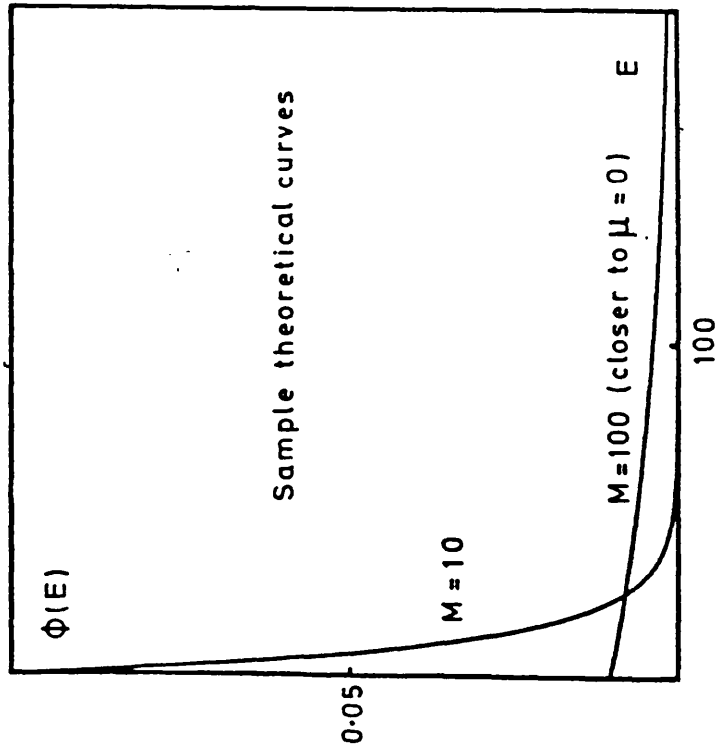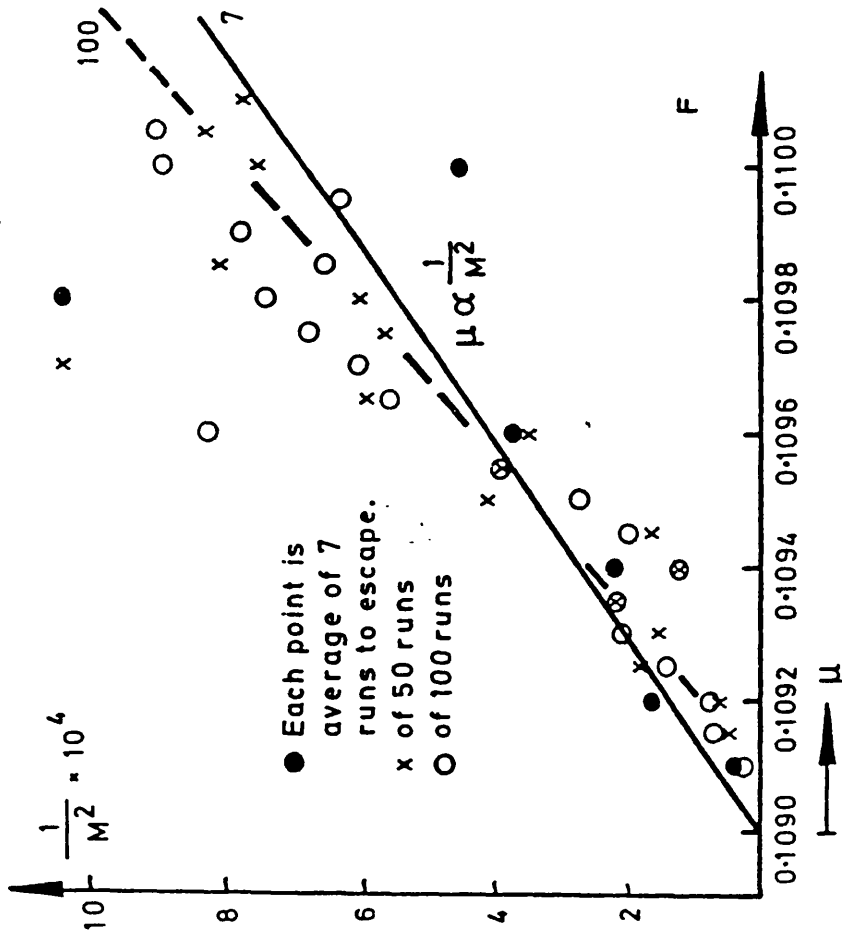
Figure 64.   Scaling of chaotic transients beyond the Chaotic Blue Sky Catastrophe, (I).

Figure 65. Scaling of chaotic transients beyond the
Chaotic Blue Sky Catastrophe, (II).

M = mean No. of forcing cycles
before escape (average of 300)

$M = k(F - F^E)^{-\gamma}$

$\gamma = 0.87$
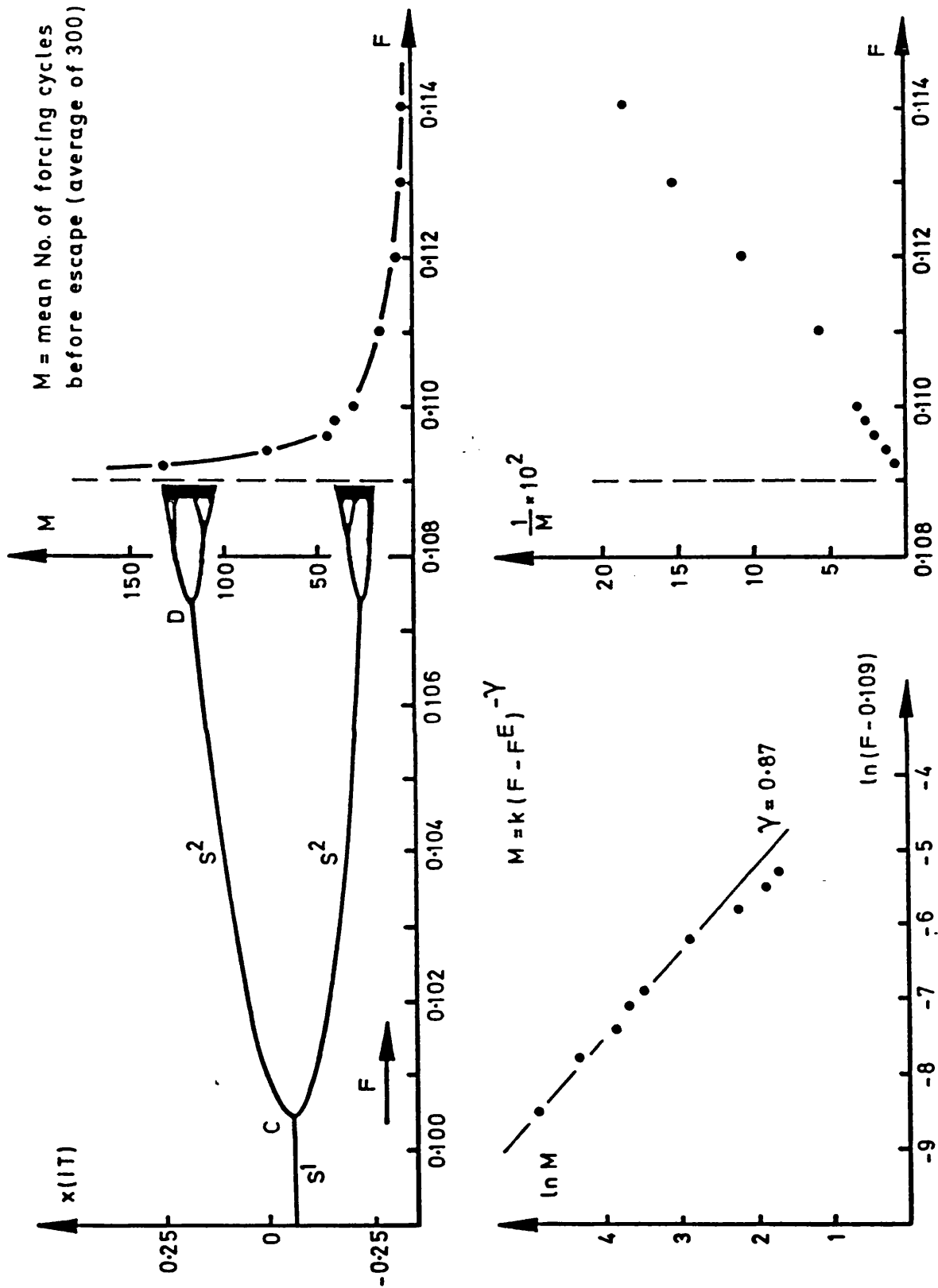
'Sketch' of the cascade

$\beta = 0.1$ $\omega = 0.85$ Naturally disposed points at F = 0.109   Ln is to base e
FC
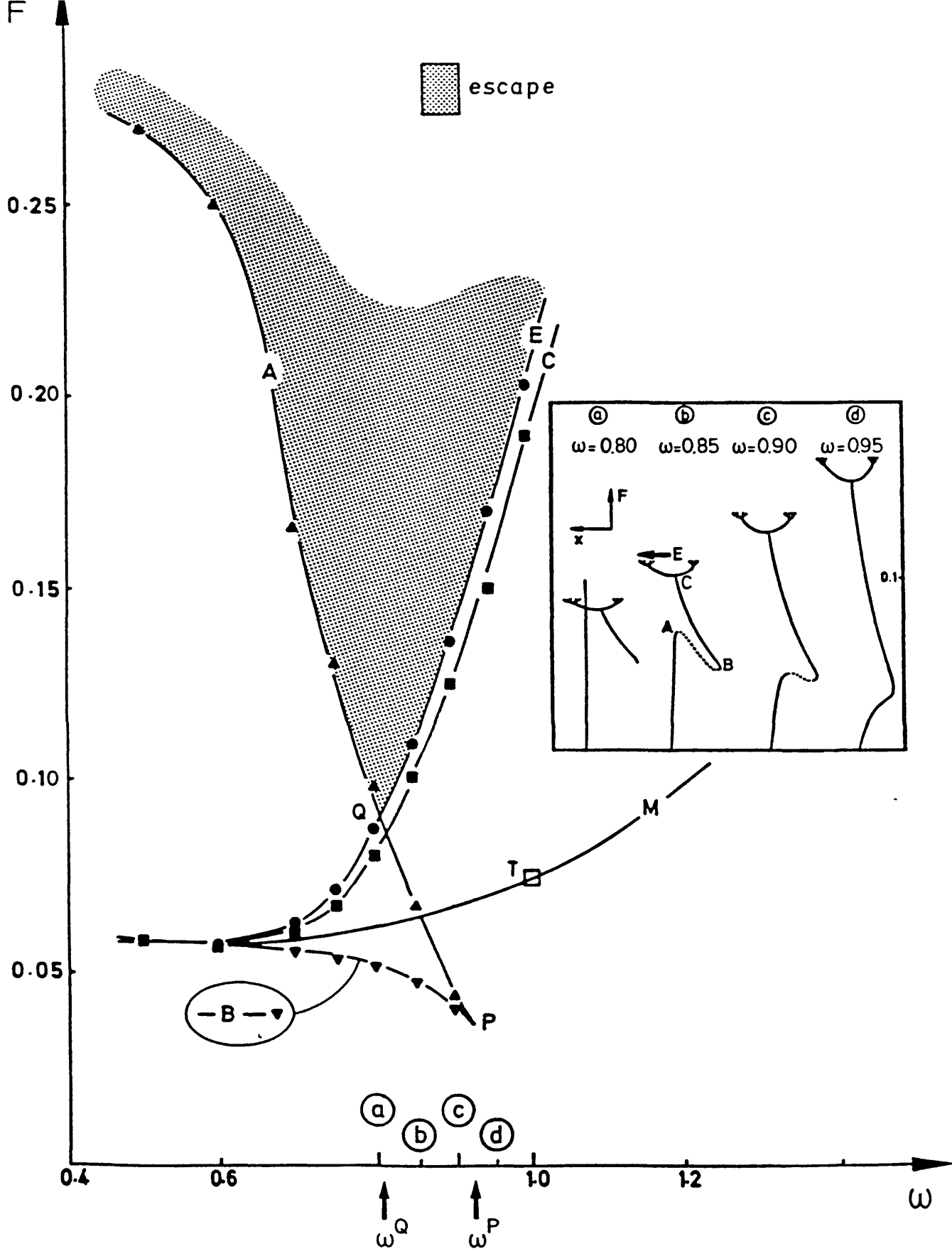
Figure 66. Two dimensional control space of the Escape Equation, (II).

GRID OF 100•100 STARTS : DOT DENOTES
ESCAPE BEYOND x=20 W.ITHIN 7•1 CYCLES
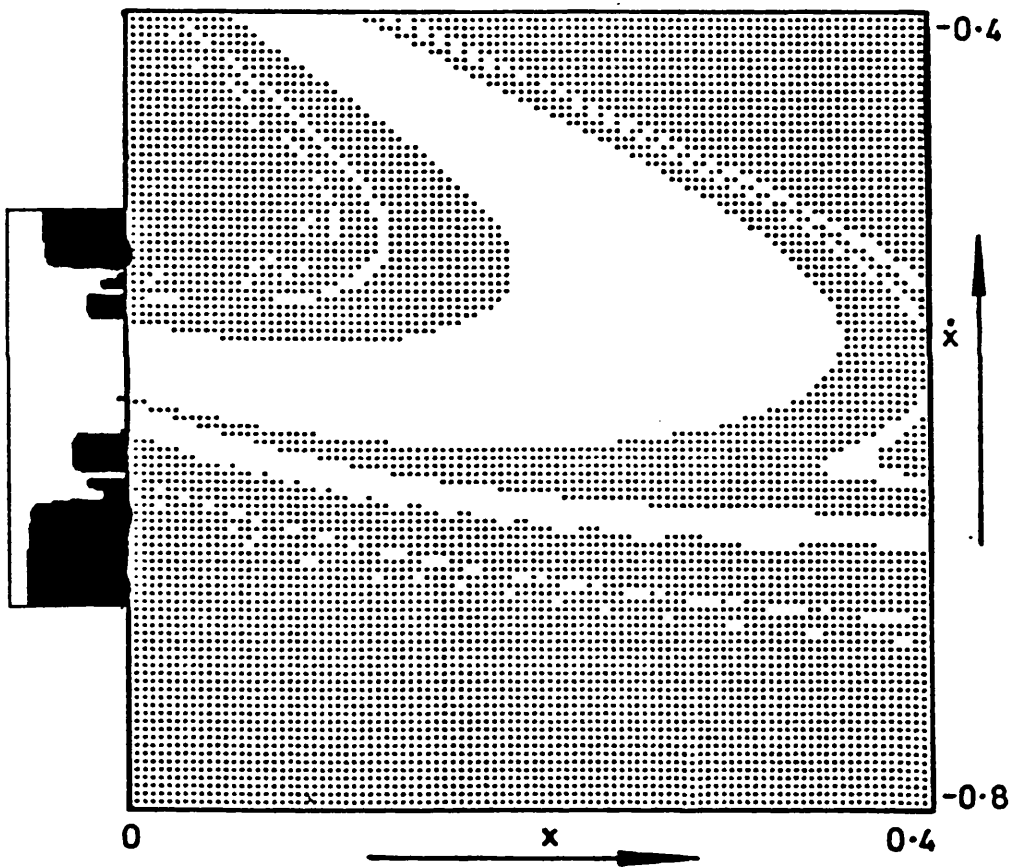
Figure 67. Fractal basin boundary after homoclinic tangency
using a grid-of-start approach.

Run : FRACTAL DOT

(Inserted in A:205 which see for data)

FC

FRACTAL ESCAPE TIMES : from line x(0) = 0
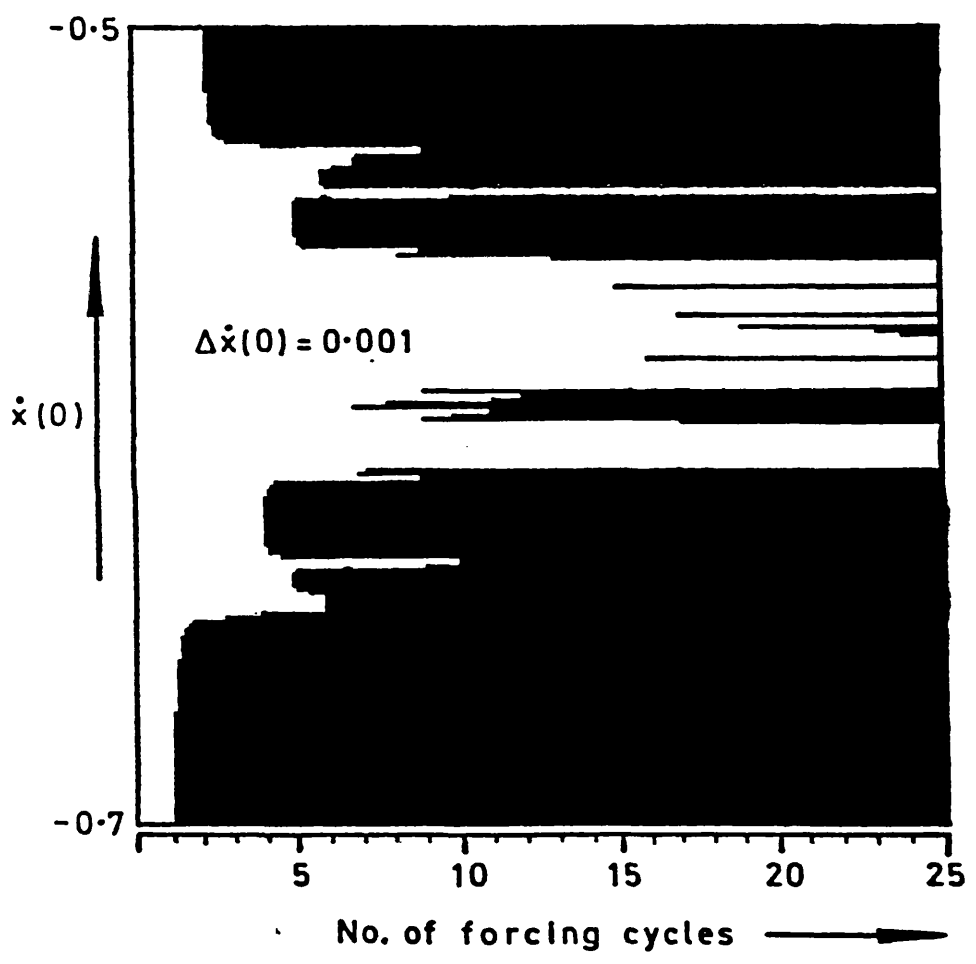
Figure 68.   Fractal escape time within a small region of
the catchment area.

Run : FRACTALNEG
(Appended to A:206 which see for data)
FC
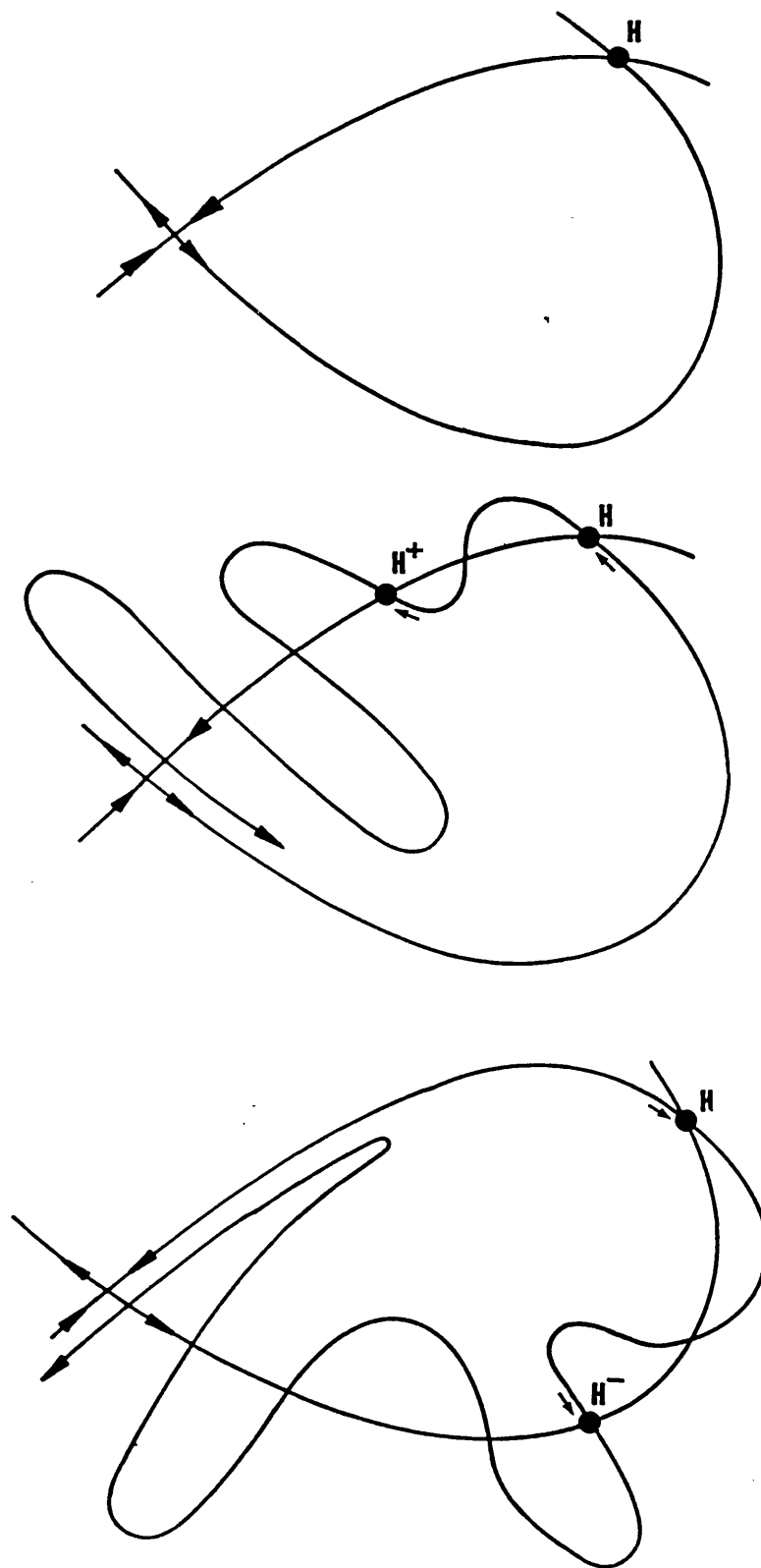
Figure 69.   Schematic   diagram   of   a   transverse   homoclinic
crossing.

Homoclinic tangle of escape equation

$\beta = 0.1$
$\omega = 0.85$
$F = 0.109$
$\phi = 0$

global saddle
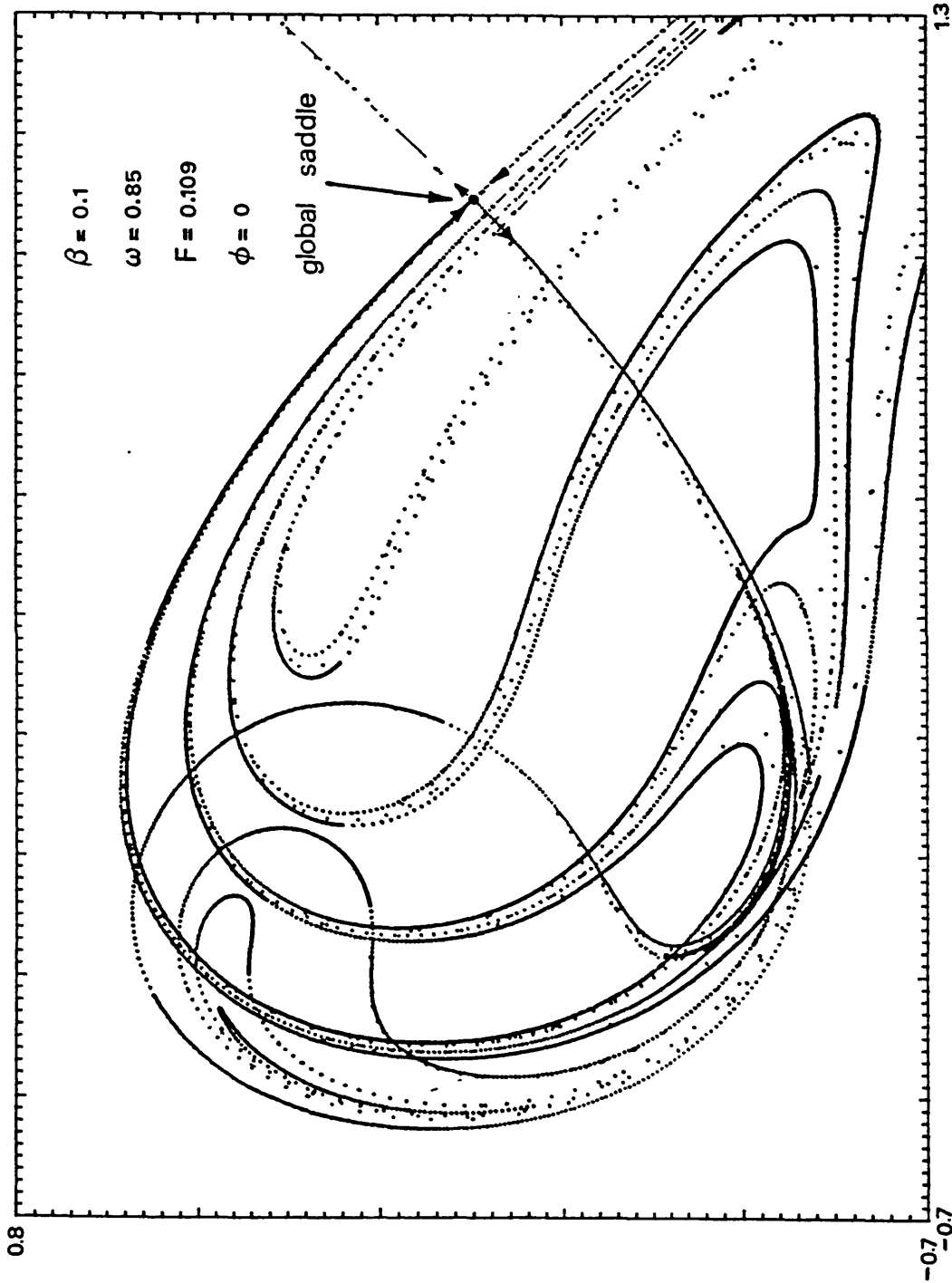
Figure 70. Homoclinic tangle of the Escape equation obtained by the ladder technique.

Figure 71. Catchment region defined by homoclinic tangle inset.

WHISKER OF B_4

Grid of starts for lower square

Unexplored region
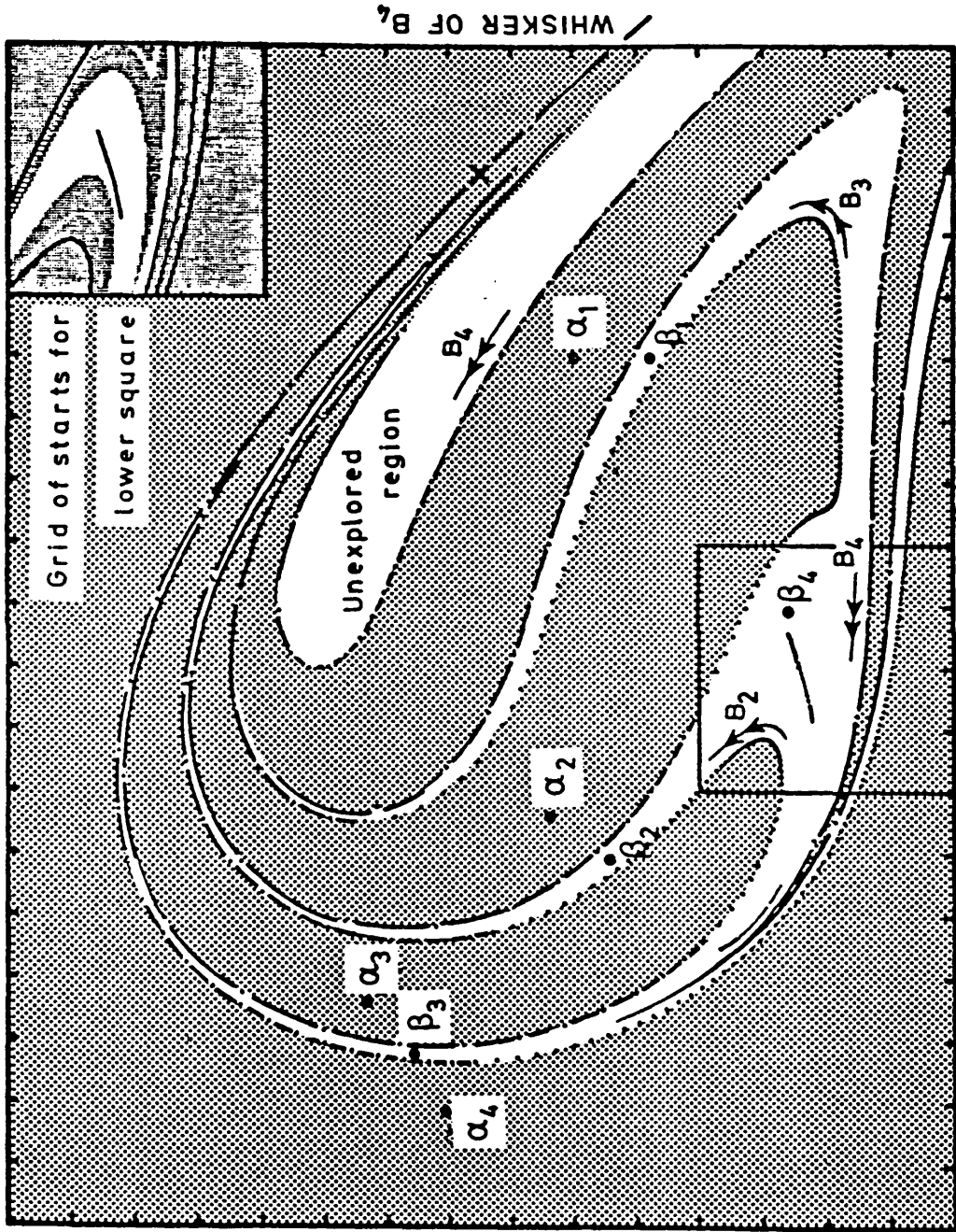
α mapping sequence diverges to infinity (x of α_5 is greater than 20)
β mapping sequence converges to the chaotic attractor

Run : FRACTAL BASIN (Data + scales as A:194) FC

Figure 72. High resolution grid-of-start approach showing
the fractal basin boundary.

A FRACTAL BASIN BOUNDARY
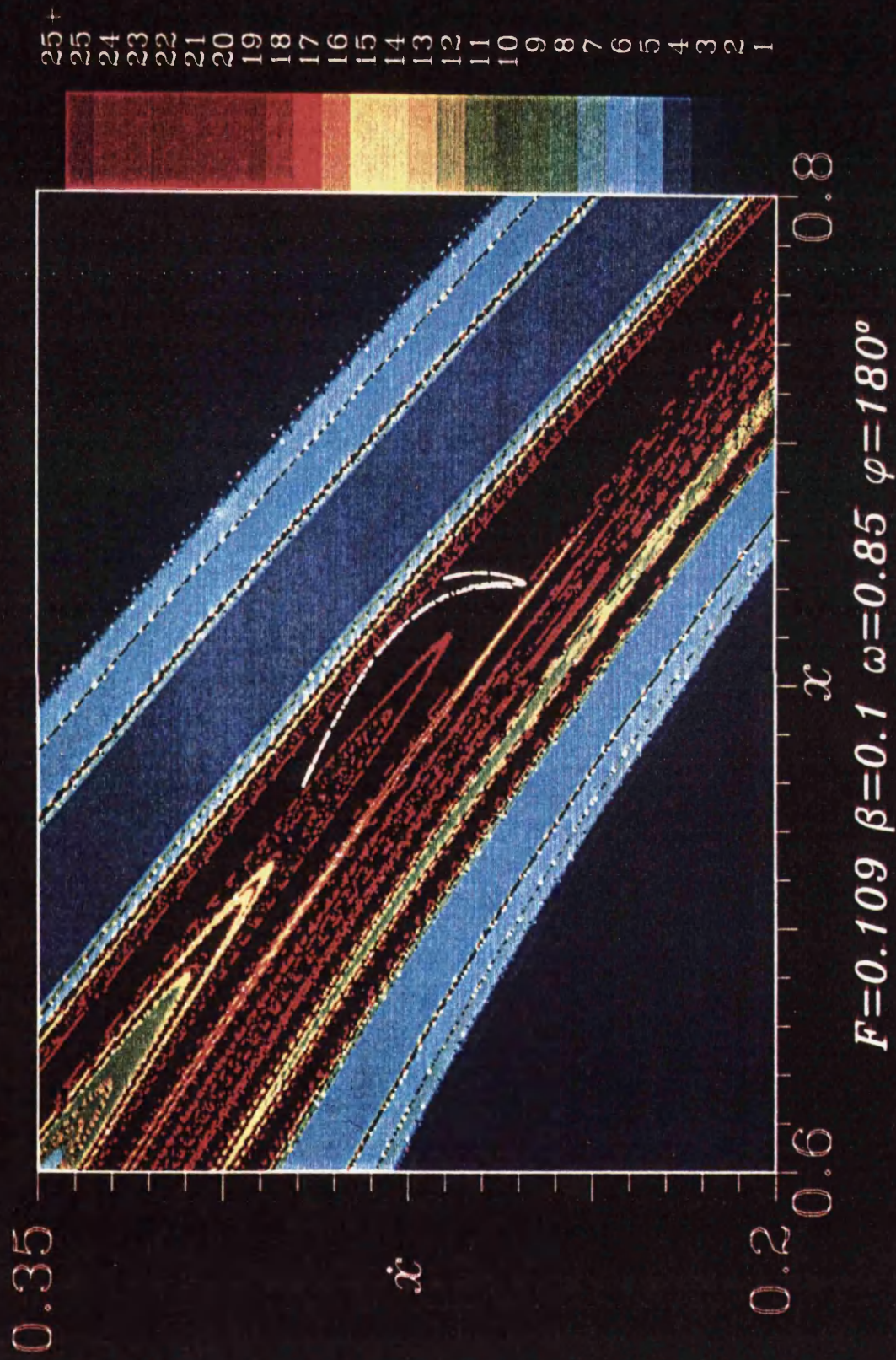
Escape before n forcing cycles

$F=0.109$ $\beta=0.1$ $\omega=0.85$ $\varphi=180°$

Figure 73. Catchment region of the Escape equation at various forcing frequencies obtained by Simple Cell Mapping technique.
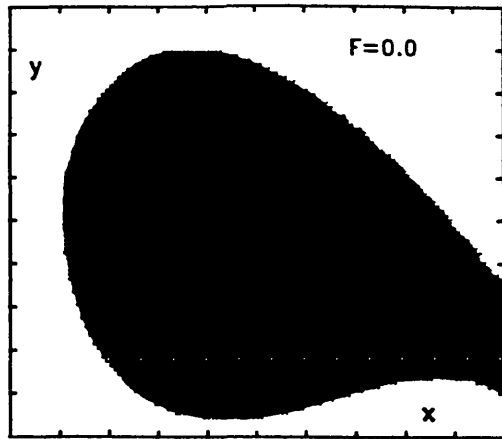
Statical equilibrium solution
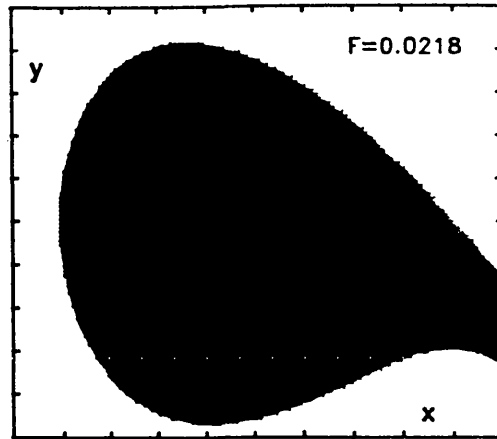
Unique n=1 attractor
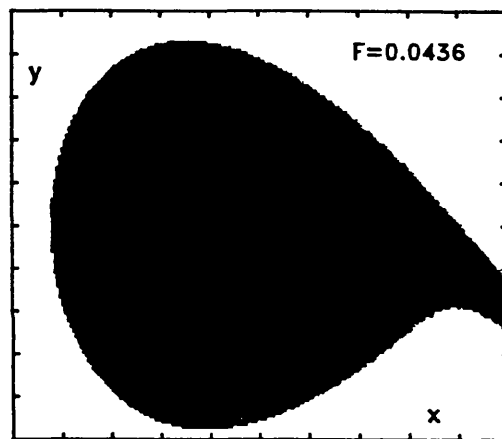
Unique n=1 attractor
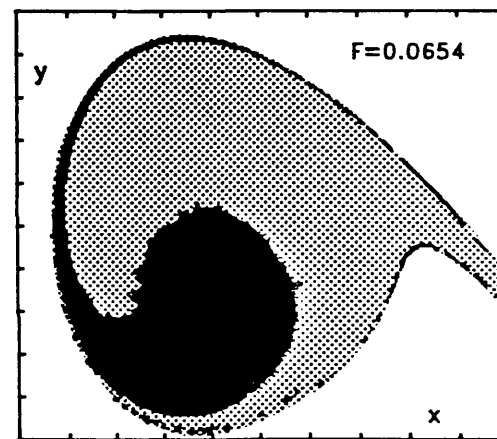
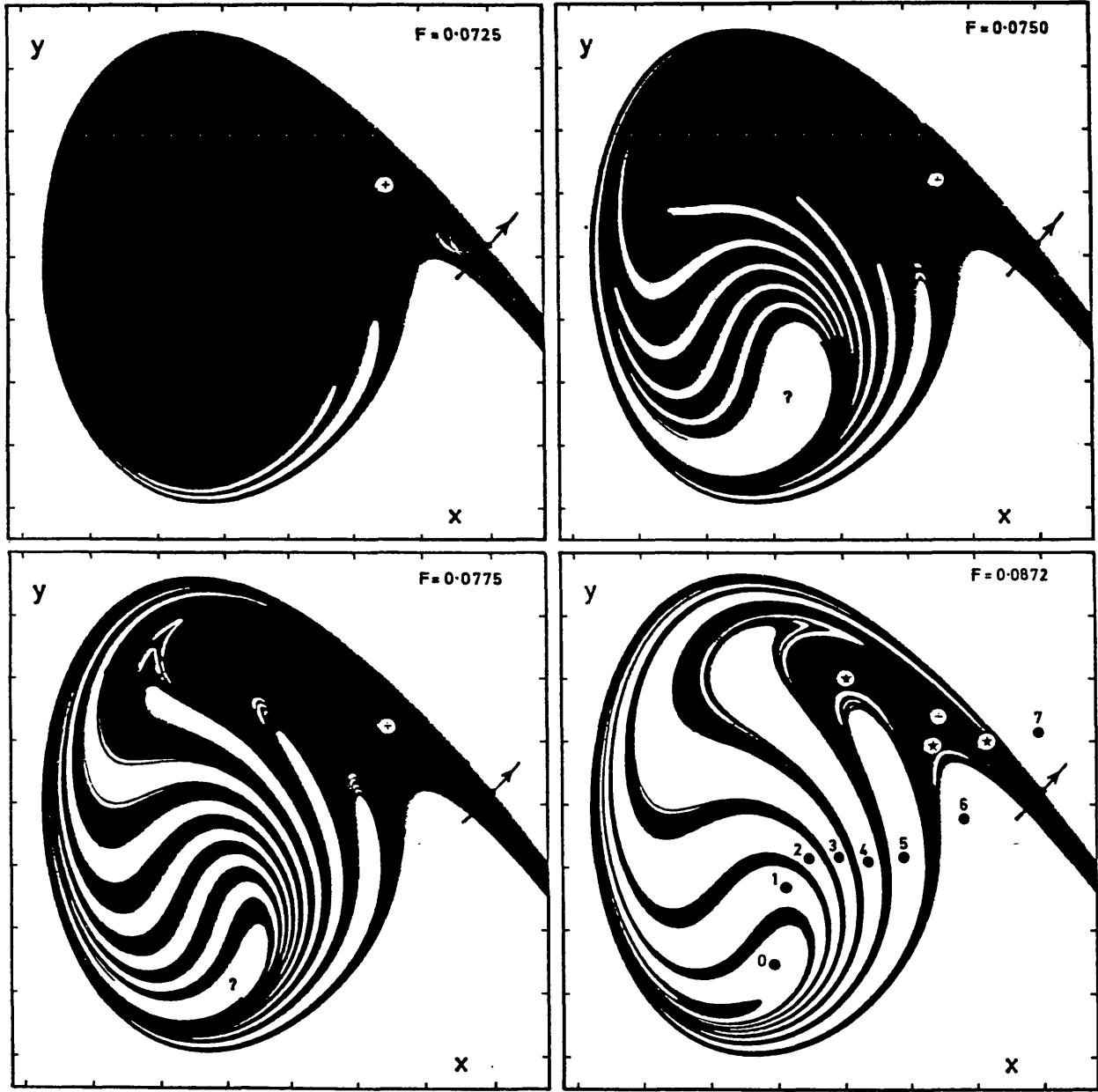Two coexisting n=1 attractors
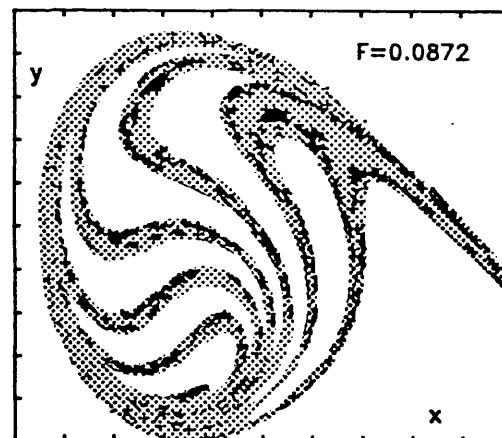
Coexisting n=1 (dots), n=3 (black)
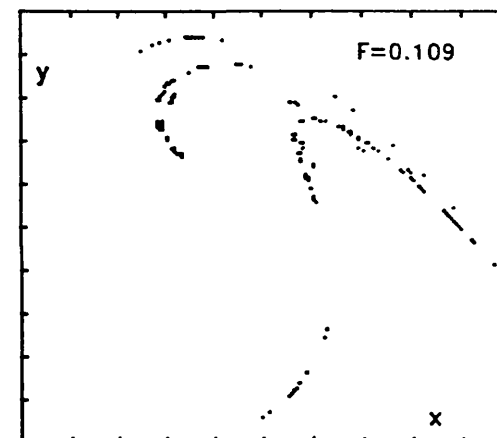
Chaotic attractor close to F^E

Parameters: $\beta = 0.1$ $\omega = 0.85$ $\varphi = 180°$. Equal F intervals. <u>Simple</u> Cell-to-Cell

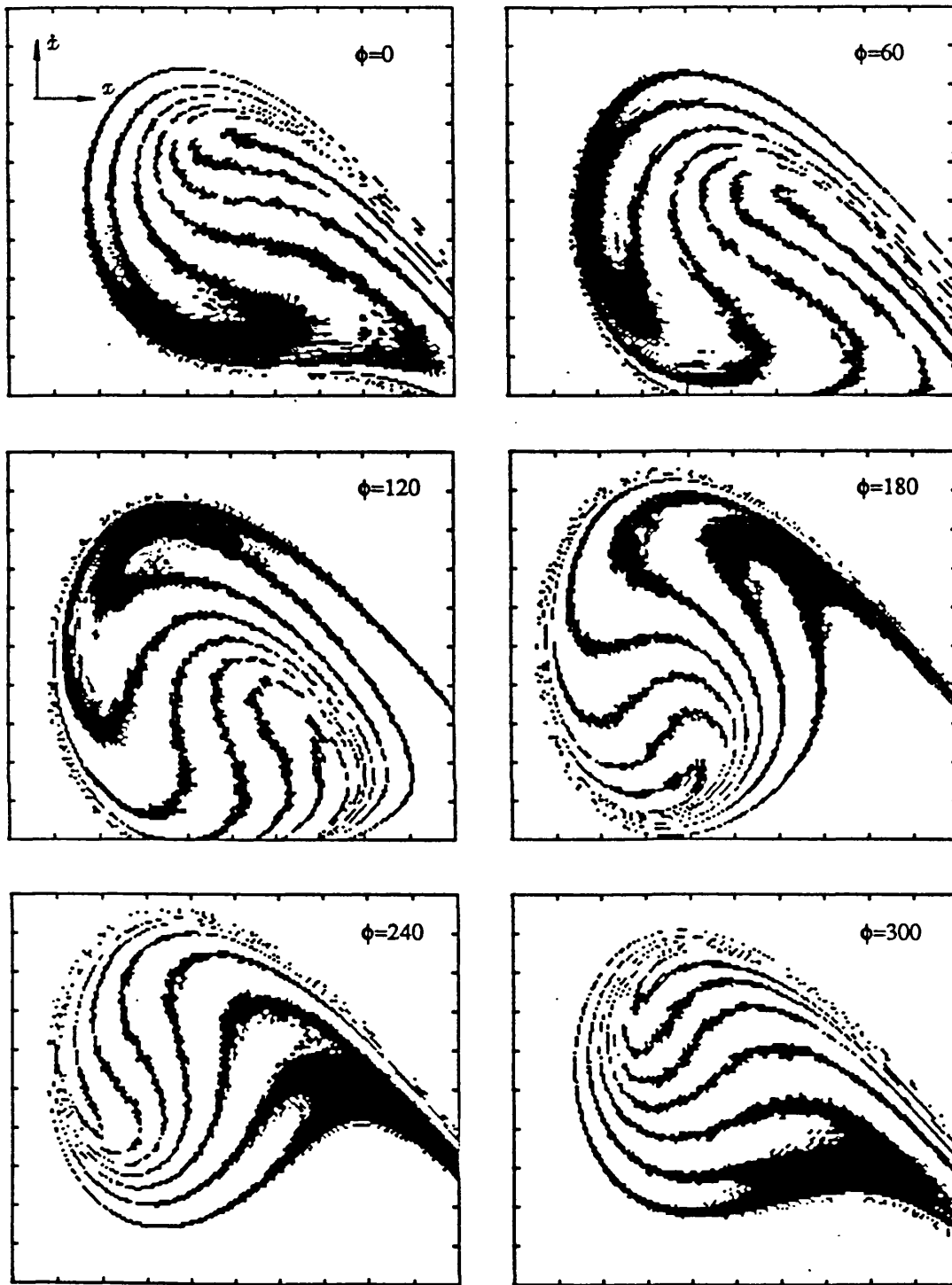Window: $-0.8 < x < 1.2$, $-0.8 < y < 0.8$ Cells: top pair 180x120, rest 200x160

FC

Figure 74. Using Simple Cell Mapping technique to show the development of the homoclinic tangle.

Parameters: $\beta = 0.1$ $\omega = 0.85$ $\varphi = 180°$ $-0.8 < x < 1.2$ $-0.9 < y < 0.8$

Attractors: $n=1$ ..... $\oplus$; $n=3$ ..... $\otimes$

Escape sequence: $0 \rightarrow 7 \rightarrow$ escape.

FC

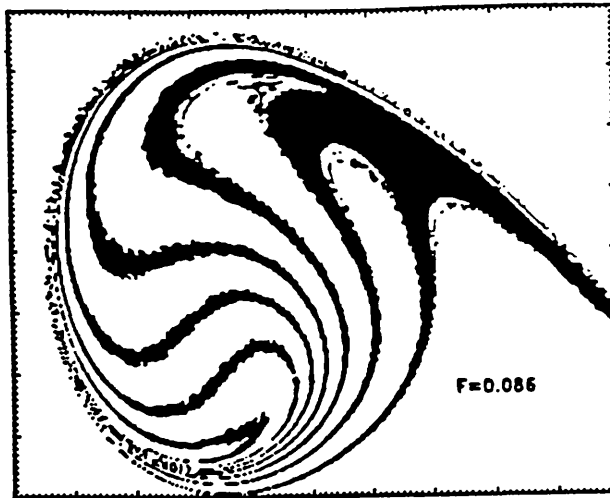Figure 75.   Using Simple Cell Mapping technique to show the fractal basin boundaries at various phase angles.
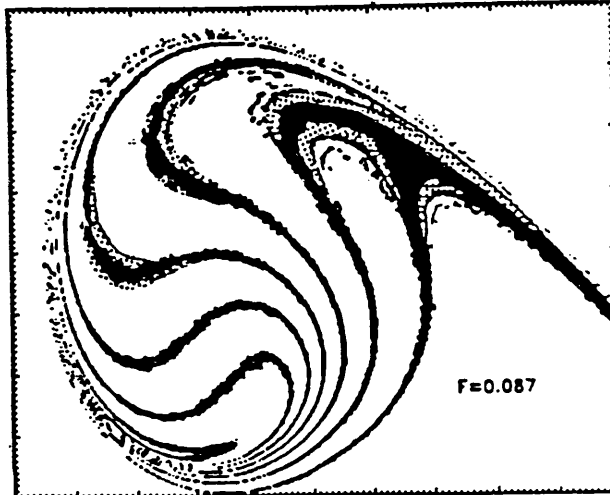

Parameters :   β=0.1   ω=0.85   F=0.086

Black regions: n=1 periodic attractor.

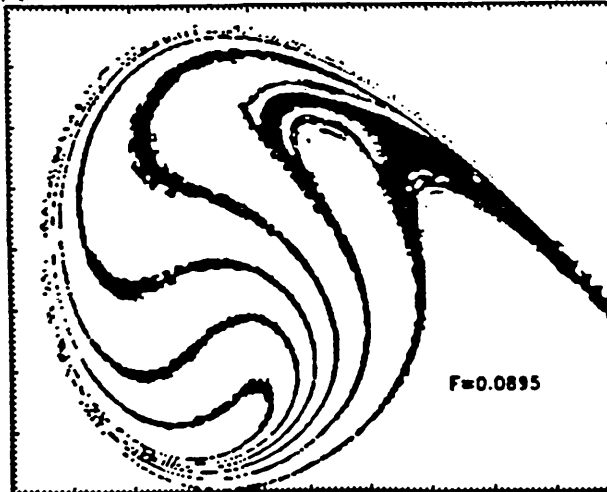-0.8 > x > 1.2   -1.0 > $\dot{x}$ > 1.0

Before n=3 saddle -node
White : escape
Black : n=1 attractor

After n=3 saddle -node
White : escape
Black : n=1 attractor
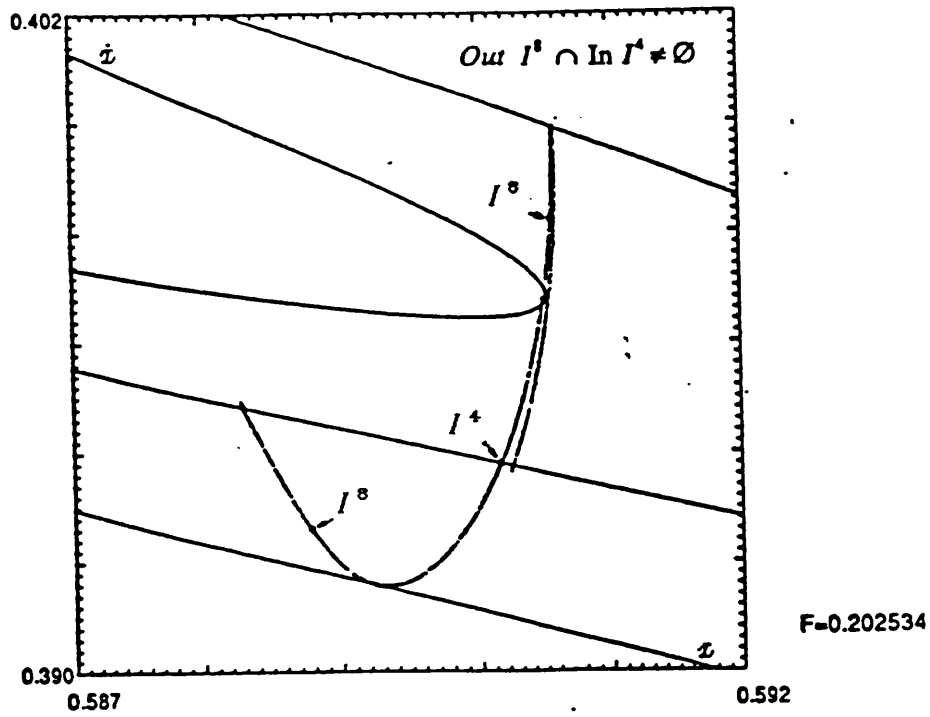Hatched: n=3 attractor
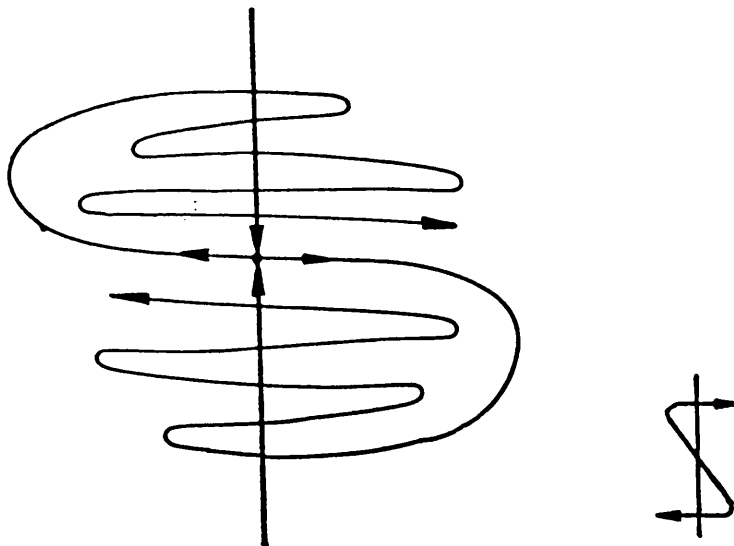
After n=3 cascade
White : escape
Black : n=1 attractor

Escape equation: $\beta = 0.1$ $\omega = 0.85$ $\phi = 180$ Grid Size = 400X320 = 128,000 points
-0.8<x<1.2 -0.8<x<0.8

Figure 76. Using Simple Cell Mapping technique to show the rapid erosion of the catchment region.

0.402

$\dot{x}$

$Out\ I^{s} \cap In\ I^{u} \neq \varnothing$

I^{8}

I^{4}

I^{8}

F=0.202534

x

0.390

0.587

0.592

Numerically computed homoclinic tangle

Schematic diagram of a dollar sign map

Figure 77. Schematic and numerical evidence of a Dollar Sign Map.

-200-

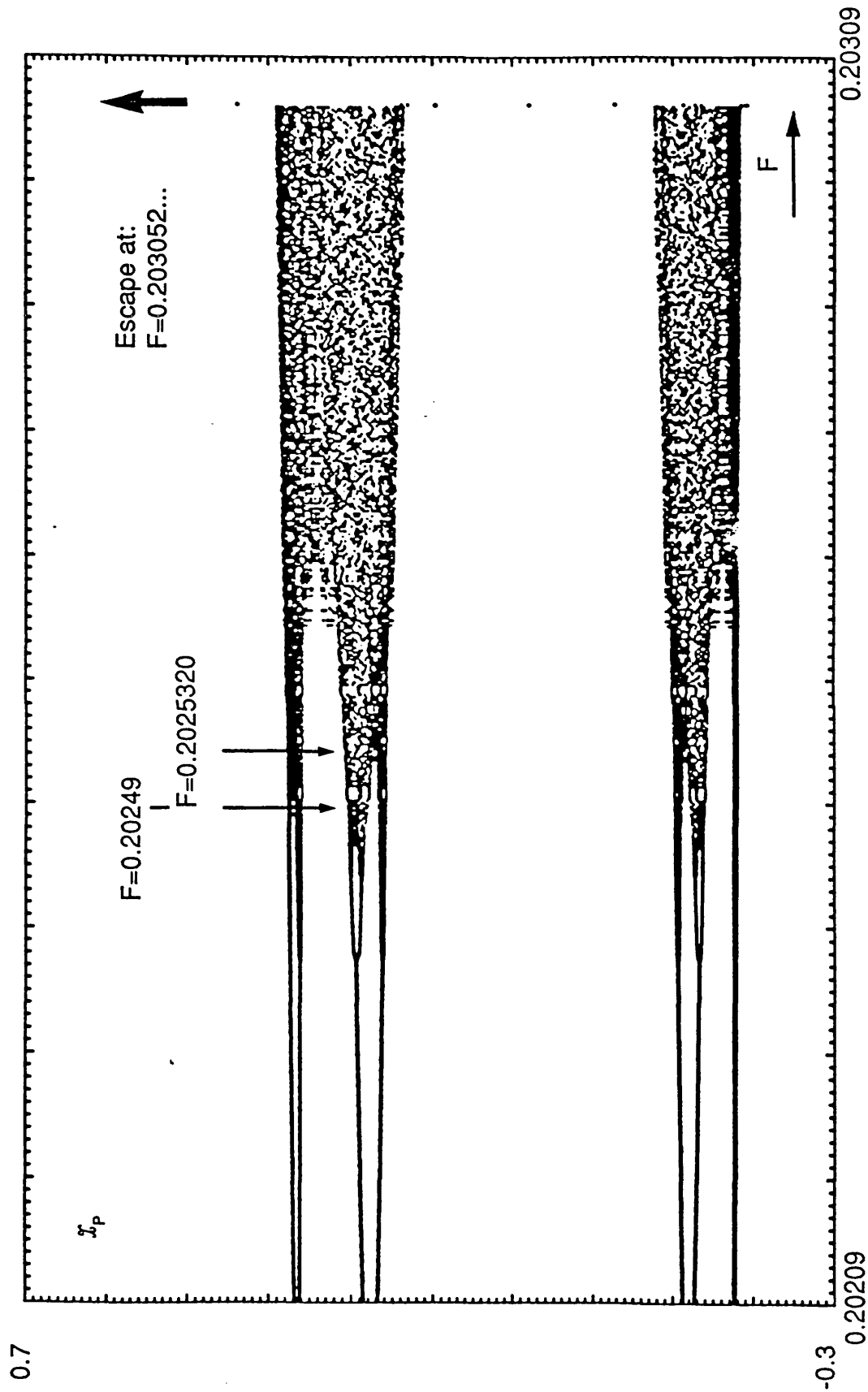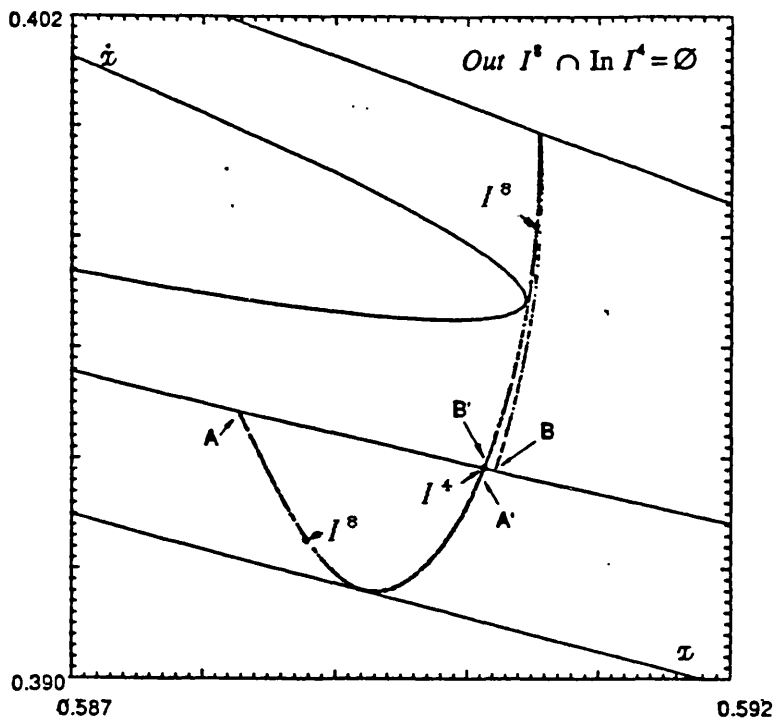Escape equation $\beta=0.1$ $\omega=1.0$ $\Delta F=2.0^{-6}$

Escape at:
F=0.203052...

F=0.20249

F=0.2025320

x_P

F

0.7

-0.3

0.20209

0.20309

Figure 78. Period-doubling cascade of the Escape equation.

Escape Equation, parameters: β=0.1 ω=1.0

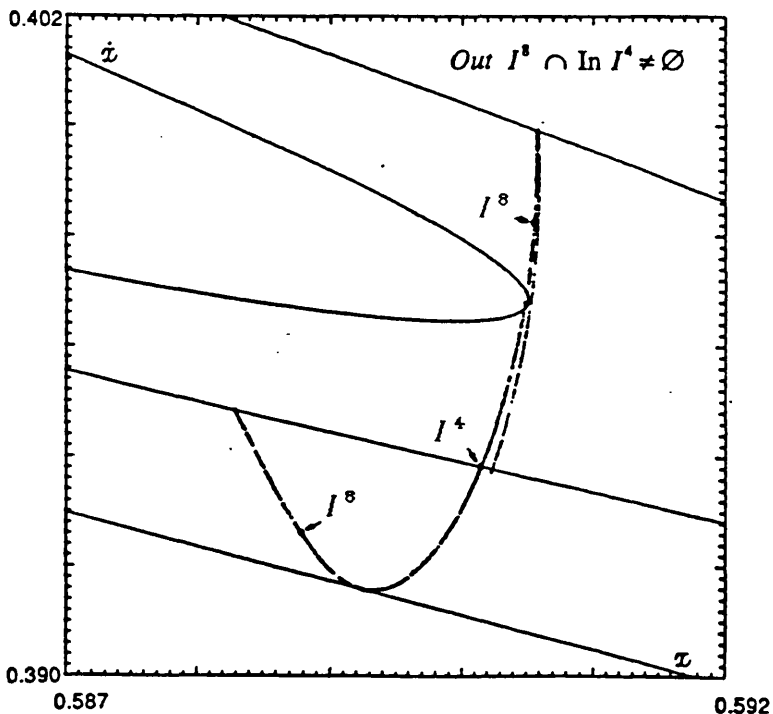

$A - A' = Out I^8$

$B - B' = Out I^8$

$A - B = Out I^4$

$Out I^8 \subset Out I^4$

$F = 0.202530$

$F = 0.202534$

Figure 80. Windows showing part of the period-doubling cascade and bifurcation points.
Escape Equation, parameters: β=0.1 ω=1.0
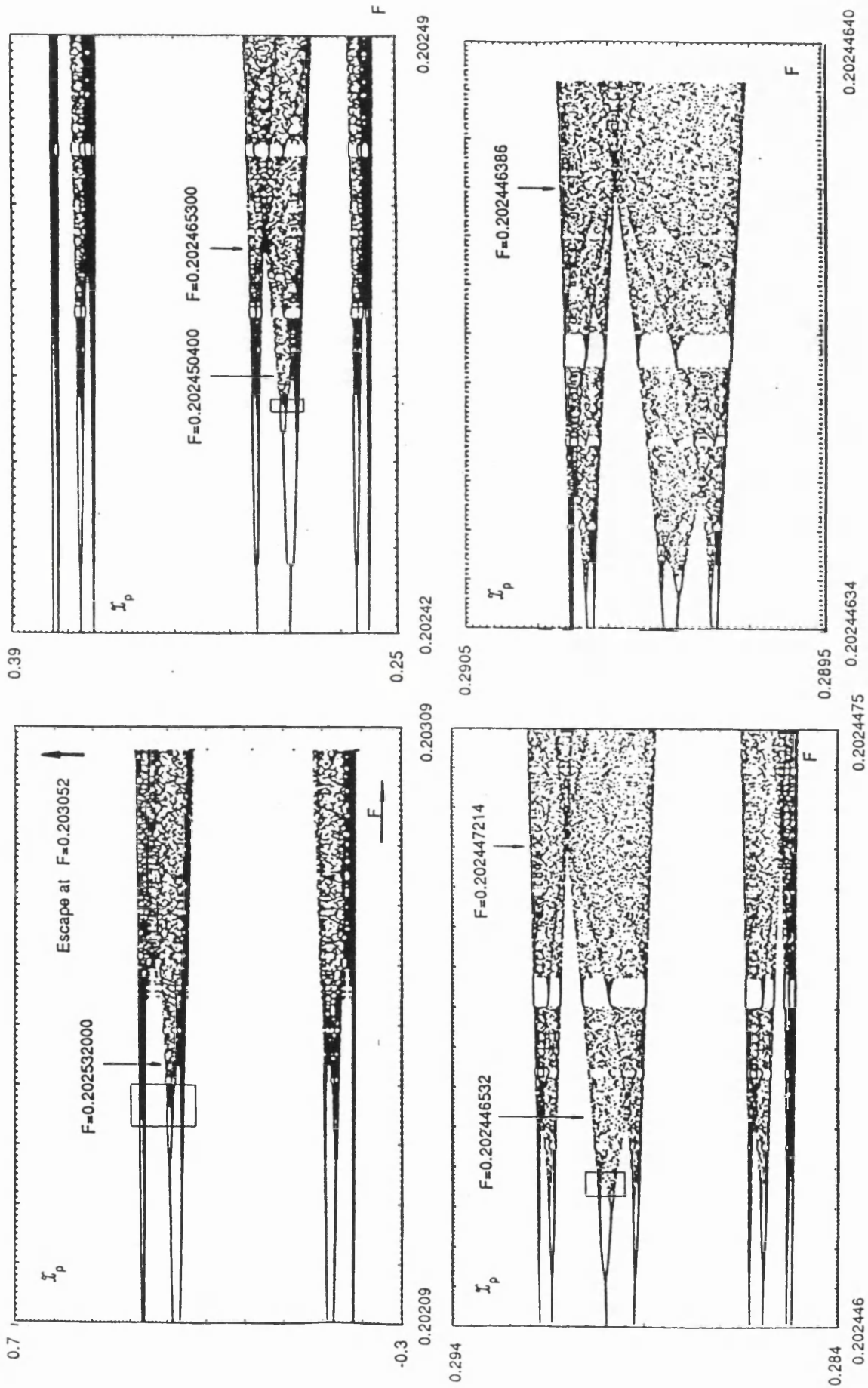
Figure 81. Blue Sky Catastrophe of the Escape equation: collision of D^6 with the two-band chaotic attractor.

BLUE SKY CATASTROPHE of Escape equation

Blue Sky jump at
F=0.1077...
(Note D^6 collides with period 6 chaotic attractor)

Blue Sky escape at
F=0.109...
(Note collision of Chaotic attractor with D^6)

Note: data is sampled at $2nT$

x

s^2

D^6

s^n
D^n — fixed point of period nT
S=STABLE
D=DIRECTLY UNSTABLE

F

0.6

0.3
0.107

0.1095

Escape equation : $\beta=0.1$ $\omega=0.85$ $\varphi=180$

- 204 -
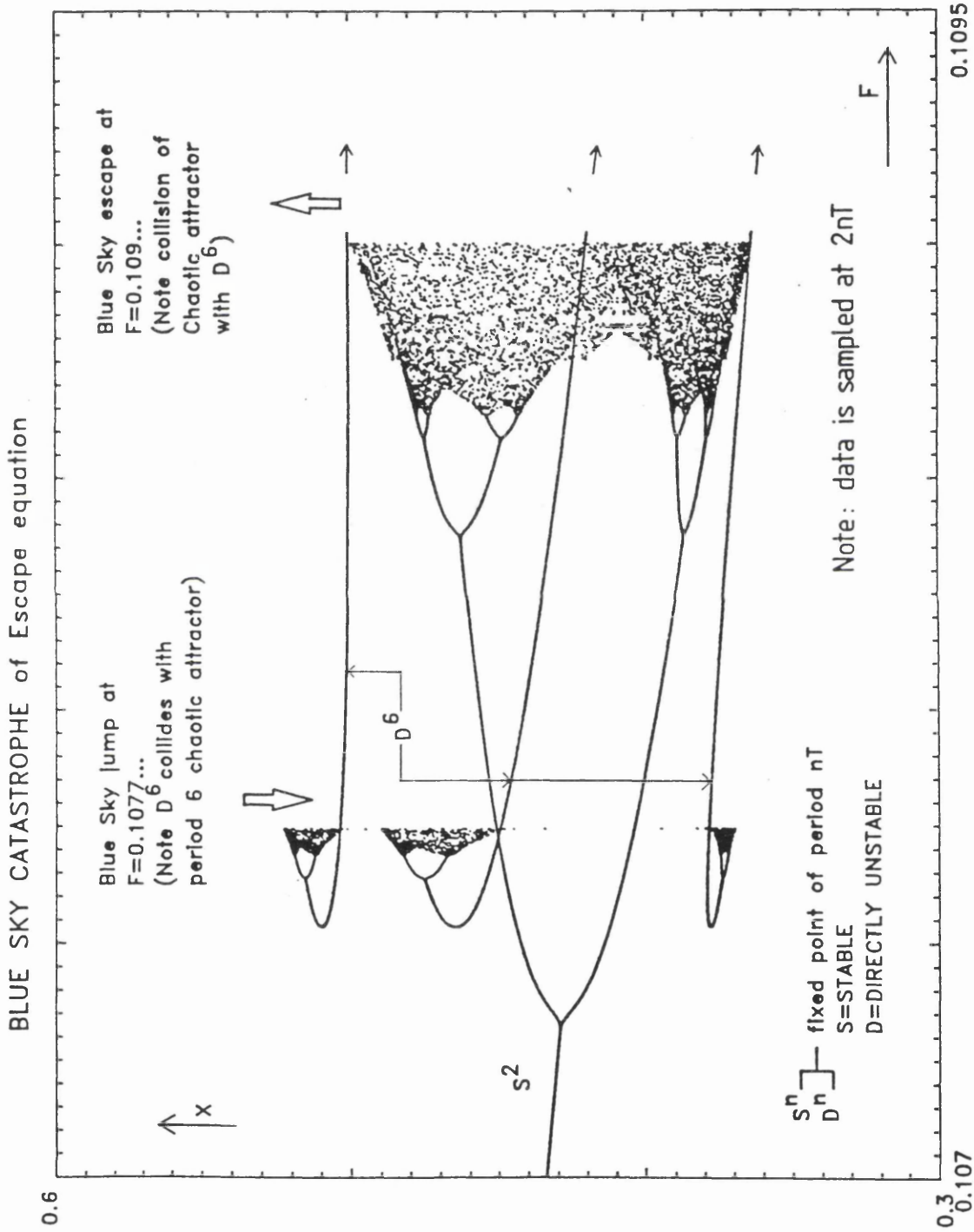
FC

Figure 82. Path of D⁶ until just before it collides with the chaotic attractor.

COLLISION of D⁶ with the two-band CHAOTIC ATTRACTOR

One band of the Chaotic Attractor at F=0.109

Path of three points of D⁶
for F=0.1072 to 0.1100 in variable steps (from path following)

Escape equation : β=0.1 ω=0.85 φ=180
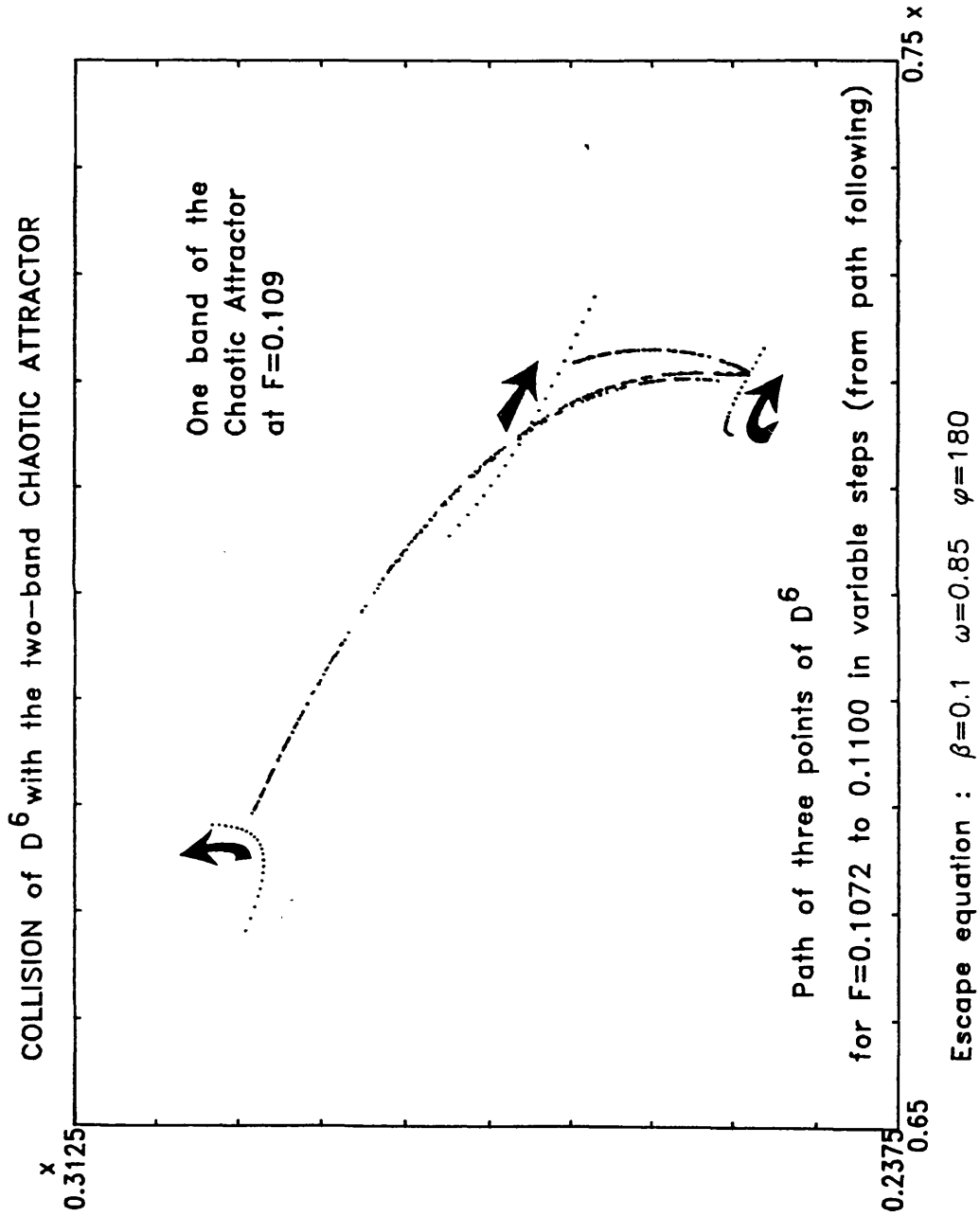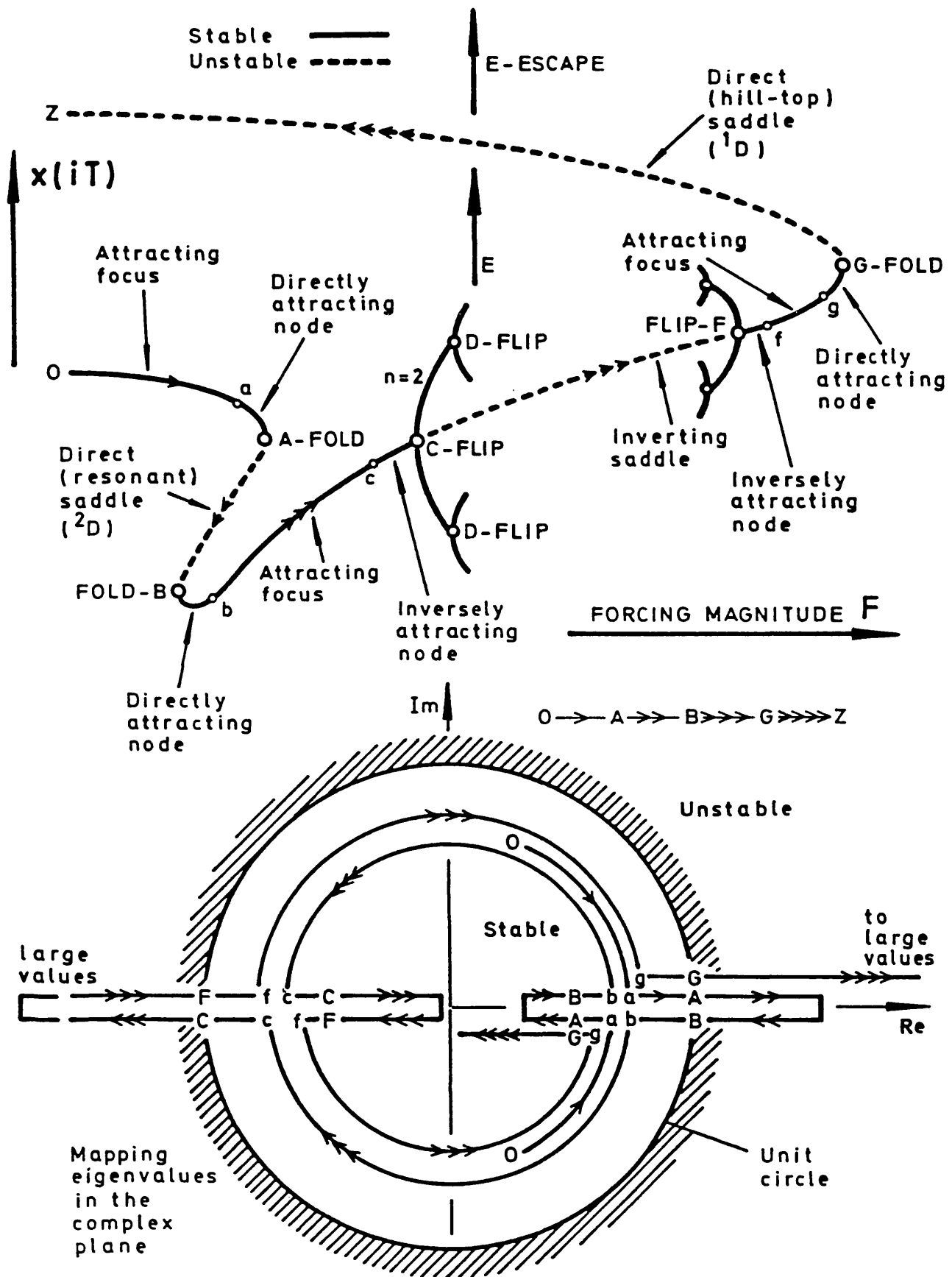
Figure 69. Schematic diagram showing the fundamental
solution path with the movement of its
corresponding eigenvalues.

Stable ──────
Unstable ━ ━ ━ ━

E-ESCAPE

$x(iT)$

Z ━ ━ ━ ━ ━

Direct
(hill-top)
saddle
(^{1}D)

Attracting
focus

Directly
attracting
node

Attracting
focus

G-FOLD

E

D-FLIP

FLIP-F

g

$n=2$

A-FOLD

Directly
attracting
node

Direct
(resonant)
saddle
(^{2}D)

C-FLIP

c

f

Inverting
saddle

Inversely
attracting
node

FOLD-B

b

Attracting
focus

D-FLIP

Directly
attracting
node

Inversely
attracting
node

FORCING MAGNITUDE F

Im

$O \longrightarrow A \ggg B \ggg G \ggg Z$

Unstable

O

Stable

large
values

to
large
values

F — f c — C

B — b a — A

g — G

C — c f — F

A — a b — B

Re

G — g

O

Mapping
eigenvalues
in the
complex
plane

Unit
circle

AT CONSTANT β AND ω THE PRODUCT OF THE EIGENVALUES IS CONSTANT

FC

Figure 84. Numerical solution path and its corresponding
eigenvalues.
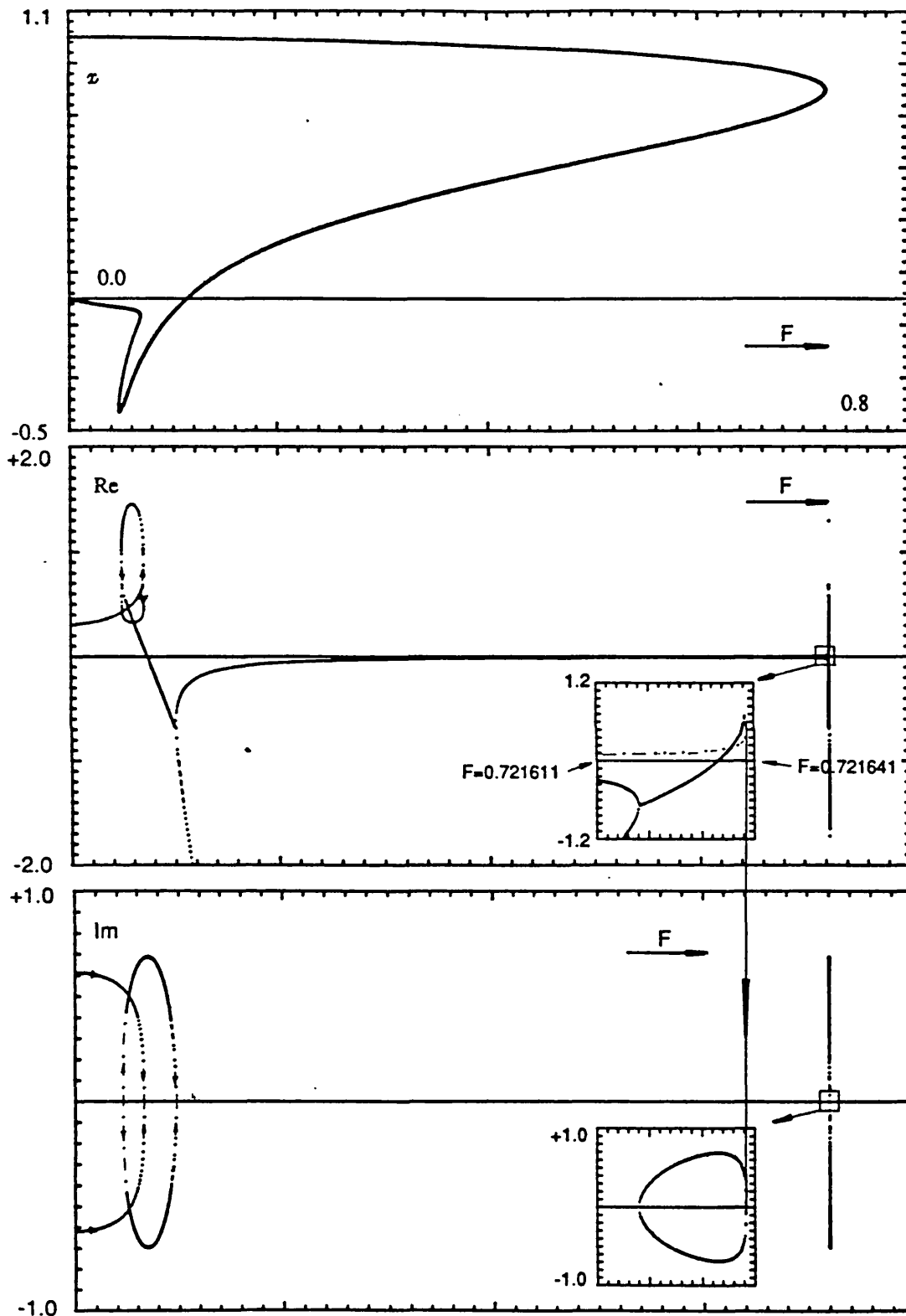
Escape equation, parameters: φ=0 ω=0.85 β=0.1

Figure 85. Schematic diagram of the three dimensional control space of the escape equation.

RESPONSE SURFACE:

Directly unstable n=1

Inversely unstable n=1

--- Inversely unstable n=2

CONTROL SPACE
Folds of n=1:
  G——G
  A——P——B
Flip of n=1:
  C——R——F
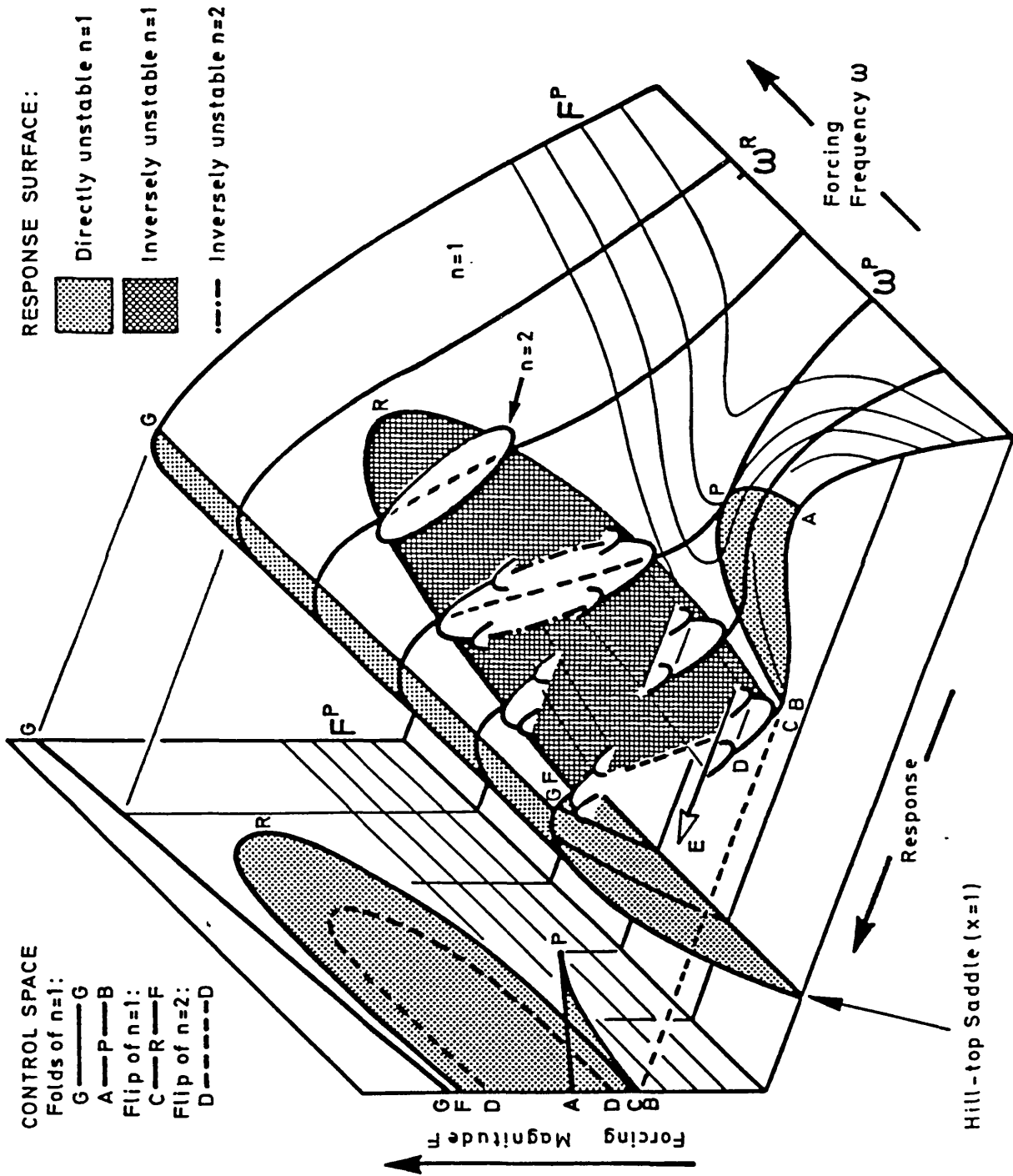Flip of n=2:
  D------D

FC

- 208 -

Figure 86. Numerical evidence of a remerging Feigenbaum
tree and degenerated period-doubling.